# Quantitative 3D real-space studies of arrested colloidal structures and processes

Cover: ‘Visie op kleine dingetjes’ by Henny van Ham
Pencil eraser print on paper, Dordrecht, 2019


PhD thesis, Utrecht University, the Netherlands, 2019.
ISBN: 978-90-9031500-3
Printed by: ProefschriftMaken || www.proefschriftmaken.nl
A digital version of this thesis is available at www.colloid.nl

# Quantitative 3D real-space studies of arrested colloidal structures and processes

---

Kwantitatieve 3D studie van stilstaande colloïdale structuren en processen in de reële ruimte

(met een samenvatting in het Nederlands)

Proefschrift

ter verkrijging van de graad van doctor aan de Universiteit Utrecht op gezag van de rector magnificus, prof. dr. H.R.B.M. Kummeling, ingevolge het besluit van het college voor promoties in het openbaar te verdedigen op maandag 18 maart 2019 des middags te 12.45 uur

door

Ernest Benjamin van der Wee

geboren op 22 december 1985 te Almelo

**Promotor:** Prof. dr. A. van Blaaderen

# Contents

# 1

# Introduction

## 1.1 Soft matter and colloids

The research field of soft matter studies systems which show drastic alterations in their properties at mild chemical or physical changes [1, 2]. For soft matter these mild changes happen typically due to thermal fluctuations, and the energies of the changes are therefore on the order of a few $kT$, where $k$ is Boltzmann's constant and $T$ the (absolute) temperature. Due to the sensitivity to the small fluctuations, the materials can easily be manipulated with external fields, such as shear and electric fields [3, 4]. Nature displays a large variety of examples of soft matter: viruses, DNA, proteins, milk, among others [2, 5]. In addition, a lot of man-made soft matter materials are present in daily life, made in the food, cosmetics, pharmaceutical, chemical and technological industries: mayonaise, creams, paints, break fluids, (smart) drug delivery systems, (electronic) ink, liquid crystal displays, *etc.* [2, 5].

One classical soft matter system is the colloidal dispersion, where particles of one phase are suspended in a continuous phase of another phase. These particles (colloids) have a typical size in the range of roughly $10^0$ to $10^3$ nm, and therefore undergo Brownian motion: a random motion induced by the continuous collisions of the much smaller atoms or molecules in the continuous phase surrounding the particles. The most well known example of a colloidal dispersion in daily life is milk: a dispersion of fat globules in water, stabilized by proteins. With the invention of the microscope in the 17th century it became possible to study the microscopic world, where Brownian motion is observable. Observations of this motion were made by Anthonie van Leeuwenhoek, Jan Ingenhousz, Lazzaro Spallanzani, Georges Buffon and John Bywater [6], but it was Robert Brown who first realized in the years 1827-1829 that the motion was not due to the particles being alive, as these motions were present for both organic and inorganic particles [7, 8]. It was until much later that the explanation for this phenomenon, the continuous collisions of atoms and molecules onto the colloidal particles, was accepted.

In the years 1905 and 1906 William Sutherland, Albert Einstein and Marian Smoluchowski independently published theories to describe Brownian motion [9–11]. The theory for Brownian motion was prove for the existence of atoms and molecules and allowed for the measurement of Avogadro's number [12]. In 1908 Jean Perrin experimentally measured both the translational as well as the rotational diffusion of particles made from the resins gamboge and mastic using light microscopy, confirming the theory posed a few years earlier [13, 14]. His work meant the final prove for the existence of atoms and molecules, and he was awarded with the Nobel Prize in Physics in 1926 [12].

Colloids are a powerful model system to study physical phenomena present in condensed matter physics such as homogeneous [15, 16] and heterogeneous crystal nucleation [17], and the glass transition [18–20]. Due to the much larger dimension of the colloids with respect to atoms or small molecules, the dynamics are slowed down by many orders of magnitude. While the colloids in the experiments by Perrin were made by the precipitation of resin, polymer and glass (silica) colloids are now widely employed for colloid research. The possibility to synthesize different monodisperse colloids, with either charge or steric stabilization, has enabled the realization of a large range of colloidal interactions.

### Hard spheres

The most simple colloidal interaction potential is that of a hard sphere. Similar to billiard balls, hard spheres are impenetrable. The absence of any attractions between the particles makes that their phase behavior is only governed by entropy [21]. The interaction potential $U(r)$ between two hard particles can be described as:

$$\begin{aligned} U(r) &= \infty && (r < \sigma) \\ U(r) &= 0 && (r \geq \sigma), \end{aligned}$$

where $r$ is the distance between the particles and $\sigma$ the diameter of the particles. Due to the simplicity of this interaction, it was the first atomic model system studied in computer simulations in the fifties of the 20th century [22, 23]. In experiments using (non-thermal) ball bearings the density of random close packed hard spheres (0.64), a jammed state where the particles are stuck in an entropic unfavorable state, was measured [24, 25].

More optimal packings are the face-centered cubic (FCC) and hexagonally close-packed (HCP) crystal structures, where in both cases a volume fraction of 0.74 can be reached. Both structures are composed of hexagonally packed layers of spheres, but both are stacked on top of each other in a different order. In the FCC structure the first, second and third layers are all shifted with respect to each other, after which the fourth layer resembles the first layer, resulting in a repeated *..ABCABC..* stacking. In the HCP structure the third layer already resembles the first layer, resulting in a repeated *..ABAB..* stacking. The stacking of the FCC structure results in a cubic unit cell where the particles occupy all the vertices (or corners) as well as the centers of all the faces of the unit cell. The hexagonally packed layers of the FCC structure correspond to the (*111*) planes of the unit cell. The HCP structure, however, is described by a hexagonal prism unit cell, where the two basal planes are formed by two similar stacked ($A$ and $A$) hexagonally packed layers, with in between a triangle of particles from the $B$ stacked hexagonally packed layer. Although Johannes Kepler already posed in 1611 that the FCC and HCP packing were the most optimal packing for spheres [26], the formal mathematical proof was accepted only recently in 2017 [27].

It was in 1986 that work on the first experimental realization of a Brownian hard sphere system was published by Peter Pusey and William van Megen, showing, like in simulations, a phase behaviour controlled by the density of the particles alone [28]. In this study sterically stabilized particles composed of the polymer poly(methyl methacrylate) (PMMA) were suspended in a mixture of non-polar solvents. The solvents were close to refractive index matched as well as sterically stabilized by a polymer coating, supressing the attractive van der Waals attractions between the particles. The authors also found that colloids were *nearly* hard sphere, as a slight larger effective size of the particles was found. This could have originated from the compressabilty of the stabilizing polymer or a slight charging of the particles, resulting in a softness of the particle interaction potential. To this day, the slight charging of colloidal particles is a still mayor challenge in the realization of an ideal experimental hard sphere system, where the particles are both refractive index and density matched [29].

### Charged spheres

Another interesting colloidal system is that of charged spheres. Here, the similarly charged particles repel each other over a distance controlled by the particle charge and the presence of ions in the continuous phase, which can be several times the particle's own diameter. This can result in soft, low density crystals known as Wigner crystals, first observed in a colloidal system composed of viruses [30]. The interaction of charged colloids can best be described by that of a hard-core screened-Coulomb or Yukawa potential [31]:

$$\beta U(r) = \infty \qquad (r < \sigma)$$
$$\beta U(r) = \beta\epsilon_{r=\sigma}\frac{exp(-\kappa(r-\sigma))}{r/\sigma} \qquad (r \geq \sigma),$$

where $\beta$ is the inverse of $kT$ and $\beta\epsilon_{r=\sigma}$ the potential at contact, given by:

$$\beta\epsilon_{r=\sigma} = \frac{\beta Z^2}{(1+\kappa\sigma/2)^2}\frac{\lambda_B}{\sigma},$$

where $Z$ is the particle charge and $\kappa$ the inverse Debye length. The Debye length is a measure for the length scale over which the repulsion due to the charge on the particles is felt by the other particle. This length scale is dependent on the concentration of ions, which screens the charges on the colloids, and is expressed by:

$$\kappa = \sqrt{4\pi\lambda_B\rho_i},$$

where $\rho_i$ is the number density of monovalent ions and $\lambda_B$ the Bjerrum length:

$$\lambda_B = \frac{\beta e^2}{4\pi\epsilon_0\epsilon_r},$$

where $e$ is the electron charge, $\epsilon_0$ the permittivity of free space and $\epsilon_r$ the dielectric constant of the continuous phase.

The first realizations of long range repulsive colloids were polystyrene or silica colloids in water, where the concentration of ions was decreased using deionized water and ion exchange resins and the interparticle distances were several times the particle diameter [30, 32]. The self-dissociation of water makes it hard to realize ion concentrations in water below 1 $\mu$M, which corresponds to a Debye length $\kappa$ of $\sim$300 nm. This limits the particle size to $<$200 nm to obtain Wigner crystals in water. In 2003 a colloidal system of PMMA particles in halogenated hydrocarbons was introduced, where the particles were 4 $\mu$m in diameter, but still a crystal with interparticles distances 6.5 times the particles diameter was reported [33]. In this system, the Debye length could be tuned from long range repulsive ($\kappa\sigma < 1$) to that of a nearly hard sphere system ($\kappa\sigma > 20$) by the addition of salt.

The phase behavior of the long range repulsive charged colloidal spheres has been studied in experiments and simulations, where next to the FCC structure, also the body-centered cubic (BCC) crystal structure was found [31, 34]. The BCC structure has a cubic unit cell, where both the vertices of the cell, as well as its center is occupied by particles.

The packing density of a close packed BCC crystal is 0.68, somewhat lower than that of the FCC or HCP structures.

The low density long range repulsive crystals are interesting as the space between the particles allows for compression of the crystals, resulting in a change of the optical properties of the crystal. This has been used to develop optical sensors of stress, temperature, chemical species and pH [35–39] and tunable optical filters for Raman scattering [36, 40]. Interestingly, the long range repulsive FCC and BCC crystals are predicted to have a negative Poisson ratio (or are auxetics), in other words, upon stretching the crystal gets thicker in the direction perpendicular to the applied force [41].

### Attractive interactions

The most well known but at the same time most unwanted attractive interaction between colloids is due to the van der Waals forces [42]. These forces arise from permanent, induced and spontaneous electric dipoles in the colloids, resulting in an interaction with a deep minimum, leading to the aggregation of the particles too strong to overcome by thermal fluctuations ($\sim$kT). This makes the interactions unwanted. One of the ways to prevent these forces is by dispersing the particles in a refractive index matching solvent (mixture), although this does not fully prevent the attractive forces, as the index matching most often only covers a small range of the electro-magnetic spectrum. Another way to prevent the aggregation due to the van der Waals forces is by steric stabilization of the particles. Here, polymers are attached (either by adsorption or chemically bound) to the surface of the particles. As the polymer chains of two particles can not physically overlap, the particles are prevented from coming too close to each other and being affected by the van der Waals forces.

A more wanted attractive interaction is the depletion interaction [43]. To induce this interaction, a non adsorbing polymer or smaller particles are added to the colloidal suspension. Around the colloidal particles there is a shell where the center of mass of the additives can not come: the exclusion zone. If then the colloidal particles touch, the total excluded volume of the system is minimized, maximizing the entropy. This induces an effective interaction between the colloids: the depletion interaction. By changing the size and/or the concentration of the additive, the effective interaction between the particles can be tuned. In the case of anisotropic particles, for example cylinders, this interaction is orientation specific: the particles will have a preference for a side-to-side confirmation [44].

When an alternating current (AC) field is applied to a dispersion of colloids with a mismatch of the dielectric constants of the particles and the continuous phase, an electric dipole is induced in the particles [4]. This results in an angle dependent interaction between the particles. The strength of the interaction depends on the dielectric contrast, the particle size and the magnitude of the applied field. In the line of the applied electric field the particles are attracted, while at an angle more than 54.7° the particles are repelled [45]. This leads to the formation of chains of particles in the direction of the field, which assemble into sheets or even body-centered tetragonal (BCT) crystals upon increasing the density of the particles. The BCT crystal is essentially a stretched BCC crystal (in this case stretched in the direction of the electric field).

### Complex colloids

In recent years, advanced synthesis methods have enabled the realization of colloids with a wide variety of shapes: cubes, discs, ellipsoids, rods, hexapods, cones, *etc.* [46, 47]. These anisotropic shapes make for a much richer phase behavior and allow for the design of far more complex materials then possible with just spheres alone [48, 49]. In addition to different shapes, directional or anisotropic interactions on colloids has increased the possibilities of designing new assemblies even further [46–48]. These interactions are realized by making patches on the particles, where the patches differ in (chemical) composition from the rest of the particle. The most classical and simple example is the Janus particle, named after the ancient Greek god Janus with two faces, looking into the future and the past [50]. The difference in the (chemical) properties of the patches with respect to the rest of the particle, for instance charge, DNA grafting, roughness or hydrophilicity, results in rotation specific interactions. This has resulted in the assembly of particles into lattices that can not be realized with particles with isotropic interactions, for instance the open Kagome lattice [51].

A relative new field of colloidal science is the study of active colloids [52]. These colloids do not only undergo Brownian motion, but also have an additional propulsion. These particles are often called self-propelled and rely on the constant addition of energy into the system. This energy can be added by for instance an applied external field (electric or magnetic) [53] or the presence of chemical fuel, with an optional activation by (UV) light [54].

### Self-assembly of colloids

The bottom-up assembly of functional materials has been one of the key focuses in the field of colloid research [21, 55, 56]. Since the interactions of colloids are typically on the order of a few $kT$, thermal fluctuations allow for the equilibration of the system to its energetically most favorable state. By designing the colloidal building blocks, a desired structure can than be obtained. This process is referred to as self-assembly: the system assembles itself into a structure. As colloids can be manipulated by external fields, these fields can be used to influence the assembly itself, through a process called directed self-assembly [4, 57, 58]. As described above, a wide variety of colloidal particles have been developed in recent years, with different shapes, materials and interactions, as well as self-propelled particles. This expansion of the toolkit for the self-assembly of functional materials has led to new materials, and will so in the future [59, 60]. The assembly of colloids into assemblies can lead to materials properties that are not just the sum of the properties of the colloidal building blocks, as collective properties can arise from specific stuctural arrangements [61, 62]. The spacing between the particles and/or the local symmetry of the particles can give rise to altered optical, catalytic and magnetic behavior [62, 63].

An example of this is the photonic crystal: a colloidal assembly with periodicity in the structure with a length scale on the order of the wavelength of light [64]. This periodicity in the structure forbids the propagation of light with a wavelength similar to this length scale, resulting in a stop band, where the light is reflected by the material. This phenomenon is abundant in nature and can be found in the iridescence of the feathers of birds, the

scales of beetles, opal stones, butterfly wings, chameleon skin, *etc.* [64–67]. As the sizes of colloids are on the order of the wavelength of light (from UV to near infrared), they make for ideal building blocks of photonic crystals, which can be made very cheaply through self-assembly. These materials could play a key role in the transition from electronics to the much faster photonics [68].

While a full (or angle independent) stop band has been realized by making an inverse FCC photonic crystal (air pockets in silicon) in the infrared [69], full-band-gap materials with a stop band in the visible spectrum by self-assembly are still to be developed. For this the attention has been turned to the (cubic) diamond and pyrochlore structure, which both have a full photonic bandgap at an experimentally realizable dielectric contrast [70]. As these two structures are open structures (34% volume packing), they cannot be formed by simple assembly of hard spheres. Instead, two different approaches have been studied: assembly using directional interactions [71, 72] and assembly of pre-assembled clusters and spheres into binary structures [73, 74]. In the first, the colloids are directed into the assembly of the diamond structure using for instance DNA functionalization [72] or DNA scaffolding [71]. In the second approach the diamond and pyrochlore structures are realized through the assembly of pre-assembled tetrahedra and single spheres into the $MgCu_2$ Laves phase, which is composed of the interpenetrating diamond and pyrochlore sub-lattices [70]. By removing one of the two sub-lattices after the assembly of the $MgCu_2$ structure, a material with a full photonic band gap remains. While the $MgCu_2$ structure composed of a binary hard sphere mixture has a higher free energy per particle than the $MgZn_2$ Laves phase [70, 74], pre-assembling the smaller particles into tetrahedra makes the $MgCu_2$ favorable over the $MgZn_2$ structure. Although the use of DNA mediated interactions have enabled the assembly of photonic crystals with the diamond symmetry and a periodicity comparable to the wavelength of the visible spectrum, the size of these crystals is limited [72, 73].

## 1.2 Microscopy

**Light microscopy**

The first observations of colloids were made with the help of the first light microscopes, as these microscopes enabled the ability to resolve objects small enough to undergo Brownian motion. The earliest version of light microscopes were transmission or bright field microscopes: light was focused on the sample from one side, while an objective (composed of one or more lenses) on the other side was used to focus the light onto the microscopist eye. The resolving power of such a microscope depends on the numerical aperture (NA) of the objective, where the NA is expressed as:

$$\mathrm{NA} = n \; sin \; \theta,$$

where $n$ is the refractive index the objective is working in (typically 1 (air), 1.33 (water), 1.47 (glycerol) or 1.52 (immersion oil)) and $\theta$ the maximal angle of the half cone of light that can exit or enter the objective [75]. The Rayleigh criterion can be used to estimate the resolving power of an objective in the lateral plane, perpendicular to the optical axis

of the microscope:

$$r_{XY} = 0.61\frac{\lambda}{\mathrm{NA}},$$

where $\lambda$ is the wavelength of the light passing the objective [75]. For the axial direction, parallel to the optical axis, the resolving power can be estimated by [75]:

$$r_Z = \frac{2\ \lambda\ n}{\mathrm{NA}^2}.$$

For a microscope equipped with an oil objective with a NA of 1.4, imaging at a wavelength of 500 nm, a lateral resolving power of ∼220 nm is found, whereas in the axial direction, the resolving power is much worse at ∼780 nm. As bright field microscopy relies on the scattering of the light due to the refractive index differences in the sample, the thickness of the sample under study is limited. The addition of fluorophores (fluorescent dye molecules) in the sample, enables the study of the sample through fluorescence microscopy, where the illumination or excitation light is separated from the much weaker emission light. In epi-fluorescence microscopy, the excitation light is focused on the sample using the same objective to collect the emission light, resulting in the ability to study the surface of samples too thick for light to pass through. Still, this technique is limited by the density of fluorophores, as out-of-focus light is collected by the objective, limiting the use to thin or low fluorophore density samples.

Confocal laser scanning microscopy (CLSM) overcomes this problem [75]. By scanning the sample point by point with an excitation laser and simultaneously recording the emission intensity, a (3D) image of the sample can be recorded. While the most well known CLSM technique is the point scanner, where the sample is scanned by a single set of mirrors, faster scanning techniques such as line scanning, multi-point and spinning disk are also used, but all with a compromise in resolving power [75–78]. In CLSM the out-of-focus light is blocked out by placing a pinhole in front of the detector, enabling the imaging of thick samples in 3D. In addition, this gives rise to a theoretical improvement in the resolving power by a factor $\sim\sqrt{2}$. In practice, the pinhole can not be infinitesimal, resulting in an improvement to ∼200 nm in the lateral and ∼500 nm for the axial direction for imaging with a 1.4 NA oil objective [75, 76].

A common way to assess the performance of a microscope is through the measurement of the point spread function (PSF) or the microscope response function: the result of imaging a point source with the microscope. This is commonly done by imaging fluorescent beads with a size well below the resolving power [79, 80]. Alternatively, beads with a size equal or close to the resolving power are imaged, after which the image is deconvolved with the volume of the bead, resulting in the PSF of the microscope [81]. In Figure 1.1a the PSF of a Leica SP8 TCS point scanning confocal microscope equipped with a 100×/1.4 NA oil objective is shown as obtained using the latter method. The particles were 200 nm fluorescent polystyrene beads, deposited on a cover glass ($n = 1.52$) and embedded in immersion oil ($n = 1.52$), ensuring the index matching of all components. The resulting image was deconvolved with a 200 nm diameter sphere using Huygens software (Scientific Volume Imaging). When a mismatched sample ($n \approx 1.45$) is imaged using the same objective, an elongated PSF with secondary maxima (tails) away from the objective is

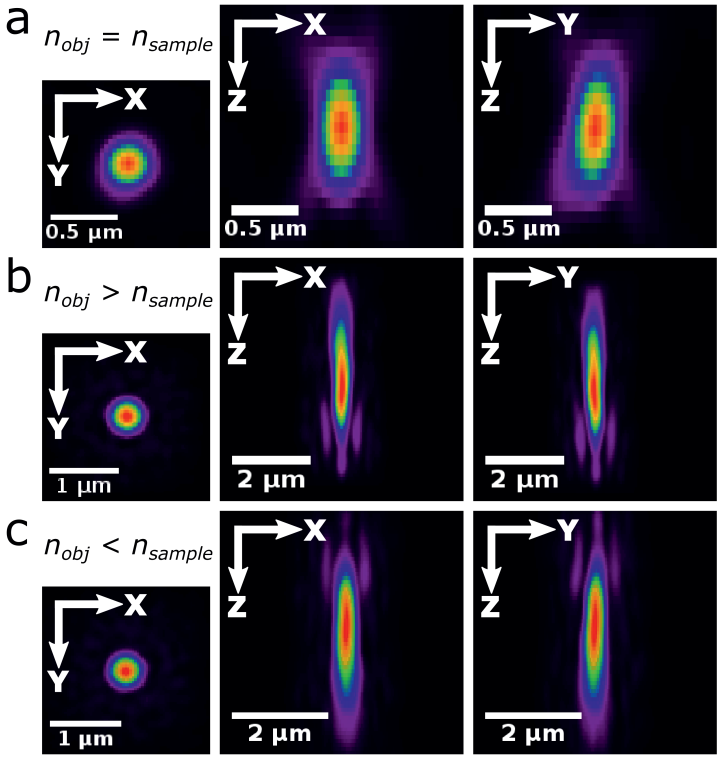


**Figure 1.1: Experimental point spread functions (PSF) of a Leica SP8 TCS point scanning confocal microscope.** PSFs obtained by recording 200 nm fluorescently labeled polystyrene beads deposited on a cover glass and embedded in a liquid, and a consequent deconvolution with a 200 nm sphere using the software Huygens (Scientific Volume Imaging). The microscope objective is located at the top of the images. a) PSF recorded with a 100×/1.4 oil objective, where the working medium of the objective, the cover glass and embedding liquid are refractive index matched ($n = 1.52$). b) PSF recorded with the same objective, but with a mismatched cover glass ($n = 1.46$) and embedding liquid ($n = 1.45$), resulting in an elongated PSF with more pronounced secondary maxima (or tails) pointing away from the objective, due to spherical aberrations induced by the mismatch. c) PSF recorded with a 100×/1.35 glycerol objective with a $n = 1.45$ working medium, while the cover slip and embedding medium are both $n = 1.52$, resulting in a similar elongated PSF, but up-side-down with respect to the PSF in (b).

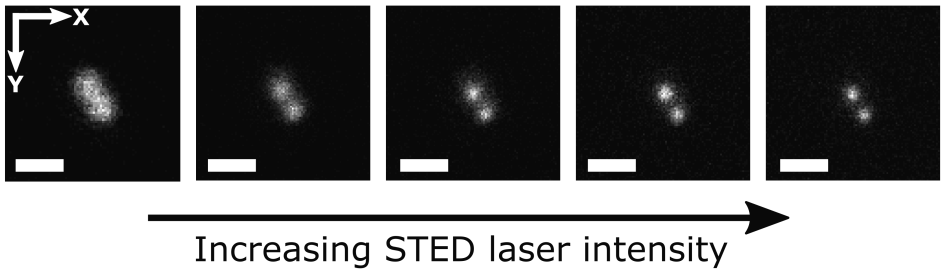


**Figure 1.2: Resolving power of stimulated emission depletion (STED) microscopy as a function of the intensity of the depletion laser.** Stimulated emission depletion microscopy images of a pair of 237 nm silica particles. The particles are composed of a 16 nm gold core, followed by a 34 nm thick fluorescently labeled silica shell and a 77 nm thick non-fluorescent silica shell. With the depletion laser at zero intensity the images of the particles overlap, while upon increasing the depletion laser intensity, the resolving power of the STED microscope increases. Scale bars are 500 nm.

obtained (see Figure 1.1b). When the mismatch is inverted, the PSF is found to turn upside down (see Figure 1.1c). While these PSFs were recorded at the cover glass, the distortion of the PSF due to spherical abberations is amplified when imaging further away from the cover glass [82, 83]. Therefore, refractive index matching the sample to the working medium of the objective is essential for maintaining the resolving power of the confocal microscope deep into the sample. For the 3D study of colloidal dispersions with confocal microscopy, this also means the particles should be refractive index matched with the continuous phase. Classic combinations include silica particles in water/glycerol or water/dimethyl sulfoxide mixtures and PMMA particles in cyclohexyl bromide (CHB)/cis-decalin mixtures, where in the latter the particles are also density matched to the solvent mixture [84].

In addition, knowledge of the PSF of a microscopy setup enables image restoration by deconvolution of the image with the PSF [85, 86]. This results in an increase of the resolution of the confocal data, especially in the axial direction where the effect of the blurring due to the PSF is largest. The knowledge of the depth dependent PSF even allows for the restoration of samples with a refractive index different from the medium of the objective [87].

Whereas confocal microscopy is limited to a resolving power of ∼200 nm in the lateral and ∼500 nm in the axial direction for a 1.4 NA oil objective, super-resolution (or super-resolved) techniques, such as stimulated emmision depletion (STED) microscopy, photo activated light microscopy (PALM) and stochastic optical reconstruction microscopy (STORM), have enabled imaging beyond the diffraction limit [88]. STED microscopy is an extension to confocal microscopy, where an additional depletion laser is added to the optical path [89]. This depletion laser has a wavelength at the higher wavelength end of the emission spectrum of the fluorophore in the sample. For 2D STED, where an improvement in the lateral resolving power is realized, the depletion laser is focused into a donut shaped

spot which is superimposed to the excitation laser spot. The fluorophores excited by the excitation laser are brought back to their ground state by stimulated emission induced by the strong depletion layer. Since there is a small spot in the center where the fluorophores have not been depleted, the emission from this spot can be recorded, resulting in a probed spot smaller than the diffraction limit. By increasing the intensity of the depletion laser, the hole in the donut can be made smaller, resulting in a higher resolving power. In Figure 1.2 the effect of the depletion laser intensity is demonstrated on imaging two adjacent 237 nm core-shell silica particles with a 84 nm fluorescently labeled core. While without the depletion laser the two particles can not be distinguished, upon increasing 2D STED laser intensity, the images of the two particles become well separated.

Initially the improvement of the resolving power of STED microscopy was only realized in the lateral (2D) plane, resulting in resolving powers well below 50 nm. More recent, STED has been extended to the axial direction, where resolving powers below 150 nm have been realized [89–91]. Using the extension of STED to 3D a colloidal crystal composed of 7 layers of 200 nm fluorescently labeled latex particles could be characterized [92]. STED microscopy is very sensitive to the alignment of the excitation and depletion lasers [93–95]. As these lasers have different wavelengths, STED requires chromatic aberration corrected objectives and benefits from objectives equipped with a correction collar, to correct for minor refractive index mismatches [94, 96].

### Electron microscopy

For particles in the lower part of the colloidal size range, *i.e.* smaller than ∼400 nm, light microscopy lacks the resolving power to study dense assemblies of these particles. With sub-nanometer resolving powers, electron microscopy can be used to image these assemblies. In addition, electron microscopes are often used for the characterization of colloidal particles after synthesis. In scanning electron microscopy (SEM) a beam of electrons is raster scanning the surface of the specimen. Simultaneously detectors measure the emission of low energy secondary or high energy back-scattered electrons from the sample. This results in a very detailed image of the sample's surface. For 3D imaging of an assembly of small colloids, the SEM can be combined with a focused ion beam (FIB) [97–99]. By repeated milling of slices of material with the FIB and imaging with the SEM, a 3D image stack of the assembly can be acquired. Here the milling step is the limit in the resolving power, where currently for gallium based FIB a reproducible step size of a few nanometer is possible.

With transmission electron microscopy the sample is exposed to a focused electron beam, while the electrons passing through are detected. This results in a high resolving power where single atoms can be identified. As the electrons need to pass through the sample, the thickness of the sample is limited to <500 nm, depending on the electron density of the material. It is therefore an appropriate technique to study assemblies of particles a few nanometer in size [100]. For quantitative 3D analysis of these assemblies transmission electron tomography can be used [101–103]. Here, the sample is imaged at different orientations from which the 3D structure can be reconstructed. As the electrons should be able to pass through the sample at every orientation of the sample, the preferred shape of the assembly is that of a sphere, as the path length of the electron through

the sample will remain constant. Consequently there have recently been more studies on such spherical assemblies (referred to as supraparticles) of nanoparticles, of which a comprehensive review is given in the introduction of ref. [104].

#### Particle fitting and tracking

Where microscopy allows for the study of colloids, in combination with particle fitting and tracking a direct comparison to computer simulations can be made. John Crocker and David Grier published an algorithm in 1996 for the fitting and tracking of particles in 2D light microscopy images using IDL [105], which has been translated to several other programming languages since [106–109]. In the algorithms the particle positions are determined by finding the centroid of the intensity blobs of the particles in the image, resulting in a sub-pixel accuracy of the obtained coordinates. For 3D confocal data sets, the particles positions in all lateral ($XY$) image planes can be identified, after which the axial ($Z$) coordinates can be obtained by fitting the intensity of the particles in the axial direction with a Gaussian distribution [18, 106, 110, 111]. Next, the fitted coordinates of subsequent frames can be linked into trajectories, enabling calculations on the dynamics of the colloidal dispersion. In recent years a lot of refinements to the classic algorithm have been published [112–119]. Moreover, a multitude of algorithms has been developed for the fitting of anisotropic particles, such as ellipsoids [120, 121], colloidal clusters [122], rods [123] and core-shell ellipsoids [124], as well as spheres [102, 103], rods [123] and cubes [125] from electron tomography data.

## 1.3 Outline of this thesis

In **Chapter 2** we describe the characterization of colloidal assemblies in the nanometer and micrometer range with focused ion beam-scanning electron microscopy (FIB-SEM) and particle fitting. We show that this method can fill the gap left by confocal microscopy and transmission electron tomography. In **Chapter 3** a sample is presented which can be used for the alignment, calibration and point spread function measurement of confocal (STED) microscopes. The sample is composed of a colloidal crystal of silica particles with a fluorescently labeled or gold core, embedded in a refractive index matching medium. Next, in **Chapter 4** a simple method is presented to arrest colloidal dispersions and processes by the polymerization of the continuous phase. This allows for the characterization of dynamic colloidal dispersions too fast for confocal imaging for a wide variety of particle interactions. In addition, we show that the method enables the preservation of meta-stable structures induced by external fields. In **Chapter 5** the method is applied to the structural study of nearly hard sphere nuclei formed in homogeneous nucleation. The method allows for the acquisition of large data sets composed of ∼500,000 particles. Finally, in **Chapter 6** we study supraparticles composed of Laves phases of binary nanoparticles using transmission electron tomography. The real-space analysis allows us to study the defects in the Laves phase. In addition, we find that a slight adjustment to the particle stoichiometry can have large consequences for the obtained crystal structure.

## 1.4 Acknowledgements

We thank Jantina Fokkema and Marc del Pozo Puig for synthesis of the silica particles. The confocal and STED microscopy images were recorded in collaboration with Peter Speets.

# 2

# 3D real-space characterization of colloidal assemblies with FIB-SEM tomography

The 3D real-space study of colloidal particle assemblies generally relies on light, electron or X-ray microscopy. These techniques enable the structural analysis of nano- to micrometers sized colloids on a single particle level. However, the imaging of large assemblies of 10-500 nanometer sized colloids remains challenging. Here, we demonstrate that focused ion beam-scanning electron microscopy (FIB-SEM) tomography in combination with image processing is capable of extending the quantitative real-space study of ordered and disordered colloidal assemblies of both nanoparticle and microns-sized particles. We illustrate that this technique can be used for the structural analysis of small anisotropic nanoparticles in spherical assemblies too thick for transmission electron tomography. In addition, we demonstrate its use in the structural characterization of large ordered and disordered assemblies containing colloids with a diameter close to the resolution limit of confocal microscopes. Using recently developed particle tracking routines, we determined both the position and orientation of each individual (nano)particle in the colloidal assemblies. The FIB-SEM methodology is not limited to index matched systems and extends the range of colloidal structures that can be analyzed quantitatively on the single particle level significantly. Such high precision structural information is essential in the understanding and design of the collective properties of new colloid based materials and processes.

## 2.1 Introduction

Assembling colloidal particles in larger ensembles gives rise to collective properties different from those of the individual particles [57, 61, 62]. The collective properties critically depend on the position and orientation of the colloidal particles. Depending on the interparticle spacing, local and global symmetry, the plasmonic, magnetic or electronic coupling between the particles can be tuned, giving rise to altered optical, catalytic and magnetic properties [62, 63, 99, 126–128]. The final 3D structure of colloidal assemblies also provides insight in the assembly process and the interactions between the colloidal particles. For example, assembled structures formed in or out of equilibrium contain information on the phase behaviour or on the glass transition/aggregation of the colloidal particles during the assembly, respectively [15, 19, 92, 100, 125, 129–138].

Various scattering- and microscopy techniques have been used to access the structural properties of these particle assemblies. While scattering techniques can directly probe long-range periodic order averaged over macroscopic volumes [139], microscopy techniques reveal local structures at a single particle level in real-space. Microscopy studies therefore provide insight in the presence of defects, which strongly influence the material properties and are generally very hard to determine by scattering techniques, as these usually average over large numbers of particles and have a strong bias in detecting order over local disorder [140].

Depending on the applied radiation source - X-rays, electrons or visible light - particle assemblies can be studied at different length scales, ranging from angstroms to micrometers. X-ray microscopy techniques enable real-space imaging of the material's local structure [141–143], whereby the large penetration length of X-rays makes it possible to study thick and opaque colloidal assemblies [142] in 3D [144, 145]. Nowadays, the spatial resolution of X-ray microscopy can be as low as 10-30 nm with a sample thickness of 0.05-20 $\mu$m depending on the X-ray energy and the material properties of the sample [146]. However, the image acquisition can only be carried out at a synchrotron facility and irradiation damage can occur, especially in soft polymer based systems [147].

For a significantly higher resolution (0.1-0.5 nm), transmission electron microscopy can be used to obtain real-space structural information. Scanning electron microscopy (SEM) allows imaging of the assembly's exterior and provides information on the surface structure, whereas transmission electron microscopy (TEM) and, in particular, transmission electron tomography in combination with particle fitting algorithms reveal the positions and orientations of the particles in the interior of the colloidal assemblies [100–103, 125, 148, 149]. When there is a sufficient difference in Z-contrast between two types of colloidal particles, 3D characterization of binary systems becomes feasible as well [101]. An important problem in the quantitative interpretation of tomography data, is the fact that it is not possible to image the object of interest over the full 180° range. This so-called missing wedge problem causes artefacts in the reconstruction. In addition, the limited penetration depth of the electron beam in larger assemblies and high Z-contrast materials limits the maximum assembly size that can be quantitatively characterized to $\leq$500 nm [100, 103].

Light microscopy techniques, on the other hand, have larger penetration depths [150]. When the sample is refractive index matched and a dye is incorporated in the particles, confocal microscopy is capable of resolving large assemblies of >500 nm colloids in

3D [18, 76, 112, 151, 152]. The sample thickness can be up to 300 $\mu$m for high NA objectives [153]. The particle positions of both spherical and anisotropic particles can be extracted using multiple particles fitting and tracking algorithms [105, 110, 123, 154]. In order to improve the resolvability of the particles, image restoration techniques using the point spread function (PSF) of the microscope can be used [86]. The advent of super-resolution techniques, such as stimulated emission depletion (STED), have made it possible to image colloidal assemblies at even higher resolutions. The axial ($Z$) direction resolution is still limiting but has been brought down recently below 100 nm allowing particle sizes of 200 nm still to be resolved in 3D [88, 89, 92]. However, STED microscopy requires better dyes and is sensitive to refractive index mismatching. In practice, large confocal-like volumes are not easily imaged with STED either. This means that neither X-ray nor conventional electron nor light microscopy, are able to image large sample volumes of (non-index matched) materials at a nanometer resolution.

Focused ion beam-scanning electron microscopy (FIB-SEM) does offer the unique opportunity for high resolution 3D real-space imaging of large, hundreds or thousands of cubic microns with a resolution down to a few nanometers [97, 98]. FIB-SEM relies on a dual beam approach, using both a focused ion and electron beam. Herein, both beams usually have their own column and lens system, allowing them to operate independently. The FIB scans a focused beam of gallium ions onto the sample surface. The momentum transfer of the gallium ions results in sputtering, a process called milling. Precision milling results in trenches at predetermined locations, allowing the SEM to record high-resolution images of cross sections of the material of interest. Consecutive slices as thin as 3 nm can be FIB milled, while the SEM records high resolution images in between the milling. This process is called FIB-SEM tomography. Successful examples of FIB-SEM tomography are found in many disciplines and it has been applied to *e.g.* inorganic nanomaterials [99, 155, 156], photonic crystals [67, 157], biological tissue [158, 159] and porous geological materials [160].

In this chapter, we demonstrate the use of FIB-SEM tomography in the 3D characterization of colloidal assemblies with nano- to micrometer sized colloidal particles. We compare these results to conventional TEM tomography and confocal microscopy characterization. First, we apply high resolution FIB-SEM tomography on a nanoparticle assembly, composed of thin silica coated Au nanorods. In this case, we show that transmission electron tomography can only be used for assembles with less than 100 particles, due to the high Z-contrast of the Au nanorods, whereas FIB-SEM tomography can be used to obtain the particle coordinates *and* orientation for ensembles with >1000 particles. Next, we demonstrate the use of FIB-SEM tomography to analyze the structure of large ordered and disordered assemblies, which are generally much harder to analyze in real-space than crystalline assemblies, with single and binary species of $\sim$0.5 $\mu$m sized silica colloidal particles. We compare the results obtained through FIB-SEM tomography with confocal microscopy in combination with image restoration and show the limitations of the latter.

## 2.2 Methods

### 2.2.1 Silica coated gold nanorod assemblies

The preparation of the gold nanorod based assemblies consisted of four steps: colloidal synthesis of high aspect ratio AuNRs (I), silica coating (II), OTMS coating (III) and self-assembly into spherical ensembles (IV).

The synthesis of high aspect ratio AuNRs was done according to the procedure by Ye *et al.* [161]. The growth mixture consisted of CTAB (7.0 g), sodium oleate (1.23 g), Milli-Q (MQ) $H_2O$ (250 mL), $AgNO_3$ (9.6 mL, 10 mM), $HAuCl_4$ (250 mL, 1.0 mM), HCl (37%, 4.8 mL), ascorbic acid (1.25 mL, 0.064 M) and gold seeds (0.40 mL). The seed solution was prepared by adding an icecold $NaBH_4$ in $H_2O$ solution (1.0 mL, 0.0060 M) to a mix of CTAB (10 mL, 0.10 M) and $HAuCl_4$ aqueous solution (51 $\mu$L, 50 mM). The resulting rods were centrifuged for 25 min at 8000 g, washed with water and re-dispersed in 30 mL 5.0 mM CTAB water ($\lambda_{LSPR}$=1250 nm, Ext=4.8, ∼40 mg/L). The resulting AuNRs had a length of 119 nm and diameter of 16 nm.

The thin silica coating was carried out as follows: to the AuNRs (1.0 mL, $\lambda_{LSPR}$=1250 nm, Ext=4.8) sodium silicate (0.15 mL, 0.54 wt% $SiO_2$) was added while stirring vigorously. The mixture was stirred for 45 minutes at room temperature after which the rods were washed with water and ethanol, and re-dispersed in ethanol (200 $\mu$L, [Au]≈200 mg/L).

To disperse the rods in an apolar solvent like cyclohexane the silica shell was made hydrophobic by coating it with octadecyltrimethoxysilane (OTMS). To this end, the silica-coated AuNR dispersion (750 $\mu$L) was diluted with ethanol (1.75 mL) to which OTMS (250 $\mu$L) and butylamine (125 $\mu$L) were added. The mixture was sonicated for 2 h at 30-40 °C. Thereafter, the reaction mixture was centrifuged at low speed (100 g for 5 min), washed with toluene, centrifuged at 7000 g for 10 min, washed twice with cyclohexane (2.0 mL) and redispersed in cyclohexane (250 $\mu$L, [Au]≈600 mg/L).

The spherical $SiO_2$@AuNR supraparticles were made via emulsification of an apolar particle dispersion in a larger polar phase [123]. The polar phase consisted of dextran (400 mg) and SDS (50 mg) dissolved in $H_2O$ (10 mL). The apolar phase consisted of cyclohexane (200 $\mu$L) containing OTMS-functionalised silica-coated AuNRs ([Au]≈600 mg/L). The emulsification was done by shortly pre-mixing the apolar and polar phase in a vortex shaker after which it was placed in a sonication bath for 1 minute. Afterwards, the vial was covered with parafilm containing several small holes and the cyclohexane droplets in the emulsion were slowly dried overnight by shaking in an orbital shaker (IKA KS260 basic). The resulting particles assemblies were collected with centrifugation (500 g for 15 min), washed with $H_2O$ (8 and 2 mL), and redispersed in $H_2O$ (500 $\mu$L).

### 2.2.2 Colloidal silica assemblies

Monodisperse 531 nm spherical core-shell silica colloids with gold and fluorescent cores were synthesized in an approach also described in Chapter 3. 15 nm gold cores were grown using the inverse sodium citrate reduction method [162, 163]: $HAuCl_4$ (3.4 mL, 25 mM) was added to a boiling solution of sodium citrate in water (345 mL, 1.0 mM) under constant vigorous stirring. After 15 minutes, water (155 mL) and sodium citrate

solution (5 mL, 2.2 mM) were added to the obtained deep red solution. After reheating and boiling for an additional 10 minutes the solution was cooled down to 90 $^o$C. Growth of the seeds to 30 nm was performed in four steps using a kinetically controlled seeded growth procedure [164]: for every growth step sodium citrate (1.7 mL, 120 mM) and $HAuCl_4$ (1.7 mL, 50 mM) were added followed by 60 minutes stirring at 90 $^o$C. 100 mL of the obtained solution of gold nanoparticles was functionalized with polyvinylpyrrolidone (PVP) [165] by the addition of PVP (5 mL, 10 mM, $Mw = 10.000$ g/mol) and 16 hours stirring. The functionalized particles were transferred to ethanol by centrifugation (10 min, 15.000 g, 5 mL eppendorfs) followed by redispersion in ethanol (100 mL).

Fluorescent rhodamine B labeled cores with a diameter of ∼45 nm were synthesized using a reverse micro-emulsion method [166, 167]. Rhodamine B isothiocyanate (RITC) was coupled to (3-aminopropyl)triethoxysilane (APTES) prior to the synthesis by mixing RITC (6.0 mg), absolute ethanol (500 $\mu$L) and APTES (12.0 $\mu$L) and stirring for 5 hours. The reverse micro emulsion was prepared by mixing cyclohexane (50 mL), igepal CO-250 (6.5 mL), tetraethyl orthosilicaat (TEOS, 400 $\mu$L) and fluorophore-APTES complex (50 $\mu$L). Particle growth was initiated by the addition of ammonia (750 $\mu$L) and after homogenization the solution was stored for 24 hours. The cyclohexane was removed by rotary evaporation under reduced pressure and the obtained pink viscous liquid was diluted in dimethylformamide (10 mL) and ethanol (10 mL) to obtain a clear pink solution.

Next, in two separate reactions, the gold and fluorescent cores were coated with a non-fluorescent silica to obtain a total diameter of ∼200 nm using a seeded growth procedure based on the Stöber method [168–170]. After cleaning via repeated centrifugation and redispersion in ethanol, the weight fractions of both solutions were determined, which were used to prepare a 1 to 100 (gold to fluorescent core) mixture in ethanol. Further silica growth was performed to obtain particles with a total diameter 531 nm (<2% polydispersity index (PDI), 100 particles, transmission electron microscopy), after cleaning by repeated centrifugation and redispersion in ethanol to remove small silica spheres caused by secondary nucleation.

396 nm monodisperse core-shell silica colloids with a fluorescent core were synthesized in the following way. First, using a reverse microemulsion method [166], a silica core of about ∼50 nm was synthesized [167]. Next, using the seeded Stöber growth method [168], a fluorescein isothiocyanate doped silica shell was grown around the core to a diameter of ∼200 nm [171], followed by two silica shells without dye, arriving at a total diameter of 396 nm (1% PDI, static light scattering).

For the assembly of a colloidal crystal of the 531 nm silica particles, an adaption at elevated temperature of the method by Jiang *et al.* [172] was used to speed up the evaporation process [173]. A cover glass (#1.5H) was placed under a small angle (∼5°) inside a particle in ethanol dispersion (8 mL, 1 v%) inside a 20 mL vial. Together with a 100 mL beaker filled with ethanol the vial was placed in a 50 °C preheated oven (RS-IF-203 Incufridge, Revolutionary Science) and covered with a large beaker placed upside down. After 16 hours the cover glass was removed from the dispersion and a crystal had formed on the cover glass. Any particles sticking to the back of the cover glass were removed by wiping it with an ethanol soaked tissue.

### 2.2.3 TEM tomography

The transmission electron microscopy (TEM) tomography was performed on a FEI Talos F200X operated at 200 kV in HAADF-STEM mode. A droplet of aqueous dispersion containing the AuNRs@$SiO_2$ assemblies was dried on a special tomography copper grid with parallel bars and a R2/2 Quantifoil film (Electron Microscopy Sciences). The tomography grid was placed in a high tilt holder (Fischione, FP90997/19 tomography holder). The sample was tilted from -70 to +70° with a tilt step of 2°. Data processing, comprising alignment of the tilt-images via cross-correlation and subsequent reconstruction using a SIRT algorithm (100 iterations), was carried out in TomoJ (2.31) [174].

### 2.2.4 FIB-SEM measurements

The AuNR assemblies dispersion was dropcasted on an aluminium SEM stub with a conductive carbon tape on top and dried overnight. The colloidal crystal and binary glass were first infiltrated with a resin to fill the air pockets between the particles. To this end, the colloidal crystal and binary glass were embedded in resin (Lowicryl HM20) and cured overnight in an oven at 65°C. The cover glasses with the colloidal crystal and the binary glass were attached on an aluminum SEM stub with carbon tape. To prevent charging of the samples under the electron beam, a conductive pathway was created by bridging the top of the cover glass and the stub with a strip of carbon tape. Additonally, the colloidal crystal and binary glass were coated with a 5 nm thick layer of platinum, using a Cressington HQ280 sputter coater.

The FIB-SEM tomography of the AuNR assembly was performed in a Helios Nanolab G3 UC FIB-SEM (Thermo Scientific) under high-vacuum conditions ($10^{-6}$ mbar). *In situ* Pt deposition (∼200 nm thick) was accomplished across an AuNR supraparticle by the FIB, prior to the tomography routine. Subsequently, the FIB (30 kV, 7.7 pA) milled 160 consecutive slices with a width of 2.5 $\mu$m and a nominal slice thickness of 3 nm. The SEM (2 kV, 100 pA) recorded images in SE and BSE mode (Ultra-High Resolution mode) with a scan resolution of 2304×2048 pixels per image, 0.324×0.411 nm/pixel and dwell time 3 $\mu$s/pixel.

FIB-SEM tomography of the colloidal crystal was performed in a Scios FIB-SEM (Thermo Scientific). Standard preparation procedures (Pt deposition, milling of trenches and polishing of the cross section to be imaged) were performed manually prior to the execution of the tomography routine. The FIB (30 kV, 300 pA) milled 212 consecutive slices with a width of 22 $\mu$m, a calculated depth of 20 $\mu$m and a nominal slice thickness of 50 nm. The SEM (3.5 kV, 100 pA) recorded images (3072 x 2048 pixels, pixel size 10 nm, dwell time 6 $\mu$s) with the T1 detector in BSE mode.

FIB-SEM tomography of the binary glass was also performed in a Scios FIB-SEM (Thermo Scientific). Again, standard preparation procedures were performed manually. Following, the FIB (30 kV, 300 pA) milled 100 consecutive slices with a width of 35 $\mu$m, a calculated depth of 15 $\mu$m and a nominal slice thickness of 50 nm. The SEM (3.5 kV, 100 pA) recorded images (3072 x 2048 pixels, pixel size 9.4 nm, dwell time 6 us) with the T1 detector in BSE mode.

### 2.2.5 Confocal microscopy

For confocal microscopy imaging, the binary glass was index matched with a glycerol/*n*-butanol mixture ($n_D^{23} = 1.44$). A Leica TCS SP8 confocal microscope equipped with a super continuum white light laser (SuperK, NKT Photonics), a HyD detector and a 100×/1.4 NA confocal objective was used to image the glass. The sample was sequentially scanned with the pinhole set to 1 airy unit to, first, image the rhodamine B dyed particles with the excitation laser set to 550 nm and the detection range from 565 to 687 nm and, second, the FITC dyed particles with the excitation laser set to 488 nm and the detection range from 498 to 590 nm. The voxel size was $31 \times 31 \times 50$ nm$^3$ ($X \times Y \times Z$).

### 2.2.6 Deconvolution

The confocal image stack was deconvoluted with a theoretical point spread function using the classic maximum likelihood estimation restoration method in the Huygens software (17.04, Scientific Volume Imaging) to a final signal-to-noise ratio of 20.

### 2.2.7 Particle identification

To find the positions and orientations of the rods we used the algorithm as described by Besseling *et al.* [123]. We colored the rods depending on their orientation with $c_{\text{red}} = |n_x|$, $c_{\text{green}} = 1/2 - n_y/2$ and $c_{\text{blue}} = 1/2 - n_z/2$ where $n_x, n_y$ and $n_z$ are the components of the normalized orientation vector $\mathbf{n}$ along the length of the rod.

To determine the positions of the spherical particles in the FIB-SEM datasets we used a new algorithm of which we will give short description here, the full details will be published separately [154]. After alignment and an initial filtering step the images were blurred with a Gaussian blur (typically with $\sigma = 1.0$ pixels), to remove noise. Next, the gradients of the image were calculated in the $x$, $y$ and $z$ directions resulting in 3 bitmaps $(G_x, G_y, G_z)$ containing both negative as well as positive values. We also produced a kernel from an ideal image containing a single particle with the same dimensions as the particles that we want to locate and blurred this by the same amount. We then calculated its gradients in 3D $(K_x, K_y, K_z)$ and the convolution (by FFT) of the gradient images with the kernel $G_x * K_x + G_y * K_y + G_z * K_z$, this final image can be seen as Hough transform [175] and produces a sharp peak at the location of each particle. We then found all local maxima in this image brighter than a predetermined threshold and fitted their position with a quadratic function to obtain sub-pixel accuracy. For the binary sample, we used several (typically 10) kernels for particles with an increasing diameter and searched for a maximum in the resulting 4D dataset ($x$, $y$, $z$ and diameter). The distribution of sizes was fitted with two Gaussians and the intersection of the two (475 nm) was chosen to distinguish the small and large particles in the assembly.

The positions of the particles in the confocal data sets were determined after image restoration using an extension to 3D [18, 110] of a classic 2D tracking algorithm [105].

### 2.2.8 Quantitative analysis

Radial distribution functions were calculated in the following way from the coordinates of the particles. First, a histogram of the distances between all pairs of $N_{exp}$ particles was calculated. Next, a box, determined by the minimum and maximum values of the coordinates in all three dimensions, was filled with $N_{ig}$ ideal gas particles, of which also a pair distance histogram was calculated. The experimental histogram was divided by the ideal gas histogram, and if $N_{ig} \neq N_{exp}$ the distribution was normalized by a factor of $(\frac{N_{ig}}{N_{exp}})^2$.

From the coordinates of the particles obtained by FIB-SEM tomography the crystal structure was identified using bond orientational order parameters [176–178]. First, a set of numbers was calculated for every particle, based on spherical harmonics $Y_{lm}$:

$$q_{lm}(i) = \frac{1}{n_c(i)} \sum_{j=1}^{n_c(i)} Y_{lm}(\hat{\mathbf{r}}_{ij}), \tag{2.1}$$

where $n_c(i)$ is the number of nearest neighbors of particle $i$, $l$ an integer (in our case 4 or 6), $m$ an integer running from $-l$ to $l$ and $\hat{\mathbf{r}}_{ij}$ the unit vector pointing from particle $i$ to particle $j$. The nearest neighbours are defined as the particles within cut-off distance $r_c$ from particle $i$. This cut-off was determined from the first minimum of the radial distribution function $g(r)$, corresponding to $r_c \approx 1.4d$, where $d$ is the particle diameter. Next, the particles are considered crystalline or liquid using the Ten Wolde criterion [177]. The correlation between the $q_{lm}(i)$ of every particle with the $q_{lm}(j)$ values of its neighbors was calculated:

$$c_l(ij) = \frac{\sum_{m=-l}^{l} q_{lm}(i) q^*_{lm}(j)}{\sqrt{\sum_{m=-l}^{l} |q_{lm}(i)|^2} \sqrt{\sum_{m=-l}^{l} |q_{lm}(j)|^2}}, \tag{2.2}$$

where $q^*_{lm}(j)$ is the complex conjugate of $q_{lm}(j)$. The neighbors $j$ of each particle $i$ were considered connected when $c_l(ij) > 0.6$ and the particle $i$ was considered crystalline when the amount of connected neighbors exceeded 7. Since hexagonal order was expected, we chose $l = 6$ to distinguish crystalline and liquid particles.

Next, the crystalline particles were classified having face-centered cubic (FCC) or hexagonal close-packed (HCP) order using the $\bar{w}_l$ order parameter [178]. To calculate this, first the $q_{lm}$ set of numbers of particle $i$ is averaged with the values of its neighbors:

$$\bar{q}_{lm}(i) = \frac{1}{N_c(i)} \sum_{k=0}^{N_c(i)} q_{lm}(k), \tag{2.3}$$

where $N_c(i)$ is the number neighbors $n_c(i)$ of particle $i$ plus itself. This set of numbers then yields the rotationally invariant averaged local bond orientational order parameter:

$$\bar{w}_l(i) = \frac{\sum_{m_1+m_2+m_3=0} \begin{pmatrix} l & l & l \\ m_1 & m_2 & m_3 \end{pmatrix} \bar{q}_{lm_1}(i) \bar{q}_{lm_2}(i) \bar{q}_{lm_3}(i)}{\left( \sum_{m=-l}^{l} |\bar{q}_{lm}(i)|^2 \right)^{3/2}}, \tag{2.4}$$

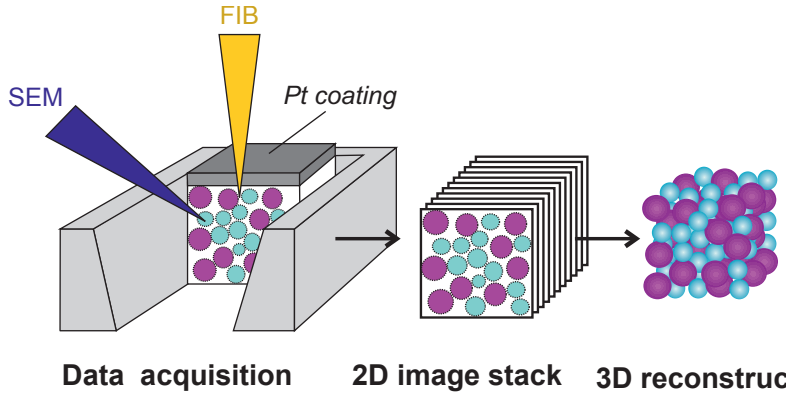


**Figure 2.1: 3D characterization of colloidal assemblies with FIB-SEM tomography.** Left: the tomography data acquisition, obtained by iteratively removing a slice of the assembly with the FIB-beam (yellow) and imaging of the assembly with the electron beam (dark blue). Middle: the obtained stack of 2D images acquired at different $Z$-depths. Right: 3D reconstruction of the particle coordinates from the 2D image stack.

where $\begin{pmatrix} l & l & l \\ m_1 & m_2 & m_3 \end{pmatrix}$ is the Wigner 3-$j$ symbol [179] and the integers $m_1$, $m_2$ and $m_3$ run from $-l$ to $+l$, but are limited to the case where $m_1 + m_2 + m_3 = 0$. The particles are classified as FCC-like when $\bar{w}_4 < 0$ and HCP-like when $\bar{w}_4 > 0$.

## 2.3 Results

### 2.3.1 FIB-SEM tomography for particle assemblies

We applied FIB-SEM tomography to two differently sized assemblies: $<1$ $\mu$m$^3$ sized nanoparticle (NP) assemblies, consisting of silica coated gold nanorods (AuNRs), and larger $\sim$1,000 $\mu$m$^3$ sized assemblies composed of micron sized silica colloids. In Figure 2.1 we depict the general approach in which FIB-SEM tomography is used in the 3D characterization of particle assemblies. The characterization can be divided in three stages: preparation of the particle assembly for imaging, acquisition of the tomography series, and data analysis, comprising the alignment of the images in the series and the fitting of the positions and orientations of the particles in 3D.

In the first step, we use two different ways of sample preparation depending on the type and size of the particle assembly. For the larger colloidal assemblies consisting of micron sized colloidal spheres, the assembly was embedded in a resin, to preserve the assembly structure during the milling process by the FIB, which is essential in correctly determining the initial particle coordinates and orientations. Thereafter, a conductive platinum layer was deposited on top of the ensemble to prevent charging during FIB-milling and/or SEM-imaging. The smaller spherical nanoparticle assemblies, called supraparticles, were not embedded in a resin, but only covered with a Pt-coating, which prevented both charging and deformation of the spherical assembly shape during the milling process. In the

second step tomography data was acquired. The slice thickness was varied for the different colloidal particle sizes and was set such that at least 6 slices through each individual particle were obtained. In the final step, the SEM images were aligned and the coordinates and orientation of the individual particles determined. For the AuNR supraparticles a rod fitting algorithm was used [123], while for the colloidal crystal and binary glass the particle coordinates were obtained using a recent gradient tracking algorithm [154].

### 2.3.2 High resolution 3D imaging of gold nanorod assemblies

For the FIB-SEM tomography on nanoparticle based assemblies, we prepared ∼200 nm to 2 $\mu$m large spherical supraparticles of silica coated gold nanorods ($l$ = 123 nm, $\sigma$ = 20 nm). This type of nanoparticle system is particularly interesting for Raman spectroscopy, where the Raman enhancement depends on the overlap between the surface plasmons of the individual gold particles, and thus on the precise position and orientation of the nanorods [99, 180]. To obtain the AuNR assemblies, we first synthesized colloidal gold nanorods [161] coated with a 3 nm thin silica shell, functionalized with a hydrophobic coating [181, 182]. Subsequently, the rods were assembled in spherical clusters by using a solvent evaporation method [102], that we recently also applied to rod-like particles [123] (See method section for details).

We applied both conventional transmission electron tomography and FIB-SEM tomography, to obtain the 3D structure of the AuNR assemblies. In Figure 2.2 we show the electron- and FIB-SEM tomography results for the characterization of a small and larger AuNR supraparticle, of which the spherical shape is best suited for TEM tomography [100, 103, 123, 125, 126] Figure 2.2a-c shows the tilt series, reconstruction and 3D model of a 230 nm assembly obtained via transmission electron tomography. In the 3D model the rods are color-coded based on their orientation, showing that the rods are preferentially ordered in the same direction. For this relatively small assembly, the positions and orientations of all 96 rods could successfully be obtained from the 3D reconstruction. However, for this type of system transmission electron tomography can only be applied to small particle assemblies, due to the limited penetration depth of the electron beam caused by the high Z-contrast of the Au atoms. To illustrate this we show in Figure 2.3 the transmission electron tomography results for a larger, 340 nm AuNR ensemble, for which no longer a high quality reconstruction could be obtained.

To access the full structural properties of larger and/or denser assemblies, we applied FIB-SEM tomography. In Figure 2.2d-f we show the secondary electron (SE) image of the exterior, the FIB-SEM slice-and-view series of the interior and the 3D reconstruction of a 500 nm AuNR supraparticle. In order to reliably distinguish the individual NRs, the lowest possible $Z$ step size of 3 nm had to be used, such that at least 6 slices per rod were obtained. The tomography series consisted of 160 $XY$-slices (2304×2048 pixels), spaced 3 nm apart resulting in a voxel size $X \times Y \times Z$ of 0.3244 × 0.411 × 3 nm. The total imaged volume was 0.300 $\mu$m$^3$. The particles coordinates and orientations were determined by making use of a rod fitting algorithm [123]. From the FIB-SEM tomography data set in Figure 2.2e, we obtained the positions and orientations of 1,279 rods.

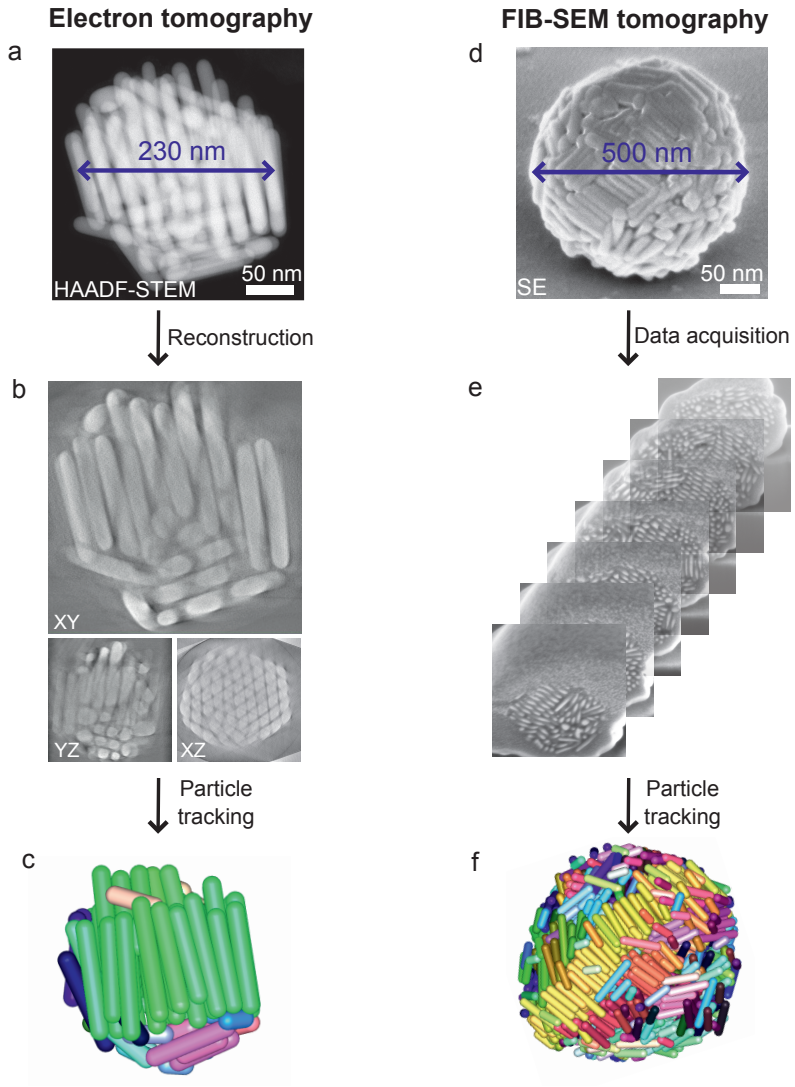


**Figure 2.2: 3D characterization of differently sized silica coated gold nanorod assemblies with electron- and FIB-SEM tomography.** Left: Transmission electron tomography of small AuNRs@$SiO_2$ assembly with $\sigma \approx 230$ nm, consisting of 96 nanorods: a) Single HAADF-STEM image, acquired at $0^o$ tilt, b)$XY$, $YZ$ and $XZ$ view of the assembly's interior, after reconstruction of the tilt series, c) tracking of the position and orientation of the nanorods in 3D, where the rods are colored according to their orientation. Right: FIB-SEM tomography of larger AuNRs@$SiO_2$ assembly with $\sigma \approx 500$ nm, consisting of 1,279 nanorods: d) SE-image of the exterior of the AuNRs@$SiO_2$ assembly, e) SE image acquired while milling into the interior of the assembly with the FIB, f) 3D representation of the tracked AuNRs in the assembly.

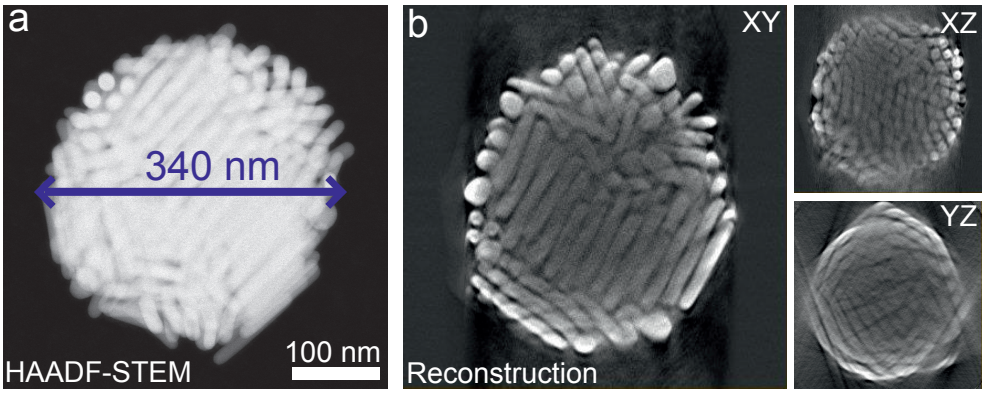


**Figure 2.3: Transmission electron tomography result for Au@$SiO_2$NR assembly with $\sigma \approx$ 340 nm, which is too large for a reliable reconstruction.** a) 0° tilt image, acquired in HAADF-STEM mode. b) $XY$, $XZ$ and $YZ$ views of the 3D reconstruction. The tilt series was acquired from -70 to +70° with a tilt step of 2°. Reconstruction was done by performing a weighted back projection.

### 2.3.3 FIB-SEM tomography of a colloidal crystal

To demonstrate the feasibility of FIB-SEM tomography to also analyze colloidal assemblies of particles with dimensions at the upper range of the colloidal domain, we prepared a colloidal crystal of monodisperse silica spheres ($\sigma = 531$ nm). About one percent of the particles had a 30 nm gold core, whereas the other 99 percent had a 45 nm fluorescently (rhodamine B isothiocyanate, RITC) labeled core. The crystal was grown by controlled vertical deposition at elevated temperature onto a cover glass [172], resulting in a thickness of $\sim$11 $\mu$m (which corresponds to $\sim$25 layers).

In Figure 2.4a we show a slice from the FIB-SEM tomogram, which was recorded with a pixel size in $X$ and $Y$ of 10.5 nm and a milling step size in $Z$ of 50.0 nm, with a total volume of 2,610 $\mu m^3$. The inset in Figure 2.4a shows a gold core in one of the silica particles, demonstrating the possibility of investigating multiple length scales in hierarchical assemblies using FIB-SEM tomography. From the full data stack we cropped a volume of 1,000 $\mu m^3$ (dashed cyan rectangle in Figure 2.4a) for reconstruction, see Figure 2.4b. Using a gradient tracking algorithm [154] the particle coordinates were obtained, as we show in Figure 2.4c where the particles positions are depicted by the cyan circles.

To get insight in the structure of the crystal, we calculated the bond orientational order of every particle in the assembly [178]. In Figure 2.4d we show a computer rendering of the particle assembly, where the particles are colored according to their local symmetry. Although the majority of the particles have local face-centered cubic (FCC) symmetry, the particles at the bottom of the reconstructed volume are packed locally with hexagonal close-packed (HCP) symmetry. Moreover, a slanted stacking fault runs through the crystal, also with local HCP symmetry. When the radial distribution function $g(r)$ is calculated from the reconstructed coordinates, a good agreement with the FCC structure is found (see

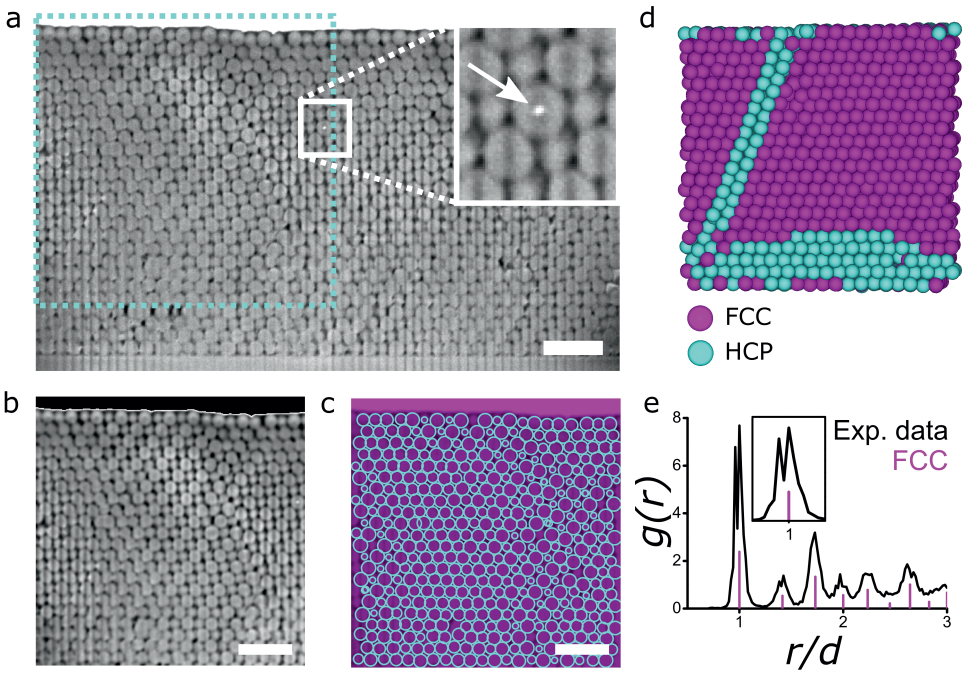


**Figure 2.4: FIB-SEM tomography on crystal of silica colloids ($\sigma = 531$ nm).** a) Slice from FIB-SEM tomogram with a total volume of 2,610 $\mu$m$^3$. Arrow in inset points at the gold core of a particle. b) Same slice, cropped to dashed cyan rectangle in (a) and processed for optimal particle identification. c) Overlay of (b) with cyan circles indicating identified particles. d) Cut-through of computer rendering of coordinates from the reconstruction in (c) with colors of particles assigned to local symmetry of particles as calculated with bond orientational order parameters showing that the crystal structure is majorly FCC (magenta) with a horizontal stacking fault at the bottom and a slanted stacking fault running through the structure, both with HCP symmetry (cyan). The reconstructed volume is 1,000 $\mu$m$^3$, with 8,891 particles. e) Radial distribution function $g(r)$ calculated from coordinates in (d) (black), compared to the peaks of an ideal FCC crystal (magenta). The inset shows the double peak in the $g(r)$ at $r/\sigma \approx 1$, due to the shrinkage in the growth direction of the crystal. The scale bars are 2 micron.

Figure 2.4e). There is however a double peak at $r/\sigma \approx 1$, which is absent in close packed crystals grown in bulk or by gravity [183]. It is known that colloidal crystals grown using the vertical deposition method are slightly deformed by a shrinkage of ∼4% in the direction of growth in the hexagonal (*111*) planes, as has been measured with X-ray diffraction [184]. From the ratio of the two values of $r/\sigma$ of the two peaks in Figure 2.4e follows this is indeed close to 4%. Confocal microscopy and FIB-SEM tomography measurements in Chapter 3 show the same deformation of a similarly assembled crystal.

### 2.3.4 Characterization of a binary colloidal glass

FIB-SEM tomography can also be used to obtain real-space information of binary particle systems. Here we intentionally made a binary glassy sample, as it is more difficult to retrieve the particle coordinates from the microscopy data with respect to a crystalline structure [185]. To demonstrate this, we mixed the previously used 531 nm RITC labeled silica colloids with smaller 396 nm silica particles, which had a fluorescently (fluorescein isothiocyanate, FITC) labeled core of ∼200 nm. For comparison, the particles were imaged with both confocal laser scanning microscopy and FIB-SEM tomography.

For confocal microscopy, the particles in ethanol were drop casted on a cover glass and refractive index matched with a mixture of glycerol and *n*-butanol ($n_D^{21}$=1.44). Image stacks of the two differently labeled particles were imaged sequentially, as shown in Figure 2.5a, spanning a volume of ∼1,200 $\mu$m$^3$. Figure 2.5b shows the stacks after image restoration using the Huygens (SVI) deconvolution software. Using a classic particle tracking routine [105] extended to 3D data sets [18, 110], we identified the coordinates of both species in the assembly. A fragment of a computer rendering of the coordinates is shown in Figure 2.5c, from which the partial radial distribution functions of the large ($g_{LL}(r)$) and small particles ($g_{SS}(r)$) were calculated (see Figure 2.5f,g).

For FIB-SEM tomography, the particles were embedded with a resin after dropcasting. With a FIB milling step size of 50 nm, a stack with a total volume of ∼1,000 $\mu$m$^3$ was recorded. From this stack, a volume of ∼500 $\mu$m$^3$ was cropped for particle identification (Figure 2.5d). The coordinates of the particles were obtained using a gradient tracking algorithm [154], where the particle sizes were fitted for every particle (Figure 2.5e). This resulted in a distribution of sizes with two peaks, where the population was divided into small and large species using a threshold diameter of 475 nm. From the coordinates of the different particles, the partial radial distribution functions $g_{LL}(r)$ and $g_{SS}(r)$ were calculated, as show in Figure 2.5f and g, respectively.

When comparing the partial radial distribution functions of the large ($g_{LL}(r)$) and small spheres ($g_{SS}(r)$) acquired using the two techniques, an agreement was found for the peak positions in the $g_{LL}(r)$, although the $g_{LL}(r)$ from FIB-SEM had a broader first peak (see Figure 2.5f). The functions for the small particles $g_{SS}(r)$, however, disagreed to a higher extend (see Figure 2.5g). The radial distribution function calculated from the coordinates obtained by confocal microscopy was non-zero at values smaller than the smallest distance the particles can be apart (∼390 nm). This points at overlapping particles due to mis-identification of the smaller particles positioned relatively close to each other in the axial direction of the confocal microscope, as reported in [115]. An example of such overlapping particles in the computer rendering of the coordinates is

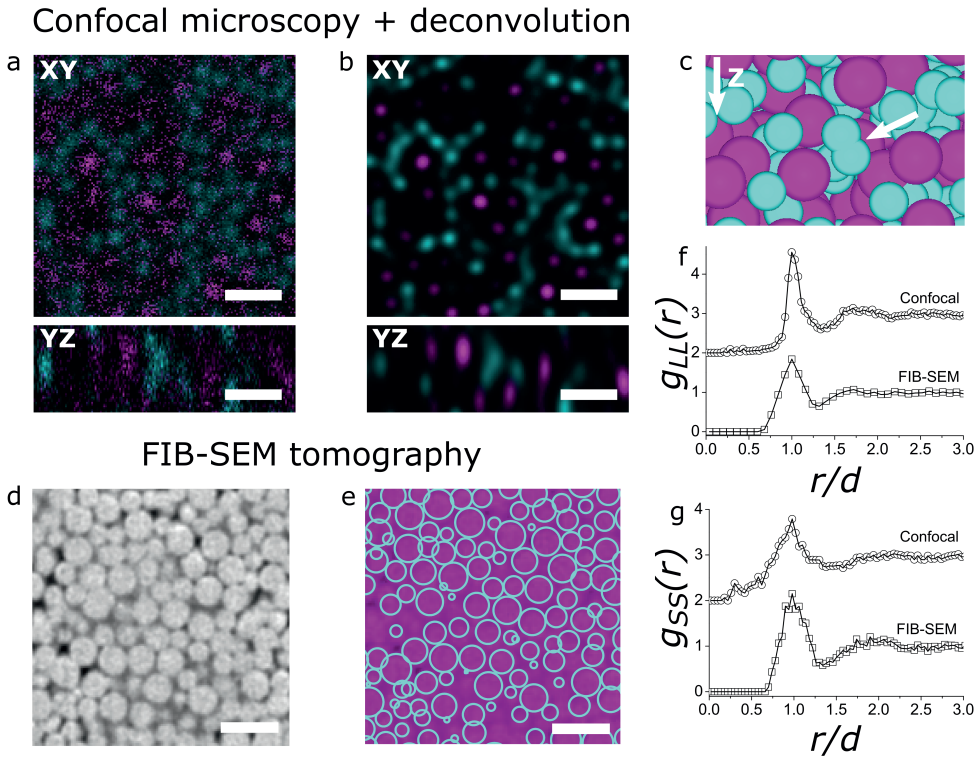


**Figure 2.5: Binary glass characterized by confocal microscopy, in combination with image restoration, and FIB-SEM tomography.** a) $XY$ and $YZ$ slices from a two channel confocal microscopy image stack of a binary glass of 396 nm fluorescein (cyan, S) and 531 nm rhodamine (magenta, L) labeled core-shell silica colloids, with a total volume of ∼1,200 $\mu$m$^3$. b) Same slices after deconvolution of the image stack. c) Fragment of computer rendering of coordinates identified from the image stack in b). The arrow points at two overlapping particles, where the particle tracking algorithm misidentified two particles with a small separation in the axial direction. d) Fragment of FIB-SEM tomogram of the same binary glass with a total volume of ∼500 $\mu$m$^3$. e) Overlay of d) with cyan circles indicating identified particles. Partial radial distribution functions $g_{LL}(r)$ (f) and $g_{SS}(r)$ (g) calculated from the coordinates obtained through confocal microscopy and image restoration, and FIB-SEM tomography. The scale bars are 1 $\mu$m.

shown in Figure 2.5c. These type of errors were absent in $g_{LL}(r)$, indicating that for the small particles, the limit of the (axial) resolving power of the confocal microscope was approached. FIB-SEM tomography, on the other hand, does have sufficient resolving power to identify the positions of the small particles correctly.

## 2.4 Discussion

### 2.4.1 Data acquisition

During the FIB-SEM data acquisition it is crucial that the colloidal particles are imaged at their original positions and orientations within the ensemble. Depending on the assembly type, different changes in the ensemble structure can occur during the tomography. Supraparticles, especially composed of NPs, are prone to deform to a more flat, non-spherical structure during FIB exposure and should therefore be encapsulated in a Pt coating before tomography. On the other hand, in the image acquisition of the assemblies composed of the micron sized colloids we noticed that particles could 'fall off' during the milling process, when the particles are no longer supported by their neighbors. This can cause a shift in the apparent position of the particles in the 3D reconstruction. To prevent this, one should embed the particle assembly in a resin prior to the image acquisition.

When imaging porous assemblies with FIB-SEM, so-called curtaining effects are likely to arise due to the different (material) densities. Curtaining occurs when the milling speed in the region of interest is inhomogeneous, resulting in different sample thicknesses in the milling direction. Such inhomogeneities in sample thickness complicate or even prohibit a quantitative reconstruction of the correct assembly structure in 3D. We observed these curtaining effects when milling the relatively porous and thick colloidal crystal and binary glass, but not for the densely packed and thin AuNR assemblies. The curtaining during the data acquisition can successfully be suppressed by embedding the colloidal assemblies in a resin beforehand. In this way, the pores in between the particles are filled, making the milling speeds more homogeneous. The remaining curtaining 'stripes' can be filtered out during the data processing by using fast Fourier transform (FFT) filtering. Herein, one calculates the FFT of the acquired image, removes the lines in the FFT patterns caused by the curtaining and performs an inverse FFT to obtain the filtered image (Figure 2.6). The curtaining effect can also be suppressed using advanced acquisition methods and image processing [186].

Another difficulty encountered during acquisition is the accumulation of charge in the sample due to the scanning electron beam, resulting in white areas in the SEM images. Although the samples were connected to the SEM stub with conductive carbon tape and coated with Pt to prevent the build up of charge, charging still occurred. One way to reduce this effect was the acquisition of SEM images at a lower beam voltage, and compensate for the loss of signal by image accumulation. Instead of modifying the acquisition parameters, the effects of charging can also be suppressed by image processing [186].

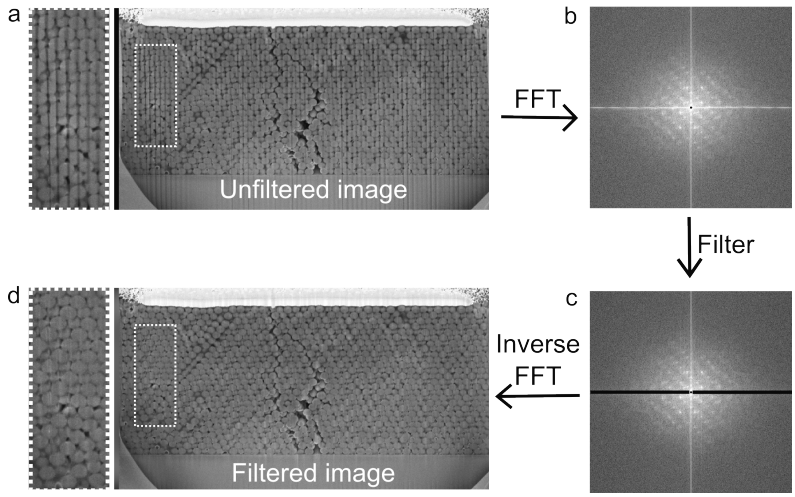


**Figure 2.6: The FFT filtering procedure to remove curtaining stripes**. a) Unfiltered image of colloidal crystal consisting of silica spheres ($\sigma$ = 531 nm). b) FFT of the image in a). c) Filtered FFT. d) The filtered image without curtaining stripes, after performing an inverse FFT of c).

### 2.4.2 Determining particle coordinates and orientations

There are several advantages in using the gradient based particle tracking algorithm used in this work. Firstly, it is not limited to the recognition of spherical particles only, but can also be applied to any anisotropic shape, such as rods and (rounded) cubes [125], plates [187] and tetrahedra [188], and therefore to a wide variety of particle assemblies. Secondly, it enables the determination of the particle orientation for each *individual* particle. The ability to exactly determine the orientation and position of each NP and all interparticle distances is crucial in, for instance, calculating the assembly's collective plasmonic properties. Previously, only average orientations of several particles per assembly volume could be obtained [99]. With our particle specific analysis method it now becomes feasible to directly compare the theoretical and experimental behavior of plasmonic particle assemblies and to predict their performance for e.g. Raman spectroscopy, which is strongly influenced by exact particle locations which can create so-called 'hot-spots'.

When there is a low Z-contrast between the particles and their surroundings, tracking is more difficult. In the spherical AuNR assembly in Figure 2.2, the Z-contrast between the Au of the NRs and the Pt of the protective coating was very low. Reliable tracking was only possible for the layers below the particle layer close to the Pt coating. Particles in or in close proximity of the Pt coating were prone to misidentification and difficult to distinguish from real particles.

### 2.4.3 Comparing the real-space microscopy techniques

We studied the AuNRs assemblies with both conventional transmission electron tomography and FIB-SEM tomography. Which method is preferred predominately depends on the size and Z-contrast of the individual nanoparticles, and the size of the total ensemble. Generally, the spatial resolution of the transmission electron microscope is superior to the resolution of the electron beam used in FIB-SEM tomography. More importantly, the resolution in the Z-direction in FIB-SEM is limited to 3 nm, which is the minimum slice thickness that can be milled with the FIB. Since a minimum of 6 slices per nanoparticle is required to reliably determine its position and orientation, FIB-SEM tomography is presently only suitable for assemblies consisting of $\geq$18 nm particles. Thus, for ensembles of small nanoparticles, transmission electron tomography is the preferred analysis technique. Still, the accuracy of the coordinates and orientations of the particles from the tracking is higher than the resolution of the FIB-SEM images, as particle tracking algorithms achieve sub-pixel accuracies [123, 133, 154].

However, for assemblies with a thickness larger than 300 nm and/or composed of high Z-contrast materials, transmission electron tomography is no longer applicable. When imaging such assemblies with transmission electron tomography, a so-called cupping artefact is likely to arise. Cupping artefacts are due to thickness dependent, non-linear damping of the recorded intensities [189]. In the 3D reconstruction this is visible as an underestimated intensity in the interior of the particle assembly, which hampers a quantitative 3D structural analysis of the particle ensembles interior. The cupping artifact is for example already visible in the reconstruction of the 340 nm AuNR assembly in Figure 2.3. Apart from post reconstruction methods to correct for the cupping effect, an alternative method to study the interior of nanoparticle assemblies larger than 300 nm is to perform microtomy prior to the transmission electron tomography measurement. Herein, one embeds the particle assemblies in a resin and cuts the sample with a diamond knife to slices as thin as 80-100 nm. Afterwards, transmission electron tomography can be performed. However, this method does not allow the analysis of a full particle assembly. Thus, to characterize a complete nanoparticle ensemble larger than 300 nm, FIB-SEM tomography is indispensable.

We also compared FIB-SEM to confocal microscopy for particle ensembles consisting of particles with a size close to the resolution limit of conventional confocal microscopy. For the binary glass (Figure 2.5) we observed that the large spheres could still be resolved with confocal microscope, but the smaller ($\sigma = 396$ nm) particles could not, even while having a core-shell morphology. The overlapping particles shown in Figure 2.5c indicate that the limit of the resolving power of the confocal microscope was reached. Despite the fact that more advanced particle fitting algorithms have been developed to increase the accuracy of particles position determination, these algorithms do not significantly lower the size limit of the smallest particles that can be imaged with confocal microscopy [112–119, 154]. By using STED one could improve both the axial and lateral resolutions significantly (even to below 100 nm), but this technique is complicated in large sample volumes and sensitive to refractive index mismatches. FIB-SEM tomography is, however, capable of quantitatively characterizing (binary) assemblies of particles too small for confocal microscopy, without the need of refractive index matching or the incorporation of dyes in the particles.

### 2.4.4 Possible future applications of FIB-SEM tomography on colloidal systems

In this study, the assemblies were composed of particles similar in size and composition. However, the high resolution of the FIB-SEM tomography would also allow the study of mixed assemblies with particle sizes ranging from 20 to 1000 nm. Either by size or the difference in material density, different particles types can be distinguished within a mixed assembly. For example, in the case of the micron size colloidal crystal, a fraction of the silica spheres contained a much smaller 30 nm, higher density gold core instead of a silica core. The gold core could be identified in the FIB-SEM image series due to its higher Z-contrast and smaller particle size (Figure 2.4a (inset)). In future research, FIB-SEM could thus be applied to fully characterize heterogeneous assemblies, e.g. photonic crystals composed of particles with strongly scattering cores.

The imaging method described in this work can also be applied to study low density colloidal dispersions. To do so, the colloidal dispersions have to be arrested prior to the imaging process. This can be done either by cryogenic quenching [190] or chemical arrest by the polymerization of the continuous phase, as described in Chapter 4. The latter technique enables a controlled timing of the arrest and would therefore allow the study of the different stages in assembly processes. Structural analysis of particle dispersions is also relevant in measuring for example the interparticle interactions, through the calculation of the radial distribution function. The high resolution of the FIB-SEM microscope would make it possible to start investigating interparticle interactions between nanoparticles, too small to be imaged with confocal microscopy.

## 2.5 Conclusions and Outlook

We have demonstrated a general approach using FIB-SEM tomography for the 3D real-space characterization of colloidal particle assemblies. We showed that this technique combines high resolution imaging with large sampling volumes, allowing the precise characterization of assemblies too large for transmission electron tomography, and containing particles too small to resolve with confocal microscopy. To this end, we first demonstrated the use of FIB-SEM tomography for the high resolution imaging of nanorod assemblies. In contrast to transmission electron tomography, the position and orientation of the individual nanorods in assemblies >300 nm could still be obtained. Next, we applied FIB-SEM tomography for the imaging of a colloidal crystal and binary glass consisting of fluorescently labeled sub-micron silica spheres for large sampling volumes ($\geq$1000 $\mu$m$^3$). From the colloidal crystal images stacking faults with local HCP symmetry could be identified in the FCC crystal. While FIB-SEM tomography was able to identify all particles in the binary glass, conventional confocal microscopy could not resolve all particles in the axial direction. Additionally, FIB-SEM tomography does not require the incorporation of dye in the particles or refractive index matching. For the data analysis we used a recently developed gradient based tracking algorithm, which can be used for different particle shapes and materials. In combination with such data analysis methodology, we have shown that FIB-SEM tomography is applicable to a broad range of materials, and particle sizes and shapes, bridging and extending several other quantitative imaging techniques.

## 2.6 Acknowledgements

The work in this chapter was done in collaboration with Jessi van der Hoeven and Petra de Jongh. Matthijs de Winter and Yang Liu are thanked for the FIB-SEM measurements, Michiel Hermes for the particle localization in the TEM and FIB-SEM data, Jantina Fokkema and Maarten Bransen for the particle synthesis, Job Fermie for the help with the sample preparation for FIB-SEM and Hans Meeldijk for EM support. Matthijs de Winter and Jessi van der Hoeven are thanked for critical reading of this chapter.

# 3

# One 3D test sample for the calibration, alignment and measurement of point spread functions of super-resolution and confocal microscopes

At present, a multitude of samples is required to monitor the quality and reliability of quantitative measurements of (super-resolution) light microscopes. In this work, one sample is presented to substitute this multitude of samples. The sample is composed of a refractive index matched colloidal crystal of silica beads with fluorescent and gold cores, and can be optimized for different objectives. The microscope can be calibrated in three dimensions using the periodicity of the crystal; the alignment of the laser lines can be checked using the reflection of the gold cores; and the point spread function (PSF) can be measured at multiple positions and depths using the fluorescent cores. It is demonstrated how this sample can be used to visualize and improve the quality of confocal and super-resolution images. In addition, it is discussed how the sample can be adjusted to meet different requirements and how it can be used to evaluate refractive index mismatches as a function of depth quantitatively.

## 3.1 Introduction

Reliable quantitative 3D light microscopy measurements require a well calibrated setup. Moreover, proper alignment of the microscope contributes to a higher resolving power, thereby enabling analysis at a smaller scale [75]. Calibration and alignment have become even more critical with the advent of super-resolution microscopy techniques, such as stimulated emission depletion (STED) microscopy [89, 93, 191]. Additionally, it has been demonstrated that image restoration with an experimentally measured 'point response function', referred to as the point spread function (PSF), allows for better image restoration than deconvolution with a theoretical PSF [75, 79, 85, 87, 118, 192]. Therefore, is it also important to be able to reliably measure the PSF of a setup.

Currently, a multitude of different samples and methods are needed for a complete evaluation of a light microscopy setup. First of all, calibration of the microscope in the lateral directions can be performed with commercially available stage micrometers. For calibration in the axial direction various methods have been reported [81, 193–195]. Secondly, the alignment of excitation beams is commonly checked with ∼100 nm gold beads [196]. For STED, the same gold beads can be used to check the alignment of the depletion beam with the excitation beam, which is crucial to maximize the performance of the system. Finally, measurements of the PSF of a confocal microscope can be performed by imaging sub-diffraction sized (<175 nm in diameter) fluorescent beads [80] or larger beads in combination with deconvolution software [81] in 3D. For STED this is more challenging, since smaller fluorescent probes (<50 nm in diameter) are required, as the size of the probe needs to be close to, or below, the resolving power of the technique. Some suitable probes are available: DNA origami techniques for example have been demonstrated to produce sub-30-nm fluorescent beads that can be used as fluorescent probes for PSF measurements and as rulers for the calibration of a STED microscope [197, 198]. In addition, it has been demonstrated that photostable quantum dots can be imaged with STED [199, 200] and could therefore be used as fluorescent probes for PSF measurements of a STED microscope. However, to the best of our knowledge, a simple method to ensure enough separation between the probes in 2D or a method to produce 3D samples is not yet available.

While the PSF measurement and alignment methods used so far are good tools to check the performance of a microscope, these methods usually only apply to measurements close to the cover glass. With recent work using (3D) STED in combination with glycerol objectives, sub-resolution imaging far from the cover glass was demonstrated in life science specimens, where the refractive index is close to 1.45 [75, 96, 201]. In addition, knowledge of the depth dependent PSF has shown to be important for accurate 3D image reconstruction [87].

In this work, a sample for the 3D calibration and alignment, as well as the PSF measurement of a confocal (STED) microscope is presented. The sample is composed of a colloidal crystal consisting of a mixture of highly monodisperse silica beads with a gold or fluorescently labelled silica core. The crystal is refractive index matched with an embedding solvent mixture, resulting in optimal imaging and an effective refractive index similar to life science specimens optimized for glycerol objectives. The periodicity of the crystal in the lateral and axial directions is used to perform calibrations. The gold cores

are used to image the excitation and depletion spots in reflection and to align the STED microscope. The fluorescent cores are individually resolvable as they are separated by a non-fluorescent silica shell and can therefore be used for PSF measurements at different positions and depths in the sample.

We will first show how the sample can be used for the calibration of lateral and axial distances of a microscope. Second, we demonstrate the alignment and PSF measurement of a confocal and STED microscope, also at different depths. Next, we demonstrate the importance of proper alignment of the excitation and depletion lasers of a STED microscope and how this can be achieved using the presented sample. In addition, we will discuss how the sample can be tailored by adjusting the synthesis of the silica beads and composition of the sample for different objectives. We will discuss how the sample can also be used to study the effects of refractive index mismatching on the PSF by intentionally mismatching the particles and the solvent mixture, as well as between the sample, cover glass and the immersion liquid of the objective.

## 3.2 Methods

### 3.2.1 Particle synthesis

A stabilized suspension of 80 nm diameter gold nanoparticles in citrate buffer (Sigma Aldrich) was used as received. Prior to silica coating, the gold nanoparticles were functionalized with polyvinylpyrrolidone (PVP) and transferred from water to ethanol by centrifugation and redispersion [165].

The fluorescent silica cores were synthesized in a reverse micro-emulsion [166, 167, 202]. Covalent incorporation of the fluorophore within the silica matrix was ensured by coupling the rhodamine B to (3-aminopropyl)triethoxysilane (APTES) prior to the synthesis [203, 204]. The reverse micro-emulsion was prepared by mixing cyclohexane, igepal CO-520, fluorophore-APTES complex and the silica precursor, tetraethylorthosilicaat (TEOS). After complete homogenization, particle growth was initiated by the addition of ammonia. After 24 hours, the cyclohexane was removed by rotary evaporation under reduced pressure. The obtained pink viscous liquid was diluted in dimethylformamide and ethanol to obtain a clear pink solution. It is important to note that this method can be extended to incorporate a great variety of hydrophobic quantum dots into the silica core, following the procedure described by Koole *et al.* [205] using the same micro-emulsion system.

The gold particles and the fluorescent cores were coated with a non fluorescent silica layer in two separate seeded growth steps to obtain particles with total diameters of approximately 200 nm. This silica growth was performed following a seeded growth procedure based on the traditional Stöber method [168–170]. After cleaning via repeated centrifugation and redispersion in ethanol, the weight fractions of both solutions were determined. These weight fractions were used to prepare a 1 to 100 number ratio (gold versus fluorescent core) mixture of both types of particles in ethanol. Further silica growth of this mixture was performed to obtain particles with a total diameter of approximately 500 nm. Again, the particles were extensively cleaned to remove small silica spheres caused by secondary nucleation by repeated centrifugation and redispersion in ethanol.

### 3.2.2 Measuring refractive index of particles

The refractive index of the particles is measured, for optimal index matching of the particles in the sample, to minimize scattering during (STED) confocal image acquisition. Because this refractive index is temperature and wavelength dependent [206] this study is carried out under the same conditions as used during confocal/STED measurements. Therefore, all measurements are carried out at 21°C, the estimated temperature in the confocal/STED setup, and transmittance is determined at ∼550 nm, close to the excitation and emission wavelengths used for the confocal measurements.

The refractive index of the particles is determined by dispersing a fixed amount of particles in solutions with increasing refractive index. These solutions are prepared by mixing two solvents with different refractive indices in various ratios [207]. Next, the transmittance of these solutions is determined because it will reach a maximum when the refractive index of the particles and the solution match. The region of refractive indices that is studied, is chosen to be around $n_D = 1.45$ because for Stöber silica, $n_D$ values ranging from 1.43 to 1.462 are reported in literature [167, 208]. Two non volatile solvent with refractive indices above and below 1.45 were selected for this: dimethyl sulfoxide (DMSO, $n_D^{25} = 1.4768$ [209]) and 1-pentanol ($n_D^{20} = 1.4100$ [210]).

First, the relationship between the vol% DMSO in 1-pentanol and the refractive index at 550 nm and 21°C ($n_{550}^{21}$) was determined. To do so, a range of solutions going from 0 to ∼85 vol% DMSO in 1-pentanol to pure DMSO was prepared. With an Atago 3T refractometer, the $n_D^{21}$ and the corresponding Cauchy's equations of these solutions were determined. The Cauchy's equations were used to calculate the refractive index at 550 nm ($n_{550}^{21}$) [206].

For refractive index matching, 6.51 mL of a 1.92 vol% solution of particles in ethanol was transferred to a 20 mL glass vial and the ethanol was evaporated by placing this vial in a 50°C preheated oven for 16 hours. Next, the particles were redispersed in 5 mL 1-pentanol by by sonication to obtain a 2.5 vol% stock solution of particles in 1-pentanol. 0.5 mL of the stock solution of particles and various volumes of DMSO and 1-pentanol were transferred to separate vials to obtain a range of 0.25 vol% solutions of particles dispersed in different 1-pentanol/DMSO ratios (0 - 85 vol%). Absorption spectra of these solution were measured at 21°C to determine the transmittance at 550 nm.

In Figure 3.1 the refractive index at 550 nm and 21°C ($n_{550}^{21}$) is plotted as a function of the vol% DMSO in 1-pentanol. A linear equation is used to fit this data. This linear relationship is used to calculate the refractive index of the particle suspensions that were used for the refractive index matching study. On the right side of the figure, the outcome of this study is presented. In this graph the transmittance at 550 nm and 21°C of suspensions of particles with different refractive indices is plotted. By fitting a quadratic equation to this data, the refractive index of maximum transmittance was determined: $n_{550}^{21} = 1.4303$.

### 3.2.3 Colloidal crystal growth

Colloidal crystal growth was performed via the vertical deposition method [172] at elevated temperature to speed up the evaporation process [173, 211, 212]. 8.0 mL of a 1 vol% of the 500 nm diameter particles in ethanol was transferred to a 20 mL glass vial. A cover

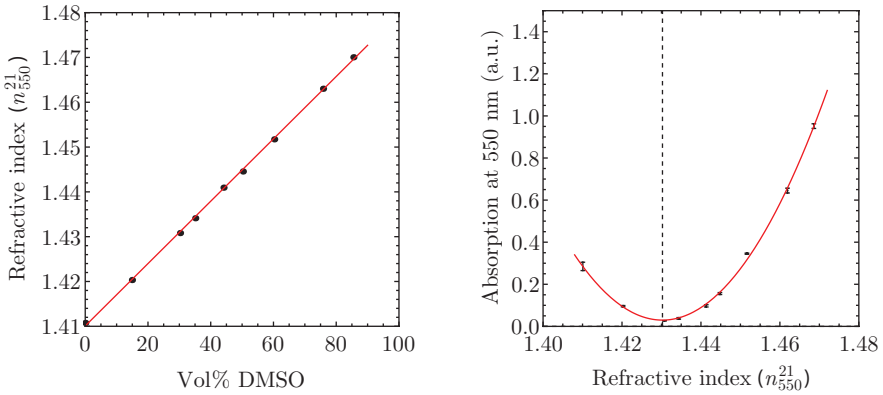


**Figure 3.1:** In the left image, the refractive index at 550 nm and 21°C ($n_{550}^{21}$) is plotted as a function of the vol% of DMSO in 1-pentanol. A linear equation is fitted to the data (red line). In the right image, the percentage of light transmitted at 550 nm it plotted as a function of the refractive index measured at 21°C ($n_{550}^{21}$). The black dots correspond to measurements of dispersions of particles in DMSO/1-pentanol mixtures with various refractive indices. A quadratic equation is fitted to the data (red line) to determine the refractive index of maximum transmittance: $n_{550}^{21} = 1.4303$.

glass (Marienfeld Superior #1.5H, 24×50 mm) was placed inside the solution under a small angle (∼5°). This vial, and a 100 mL beaker filled with ethanol were placed inside a 50 °C preheated oven (RS-IF-203 Incufridge, Revolutionary Science) and covered with a large beaker. After approximately 16 hours, the cover glass was removed from the solution. An opaque deposition of particles was observed on one side of the cover glass. Under the right illumination angle Bragg reflections were observed, which indicates the formation of a crystalline structure. For the growth of thicker crystals, growth steps were performed by repeating this process up to three times.

### 3.2.4 Calibration and alignment sample preparation

Using the colloidal crystal, the calibration and alignment sample was prepared. Two spacers (Menzel #00 cover glass) were glued onto a microscope slide using UV-glue (Norland 68 Optical Adhesive), about 5 mm apart. Next, the cover glass containing the crystal was glued onto the spacers, such that the crystal was inside the created channel. This channel was then infiltrated with a mixture of *n*-butanol and glycerol ($n_D^{21} = 1.4286$, measured using a Atago 3T refractometer) in order to refractive index match the particles to the surrounding liquid, to reduce scattering and optimize the imaging conditions. The use of water in the matching solvent mixture was omitted, as it has been reported to change the refractive index of silica particles [208]. Finally, the channel was closed using UV-glue. While curing the glue, the crystal was covered with aluminum foil as protection from the UV radiation to prevent bleaching of the dye in the particles.

### 3.2.5 HeLa cell sample

A HeLa cell sample (Active Motif/Leica Microsystems) was used for 2D STED demonstration, where the $\alpha$-tubulin was stained with BD Horizon V500-streptavidin (BD Biosciences) for imaging. The cells in the sample were mounted using Mowiol 4-88 on a $170\pm10$ $\mu$m thick cover glass (Hecht Assistent #1014), resulting in a sample refractive index of $n \approx 1.52$.

### 3.2.6 Confocal and STED measurements

Calibration and alignment measurements were performed on an inverted Leica TCS SP8 STED 3X confocal microscope, equipped with a Leica HC PL APO 100×/1.40 OIL STED WHITE or a Leica HC PL APO 93×/1.30 GLYC motCORR STED WHITE objective with a correction collar. In case of the oil objective Type F immersion oil ($n_{546}^{23} = 1.518$, Leica Microsystems) was used as immersion liquid, while for the glycerol objective a 85 w% glycerol/water mixture ($n_D^{20} = 1.452$) was used. To image the fluorescent cores of the particles, a pulsed (80 MHz) supercontinuum white light laser (SuperK, NKT Photonics) was tuned at 543 nm, while the emission was detected using a gated (0.3-6.0 ns) HyD detector (553-650 nm). For STED imaging of the fluorescent beads a continuous wave (CW) depletion laser with a wavelength of 660 nm was used. The depletion laser was either fully focused into a 'donut'-shaped spot (2D STED) or into an axial depletion spot (3D STED). The gold cores were imaged by detecting the reflection of the excitation or depletion laser using a photomultiplier tube (PMT). The correction collar of the glycerol objective was used to compensate for the refractive index mismatch between the sample (1.43) and the objective (1.45), and allowed to fine tune the depletion laser pattern, as discussed in more detail in the supplementary information of [96]. For the $\alpha$-tubulin images, the white light laser was tuned to 470 nm, with the wavelength range of the HyD detector set to 485-580 nm while a 592 nm CW depletion laser was used. Acquisition parameters of the confocal and STED images are listed in Table 3.1.

The confocal 3D stack of the fluorescent beads was deconvoluted using Huygens Software (Scientific Volume Imaging, 17.04). Any image filtering was done using Fiji [213] (ImageJ 1.52d).

### 3.2.7 Calibration measurements

For the lateral calibration Fast Fourier transforms of the XY slices were calculated using iTEM (Soft Imaging System GmbH, 5.0) and a 1 pixel Gaussian blur was applied using Fiji [213] to reduce noise. To measure the $\Delta_X$ and $\Delta_Y$ distances (see Fig. 3.4e), intensity profiles parallel to the direction of interest were drawn through the origin. Using OriginPro (v8.0891, OriginLab Corporation) Gaussian functions were fitted to the peaks nearest to the origin in the intensity profiles, to obtain the distance of these peaks to the origin $\Delta_X$ and $\Delta_Y$.

For the axial calibration, Fiji was used to plot the intensity of the deconvoluted confocal z-stack as a function of $Z$-height. Using OriginPro the peaks in the profile were fitted with Gaussian functions. The peak positions were plotted as a function of peak number and fitted using a linear function using OriginLab. The slope of this function was used as interlayer distance.

| Figure | imaging mode | objective* | pinhole (Airy units) | pixel sizes (nm) X / Y / Z | pixel dwell time ($\mu$s) | line accumulation | frame accumulation | frame averaging |
|---|---|---|---|---|---|---|---|---|
| 3.4a | Confocal | 93× glycerol | 0.7 | 35 / 35 / 50 | 2.0 | 2 | 4 | 1 |
| 3.5a | Confocal | 100× oil | 0.7 | 31.4 / 31.4 / 50 | 7.8 | 6 | 6 | 1 |
| 3.5b (l) | Reflection | 100× oil | 4.7 | 15 / 15 / - | 6.5 | 1 | 1 | 10 |
| 3.5b (r) | 2D STED | 100× oil | 1.0 | 20.5 / 20.5 / - | 4.3 | 6 | 4 | 1 |
| 3.5c (l) | Reflection | 93× glycerol | 4.7 | 17 / - / 17 | 3.9 | 1 | 1 | 10 |
| 3.5c (r) | 3D STED | 93× glycerol | 1.0 | 41 / - / 41 | 4.3 | 4 | 12 | 1 |
| 3.5d (l) | Reflection | 93× glycerol | 4.7 | 20 / - / 20 | 6.5 | 1 | 1 | 10 |
| 3.5d (r) | 3D STED | 93× glycerol | 1.0 | 41 / - / 41 | 4.3 | 4 | 12 | 1 |
| 3.6a | 2D STED | 100× oil | 1.0 | 11.3 / 11.3 / - | 2.2 | 2 | 1 | 8 |
| 3.6b | 2D STED | 100× oil | 1.0 | 11.3 / 11.3 / - | 2.2 | 4 | 1 | 8 |
| 3.6c | Reflection | 100× oil | 1.0 | 19.2 / 19.2 / - | 4.3 | 2 | 1 | 12 |
| 3.6e | 2D STED | 100× oil | 1.0 | 11.3 / 11.3 / - | 2.2 | 2 | 1 | 8 |
| 3.6f | 2D STED | 100× oil | 1.0 | 11.3 / 11.3 / - | 2.2 | 4 | 1 | 8 |
| 3.6g | Reflection | 100× oil | 1.0 | 19.1 / 19.1 / - | 4.3 | 2 | 1 | 12 |

**Table 3.1:** Acquisition parameters of microscope images in figures 3.4, 3.5 and 3.6. *93× glycerol = Leica HC PL APO 93×/1.30 GLYC motCORR STED WHITE, 100× oil = Leica HC PL APO 100×/1.40 OIL STED WHITE.

### 3.2.8 Axial scaling factor

To determine the scaling factor of the axial distances in our sample as measured by confocal microscopy, we used the method described in [81]. A sample cell was constructed by gluing two Menzel #00 cover glasses as spacers on a microscope slide, after which a channel was created by bridging the spacers with a Menzel #1.5 cover glass. The Fabry-Pérot fringes were measured using a Fourier-transform infrared (FTIR) spectrometer (Vertex 70, Bruker) and fitted to determine the cell height: 94.257±0.008 $\mu$m. Next, rhodamine B dyed poly(methyl methacrylate) spheres (70 nm diameter) were deposited from hexane on the inside of the cell and the height of the cell was measured in fluorescent mode on a confocal microscope equipped with a 20×/0.7 NA air objective: 98.0±0.2 $\mu$m, resulting in a miscalibration of the microscope stage of 4.0±0.2%. After filling the cell with the glycerol/*n*-butanol mixture ($n_D^{21} = 1.4286$) and closing it with UV-glue a height of 99.9±0.2 $\mu$m was measured, which was corrected for the mis-calibration of the microscope stage: 96.0±0.3 $\mu$m. This gives a scaling factor of 0.982±0.003 for axial distances in a sample with a refractive index of 1.43 recorded with a 1.3 NA glycerol objective.

### 3.2.9 FIB-SEM tomography measurements

In focused ion beam scanning electron microscopy (FIB-SEM) tomography [214], a focused ion beam (FIB) scans a focused beam of Ga+ ions across the sample. The momentum transfer of the Ga+ ions sputters away atoms from the sample, allowing to mill cross sections with typical depths and widths of some tens of microns [215]. Subsequently, the cross sections can be directly imaged in-situ by the scanning electron microscope (SEM). The automated FIB-SEM tomography routine consists of alternately FIB milling away thin consecutive slices and SEM imaging of the resulting cross sections. This routine results in a series of images that can be reconstructed into a 3D representation of the analyzed volume.

A colloidal crystal with slightly larger particles ($\sigma$ = 531 nm, < 2% PDI) than used in the calibration sample was studied using focused ion beam scanning electron microscopy (FIB-SEM) tomography. After growth, the colloidal crystal was infiltrated with the resin Lowicryl HM20. Infiltration of the crystal improves the finish of the milling process. Moreover, embedding the individual particles into a matrix prevents the particles to fall out of the crystal whilst slicing. The resin was composed of a 3:17 weight ratio mixture of Crosslinker D (Electron Microscopy Sciences) and Monomer E (Electron Microscopy Sciences). As initiator 0.5 w% dibenzoyl peroxide (Merck) was added. The crystal was infiltrated with resin, which was subsequently cured at 65°C in an oven overnight.

The glass slide with the embedded crystal was attached to an aluminum SEM stub with carbon tape. A strip of carbon tape made contact between the crystal on top of the glass slide and the SEM stub, to create an electrically conductive pathway. Subsequently, the ensemble was coated with a 5 nm thick layer of platinum, using a Cressington HQ280 sputter coater.

A standard FIB-SEM tomography (Scios, AutoSliceAndViewG3 1.7.2, Thermo Fisher, former FEI) routine was carried out after protecting an area of interest with in-situ platinum deposition (∼1 $\mu$m thickness) and preparing side trenches and an alignment

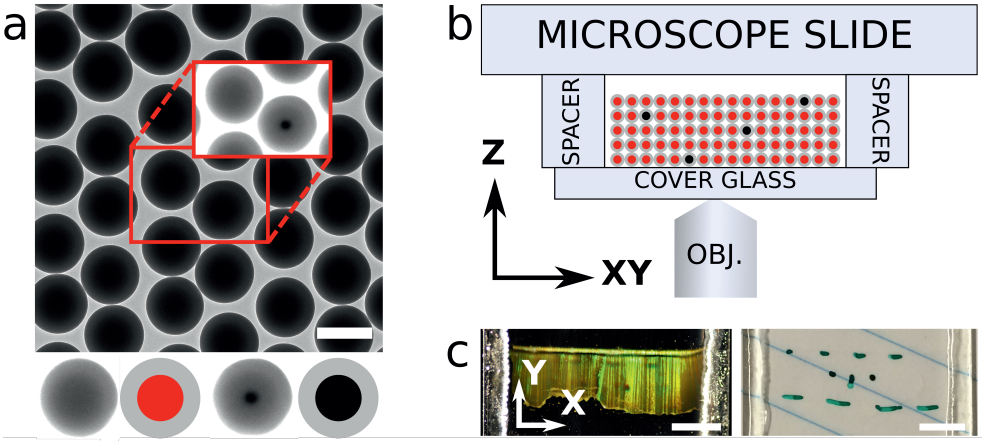


**Figure 3.2: Calibration and alignment sample.** a) Transmission electron micrograph (TEM) of the two building blocks of the sample: monodisperse silica-coated 45 nm fluorescent silica (red) and 80 nm gold (black) cores. The cores of the schematic particles are not drawn to scale. Inset: upon (TEM) contrast variation the gold cores become visible. The scale bar is 500 nm. b) Side view of the sample consisting of a crystal composed of the particles in (a), refractive index matched for optimal imaging. c) Top view of the sample showing the bright Bragg reflections of the index matched crystal upon illumination from the side (left) and full transparency under available light (right). The direction of crystal growth during vertical deposition is parallel to the $Y$ direction. The scale bars are 0.5 cm.

marker. Milling conditions during the tomography run were 30 kV, 300 pA. The slice thickness was 75 nm. Images were recorded in BSE mode with 3.5 kV, 25 pA. The scan resolution was 3904×4096, which corresponded to a (horizontal) pixel size of 6.2 nm. The pixel dwell time was 10 $\mu$s. The series were recorded with the build-in auto-focus routine to ensure a high quality focus during the series.

The coordinates of the particles in the crystal were determined from the FIB-SEM tomogram as described in Chapter 2.

## 3.3 Results

### 3.3.1 The sample

The sample used for calibration, alignment and PSF measurement is depicted in Fig. 3.2. It is composed of a colloidal crystal of silica beads with an average total diameter of 505 nm ($<$ 2% polydispersity index (PDI)), assembled on a cover glass by vertical deposition [172] (Fig. 3.2a). The thickness of this crystal can be tuned by performing repeated deposition steps or the concentration of particles during deposition. The cores of the silica beads consist of either gold (80 nm in diameter) or rhodamine B fluorescently labelled silica (45 nm in diameter). The number ratio between the two types of particles was chosen to be approximately 1 to 100, respectively.

To characterize the structure of the sample, a crystal grown using the same method but with slightly larger particles, was imaged using focused ion beam scanning electron microscopy (FIB-SEM) tomography [214] (see Figure 3.3a). From the recorded FIB-SEM data the coordinates of the particles were determined, as described in Chapter 2. From the coordinates we could identify the crystal structure as face-centered cubic (FCC) with stacking faults of hexagonal close-packed (HCP) order (see Figure 3.3b,c) using bond orientational order parameters [178] (see Section 2.2.8). It was also observed that the hexagonal arrangement of the particles in the (111) plane of the FCC crystal is not perfectly hexagonal. In the direction of crystal growth ($Y$ in Figure 3.2c) the distance to the nearest neighbour was $\sim$4% smaller than in the two other nearest neighbour directions of the hexagon. This is in agreement with earlier studies using X-ray diffraction where a similar crystal growth method was used [184] and the FIB-SEM tomography results in Chapter 2. In addition, the layer spacing of the crystal perpendicular to the (111) plane was constant throughout the crystal (see Figure 3.3d,e).

The sample was prepared from the crystal as follows: a cover glass with the crystal was glued onto two glass spacers fixed onto a microscope slide (Fig. 3.2b). To suppress scattering during imaging of the sample and distortions of the PSF, the crystal was infiltrated with a refractive index matching solvent mixture composed of glycerol and $n$-butanol ($n_D^{21} = 1.4286$ and $n_{550}^{21} \approx 1.431$, see Section 3.2.2). After infiltration, the sample was fully transparent under available light, whereas bright Bragg reflections were observed upon illumination from the side (Fig. 3.2c). The sample was sealed using UV glue, to ensure a shelf life of, by the time of writing, at least months.

### 3.3.2 Lateral and axial calibration

A z-stack of the silica beads with rhodamine B labelled cores was recorded in fluorescent mode using a HC PL APO 93×/1.30 GLYC motCORR STED WHITE objective (Fig. 3.4a). The periodicity of the crystal in both the lateral as well as the axial direction becomes visible after deconvolution of the z-stack (Fig. 3.4b-d). The (111) plane of the FCC crystal is parallel to the lateral plane, while the $(\bar{1}10)$ and $(11\bar{2})$ planes are paralel to the $XZ$ and $YZ$ directions, respectively, of the confocal z-stack. The growth direction of the crystal was parallel to the $Y$ scanning direction of the confocal microscope.

For calibration in the lateral direction the Fast Fourier transforms (FFT) were calculated of three $XY$ slices from the deconvoluted 3D confocal stack, respectively 1.3, 3.6 and 5.9 $\mu$m away from the cover glass. Figure 3.4e shows the FFT of the $XY$ slice 3.6 $\mu$m away from the cover glass, with the arrows pointing at the two characteristic distances of the crystal in both the $X$ (green) and $Y$ (magenta) directions (see inset). From the three slices the characteristic distances $\Delta_X$ and $\Delta_Y$ were determined to be 481±4 nm and 269±2 nm, respectively. These values can be used to calibrate the two lateral directions of the microscope. Since the hexagonal arrangement is slightly distorted by a shrinkage in the direction of crystal growth, $Y$ in this case, the orientation of the hexagonal arrangement (and therefore the crystal growth direction) with respect to the confocal scanning direction should be taken into account during the calibration. The $\sim$4% shrinkage found in FIB-SEM tomography (Section 3.3.1 and Chapter 2) corresponds well to a value of $\sim$3% that follows from the distances measured by confocal microscopy. As the particles are touching in the

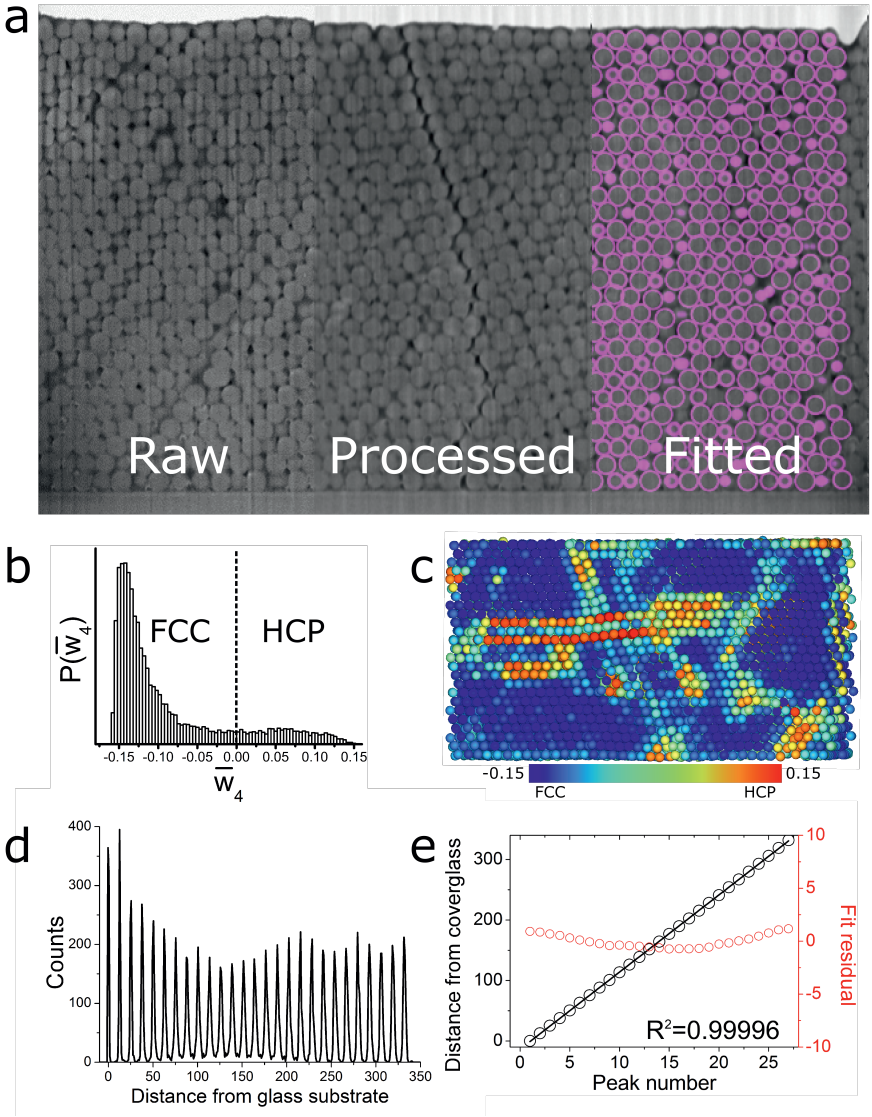


**Figure 3.3: FIB-SEM tomogram of colloidal crystal.** a) Slice from FIB-SEM tomogram. As recorded (left), after filtering (middle) and with overlay of fitted particles coordinates (right). b) Histogram of the $\overline{w}_4$ bond orientational order parameter values calculated from the coordinates in a), confirming the face-centered cubic structure of the crystal. c) Computer rendering of particles from coordinates obtained by particle identification, colored to the $\overline{w}_4$ values of the particles. d) Histogram of distance from the cover glass for every coordinate demonstrating the layering of the particles in the crystal. e) Linear fit of the peak positions in d) confirming close to perfect linearity.

$Y$ direction the effective particle diameter $\sigma_{eff}$ can be estimated by $2\Delta_Y$. We find that $\sigma_{eff} = 538\pm4$ nm and therefore $\sigma_{eff} \sim 1.07\sigma_{TEM}$. This slightly larger effective diameter compared to the diameter as measured in TEM is expected because the particles shrink due to electron beam exposure during the TEM measurements [216].

For the axial calibration of the setup, the intensity of the deconvoluted confocal z-stack is plotted as a function of the $Z$ height (Fig. 3.4f). The relative positions of the peaks in this intensity profile display almost perfect linearity ($R^2 = 0.9998$, Fig. 3.4g) and a linear fit results in a distance of 448±2 nm between the lateral layers of the crystal. It should be noted that axial distances, as recorded by confocal microscopy using high NA objectives, are sensitive to refractive index mismatches between the sample medium and the immersion medium of the objective. This results in an elongation or shrinkage of measured distances [81, 217]. The presented sample has a slightly lower refractive index (1.43) than the refractive index of the immersion liquid (1.45). Therefore, the axial scaling factor was determined using the method described by Besseling *et al.* [81] (see Section 3.2.8). A scaling factor of 0.982±0.003 was determined, resulting in a (*111*) layer spacing $d_{111}$ of the sample of 440±2 nm. For a perfect FCC crystal $d_{111}$ can be calculated using: $d_{111} = \sqrt{6}\sigma/3$, where $\sigma$ is the particle diameter [184]. Using $\sigma_{eff}$ as estimated before, a value of $d_{111}$ of 439±3 nm is found, which corresponds to the measured value.

### 3.3.3 PSF measurement and laser lines alignment

Using the fluorescent cores of the beads in the colloidal crystal, the PSF of a confocal microscope can be recorded. Figure 3.5a shows the sub-resolution fluorescent cores close to the cover slip, imaged in confocal mode with a HC PL APO 100×/1.40 OIL STED WHITE objective and the pinhole set to 0.7 Airy units. The PSF of this microscope has an expected ellipsoidal shape in the axial planes, but is slightly rotated in the *YZ* plane.

The gold cores in the crystal were used to check the shape of the depletion laser spot and the overlap with the excitation laser spot, which are both critical for an optimal STED resolution. Figure 3.5b shows the excitation spot (cyan) and the 2D STED 'donut'-shaped depletion spot (magenta), imaged in reflection mode using a HC PL APO 93×/1.30 GLYC motCORR STED WHITE objective with the pinhole set to 4.7 Airy units. Subsequent imaging of the fluorescent cores with the pinhole set to 1 Airy unit shows an increase in lateral resolution of the STED microscope as compared to confocal (Figure 3.5a), even when using a lower NA objective. Since 2D STED microscopy only improves the resolution in the lateral plane compared to confocal microscopy, it is primarily employed on thin samples, close to the cover glass. 3D STED, however, enables imaging at sub-diffraction resolution in both lateral and axial directions, which allows imaging of samples at sub-diffraction resolutions also far away from the cover glass [91]. Figure 3.5 shows the excitation and depletion laser spots of a 3D STED confocal microscope equipped with a HC PL APO 93×/1.30 GLYC motCORR STED WHITE objective, as imaged in reflection mode close to the cover glass (Fig. 3.5c) and ∼50 $\mu$m away from the cover glass (Fig. 3.5d). The correction collar of the objective was used to keep the intensity of the top and bottom depletion spots balanced when imaging more than ∼30 $\mu$m from the cover slip. This was necessary because the refractive index of the sample (1.43) is slightly lower than the ideal index for a glycerol objective (1.45). To check the results of the alignment of the lasers,

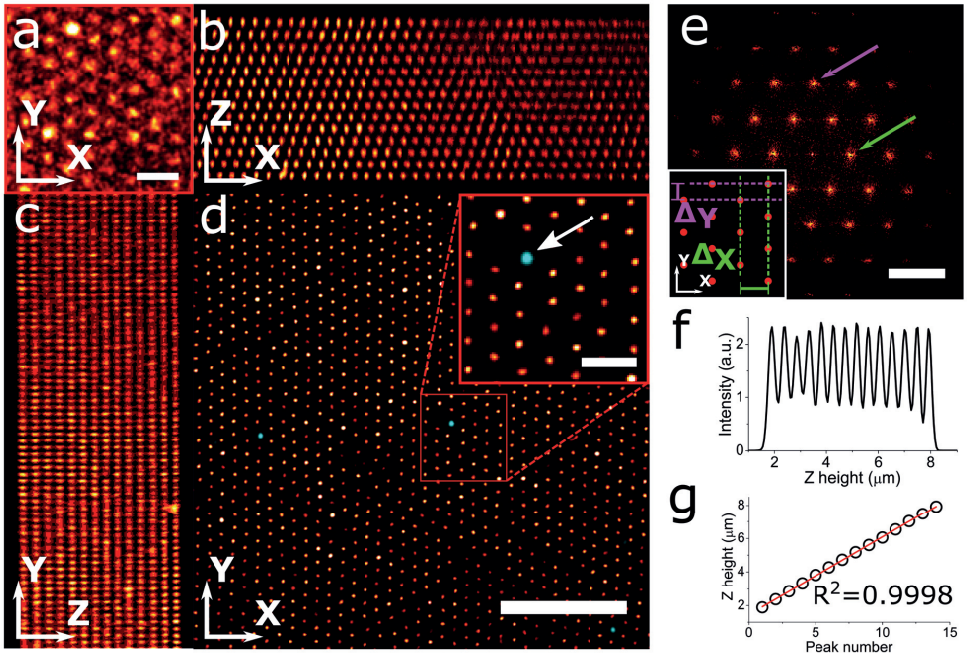


**Figure 3.4: Calibration of confocal microscope.** a) Close-up of a slice 3.6 $\mu$m from the cover glass from a confocal stack of the colloidal crystal (1 pixel gaussian blur) acquired using a HC PL APO 93×/1.30 GLYC motCORR STED WHITE objective and a pinhole of 0.7 Airy units. The scale bar is 1 $\mu$m. b) Average projection of the $XZ$ planes of the confocal z-stack shown in (a) after deconvolution, showing the ABC stacking in the $(\bar{1}10)$ plane of the FCC crystal. c) Average projection of the $XY$ planes of the deconvoluted confocal z-stack, showing the $(11\bar{2})$ plane of the FCC crystal. d) Overlay of an $XY$ slice of the confocal stack of both reflection (cyan) and deconvoluted fluorescence (red) 3 $\mu$m from the cover glass. The arrow points at a gold core bead imaged in reflection mode. The scale bars are 5 and 1 (inset) $\mu$m. e) Fast Fourier transform of d) demonstrating long range hexagonal order. The arrows point to the peaks in the FFT image used for calibrating distances in the X (green) and Y (magenta) direction. The scale bar is 3 $\mu$m$^{-1}$. The inset shows the characteristic distances $\Delta_X$ (green) and $\Delta_Y$ (magenta) in the real space crystal corresponding to the peaks in the FFT image. f) Intensity profile in the z-direction, demonstrating the periodicity in the axial direction. g) Linear fit of the peak positions in f).

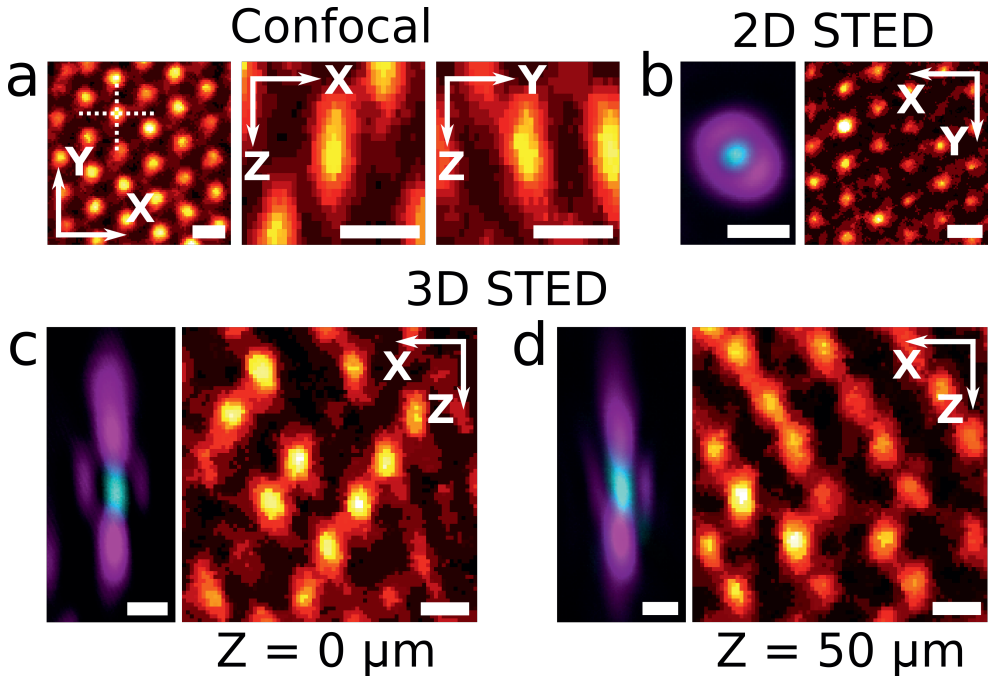


**Figure 3.5: Alignment of confocal STED microscope.** a) Slices from confocal z-stack of fluorescent cores in colloidal crystal close to the cover glass, recorded with a HC PL APO 100×/1.40 OIL STED WHITE objective (2 pixel 3D median filter), showing the response function of the microscope in the lateral plane (left), $XZ$ plane (middle) and $YZ$ plane. The two axial planes are marked by the dashed lines in the lateral plane (left). Alignment of 2D (b) and 3D (c,d) STED excitation (cyan) and depletion (magenta) lasers in the lateral plane, as imaged using a HC PL APO 93×/1.30 GLYC motCORR STED WHITE objective in reflection mode (left) using a gold core particle close to (b,c) and 50 $\mu$m (d) from the cover glass, and the resulting STED images (2 pixel median filter) of the fluorescent cores in the crystal (right), showing increased resolvability of the particles in the crystal as compared to a). All scale bars are 500 nm.

the fluorescent cores were imaged using a confocal microscope in 3D STED imaging mode at a pinhole size of 1 Airy unit (Figure 3.5c,d). The improved axial resolution is visible from the decreased aspect ratio of the ellipsoidal fluorescent spots as compared to the confocal PSF (Figure 3.5a).

In addition, to show the importance of a proper alignment of the excitation and depletion spots in STED microscopy, fluorescently labelled $\alpha$-tubulin in HeLa-cells was imaged using 2D STED microscopy using a HC PL APO 100×/1.40 OIL STED WHITE objective (Figure 3.6). When the two laser spots were properly aligned using our sample, an increase of the lateral resolution is visible (Figure 3.6a-d). When the minimum of the depletion spot is slightly off-center with respect to the maximum of the excitation spot, the depletion of the fluorophores by the depletion beam results in a higher level of noise in the resulting image and no improvement in the resolution compared to the confocal image (Figure 3.6f-h).

## 3.4 Discussion

The test sample as presented here is a robust standard for the quality control of a laboratory's confocal and STED microscopes. By the time of writing, the shelf life of the sample is on the order of months. Although the small fluorescent cores tend to bleach upon prolonged excitation, the sample can be used repeatedly because the crystal contains over $10^{10}$ particles due to its larger size (close to 2 cm$^2$ see Fig. 3.2c).

In the measurement of the characteristic lateral length scales $\Delta_X$ and $\Delta_Y$ an error below 1% is found (obtained by measuring at three depths). In addition, for the axial interlayer spacing an error of less than 0.5% is found (obtained from a linear fit of the intensity peaks of the crystal layers). This low error is supported by the perfect linearity of the axial interlayer spacing, as found by FIB-SEM tomography and particle tracking. These low errors make the sample suitable for the calibration of microscopes at a high precision.

Due to the bottom-up assembly, the sample is highly tunable. This makes it possible to adjust the sample to, for example, meet the requirements for different high NA lenses (e.g. oil immersion) and/or different techniques. This can be achieved by changing the core, the ratio between different types of cores, the shell and the total size of the particles, which will be discussed below.

While it was demonstrated that rhodamine labelled silica cores can be used, the synthesis method of these cores allows for the incorporation of a wide variety of dyes [203, 204, 218–222]. This can be useful because by mixing cores with different dyes in the non-fluorescent silica growth step, to accommodate microscope setups with multiple laser lines. This can also be used to produce a sample where fluorescent cores labeled with two different dyes are combined at a strongly asymmetric number ratio. Within such a geometry, one of the two fluorescent particles can be used for the calibration measurements whereas the other core allows for PSF measurements. The axial tails of the PSFs can then be well separated by ensuring that the ratio of the second type of core particle is low enough compared to the first type. This separation is required for commercial deconvolution software often used in life sciences (see Section 3.2.6). The axial tails of PSFs are especially prominent

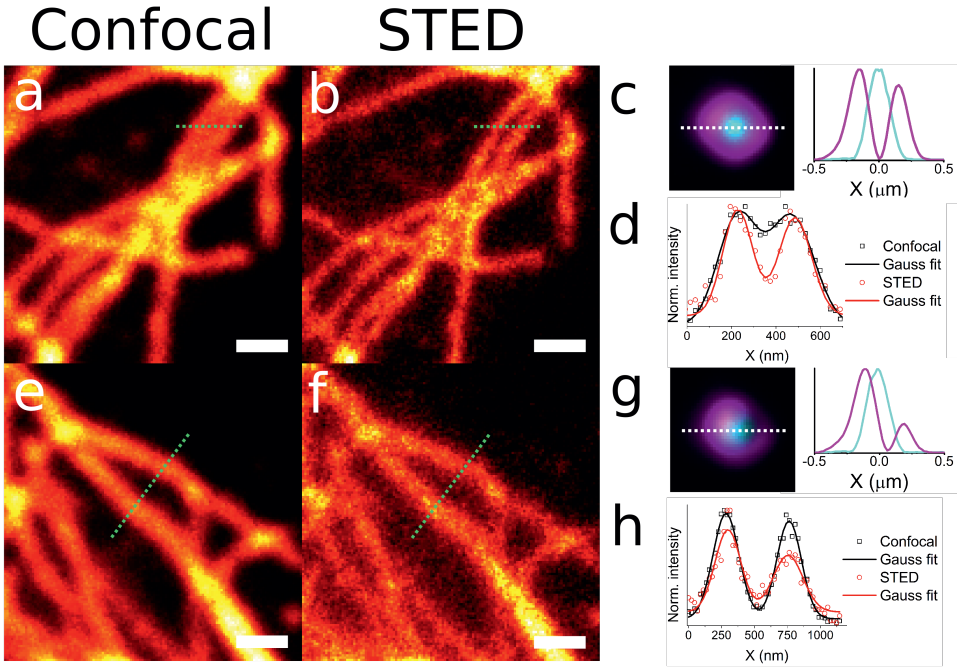


**Figure 3.6: The importance of a proper alignment of the STED microscope.** Results of alignment of the laser beams in STED microscopy on imaging of $\alpha$-tubulin (HeLa-cell) with a HC PL APO 100×/1.40 OIL STED WHITE objective. a) Confocal micrograph. b) 2D STED image at same region as a) after aligning the minimum of the 'donut'-shaped depletion laser spot to the maximum of the excitation laser spot. c) Alignment of excitation (cyan) and STED (magenta) lasers in b). d) Intensity profiles along the lines in a) and b), showing the increased resolving power of the STED compared to confocal microscopy. e) Confocal micrograph. f) 2D STED image at same region as e) with slightly misaligned excitation and depletion laser spots. g) Alignment of excitation (cyan) and STED (magenta) lasers in f). h) Normalized intensity profiles along the lines in e) and f), showing no increase in the resolving power of the (2D) STED compared to confocal microscopy. Scale bars are 500 nm.

in samples where the mounting medium is not matched with the immersion liquid of the objective used and imaging of these tails is needed for accurate 3D reconstruction.

Instead of keeping the gold and dye separated within the sample, the two can also be combined within a single particle, by growing a fluorescent layer around the gold core. Another option is to use a silver core instead of a gold core. This flexibility opens up the possibility to design nanocomposite particles where the fluorescence is enhanced by the presence of the metal core [223], which has recently been demonstrated to be compatible with STED microscopy [224].

The possibility to exchange the fluorescent cores with quantum dots is also worthwhile exploring, since quantum dots have excellent photostability, are only a few nanometer in size and have shown to be compatible with STED microscopy [199, 200]. As the absorption and emission wavelengths of quantum dots are size dependent [225], they can be tailored to the wavelength of the excitation and STED lasers. When measuring a PSF using quantum dots, the challenge is to ensure there is enough separation between them which can be achieved by coating the quantum dots with silica [205, 226]. This seeded growth method is directly compatible with the work presented here, because silica coating is performed in the same reverse micro-emulsion system used to synthesize the fluorescent cores. The most promising quantum dots to use are so-called CdS/CdSe/CdS quantum well dots, as these can be coated with silica while maintaining a high photoluminescence quantum yield [227, 228].

Next to quantum dots, a variety of nanometer sized probes have been put to use in STED imaging [229], such as fluorescent nanodiamonds [230], upconversion nanocrystals [231] and carbon dots [232]. These particles can be coated with silica [233–235], and could be integrated in our demonstrated sample. However, to the best of our knowledge, no STED microscopy has been demonstrated on these probes after silica coating.

Another method to tune the sample, is by adjusting the silica shell that is used to ensure separation between the cores. While in this work the focus was on a refractive index of 1.43 compatible with glycerol objectives, it can also be tuned to a higher refractive index. This can be achieved by synthesizing a shell of titania/silica composite with a higher refractive index [236–238]. Doing so, the refractive index can easily be increased to match the refractive index of oil objectives (1.52), or any other intermediate refractive index that is comparable to the refractive index of life science specimens of interest. Another option is to increase the size of the shell to increase the spacing between the probes. This makes the sample compatible with lower NA objectives, where the axial resolving power is smaller. For this, the assembly method needs to be adjusted due to a faster settling rate of the particles, as has been demonstrated for close to 1 $\mu$m silica particles [239].

Finally, by introducing a refractive index mismatch between the particles and the embedding solvent, the effect of the mismatch on the PSF can be measured as a function of the distance to the cover glass. Moreover, the periodicity of the crystal in the axial direction and the known refractive indices of the beads and the embedding mixture, can be used to test effective refractive index theories developed in the photonic crystal community.

## 3.5 Conclusions and Outlook

In this chapter we demonstrated a robust sample that can be used as a standard to assure the quality of (STED) confocal microscopes equipped with high NA objectives. The sample is composed of a crystal of fluorescently labeled silica colloids, mixed with a small amount of gold core silica colloids. As the sample is infiltrated with a refractive index matched solvent mixture, it is perfect for imaging with (STED) confocal microscopy, far from the cover glass. The periodicity of the crystal in all three dimensions can be used to calibrate the microscope setup. In addition, the gold cores can be used to align the excitation and depletion lasers of a STED microscope. The effect of the alignment can then be checked on the fluorescent cores by measuring the point spread function (PSF). As the sample has a refractive index of $n = 1.43$, the sample is optimized for glycerol objectives, which have been shown to be ideal for deep super-resolution imaging of life science specimens [96].

The bottom-up assembly of the sample allows for tailoring of the sample to its users needs. As the reported labeling method is compatible with a wide variety of dyes, the sample can be made suitable for different laser lines. Moreover, the synthesis methods allows for the incorporation of different metal cores, as well as quantum dots. Next to modification of the cores of the particles, the particles themselves can be grown larger to make the sample compatible with lower NA objectives. In addition, by incorporating titania into the particle shells and matching with higher refractive index solvents, the sample can be tailored for use with oil objectives. Finally, by introducing a mismatch between the particles and the embedding solvent mixture, the sample can be used to test effective refractive index theories and the effect of the mismatch on the PSF.

## 3.6 Acknowledgements

The work in this chapter was done in collaboration with Jantina Fokkema, Hans Gerritsen, Peter Speets and Marc del Pozo Puig. We thank Matthijs de Winter for the FIB-SEM measurements, Michiel Hermes for the particle localization in the FIB-SEM data and Judith Wijnhoven for help with the synthesis of the PMMA particles. Finally, we thank Jantina Fokkema, Hans Gerritsen and Matthijs de Winter for critical reading of the chapter.

# 4

# Arrest of colloidal dispersions with conservation of structure for quantitative 3D real-space analysis

Confocal microscopy is a powerful tool to characterize 3D colloidal dispersions quantitatively on the single particle level in real-space. However, the finite time it takes to obtain a 3D data set can limit its use and accuracy for dynamical systems and processes. In this chapter, we present a general and relatively simple method to arrest colloidal structures and processes by the polymerization of a component of the solvent. We effectively arrest colloidal model dispersions of micron sized particles in $\sim$0.65 seconds by addition of a trifunctional monomer and a photo initiator to the dispersions and subsequent exposure to UV light. This relatively fast arrest on the time scale of the mobility of many colloidal particles and processes enables the acquisition of higher quality 3D information. By quantitative comparison of the structure before and after the arrest, we show that the full 3D configuration of the particles can be preserved. We demonstrate how this method can be applied to the two colloidal model systems with which almost all quantitative 3D model studies are done: poly(methyl methacrylate) (PMMA) and silica particles. In addition, we show that for both these systems the complete range of possible interparticle interactions, from long ranged repulsive (several times the particle diameter), to hard, dipolar and attractive (due to depletion effects) is compatible with our methodology. Finally, we demonstrate how this method can be applied to preserve meta-stable structures induced by electric fields or shear and structures for which the effects of gravity have been canceled out by slow rotations in a gravitational field. Although our paper focuses on model studies for (confocal) microscopy measurements, the methodology is also of interest in preparing new tunable materials from colloidal particles as well.

## 4.1 Introduction

Confocal microscopy has proven to be, so far, the only light microscopy technique with which 3D single particle data in concentrated colloidal dispersions can be obtained if certain criteria are met. Therefore it is a powerful tool in the field of soft matter and materials science [75, 76, 112, 113, 240–242]. Confocal microscopy is used for real-space 3D study of a wide range of soft matter systems, including colloids [15, 18, 76, 111–113, 243–246], emulsions [247, 248], polymers and DNA [249–251], microfibers [199, 252, 253] and liquid crystals [254, 255]. Processes like the nucleation of colloidal crystals [15, 136] and the structure of colloidal crystals [33, 244], glasses [19, 20] and gels [111] have been studied using confocal microscopy.

The main advantage of confocal microscopy over wide-field microscopy, is the optical sectioning of the confocal microscope, rejecting the out-of-focus light by placing a pinhole in front of the detector and therefore enabling one to resolve information at different heights in the specimen. This results in an axial resolution of ∼500 nm for high numerical aperture objectives. The pinhole also results in an improvement of the resolution in the lateral plane to ∼200 nm and allows to study smaller objects [88, 256]. More recent, the advent of super-resolution microscopy, such as stimulated emission depletion (STED) microscopy, stochastic optical reconstruction microscopy (STORM) and photoactivated localization microscopy (PALM), has enabled resolving powers in the lateral and axial directions below 50 and 100 nm, respectively [88, 89, 92, 112, 257, 258].

The quantitative real-space acquisition of confocal microscopy in combination with particle tracking algorithms, makes it possible to directly compare the results to computer simulations and theory [102, 112, 113, 259, 260]. The last two decades have seen a lot of improvements, that are still continuing to this day, in the ability to access quantitative information on the single particle level by including the physics of the imaging system whilst obtaining this information [112, 118]. This can be as simple as a deconvolution with a, preferably measured, point spread function of the microscope [79, 81, 85, 86]. In addition, improved algorithms have enabled the determination of the positions and orientations of rod-like particles [123], core-shell ellipsoids [124], as well as other complex-shaped particles [154].

Although confocal microscopy enables quantitative 3D real-space analysis, it can be limited by the scanning speed of the microscope. For the current fast point scanning confocal microscopes, for instance a Leica SP8 equipped with a 12,000 Hz resonance scanner, a typical 2D image with a size of 512×512 pixels can be recorded with a frame rate of >20 frames per second (fps). However, when a z-stack is recorded with the same amount of pixels in the axial direction, this rate drops to >0.04 fps, equivalent to a total recording time of > 20 seconds. In practice, the amount of pixels needed in the axial direction is lower than the lateral direction, as the resolving power is three times lower. At these fast scanning speeds, the signal-to-noise ratio might become too low, forcing the user to the accumulation of lines or frames during the acquisition, which slows down the frame rate. For comparison of the scanning rate with the relevant dynamic time scales of significant motions on the single particle level, we calculate the time it takes for a colloid to diffuse over its own radius $a$, which can be estimated by $\tau_a \sim \frac{a^2}{D} \sim \frac{6\pi\eta a^3}{kT}$, where $D$ is the self diffusion constant and $\eta$ the solvent viscosity [261]. For a colloid with a diameter

of 1.2 $\mu$m in water, the self-diffusion time $\tau_a \approx 1$ second, where we have taken the free diffusion coefficient for the self diffusion coefficient. This shows, that in order to follow such colloids in 3D, even current fast point scanning confocal microscopes are often not fast enough at low particle volume fractions, where the diffusion coefficient is close to that of a single particle freely diffusing [76, 181].

One way to circumvent this, is by scanning the sample using multi-point illumination, for instance with a spinning disk confocal, where a frame rate of 600 fps is feasible [15, 75–78]. A drawback of this multi-pinhole system is a reduced resolution of the recorded images, caused by the leaking of light from neighboring pinholes [75, 76]. Another way to overcome the difference in the time scales of scanning and the dynamics of the system under study, is by slowing down the dynamics using more viscous solvents [84, 262]. A disadvantage of this, is often the loss in the ability to tune the interactions in the sample studied. Solomon and co-workers combined the use of a viscous solvent with the introduction of a monomer and photo initiator, and a subsequent polymerization using UV light, when studying colloidal particles with a hard-sphere-like potential [263, 264]. In another approach, surfactant micelles were arrested in a mixture of sugar and urea, where the arrest was induced by a fast quench in temperature, for high resolution transmission electron microscopy imaging [265].

Polymerization of the continuous phase has also been employed for the production of polymerized colloidal crystal arrays (PCCAs) [35]. Initially Asher and co-workers developed this method to optimize the mechanical properties of tunable optical filters for Raman scattering [36, 40]. Later on, based on the same procedures, they produced PCCAs consisting of colloidal particles trapped in hydrogels, responsive to temperature [37], specific chemical compounds [38] and pH [39]. Subsequently, other groups applied the method on more close packed crystals to create e.g. large free standing PCCA films [266, 267]. This was done by spincoating dense colloidal dispersions and subsequent polymerization of the continuous phase, the trifunctional monomer ethoxylated trimethylolpropane triacrylate (ETPTA). After additional etching steps inverse photonic crystals could be obtained. More recently, membranes of the same polymer around droplets containing colloidal particles were used to manipulate the structural color of the colloidal crystal or glass within the droplets by osmotic pressure [268, 269]. As the continuous phase in the aforementioned responsive PCCAs were water-based, the distance between the particles is limited by the largest realizable Debye length ($\kappa^{-1} \approx 300$ nm) in water, as the ionic strength in this solvent is limited by the self-dissociation of water. In lower polar solvents, however, a much larger Debye length can be achieved ($\kappa^{-1} > 10$ $\mu$m) [33, 181, 182, 270]. This means that softer, photonic crystals with e.g. lattice spacings of more than 10 $\mu$m can be realized [33, 181] in solvents like cyclohexyl bromide (CHB, $n_D \approx 1.49$ [271]) or cyclohexyl chloride (CHC, $n_D \approx 1.45$ [272]). To the best of our knowledge, no PCCAs have been reported in low polar solvents yet.

Here, we present an extension of the method first used by Solomon *et al.* [263, 264] where colloidal dispersions were arrested by the addition of a monomer and photo initiator to the continuous phase and a subsequent exposure to UV light (Fig. 4.2A). We extend the method to the low to intermediate polar range of solvents, enabling the full range of interactions between the particles, including hard-sphere-like, long range repulsive, dipolar and depletion induced attractions. We demonstrate its compatibility with both

sterically stabilized PMMA and silica model particles, which represents almost all previous work in which quantitative 3D particles resolved studies were performed, for examples see references [3, 15, 18–20, 33, 76, 81, 110, 111, 136, 181, 244–246, 259, 260, 263, 264, 267, 273, 274].

We focus on how we can arrest colloidal dispersions without changing their structure for reliable 3D real-space imaging. But as the method is applicable to both PMMA and silica, it is as well of interest for materials science in general, and the field of photonic applications of colloids in specific. One reason for this, is that by arresting the structures in a 3D polymerized (solvent swollen or not) network, the visco-elastic properties can be drastically changed. In addition, particles with completely different materials properties can be coated by PMMA [19] and/or silica layers [165], making it possible to include highly scattering cores in the arrested photonic crystal.

This chapter consists of three parts. First, a long-range repulsive colloidal crystal of poly(methyl methacrylate) (PMMA) colloids in a low polar solvent mixture [33] is used as a model system to demonstrate the method. Since the interactions in this system are very sensitive to small changes in the ionic strength of the solvent ($\sim$1 $\mu$M), it is used as a benchmark for our method. Using both the local density (as represented by lattice parameters of the crystal structure and the radial distribution function $g(r)$) and the local symmetries of the neighboring particles (as measured by so-called bond order parameters) we show that the body-centered cubic (BCC) structure of our system is preserved without distortion during the arrest. Second, we will show the arrest of external field induced structures, such as electric field induced dipolar chains and shear induced crystals. Third and finally, we will demonstrate how the method can be used in combination with gravitational averaging by slow rotations to negate the effects of gravity on depletion induced liquid crystal formation of micron sized silica rods [273, 275].

## 4.2 Methods

### 4.2.1 Particles

Fluorescent poly(methyl methacrylate) particles were synthesized using the dispersion polymerization method of Bosma *et al.* with poly(12-hydroxystearic acid) (PHSA) as stabilizer [276, 277]. The particles were either fluorescently labeled using (rhodamine isothiocyanate)-amino styrene (RAS) or 4-methylaminoethylmethacrylate-7-nitrobenzo-2-oxa-1,3-diazol (NBD-MAEM) dye. The particle size and polydispersity index (PDI) of the PMMA particles in hexane were determined using static light scattering (SLS). Fluorescent silica rods were synthesized using the method described by Kuijk *et al.* [278, 279]. Non-fluorescent silica rods were synthesized and coated with a fluorescein isothiocyanate (FITC) labeled silica shell, followed by two non-fluorescent silica layers. Small spherical silica particles were synthesized using the Stöber method [168]. The size and polydispersity index of the silica particles were determined using transmission electron microscopy.

### 4.2.2 Solvent mixtures

The particles were dispersed in different solvent mixtures, depending on the desired dispersion characteristics. The monomer trimethylolpropane ethoxylate triacrylate (ETPTA, $M_w$ = 428 g/mol) was used at a concentration of 6 or 10 v%. The monomer has a refractive index $n_D = 1.47$ as a monomer and $n_D = 1.49$ as polymer [267]. For the arrest of the long range repulsive PMMA particles, cyclohexyl bromide (CHB) was deionized using molecular sieves and mixed with cis-decahydronaphtalene (cis-decalin) [45]. The monomer ETPTA was treated with aluminum oxide, to remove polar contaminants, and was added to the CHB/cis-decalin mixture, arriving at the following volume ratio: 58.0 v% CHB, 35.5 v% cis-decalin and 6.5 v% ETPTA. For the arrest of hard-sphere-like PMMA particles, CHB was saturated with tetrabutylammonium bromide (TBAB) salt ($c \approx 260$ $\mu$M and mixed with cis-decalin). The ETPTA was used as received and mixed with the CHB/cis-decalin at the same ratio as above. Through measurement of the conductivity using a CDM 230 conductometer (Radiometer analytical) the Debye length of the solvent mixture was estimated: $\kappa^{-1} \approx 140$ nm. For the attractive silica rod dispersion, silica spheres as depletant where dispersed in a mixture of *n*-butanol, dimethyl sulfoxide (DMSO) and ETPTA arriving at the following volume ratio: 8 v% *n*-butanol, 70 v% DMSO, 10 v% ETPTA and 12 v% silica spheres.

For the arrest of the dispersions two different photo initiators were used: Irgacure 2100 and 2-hydroxy-2-methylpropiophenone. For the arrest of long range repulsive PMMA particles, 10 v% Irgacure initiator was mixed with deionized CHB and treated with aluminum oxide. Next, the mixture was stored on molecular sieves. The initiator mixture was added to the dispersion, where the volume ratio of initiator to monomer was 1:100. For the arrest of hard-sphere-like PMMA particles, the initiator was mixed with TBAB saturated CHB without washing and mixed with the solvent mixture, again at a 1:100 initiator to monomer volume ratio. For the arrest of the attractive silica rod dispersion, 2-hydroxy-2-methylpropiophenone was added directly to the dispersion at the same 1:100 initiator to monomer volume ratio. Before sample preparation, oxygen was removed from all dispersions, as oxygen can act as a radical scavenger [280], slowing down the polymerization. This was done by either bubbling nitrogen gas through the dispersion, or the repeated cycle (3 times) of exposure to vacuum and flushing with nitrogen of the dispersion using a glove box. The latter was found to increase the speed of polymerization the most.

### 4.2.3 Sample preparation

To enable confocal microscopy imaging of the dispersions, different cells were prepared. For the arrest of long range repulsive PMMA particles and the attractive rod dispersion, borosilicate capillary tubes (2.0×0.2 or 2.0×0.1 mm, Vitrocom, $n_D = 1.474$) were filled with the dispersion and closed and glued to a microscope slide with either UV glue (NOA 68, Norland Adhesives) or candle wax. The UV glue was exposed to UV light (365 nm, UVGL-58, 6 W, UVP) for half a minute while the capillary was covered with aluminum foil to prevent the polymerization of the ETPTA. For the most optimal arrest of the particles, the microscope slide was modified to prevent the UV light passing through the 2 mm

**Figure 4.1: Schematic of sample for optimal arrest of the colloidal dispersion.** The sample was prepared by gluing two ends of a microscope slide onto a half of a microscope slide cut over its long axis, onto which a capillary with the particle dispersion was glued using UV glue. The sample configuration enables the simultaneous imaging and exposure to UV light of the dispersion, without obstructing of the thick microscope slide glass.

thick glass slide the capillary was mounted on. To this end, two ends of a microscope slide were cut using a glass cutter. In addition, a microscope slide was cut in half over its long axis. One of these halves was used to glue the other two ends to, resulting in a U-shaped microscope slide on which the capillary was mounted (see Figure 4.1).

For the hard-sphere-like PMMA spheres, an electric cell was constructed composed of parallel two indium tin oxide (ITO) coated cover glasses (#1, Diamond Coatings) separated by a 120 $\mu$m thick cover glass (#0 Menzel Gläser). The glasses were glued to a microscope slide using UV glue, and the two ITO coated cover glasses were connected to thermocouple alloy wires ($\sigma = 50$ $\mu$m, Goodfellow) using silver paint (SPI-paint). These were connected to standard electronic wires for the connection to electronic equipment. After loading the dispersion inside the cell, the cell was closed with UV glue. The glue was cured for $\sim$30 seconds while the dispersion was protected from UV light by aluminum foil. For the shear of long range repulsive particles the dispersion was loaded between the two shearing glass plates, without further closing of the cell, as explained in more detail in literature [267] and in the following section.

### 4.2.4 External fields

For shearing the long range repulsive colloidal dispersion, a home-built parallel plate shear cell was used [281]. The shear cell was mounted on top of an inverted microscope, equipped with a Leica SP2 confocal microscope. The cell was composed of two translational cassettes with glass slides to allow the imaging of the dispersion during the application of oscillatory shear. The distance between the parallel glass slides was $\sim$55 $\mu$m.

For the application of an electric field in the previously described electric cell, a signal generator (Agilent, Model 33120A) and amplifier (KrohnHite, model 7602M) were used to generate a 1 MHz electric field. The signal was passed through a transformer (in-house) to increase the voltage and remove any DC components in the signal, which was monitored using an oscilloscope (Tektronix, Model TDS3052).

To average out the effects of gravity on the dispersion of attractive rods, a home-built rotating stage was used, described in [273]. The stage was composed of an elastomer sample holder connected to the rotor of a peristaltic pump. To ensure the axis of rotation of the sample was parallel to the long axis of the sample, the rotation plane of the rotor was held parallel to gravity. The rotator was operated at a speed of $\sim$5.5 rpm.

### 4.2.5 Confocal imaging and UV exposure

The confocal imaging of the arrest of the attractive silica rods, long range repulsive and hard-sphere-like PMMA colloids was done using an inverted Leica SP8 confocal microscope with a 12,000 Hz resonance scanner. The microscope was equipped with a white light laser, photo multiplier tubes (PMTs) and HyD detectors. For particle imaging, the FITC and NBD dyes were excited at 490 nm, while the RAS dye was excited at 545 nm. To arrest the colloidal dispersions, a collimated 365 nm UV LED source (M365LP1-C2, Thorlabs) was mounted on the condenser of the microscope. The UV light was focused on the sample using a 0.9 NA condenser lens (Geometry 1, see Fig. 4.2B), resulting in a spot power of 6 mW, measured using a microscope slide power meter (S175C, Thorlabs). Using a signal generator (Agilent, Model 33120A), a block pulse was fed into a LED driver (LEDD1B, Thorlabs) to create the UV pulse. To correlate the movement of the particles with the UV pulse, a PMT in the confocal microscope was set to detect at a wavelength as close as possible to the UV wavelength. The arrest of the attractive silica rod dispersion was done by exposure to a handheld UV lamp (UVGL-58, 6 W, UVP). For the confocal imaging of the long range repulsive PMMA colloids under shear, an inverted Leica SP2 confocal equipped with PMTs was used. A 488 nm laser was used for the excitation of the NBD labeled PMMA particles. For UV exposure the UV LED source was used, but here the UV light was focused on the sample with the same objective as used for confocal scanning (Geometry 2, see Fig. 4.2B). To enable this, a 425 nm long pass dichroic mirror was placed in the excitation/emission beam path, directing the UV light to the objective. Two PMTs were set up, one in the range from 498 to 600 nm to detect the particles, the other from 350 to 478 nm to detect the UV pulse.

### 4.2.6 Analysis

#### Image analysis

ImageJ 1.51p was used to calculate the maximum projection of a time series of confocal images, FFT calculations and to measure the angle in the FFT patterns. The displacement of the particles in the time series were tracked using the tracking algorithm by Crocker and Grier [105]. For 3D particle localization the same code was used with an extension to 3D [18, 110].

#### Structural analysis

Radial distribution functions were calculated from the 3D coordinates obtained through particle localization. To account for the finite size of the set of coordinates, a box of the same dimensions filled with ideal gas particles was generated to normalize the histogram of distance calculated from the experimental set (see Chapter 2).

Crystalline order was calculated using the Ten Wolde *et al.* criterion [282], based on the Steinhardt *et al.* bond order parameters [176]. For this the set of numbers $q_{lm}$ was calculated for every particle, based on spherical harmonics $Y_{lm}$:

$$q_{lm}(i) = \frac{1}{n_c(i)} \sum_{j=1}^{n_c(i)} Y_{lm}(\hat{\mathbf{r}}_{ij}), \tag{4.1}$$

where $n_c(i)$ is the number of nearest neighbors of particle $i$, $l$ an integer (in this case 6), $m$ an integer running from $-l$ to $l$ and $\hat{\mathbf{r}}_{ij}$ the unit vector pointing from particle $i$ to particle $j$. The nearest neighbors are defined as the particles within cut-off distance $r_c$ from particle $i$. This cut-off was determined from the first minimum of the radial distribution function $g(r)$, corresponding to $r_c \approx 1.4\sigma$, where $\sigma$ is the particle diameter. Next, the correlation between the $q_{lm}(i)$ of every particle with the $q_{lm}(j)$ values of its neighbors was calculated:

$$c_l(ij) = \frac{\sum_{m=-l}^{l} q_{lm}(i) q^*_{lm}(j)}{\sqrt{\sum_{m=-l}^{l} |q_{lm}(i)|^2} \sqrt{\sum_{m=-l}^{l} |q_{lm}(j)|^2}}, \tag{4.2}$$

where $q^*_{lm}(j)$ is the complex conjugate of $q_{lm}(j)$. The neighbors $j$ of each particle $i$ were considered connected when $c_l(ij) > 0.5$ and the particle $i$ was considered crystalline when the amount of connected neighbors exceeded 7. As our data sets were finite, we had to correct for the lack of neighbors for particles close to the edge of our data set box. In case a particle was within the cut-off distance $r_c$ of the rectangular box comprising all coordinates, it was used to calculated the bond order parameters, but was not taken into account when determining the crystalline fraction of particles.

To further analyze the crystal structure of the particles, we used the averaged local bond orientational order parameters [178]. Using the earlier determined $q_{lm}$, the averaged parameters $\bar{q}_{lm}$ were calculated:

$$\bar{q}_{lm}(i) = \frac{1}{N_c(i)} \sum_{k=0}^{N_c(i)} q_{lm}(k), \tag{4.3}$$

where $N_c(i)$ is the number of neighbors $n_c(i)$ of particle $i$ plus itself. From this the averaged local bond orientational order parameter $\bar{q}_l$ was calculated:

$$\bar{q}_l = \sqrt{\frac{4\pi}{2l+1} \sum_{m=-l}^{l} |\bar{q}_{lm}(i)|^2}. \tag{4.4}$$

In addition, the $\bar{w}_l$ order parameter was calculated:

$$\bar{w}_l(i) = \frac{\sum_{m_1+m_2+m_3=0} \begin{pmatrix} l & l & l \\ m_1 & m_2 & m_3 \end{pmatrix} \bar{q}_{lm_1}(i) \bar{q}_{lm_2}(i) \bar{q}_{lm_3}(i)}{\left( \sum_{m=-l}^{l} |\bar{q}_{lm}(i)|^2 \right)^{3/2}}, \tag{4.5}$$

where $\begin{pmatrix} l & l & l \\ m_1 & m_2 & m_3 \end{pmatrix}$ is the Wigner 3-$j$ symbol [179] and the integers $m_1$, $m_2$ and $m_3$ run from $-l$ to $+l$, but are limited to the case where $m_1 + m_2 + m_3 = 0$. As the $\bar{q}_l$ and $\bar{w}_l$ order parameters average over an extra shell of neighbors, particles closer than $2r_c$ to the edge of the data set box were used for the calculations of the $\bar{q}_{lm}$ parameters, but left out in the final analysis.

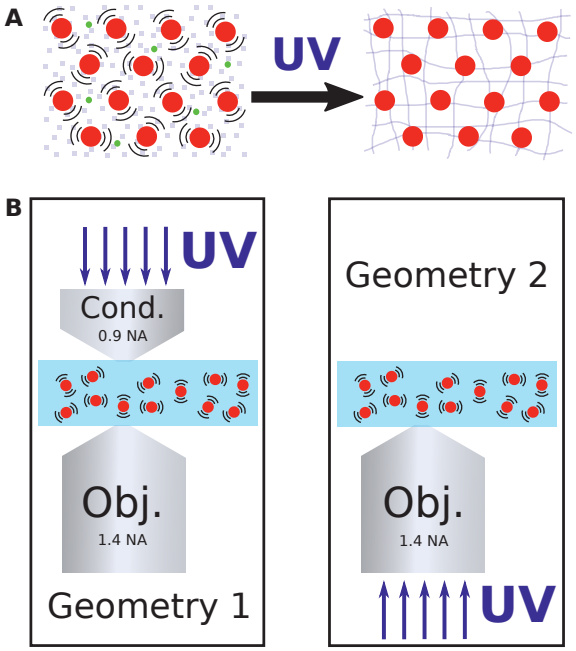


**Figure 4.2: Schematic of method to arrest colloidal dispersions.** UV light induced polymerization of a crosslinking monomer (grey squares) using a photo initiator (green circles), which are both part of the solvent (**A**). The two different geometries (**B**). Geometry 1: UV light ($\lambda = 365$ nm) is focused on the dispersion through a 0.9 NA condenser lens, while the dispersion is imaged using a high NA inverted confocal objective. Setup 2: UV light is focused on the sample using the same inverted high NA objective as for scanning.

## 4.3 Results

### 4.3.1 Arrest of a long range repulsive colloidal crystal

We first demonstrate our method of dynamic arrest by polymerization of a component in the continuous phase of a dispersion of long range repulsive PMMA colloids [33]. The PMMA particles were 3.3 $\mu$m in diameter (4% polydispersity index (PDI), static light scattering (SLS)) and fluorescently labeled with the dye 7-nitrobenzo-2-oxa-1,3-diazol (NBD). To enable the arrest, the monomer ETPTA (trimethylolpropane ethoxylate triacrylate, 6.5 v%) was added to the solvent mixture of cyclohexyl bromide (CHB) and cis-decalin. The monomer used here, trimethylolpropane ethoxylate triacrylate (ETPTA), needs to be miscible with the solvent mixture of the colloidal dispersion for the arrest method to work. We found that ETPTA was miscible at 10 v% with a variety of solvent mixtures with low to intermediate polarity, with effective dielectric constants $\epsilon_{eff}$ ranging from $\sim$6 (22 w% cis-decalin/CHB) to $\sim$44 (10 v% *n*-butanol/DMSO). Next, the PMMA particles were dispersed in the solvent mixture and the photo initiator Irgacure 2100 (0.0065 v%) was added to the dispersion. After the dispersion was loaded into a capillary, the arrest was triggered using a UV light pulse (365 nm), focused onto the sample using a 0.9 NA condenser lens as shown in Figure 4.2B (Geometry 1, spot intensity: 6 mW). We found that removal of oxygen from the colloidal dispersion before sample preparation increased the speed of polymerization. The interactions of the particles are very sensitive to the ionic strength. Therefore, a structural change is expected if the timescale of the arrest is larger than the timescale of the diffusion of the particles over which the particles significantly change their configuration. The dispersion was prepared at a volume fraction where the particles formed a long range repulsive crystal, which allows for a quantitative check of any structural change. This can be checked by comparing the lattice parameters of the crystal, the rotationally averaged distances as provided by the radial distribution function $g(r)$ and the local symmetry of the particles and their neighbors as expressed by so-called bond order parameters [176, 282], before and after the arrest.

Fig. 4.3A shows a maximum projection of a confocal time series of the crystallized dispersion, indicating the movement of the particles around their equilibrium position in the crystal. After a one second pulse of UV light (365 nm), focused on the sample using the condenser lens of the microscope (Geometry 1, spot intensity: 6 mW, Fig. 4.2B), the particles were arrested (Fig. 4.3B and Supporting File 4.1). The typical total arrested area for this geometry was $\sim$7 mm$^2$, and could be reduced to as small as $\sim$0.8 mm$^2$ by decreasing the size of the condenser aperture. When the particle positions were tracked in 2D [105] during the arrest, a decrease in the dynamics of the particles was observed after the UV light pulse (Fig. 4.3C). The frame averaged displacement $\langle\sqrt{(\Delta x)^2 + (\Delta y)^2}\rangle$ of the particles after the arrest was non-zero, due to the static error of the particle tracking, caused by the low signal to noise ratio during the relatively fast confocal scanning [283]. The frame averaged displacement of the particles was fitted with a logistic dose-response curve, from which the center of the sigmoid was used as an estimate for the time by which the dynamics of the particles were stopped $t_{stop}$. When compared to the time the UV pulse was applied $t_{UV}$, the arrest time could be estimated as $t_{arrest} = t_{stop} - t_{UV} \approx$ 0.65 seconds. The arrest time $t_{arrest}$ was found to vary in the range of 0.1-0.8 seconds in

repeated experiments using this method. The time it takes for a colloid in this system to diffuse over its own radius $a$ can be estimated by $\tau_a \sim \frac{a^2}{D} \sim \frac{6\pi\eta a^3}{kT}$, where $D$ is the free diffusion constant and $\eta$ the solvent viscosity [261]. Here, $\eta$ is >2.7 mPa·s [84] and therefore $\tau_a > 10$ seconds. This means that the arrest of the particles happened well before the particle configuration had time to change significantly due to a drop in the ionic strength, especially since the actual self-diffusion coefficient is significantly reduced with respect to the free diffusion coefficient used in this estimate, due to the interactions of the particle with its neighbors slowing down the self-diffusion.

To further verify the preservation of the structure, confocal z-stacks were recorded before and after the arrest described in the previous paragraph. Using 3D particle fitting algorithms [105, 110] the coordinates of the particles were extracted to calculate the radial distribution functions (see Fig. 4.3D and Supporting File 4.2). The radial distribution functions after the arrest show no significant difference to the one before the arrest, with only a small difference visible in the second peak ($r \approx 12.5$ $\mu$m). In addition, we calculated the fraction of crystalline particles from the coordinates using the Ten Wolde criterion, based on bond orientational order parameters [176, 282]. Before the arrest 93% of the particles had crystalline order, while after the arrest this slightly decreased to 92%. For further structural analysis, the averaged local bond orientational order parameters $q_6$ and $q_4$ were calculated from the coordinates of the particles [178]. In Figure 4.3E the histograms of the two order parameters, as well as their scatter diagrams, are plotted for the coordinate sets before (red) and after (blue) the arrest. In both case the parameters indicate a mixture of the body-centered cubic (BCC), hexagonal close-packed (HCP) and face-centered cubic (FCC) crystal structures. As there was some time between the recording of the confocal z-stack before the arrest and the arrest itself, a random displacement of the particles is expected, leading to different positions of the data points in the scatter plot. Still, in addition a very small, almost insignificant, shift to lower $\bar{q}_6$ and $\bar{q}_4$ values by ∼0.01 is visible in the scatter plots and histograms.

Where particles in the z-stack recorded after the arrest were immobilized, the particles in the z-stack recorded before the arrest were still undergoing Brownian motion. This leads to so-called dynamic errors in the tracking of the particles [283]. The z-stack before arrest was recorded with a stack size of 512 × 512 × 119 pixels at a frame rate of 16.8 frames per second. As each particle appeared in 9 consecutive frames, the time to fully image a single particle was ∼0.5 seconds. The maximum displacement of the particle in this time is 0.05 times its own radius, in this case <80 nm, as can be estimated from the self-diffusion time of the particle. The error in the tracking in the position of the particle then equals half this displacement, as the position of the particle is averaged over the 9 frames recorded when the particle was moving. In practice this error will be lower, as the self-diffusion of the particle is smaller in the dense suspension. Still, as the positions of the particles are time averaged over just less than a second, a bias of the position of the particle to the equilibrium position of the particles in the crystal will be present. This could explain the apparent small decrease in order of the particle data sets recorded after the arrest, where the particle are arrested in their off-equilibrium positions.

In literature the polymerization of the pure monomer used here is reported to coincide with a volume shrinkage of ∼7% [267, 284]. In addition, it was found that for the shrinkage of a thin film, the contraction happens mostly in the $Z$-direction [267]. Fig. 4.3H shows

the distribution of $Z$ coordinates of the particles before and after the arrest. The average inter-layer spacing was determined by fitting a linear function through the peak positions. This resulted in an inter-layer spacing of $6.28 \pm 0.02$ $\mu$m before, and $6.30 \pm 0.02$ $\mu$m after the arrest, both with a fit where $R^2 = 0.9998$. Apparently, the dilution of the monomer to 6.5 v% results in the absence of a densification of the structure due to a contraction of the polymer matrix the particles are trapped in.

To investigate whether the arrest induced any in-plane deformation the distances $a$ and $b$, as shown in Figure 4.3F and G, were measured for every plane in the coordinates obtained from the confocal z-stack recorded before and after the arrest. To do this the coordinates of each plane of particles were projected on a plane, of which the fast Fourier transform was calculated. From the pattern the ratio $b/a$ was measured and compared before and after the arrest. In both data sets the $b/a$ ratios measured were in the range of 1.50 to 1.65, and no change of the $b/a$ ratio larger than 3% was observed between the confocal z-stack recorded before and after the arrest.

Long range repulsive colloidal crystals confined between two glass walls (for instance in capillaries like the ones used here), tend to orient their (111) planes or (110) planes parallel to the glass walls, for the face-centered cubic (FCC) and body-centered cubic (BCC) crystal structures, respectively [45]. The $b/a$ ratio in these planes are then equal to $\sqrt{3} \approx 1.73$ (FCC) and $\sqrt{2} \approx 1.41$ (BCC). Here, the $b/a$ values of the planes are found to be somewhere in between. In Figure 4.3I three consecutive planes of particles of the z-stack recorded after the arrest are plotted in one image, where the middle layer is colored green, while the two other planes are colored blue and red. In the left of the image the outer layers of particles are found to overlap frequently (visible as magenta particles), while in the right part of the image they are shifted with respect to each other. As the values of the in-plane $b/a$ ratios are in between the values expected for the (111) plane of FCC and the (110) plane of BCC and the stacking of the layers is irregular, we conclude that the crystal arrested here is out of equilibrium. The shift of the $\bar{q}_4$ values of the particles towards zero (see Figure 4.3E) could be hinting at an increasing BCC order of the crystal between the recorded z-stack and the arrest itself.

### 4.3.2 Arrest of external field induced assemblies

As an illustration of the advantages of our arresting methodology, we will show how external field induced structures can be analyzed in detail after the 3D structure is arrested. This allows for instance the preservation of structures that are actually metastable without the presence of the external field and thus would otherwise collapse after the external field is removed. Moreover, it enables careful analysis of the structure and the use of the metastable structures in for instance photonic applications of colloidal crystals created using these external fields. Two external fields are demonstrated here: oscillatory shear [3, 259] and electric field [33, 110].

#### Shear induced (para-)crystallization of long range repulsive colloids

To demonstrate the method on shear induced colloidal crystals, or para colloidal crystals, which melt in absence of the shear [259], a colloidal dispersion of PMMA particles in a

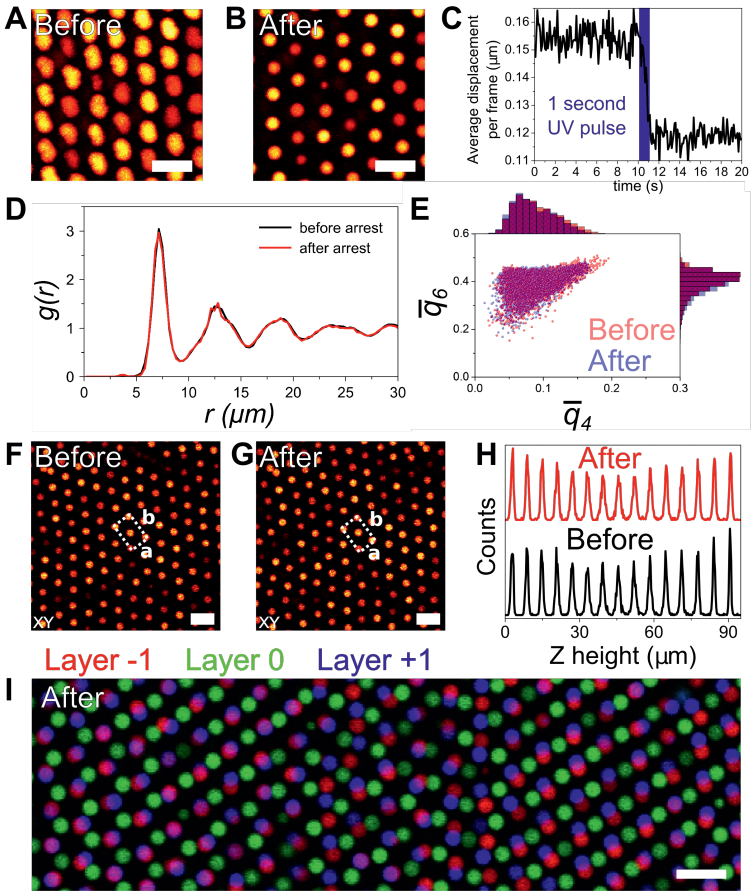


**Figure 4.3: Arrest of long range repulsive PMMA colloids in a CHB/cis-decalin solvent mixture with an added monomer and photo initiator.** Maximum intensity projections of two time series of a colloidal dispersion before (**A**, 872 frames) and after (**B**, 424 frames) arrest demonstrating the immobilization of the particles. The arrest induced by the UV light pulse ($\lambda$ = 365 nm, 1 second, spot intensity: 6 mW) is also visible in the average displacement per frame of the particles as a function of time (**C**), obtained through 2D particle tracking [105]. The radial distribution functions (**D**) calculated from the particle coordinates obtained by particle fitting of a confocal z-stack before (black) and after (red) arrest show little structural difference between the two. In addition, the $\bar{q}_6$ and $\bar{q}_4$ bond order parameters (**E**) show a very slight shift in the order of the particles, while there is no visible difference between two $XY$ images of the same crystal plane before (**F**) and after (**G**) the arrest. The histograms of the particle $Z$ coordinates (**H**) show the absence of contraction of the crystal, as the inter-layer spacing remains constant: $6.28 \pm 0.02$ $\mu$m (before) and $6.30 \pm 0.02$ $\mu$m (after). Plotting an overlay (**I**) of a particle layer (green) and its two neighboring layers (red and blue) of the confocal z-stack recorded after the arrest, reveals an irregular stacking of the crystal planes. The scale bars are 10 $\mu$m.

CHB, cis-decalin, monomer and photo initiator mixture was sheared using a parallel-plate shear cell [281]. The particles were 3.3 $\mu$m in diameter (4% PDI, SLS) and fluorescently labeled with NBD dye. The volume fraction $\phi$ of the dispersion was 0.18 and the Debye length $\kappa^{-1}$ was estimated to be 4 $\mu$m by measuring the conductivity of the solvent mixture, although due to contact of the dispersion to the epoxy glue used to keep the glass plates in the shear cell in place, we estimate a lower $\kappa^{-1}$ of $<3$ $\mu$m ($\kappa\sigma > 1$). After loading the dispersion in the shear cell, a disordered fluid was observed (Fig. 4.4A). The distance between the two parallel plates was $\sim$55 $\mu$m. When shear was applied (1 Hz linear shear rate, 200 $\mu$m amplitude), hexagonal order started to emerge after 3 seconds (Fig. 4.4B,C). After $\sim$15 minutes pronounced hexagonal order was established (Fig. 4.4D). The hexagonal order of the particle layer was confirmed by measuring the angles in the time averaged fast Fourier transform (FFT) of a time series of the zero-velocity plane (Table 4.1, for a single image, see Figure 4.4D). In the measured FFT pattern the angles deviated with a maximum of 2° from the 60° expected in perfect hexagonal order. For comparison, the very similar (110) plane of a BCC crystal [181], which is often found parallel to glass walls and therefore in the lateral ($XY$) direction of the confocal microscope [45], shows a deviation up to 10° from the perfect hexagonal order (see Table 4.1).

Next, the shear was stopped and the sample was immediately exposed to a one second UV light (365 nm, spot intensity: 0.7 mW) pulse using geometry 2 (see Fig. 4.2B). The maximum projections of two confocal time series recorded just before and after the arrest are shown in Figure 4.4E. While the particles are diffusing around their equilibrium position in the shear-induced crystal, the particles became arrested after the UV exposure. The use of a high NA objective to focus the UV light resulted in a smaller area to be arrested: a circular area with a diameter of $\sim$200 $\mu$m was arrested (see Fig. 4.4F). At the edge of the arrested area, a thin low density ring was formed, followed by a zone where the particles seem to have lost some of their long range repulsive interactions. Further away, $\sim$50 $\mu$m, the particles were still long range repulsive. To investigate the 3D structure of the arrested volume, a confocal z-stack was recorded. The average of all the FFTs of that stack is shown in Fig. 4.4G, demonstrating the same hexagonal order as found in the zero-velocity plane before the arrest. As there is hexagonal order in the crystal planes, these are most likely the (111) plane of either a face-centered cubic (FCC) or body-centered cubic (BCC) structure. The two structures can be distinguished by the ratio $r/d_{111}$, where $r$ is the shortest distance between the particles in the hexagonal (111)

| Shear induced crystal | (110) plane BCC (Liu *et al.* [181]) |
|---|---|
| 59° | 70° |
| 61° | 54° |
| 60° | 55° |
| 58° | 70° |
| 61° | 55° |
| 61° | 54° |

**Table 4.1:** Measured angles in the inner ring of the time average of fast Fourier transforms (FFTs) of a confocal time series of the zero-velocity plane of a shear induced crystal compared to the FFT pattern of the (110) plane of a BCC crystal as reported by Liu *et al.* [181].

plane and $d_{111}$ is the distance between the (111) planes: $r/d_{111} = \sqrt{3/2} \approx 1.225$ (FCC) or $r/d_{111} = \sqrt{6} \approx 2.449$ (BCC). Here, we find that $r/d_{111} \approx 1.26$, which corresponds quite well to the FCC structure. The stacking of the crystal in the $(\bar{1}10)$ plane can be viewed in Figure 4.4H, where predominant *ABC* stacking of the hexagonal layers is visible (as expected for FCC), while there are also a few *ABA* stacked layers present, as present in the hexagonally close packed (HCP) structure. From the confocal z-stack, the 3D coordinates of the particles were obtained [105, 110]. Using the earlier mentioned Ten Wolde criterion [176, 282] and the bond orientational order parameter $\bar{w}_4$ [178], the crystal structure of the crystalline particles was confirmed to be FCC ($\bar{w}_4 < 0$) with some HCP ($\bar{w}_4 > 0$) layers present.

**Electric field induced dipolar chains**

To demonstrate the method on electric field induced structures [33, 110], PMMA particles were dispersed in a mixture of CHB (saturated with tetrabutylammonium bromide (TBAB)), cis-decalin, monomer and photo initiator at a volume fraction $\phi = 0.25$. The PMMA particles were 1.7 $\mu$m in diameter (4% PDI, SLS) and fluorescently labeled with a rhodamine dye. The screening length $\kappa^{-1}$ was estimated to be 140 $\mu$m ($\kappa\sigma \approx 12$) from conductivity measurements of the solvent mixture.The mixture was loaded into a cell with two parallel indium titanium oxide coated cover glasses as electrodes, separated using a #0 cover glass as spacer, resulting in a distance between the cover glasses of $\sim$120 $\mu$m. To induce the formation of particle chains, a 1 MHz AC electric field of 0.3 V/$\mu$m was applied for 25 minutes. A frequency of 1 MHz was used as at this frequency the electric double layer around the particles cannot follow the field, and the field only induces the dipolar interactions between the particles [33]. Due to the field induced dipolar interactions of the particles, chains of particles were formed parallel to the electric field. These chains, however, would still undergo Brownian motion perpendicular to the field and would be attracted to other chains to form sheets [33, 285]. The PMMA particles were imaged with confocal microscopy, where the axial direction of the microscope is parallel to the field (see Fig. 4.4I,J). In the lateral *XY* plane (Fig. 4.4I), the particles formed square patterns, while in the axial *XZ* plane the strings and sheets are visible. Although the structure in the lateral plane can easily be resolved, the imaging in the axial plane is hindered by the limited scanning speed of the microscope. While the chains of particles can be resolved, the single particles in the strings can not. The use of core-shell particles would largely overcome this problem [19], but the synthesis of core-shell systems is generally more involved [286].

After the dispersion was arrested by a two second UV pulse (365 nm, spot intensity: 6 mW) using geometry 1 (see Fig. 4.2B), it could be imaged with a much slower acquisition time, and therefore a higher image quality. Fig. 4.4K shows the lateral plane of the arrested dispersion and a major increase in the image quality. The biggest improvement, however, is in the axial plane, where the individual particles in the chains of particles could now be resolved and tracked in 3D [105, 110] (Fig. 4.4L and Supporting File 4.3). This makes it unnecessary to use core-shell colloids synthesized with more involved synthesis procedures.

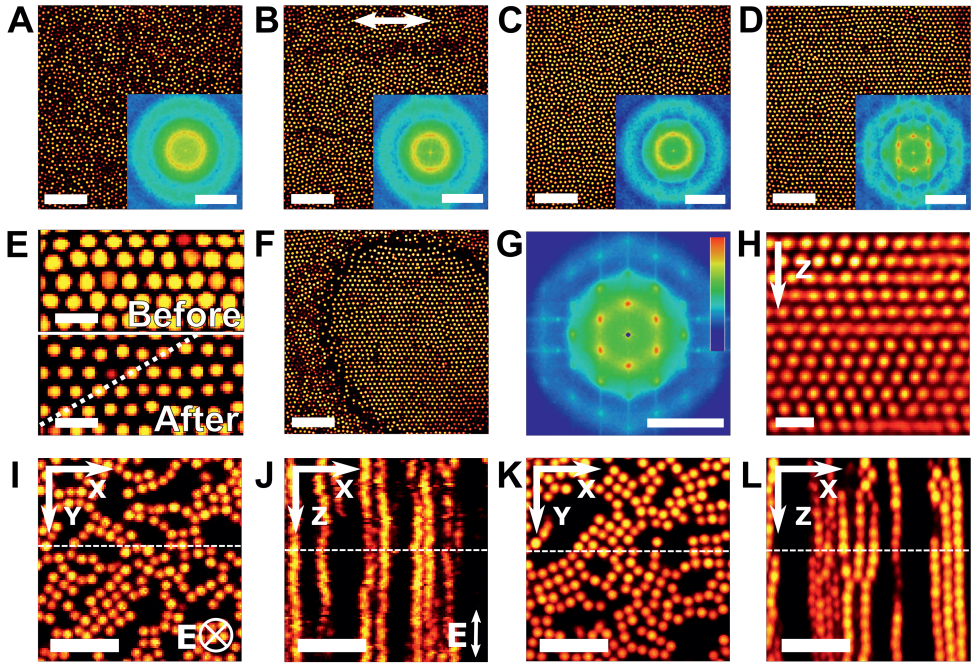


**Figure 4.4: Arrest of external field induced assemblies.** Confocal images at the zero velocity plane of a long range repulsive colloidal fluid undergoing shear induced crystallization at 0 (**A**), 3 (**B**), 191 (**C**) and 878 (**D**) seconds, with the insets showing the fast-Fourier transform (FFT) of the confocal images. The arrows in (**B**) denote the direction of the oscillatory shear. The linear shear rate was 1 Hz with a shear amplitude of 200 $\mu$m. After exposure to UV light focused by the confocal scanning objective, the particles are arrested, as visible in the maximum projections of confocal time series before (95 frames) and after (115 frames) the arrest (**E**). A spot with a diameter of $\sim$200 $\mu$m was arrested (**F**). The average of the FFTs of a confocal z-stack of the arrested volume shows the preservation of the hexagonal order present in the particle layers of the crystal (**G**). The average projection of the confocal z-stack along the $(\bar{1}10)$ plane (dashed line in (**E**)) shows the dominant $ABC$ stacking of the hexagonal layers, with some $ABA$ stacked layers present (**H**). Confocal z-stacks of AC electric field (0.3 V/$\mu$m, 1 MHz) induced colloidal chains before (**I**,**J**) and after arrest (**K**,**L**). While the single particles can be resolved in the lateral ($XY$) plane before the arrest (**I**), the slow scanning of the confocal results in a smeared out image of the particles in the axial ($XZ$) plane (**J**). After the arrest the particles can be resolved in both planes (**K**,**L**) . The dashed white lines in (**I**-**L**) correspond to the intersections of the corresponding perpendicular imaging planes. The scale bars are 50 (**A**-**D**,**F**) and 10 (**E**, **H**-**L**) $\mu$m for the confocal images and 0.5 $\mu$m$^{-1}$ for the FFT images (**A**-**D**,**G**).

### 4.3.3 Averaging out the effects of gravity in combination with arrest

Earth's gravitational field influences many colloidal processes, such as gelation and crystallization, if the particles are not fully density matched with the continuous phase [287–291]. For instance, after experiments on hard sphere crystallization in space, it became clear that in the same experiments on Earth, the roughened layers at the interface of the nuclei were almost always sheared off by sedimentation [290]. One relatively easy way to overcome this, is by averaging out gravity by slow rotation of the colloidal dispersions [273, 275]. The down side is that this does not allow for imaging of the dispersion during the process. In addition, when the rotational averaging is stopped, any structures that have formed (e.g. in a colloidal crystallization and/or a phase separation) sediment even significantly faster than single colloidal particles would. This gives only very short time scales for full 3D imaging of the structures formed before they are strongly influenced by gravity. The obvious solution is combining our arresting procedure either when the rotational averaging is still ongoing or within a fraction of a second after it. Even if the density matching of the particles with the continuous phase is done well, say leaving only 0.01 $g$ of the ordinary gravitational field, it would still result in over 1 $\mu$m sedimentation for e.g. a small colloidal crystal composed of only a few thousand particles, and the resulting configuration of the particles will significantly change during the recording of a confocal z-stack, due to gravity remaining. By using a slight modification of the method as described before, the dispersion can be arrested before the imaging, allowing to sample the colloidal process to first approximation without the effects of gravity.

We demonstrate this by studying the nucleation of a liquid crystal and/or the initial aggregation of attractive silica rods, where the attractions are induced by the presence of much smaller spherical particles [43]. The silica rods were refractive index matched with the solvent, but have a large density mismatch ($\Delta\rho = |\rho_{part} - \rho_{solvent}| \approx 1$ g/mL). The particles had a length $l$ of 2.65 $\mu$m (10% PDI, TEM) and a diameter $d$ of 0.62 $\mu$m (12% PDI, TEM) and were fluorescently labeled with fluorescein dye for confocal imaging [279]. The rods were dispersed ($\phi = 0.15$) in a mixture of butanol, dimethyl sulfoxide (DMSO), monomer and photo initiator, with small silica spheres ($\sigma = 120$ nm, 9% PDI, TEM) added ($\phi = 0.12$) to induce depletion attractions between the rods. This solvent mixture is refractive index matched with the silica rods ($n \approx 1.45$ [278]) to ensure optimal imaging conditions. The gravitational length $l_g$ of the silica rods in this solvent mixture was estimated to be 0.6 $\mu$m ($\sim 1d$) [84, 260, 292]. Two capillaries were filled with the dispersion and closed using candle wax. Immediately after sealing the capillaries, the samples were put on a slowly rotating stage ($\sim$5.5 rpm, same stage as in [273]) and left to equilibrate. To study the nucleation, the colloidal dispersion was sampled 2 and 72 hours after preparation. To this end, the samples were removed from the rotating stage and quickly put under a UV lamp (365 nm, UVGL-58, 6 W, UVP) for 2 minutes. Next, the samples were imaged using confocal microscopy.

Figure 4.5 shows typical images from confocal microscope 3D data sets recorded after the arrest of the dispersions. Due to the arrest, the particles were evenly distributed along the direction of gravity during imaging and could be imaged in 3D with confocal microscopy. Figure 4.5A shows a typical confocal image of the dispersion after 2 hours

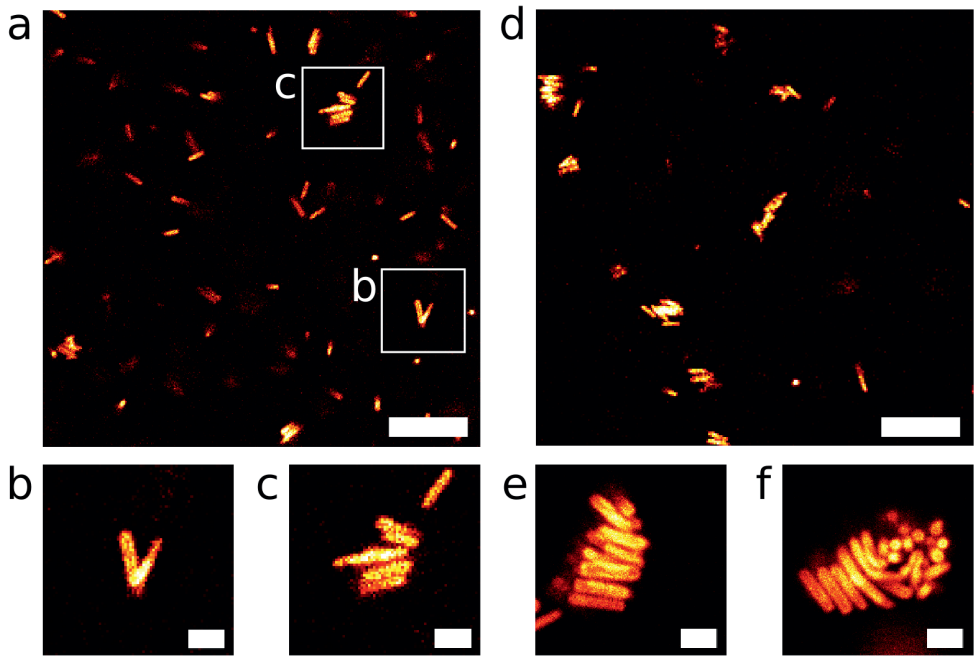


**Figure 4.5: Nucleation of a liquid crystal studied using gravitational averaging and the arrest method.** Confocal images of the nucleation of a liquid crystal of attractive silica rods after 2 (**A**-**B**) and 72 (**D**-**F**) hours equilibration on a slowly moving rotation stage. Before imaging, the dispersion was arrested using UV light (365 nm). After 2 hours of equilibration most particles were still diffusing freely (**A**), with only a few small clusters present (**B**,**C**). After 72 hours of equilibration, only small amount of particles were unbinded (**D**), while significantly larger clusters could be found (**E**,**F**). Note that the colloids preferably attached along their long side, expected for depletion interactions [44]. The insets in (**A**) correspond to (**B**) and (**C**). The scale bars are 10 (**A**,**D**) and 2 (**B**,**C**,**E**,**F**) $\mu$m.

of equilibration. Most particles were still diffusing freely before the arrest, with only a few clusters present (see Fig. 4.5A-C). After 72 hours of equilibration, only a few single particles were visible, with the majority of the particles trapped in liquid crystal clusters (see Fig. 4.5D-F). In these clusters the particles preferentially attached along their sides, as is expected for depletion interactions [44]. The big clusters could be found half way into the capillary, while without arrest they would have sedimented to the bottom glass wall during acquisition.

## 4.4 Discussion

We have demonstrated the use of this method for low up to intermediate polar solvent mixtures with 10 v% monomer (ETPTA). For PHSA-stabilized PMMA particles the

monomer ETPTA can be used in combination with the solvent mixture composed of CHB and cis-decalin, where the density and refractive index of the particles and solvent can be matched. The interactions of the particles can be tuned from nearly hard sphere to long range repulsive by the addition of tetrabutylammonium bromide (TBAB) and the deionization of the solvent [45]. For silica particles, the monomer ETPTA is compatible with different solvent mixtures used for index matching of the particles to the solvent. To realize refractive index matched long range repulsive silica particles for the arrest, the monomer can be mixed with the deionized solvent cyclohexyl chloride (CHC) [181]. For refractive index matched silica with hard sphere interactions, a 10 v% *n*-butanol/DMSO mixture combined with the monomer and lithium chloride salt can be used. This is a good replacement for the 85 w% glycerol/water solvent mixture, often used for confocal studies of hard silica colloids [84, 292], but which is too polar to be miscible at 10 v% ETPTA. Alternatively, more polar acrylates functionalized with poly(ethylene glycol) (PEG), such as poly(ethylene glycol) diacrylate (PEGDA) [293, 294], can enable the arrest method for these high polar solvent mixtures.

The arrest of colloidal dispersions can be used to study colloidal processes, too fast for 3D real-space imaging using confocal microscopy, for instance the accurate imaging of nuclei in colloidal crystallization (see Chapter 5). Combined with the rotational averaging of gravity it provides a way to study processes that are affected by a gravitational field, without the need to study these processes in space [290]. This enables the study of processes which are usually strongly affected by a gravitational field, even when density matched, like colloidal crystallization or gellation/aggregation [273, 288, 291, 295].

Next to fast processes, the method can also be used to study colloids where the signal to noise ratio, when imaging the dispersion, is small. The arrest allows the accumulation of images, reducing the noise. This is useful to study for instance smaller colloids, where the fluorescent volume is small. This would make it possible to measure the interaction potential of nanoparticles through the measurement of the radial distribution function from the coordinates of the particles.

While in this chapter the use of this method is demonstrated using confocal laser scanning microscopy, the method can also be applied for improved studies using different techniques. Super resolution microscopy techniques like STED, STORM and PALM require longer acquisition times than (confocal) microscopy [88]. In addition, the higher resolving power of these techniques makes them ideal for studying smaller colloids, but these require faster 3D image acquisition. With the arrest of the colloidal dispersion, there is no limit to the acquisition time of images, although possibly the arresting will need to be done at an even shorter time scale than presented in this chapter. However, there is still room for improvement of the polymerization process, for instance by increasing the intensity of light, resulting in a faster time of arrest.

Recently, the use of confocal tomography was proposed to study colloidal dispersions [274]. In this technique the point spread function is rotated with respect to the sample, after which an image can be reconstructed at a 3D resolution without the limited axial resolution of the confocal. The rotation can be achieved, either by rotating the sample, or by the rotation of the objective around the sample. One condition, however, is that the sample's configuration does not change during the acquisition, which can be realized using our arresting methodology.

In addition, next to light microscopy, the arresting methodology can also be applied to electron microscopy. When the continuous phase is composed solely of monomer, the dispersion can be studied with focused ion beam scanning electron microscopy (FIB-SEM) tomography. Yang *et al.* demonstrated this in studying the packing of soft repulsive silica spheres in cylindrical confinement [296]. In Chapter 2 we have shown that FIB-SEM tomography can be used to quantitatively analyze 3D assemblies of colloidal particles for which conventional methodologies like STED confocal or transmission electron microscopy tomography will not work. When the interactions between the colloidal particles need to be tuned in a way that is not possible with using pure monomers as solvent, the arresting procedure can also be followed by a cryogenic step, freezing the remaining solvent in between the polymer network. This makes it possible to study the dispersion under the high vacuum conditions at cryogenic temperatures in electron microscopes ((FIB-)SEM or transmission electron microscopy), and most likely also reduces damage induced by the electron beam irradiation.

While this chapter focuses mainly on the application of the arrest method on the imaging of colloidal dispersions for model studies, it can also be applied to samples intended to provide new materials properties. As mentioned earlier, many colloidal particles with e.g. different dielectric, magnetic and other properties can be coated by PMMA and/or silica layers. Thereby making direct connections with the range of potentials and processes described in this chapter, including systems that are not index matched. The method allows to arrest external field induced metastable structures, that would otherwise collapse when the external field is removed. These structures include the so-called string and tilted layer phases found in hard-sphere-like dispersions under shear [259, 297], as well as electric field induced colloidal chains, sheets and body-centered tetragonal crystals [33]. For instance, the polymer matrix around the particles allows the reversible squeezing of the structures, resulting in new mechanically responsive materials [35].

## 4.5 Conclusions and Outlook

We have demonstrated a general method to arrest colloidal dispersions containing PMMA or silica particles by the polymerization of a component of the continuous phase. The dispersions were arrested by addition of a monomer and photo initiator and a timed exposure to UV light. As the arrest happened in a fraction of a second, it had no effect on the structure of the dispersion, as we have demonstrated for a long range repulsive colloidal crystal. We have shown the method can be applied to colloidal dispersions with interactions ranging from hard-sphere-like, to long range repulsive, dipolar and depletion-induced attractive. Moreover, it works with particle dispersions commonly used for confocal microscopy study, as they can be refractive index matched. As many particle systems are comparable in their stabilization to our PMMA and silica particles, there is a high likelihood this method can be applied to many other colloidal systems. Moreover, methods exists to coat a variety of particles with either PMMA or silica, in case the particles would not be compatible with our method. The method enables the preservation of metastable structures induced by an external electric field and/or field gradient (electric bottle), for careful 3D real-space study or the development of new switchable materials. Moreover, in

combination with gravity averaging methods it can be used to study the dynamic processes of density mismatched colloidal dispersions. Next to confocal microscopy studies, the method can be used for other imaging methods, such as super-resolution light microscopy as well as FIB-SEM tomography.

## 4.6 Acknowledgements

The work on the arrest of the colloidal crystal and the electric field induced chains was done in collaboration with Anna Nikolaenkova. Albert Grau Carbonel performed the arrest of the silica rods. We thank Johan Stiefelhagen, Teun Vissers and Albert Grau Carbonel for particle synthesis. In addition, we thank Peter Helfferich for technical assistance, Ajoy Kandar for the assistance on using the shear cell and Anna Nikolaenkova for critical reading of this chapter. We also thank Burak Eral, Wessel Vlug and Johan Stiefelhagen for useful discussions. BASF is thanked for providing a sample of Irgacure 2100.

# 5

# Confocal microscopy study of homogeneous crystallization of nearly hard sphere colloids by the arrest of the dispersion

Homogeneous hard sphere nucleation has been widely studied in theory, simulations and experiments. The structure of the nuclei has been reported to be random hexagonal close packed (RHCP), while the face-centered cubic (FCC) stacking was found to be more favorable over the hexagonal close-packed structure in simulations. In this chapter we employ confocal microscopy in combination with the arrest method described in Chapter 4 to study homogeneous crystallization of a poly(methyl methacrylate) (PMMA) sphere dispersion. By dielectrophoretic compression of the colloidal dispersion in an electric bottle cell, the volume fraction of the dispersion is increased to control the amount of supersaturation. We show that using this method, large volumes of ∼500,000 crystallizing colloidal particles or more, as the method is trivially extendable, can be characterized in real-space. As it is possible to analyze very large volumes (e.g. milliliter sized), this opens up the possibility to study nucleation at low supersaturation as well, where the number of nuclei per unit volume is low. Using bond order parameters, we find that the local symmetry of the crystalline particles shows no preference for the FCC stacking sequence and find an essentially negligible preference for the HCP stacking sequence, in contrast to earlier studies. In addition, we compare three methods for the estimation of the effective hard sphere diameter of PMMA in these experiments.

## 5.1 Introduction

Nucleation during the crystallization of supercooled liquids is a much studied physical process, with interest for, amongst others, the fields of condensed matter, food, materials and pharmaceutical sciences [298–310]. Homogeneous nucleation, where the nuclei form in the bulk, is commonly described using Classical Nucleation Theory (CNT) [311–313]. However, evidence has been accumulating for non-classical pathways in certain systems [298, 299, 314, 315]. By the end of the forties in the previous century, Turnbull was able to experimentally study homogeneous nucleation in metals, captured in droplets to suppress heterogeneous nucleation induced by clusters or foreign ('dust') particles [316]. Although CNT describes homogeneous nucleation well in a qualitative way, a large discrepancy is often found between theoretical and experimental nucleation rates, for instance for the nucleation of argon where a difference of ∼20 orders of magnitude is found [317].

Colloidal dispersions have proven to be a suitable model system to study crystallization, due to the fact that they can be several magnitudes larger than atoms or simple molecules [300–306, 315]. Their increased size with respect to atomic/molecular systems results in slower dynamics, by many order of magnitude. If the particles have a certain minimum size, they can be quantitatively studied on the single particle level by confocal microscopy [15, 136, 150, 291, 318–320]. In addition, light scattering can be used to study these particle systems, where a direct comparison to the scattering of atomic systems is possible [28, 290, 321, 322]. The most simple and commonly used colloidal model system is the hard sphere system [323], where the phase behavior of the particles is solely governed by entropy [21]. Where the experiments on colloidal hard-sphere-like suspensions started in the eighties [28, 324], the first simulation studies were already done in the fifties [22, 23], and have been contributing to the understanding of colloidal crystallization ever since [307, 309, 325–335]. The hard sphere system has a freezing transition at a volume fraction $\phi_{HS}^{f} = 0.494$ with a fluid-crystal coexistence up to the melting transition at $\phi_{HS}^{m} = 0.545$ [336].

### Homogeneous nucleation theories

According to CNT, the transition from liquid to crystal occurs in a single activated step with a transition state controlled by the size of the crystal embryo: the nucleus [311–313]. The Gibbs free energy $\Delta G$ of the nuclei with radius $r$ is determined by a surface and a volume term:

$$\Delta G = 4\pi r^2 \gamma + \frac{4}{3}\pi r^3 \Delta g, \tag{5.1}$$

where $\gamma$ is the interfacial free energy of the solid-fluid interface and $\Delta g$ is the free energy difference between the solid and the fluid per unit volume [307, 337]. For a supersaturated solution, where $\Delta g$ is negative, the surface term dominates at small $r$ and the formation of nuclei is unfavorable. For large $r$ the volume term starts to dominate and the nucleus becomes stable. This critical value of $r$ is called the critical nucleus size $r^*$. From $r^* = 2\gamma/\Delta g$ the nucleation barrier height $\Delta G^*$ can be calculated:

$$\Delta G^* = \frac{16\pi\gamma^3}{3(\Delta g)^2}. \tag{5.2}$$

From the nucleation barrier the steady-state nucleation rate $J$ can be calculated, assuming, amongst others [308, 337], that once a nuclei has crossed the barrier it continues growing into a bulk crystal:

$$J = J_0 e^{\left(-\frac{\Delta G^*}{kT}\right)}, \tag{5.3}$$

where $k$ is Boltzmann's constant and $T$ temperature. The prefactor $J_0$ is usually written as:

$$J_0 = \rho Z A_{kin}, \tag{5.4}$$

where $\rho$ is the number density of the supersaturated fluid, $Z$ the Zeldovich factor, which corrects for the possibility of postcritical nuclei melting back into the liquid, and $A_{kin}$ a kinetic prefactor [307, 330, 337]. The kinetic prefactor $A_{kin}$ is often connected with a self-diffusion constant of the fluid $D$. Consequently, the nucleation rate for diffusion limited nucleation first increases for higher supersaturation, while a further increase limits the diffusion of the fluid, and therefore decreases the nucleation rate.

While CNT describes homogeneous nucleation well in a qualitative way, large differences are found between the nucleation rate of hard spheres determined through experiments and simulations [319, 330], independent of the simulation techniques used [328]. These differences have been explained to be due to neglected hydrodynamics in simulations [330, 334], or the large uncertainties in experiments of e.g. the volume fraction [331, 338] or the effects of sedimentation [290, 291, 319, 339] (see following sections for more details). CNT assumes on average spherically shaped nuclei. In experiments, nuclei of hard sphere like colloids were found to be ellipsoidal in shape with rough surfaces [15]. In addition, in simulations at high supersaturation, fractal shaped nuclei were found [335].

More recently, alternatives and extensions to CNT have been proposed, involving a so-called two-step nucleation process [299, 307, 314, 315]. In the two-step crystallization process the fluid first produces pre-ordered or dense domains, within which the crystal nucleates in a second step. In the last decade, evidence for this has been found in experiments [136, 340] and simulations [315, 329, 331–333, 341]. For hard sphere crystallization, Schilling *et al.* found in simulations that the crystallization is preceded by a local density increase, followed by an increase in order of these dense regions [332]. Alternatively, it has been suggested that the nucleation is initiated by a structural fluctuation, followed by an increase in density of this locally structured region [315]. Work by Royall and co-workers showed that local five-fold symmetry in the supercooled fluid surpresses nucleation [318, 320].

**Heterogeneous nucleation studies**

Colloids have also been used to study heterogeneous crystallization, where the crystal nucleates from a surface [17]. The presence of a straight hard wall speeds up the crystallization of hard spheres in comparison to bulk crystallization [304], as found in simulations [342, 343] and experiments [343–345]. More specifically, hard sphere crystals wet a flat wall, which means that heterogeneous crystallization happens before bulk (homogeneous) nucleation starts [342]. Crystallization rates of heterogeneous crystallization from a low curvature

cylindrical or spherical hard wall have also been found to be increased, while the curvature induces frustations in the crystal [346]. As the curvature of the wall increases towards the curvature of the particles themselves, the wall is seen as an impurity, hindering the nucleation in respect to crystallization in the bulk [347, 348]. Recently, a spherical impurity with a radius ∼15 times the radius of the particles was found to catalyze the crystallization by an initial nucleation of the crystal near the impurity, after which the crystallite was detached and grew further in the bulk fluid [349].

The introduction of small crystallites as seeds into the supercooled fluid has enabled the measurements of nucleation rates at low supercooling, where nucleation events are too rare for traditional simulation methods [350]. In addition, the influence of the structure of the small crystallites on the shape, orientation and domain size of the resulting crystal has been studied in simulations and experiments [351, 352].

**Influences on the nucleation of nearly hard spheres**

For the experimental realization of the colloidal hard sphere system there are three major challenges: polydispersity, charge and sedimentation of the particles [29]. The polydispersity of the particles is known to influence the crystallization of hard spheres [310, 327, 353]: above a polydispersity index (PDI) of 7% crystallization is prevented. For particles with a PDI of 5-6% crystallization still happens, but the nucleation is slowed down [310]. Very recently, however, it has been observed in significant polydisperse (12-14%) hard sphere systems that the particles fractionate into different binary crystals with Laves phase structures, and therefore effectively reduce their polydispersity, both in simulations [354] and experiments [355].

For the most studied nearly hard sphere colloids, sterically stabilized poly(methyl methacrylate) (PMMA) spheres, PDI's below 5% can be realized [276]. These particles are often used as they can be density and refractive index matched using halogenated solvents [33], making them ideal for studying nearly hard spheres with confocal microscopy. The use of these halogenated solvents makes the particles prone to swelling and significant charging [29]. The introduction of salt (e.g. tetrabutylammonium bromide (TBAB)) minimizes the effects of the charges by screening, but due to the limited solubility of these salts, a typical minimal Debye length $\kappa^{-1}$ of ∼100 nm cannot be easily further reduced [29, 45, 356].

The effect of charges on the nucleation of spheres has been studied in simulations and experiments [304, 327, 357, 358]. Presence of charge on the colloidal particles shifts the phase behaviour to lower values of the volume fraction [304], for which can be corrected by estimating the effective particle diameter [29]. The presence of charge on the particles also lowers the interfacial free energy of the solid-fluid interface, resulting in higher nucleation rates [357, 358]. Recently, by careful comparison of experimental nearly hard sphere measurements with Brownian dynamics simulations using a Yukawa potential, a reasonable agreement was found between the nucleation rates of the two at moderate supersaturation ($\phi - \phi^m > 0.01$) [318]. Here, the dynamics were matched by fitting the structural relaxation times from the intermediate scattering functions of the experiments and the simulations. For lower supersaturations, and therefore lower crystallization rates, no agreement was found between the simulations and experiments. It was hypothesized,

this was due to the limited size of the particle systems in the simulations with respect to the experiments.

Sedimentation has a pronounced influence on the crystallization of hard spheres, not only on the structure of the crystal [290], but also on the nucleation rates [291, 319, 339]. In experiments, a local enhancement of the particle dynamics due to a density difference between the particles and the solvent mixture was reported [291]. In addition, a study of combined experiments and simulations showed a decrease of local five-fold symmetry in the supersaturated fluid for larger density mismatches [319], resulting in higher nucleation rates. Still, the increase in nucleation rates due to sedimentation can not account for the large difference between the nucleation rates between experiments and simulations [319]. For the nearly hard sphere system composed of PMMA particles in a halogenated solvent mixture [33], the particles can be density matched, resulting in sedimentation lengths of the particles much larger than the height of the experimental container [76].

### Structural study of hard sphere nucleation

The equilibrium crystal structure of hard spheres is the face-centered cubic (FCC) structure, with a free energy difference with respect to the hexagonally close-packed (HCP) structure on the order of $10^{-3}\ k_BT$ per particle at the melting density [328, 357]. As this difference is so small, a random stacking of hexagonal layers (RHCP) is found in experiments [290, 359, 360]. When the particles are slightly charged, the free energy difference increases, resulting in a preference for the FCC crystal structure [357, 360]. The structure of nuclei during the crystallization of a supercooled liquid of hard spheres has been studied in experiments and simulations [15, 150, 328, 361, 362]. In experiments, both RHCP and FCC with stacking faults have been reported in microscopy studies [15, 150]. In simulations, the RHCP structure was reported [361]. Later, the fraction of FCC stacking in the RHCP $\alpha$ was determined to be in the range of 0.55 to 0.8 [328]. In one study, five-fold symmetric stacking faults of FCC were reported, next to RHCP packings [362].

Confocal microscopy is, so far, the only experimental technique for real space structural characterization of nucleation on the single particle level [15, 318, 320]. The speed of the confocal microscope, however, is finite and results in acquisition times of full 3D stacks suitable for particle tracking on the order of seconds. Consequently, this can result in dynamic errors in the particle tracking [283] and can therefore influence the structural characterization. As the speed of the confocal microscope depends on the amount of points or voxels scanned in 3D, and a minimal amount of voxels per particle is needed for particle tracking, a limited volume can be scanned, containing typically $\sim$4000 particles in a system of micron sized particles close to the freezing density [15]. This makes that a repetition of experiments is needed to build good statistics, which can lead to differences in the system parameters of each experiment. Especially when the hardness of the particles and therefore the effective volume fraction differs between the experiments [15].

### Outline of this chapter

In this chapter, we study the structure of nuclei in the crystallization of nearly hard sphere suspensions by confocal microscopy and an additional arresting step (see Chapter 4). The suspensions are composed of sterically stabilized poly(methyl methacrylate) (PMMA)

spheres dispersed in tetrabutylammonium bromide salt (TBAB) saturated cyclohexyl bromide and cis-decalin. The electric double layer is estimated to be ∼140 nm, which is somewhat larger than the thickness of the steric stabilizer (PHSA), which can be estimated to be ∼10 nm [363]. As the particles are refractive index matched with the solvent mixture, van der Waals forces can be neglected. In addition, the particles and the solvent mixture are density matched to a sedimentation length of >1 mm [76], larger than the height of the experimental container (∼0.2 mm). To prevent pre-freezing of the fluid at the glass wall, the walls of the sample were made rough on the length scale of the particles. The arrest is realized by adding a monomer and photo initiator to the solvent mixture and a short UV light exposure, which arrests the system in less than a second, as shown in Chapter 4. This enables careful scanning of the sample at large volumes (∼500,000 particles), yielding high statistics in single data sets. We compressed the fluid using a dielectrophoretic bottle, where the density of the particles is increased using an electric field gradient [364], making it possible to increase the density of the supercooled fluid and probe higher supersaturations.

## 5.2 Methods

### 5.2.1 Particles

Poly(12-hydroxy stearic acid) (PHSA) stabilized poly(methyl methacrylate) (PMMA) particles were synthesized by dispersion polymerization using the method described by Bosma *et al.* [276]. After the synthesis, the stabilizer was covalenty bound to the particles [363]. The particles were fluorescently labeled with (rhodamine isothiocyanate)-amino styrene (RAS) and had a diameter of 1.88 $\mu$m (3% polydispersity index (PDI)), as characterized by fitting the scattering curve of the particles obtained by static light scattering in hexane with Mie theory.

### 5.2.2 Solvent mixture

The particles were dispersed in a mixture of cyclohexyl bromide (CHB), cis-decahydronaphthalene (cis-decalin) and trimethylolpropane ethoxylate triacrylate (ETPTA, $M_w$ = 428 g/mol). The weight ratio of the mixture was 69.4 : 21.4 : 9.2 (CHB : cis-decalin : ETPTA). Before mixing, the CHB was saturated with tetrabutylammonium bromide (TBAB) salt ($c \approx 260$ $\mu$M [45, 356]). The effective dielectric constant of the mixture was estimated using the method described in [365] and the literature values of the solvent components: 3.0 (ETPTA [366]), 7.92 (CHB [271]) and 2.2 (cis-decalin [367]). This resulted in an effective dielectric constant $\epsilon_{mixt}$ of ∼5.0. The conductivity of the solvent mixture was measured using a CDM 230 conductometer (Radiometer analytical) with a CDC 749 probe. A conductivity of 27 nS/cm was found. This corresponds to a Debye length $\kappa^{-1}$ of 140±10 nm, corresponding to an earlier reported value of the Debye length of a TBAB saturated CHB/cis-decalin mixture where $\kappa^{-1} \approx 130$ nm was found [84].

To reduce the influence of gravity on the particles during crystallization, the solvent mixture was density matched to the particles. This was done by dispersing particles at a volume fraction $\phi \approx 0.01$ and after a minimum of 48 hours (to allow the swelling of the

particles [364]) the sedimentation direction was checked using confocal microscopy. 9.2 w% mixtures of ETPTA in CHB (TBAB saturated) or cis-decalin were added in case the particles were sinking (CHB) or floating (cis-decalin).

In order to be able to arrest the dispersions, a mixture of photo initiator and CHB was added just before filling the cell (preparation of the cell is discussed below). The photo initiator Irgacure 2100 (BASF) was mixed with TBAB saturated CHB in a 10 v% concentration. The volume ratio of ETPTA : photo initiator was 1 : 100 in the final dispersion. Before filling the cell with the dispersion, oxygen was removed from the dispersion by placing it in vacuum in the airlock of a glove box, and the subsequent transfer to a nitrogen atmosphere. After this the cell was quickly filled with the dispersion and closed with UV glue (no. 68, Norland). The glue was cured for a maximum of 2 minutes using a UV handheld lamp (365 nm, UVGL-58, 6 W, UVP), while the dispersion was protected from the UV light using aluminum foil, with the inner side of the foil covered with black tape, to prevent the reflection of UV light onto the sample.

For radial distribution function measurements, a dispersion was prepared with a volume fraction at the freezing volume fraction. The dispersion was left to equilibrate for 6 days, after which a capillary was filled with the dispersion. After 6 hours, no crystallization was visible upon inspection with confocal microscopy. Next, the photo initiator/CHB mixture was added to the dispersion and a rectangular capillary (2.0 × 0.2 mm, Vitrocom) was filled with the dispersion, and closed with UV glue as described above. The sample was arrested on the confocal microscope and a z-stack was recorded (see Section 5.2.4). Next, the original dispersion was diluted with the solvent mixture with photo initiator/CHB added. This dispersion was then put in a capillary, arrested on the confocal microscope and a z-stack was recorded. This was repeated until the radial distribution function of the colloidal liquid at 7 different densities was obtained.

### 5.2.3 Electric bottle

In order to induce the crystallization of the PMMA particles the dispersion was compressed by dielectrophoretic compression [364]. For this an electric bottle cell was build in the following way: a rectangular borosilicate capillary (2.0×0.2 mm, Vitrocom) was coated with a ∼3 nm layer of chromium and subsequently a ∼9 nm layer of gold using a sputter coater (Cressington HQ280), where the chromium layer enhanced the wetting of the gold on the glass surface [45]. Electrode-free slits with a thickness of ∼0.5 mm with their long axis perpendicular to the long axis of the capillary were made by protecting the capillary using tape (SWT 10, Nitto) during the sputter coating. The cell was mounted on a cover glass with a hole in the middle with a diameter of 1.5 cm, for optimal UV exposure during the arrest. Using silver paint (SPI supplies) the electrodes were connected to thin thermocouple alloy wires (50 $\mu$m diameter, Goodfellow). The thin alloy wires were wrapped around standard electric wires for the connection to the electronic equipment. To suppress heterogeneous crystallization from the wall, large polydisperse PMMA particles were dried from hexane in the cell and sintered in an oven at 160 °C for 1 minute, creating a rough surface on the walls. A 1 MHz AC electric field was generated using a signal generator (Agilent, Model 33120A), which was fed into an amplifier (KrohnHite, model 7602M). The signal then passed through a transformer to increase the voltage of the

signal, but also to remove any DC component in the signal, which was monitored using an oscilloscope (Tektronix, Model TDS3052).

### 5.2.4 Confocal microscopy and UV exposure

An inverted Leica TCS SP8 confocal microscope equipped with a 63×/1.3 NA glycerol confocal objective was used to record z-stacks of the samples. The fluorophores in the PMMA particles were excited using a super continuum white light laser (SuperK, NKT Photonics) tuned to 543 nm, and the emitted light was detected in the range of 554-691 nm using a HyD detector. For UV exposure, a collimated LED source (365 nm, M365LP1-C2, Thorlabs) was mounted on the condenser and the UV light was focused by the condenser lens (0.9 NA) on the sample, resulting in a spot power of 6 mW (see also Chapter 4). Using a signal generator (Agilent, Model 33120A) a block pulse was fed into a LED driver (LEDD1B, Thorlabs) to create the UV pulse.

### 5.2.5 Analysis

#### Image analysis

The particles in the confocal z-stacks were located using a 3D extension of a classic particle tracking algorithm [18, 105, 110]. Within a distance $\sigma$ from the border of the volume imaged by the confocal microscope, the particle localization cannot be trusted, due to an incomplete image of the particles. As the volume fraction calculated from particle coordinates obtained by the localization in confocal microscope z-stacks is sensitive to miscounting of the particles [338], the box over which the volume fraction is calculated was made smaller than the imaged volume. We find, as expected, that for smaller z-stacks this has a large influence, while for a z-stack containing >200,000 particles, this influence is small. For the calculation of the Voronoi cells, the Voro++ package in the scientific visualization and analysis software OVITO was used [368–370]. For the local densities calculations using the Voronoi cells, particles closer than one particle diameter to the box edge are left out of the analysis.

#### Radial distribution functions

Radial distribution functions were calculated in the following way from the coordinates of the particles. First, a histogram of the distances between all pairs of $N_{exp}$ particles was calculated. Next, a box, determined by the minimum and maximum values of the coordinates in all three dimensions, was filled with $N_{ig}$ ideal gas particles, of which also a pair distance histogram was calculated. The experimental histogram was divided by the ideal gas histogram, and if $N_{ig} \neq N_{exp}$ the distribution was normalized by a factor of $(\frac{N_{ig}}{N_{exp}})^2$.

#### Bond orientational order parameters

Using the coordinates obtained from the tracking of the particles in the confocal images, a bond orientational order analysis was performed [176, 178, 282]. First, in order to find all

crystalline particles, a set of numbers was calculated for every particle, based on spherical harmonics $Y_{lm}$ [176]:

$$q_{lm}(i) = \frac{1}{n_c(i)} \sum_{j=1}^{n_c(i)} Y_{lm}(\hat{\mathbf{r}}_{ij}), \tag{5.5}$$

where $n_c(i)$ is the number of nearest neighbors of particle $i$, $l$ an integer (in this case 6), $m$ an integer running from $-l$ to $l$ and $\hat{\mathbf{r}}_{ij}$ the unit vector pointing from particle $i$ to particle $j$. The nearest neighbors are defined as the particles within cut-off distance $r_c$ from particle $i$. This cut-off was determined from the first minimum of the radial distribution function $g(r)$, corresponding to $r_c \approx 1.4\sigma$, where $\sigma$ is the particle diameter. Next, the particles are considered crystalline or liquid, according to the combination of criteria as proposed in ref. [177]. The correlation between the $q_{lm}(i)$ of every particle with the $q_{lm}(j)$ values of its neighbors was calculated:

$$c_l(ij) = \frac{\sum_{m=-l}^{l} q_{lm}(i) q^*_{lm}(j)}{\sqrt{\sum_{m=-l}^{l} |q_{lm}(i)|^2} \sqrt{\sum_{m=-l}^{l} |q_{lm}(j)|^2}},$$

where $q^*_{lm}(j)$ is the complex conjugate of $q_{lm}(j)$. The neighbors $j$ of each particle $i$ were considered connected when $c_l(ij) > 0.5$ and the particle $i$ was considered crystalline when the amount of connected neighbors exceeded 7. Since hexagonal order was expected, we chose $l = 6$ to distinguish crystalline and liquid particles. The parameters are identical to the values used by Gasser *et al.* in a previous study of colloidal crystallization using confocal microscopy [15].

Finally, in order to classify the local symmetry of the crystalline particles as either face-centered cubic (FCC) or hexagonally close-packed (HCP), the $\bar{w}_4$ order parameter was used [178]. First, using Equation 5.5 the set of numbers $q_{lm}(i)$ was calculated for all particles, with $l = 4$. Next, the set of $q_{lm}(i)$ numbers was averaged with the values of the neighbors of particle $i$:

$$\bar{q}_{lm}(i) = \frac{1}{N_c(i)} \sum_{k=0}^{N_c(i)} q_{lm}(k),$$

where $N_c(i)$ is the number of neighbors $n_c(i)$ of particle $i$ plus itself. This set of numbers then yields the rotationally invariant averaged local bond orientational order parameter:

$$\bar{w}_l(i) = \frac{\sum_{m_1+m_2+m_3=0} \begin{pmatrix} l & l & l \\ m_1 & m_2 & m_3 \end{pmatrix} \bar{q}_{lm_1}(i) \bar{q}_{lm_2}(i) \bar{q}_{lm_3}(i)}{\left( \sum_{m=-l}^{l} |\bar{q}_{lm}(i)|^2 \right)^{3/2}},$$

where $\begin{pmatrix} l & l & l \\ m_1 & m_2 & m_3 \end{pmatrix}$ is the Wigner 3-$j$ symbol [179] and the integers $m_1$, $m_2$ and $m_3$ run from $-l$ to $+l$, but are limited to the case where $m_1 + m_2 + m_3 = 0$. The particles were considered FCC-like when $\bar{w}_4 < 0$ and HCP-like when $\bar{w}_4 > 0$.

## 5.3 Results

### 5.3.1 Estimation of the effective hard sphere diameter $\sigma_{eff}$

Although PMMA spheres in low polar solvents are regarded as a close-to-hard-sphere system, their intrinsic softness, due to charges and the steric stabilizer on the particles, can influence the phase behaviour [29]. In order to still use them for comparison with hard sphere systems, the particles need to be mapped to an effective hard sphere by determining the effective hard sphere diameter $\sigma_{eff}$. Here we compare three methods: determining the Barker-Henderson effective hard sphere diameter $\sigma_{eff}^{BH\ exp.}$ [29, 371], estimating the Barker-Henderson effective hard sphere diameter $\sigma_{eff}^{BH\ est.}$ from an estimate of the particle interactions and fitting measured radial distribution functions using Percus-Yevick liquid state theory [372, 373].

The effective diameter of the particles can be determined through the measurement of the interaction potential [29]. The interaction potential $u(r)$ can be measured from the radial distribution function $g(r)$ in the limit where the volume fraction $\phi$ goes to zero and at most pairs of particles interact:

$$\lim_{\phi \to 0} g(r) = e^{-\beta u(r)}. \tag{5.6}$$

Still, for moderate densities ($\phi = 0.25$) a good agreement has been reported in hard sphere simulations [374]. When knowing the interaction potential, the effective hard sphere diameter $\sigma_{eff}^{BH}$ can be calculated using the method described by Barker and Henderson [371]:

$$\sigma_{eff}^{BH} = \int_0^\infty (1 - e^{-\beta u(r)}) dr. \tag{5.7}$$

For a determination of the Barker-Henderson effective hard sphere diameter $\sigma_{eff}^{BH\ exp.}$ confocal z-stacks were recorded of particle dispersions in a range from approximately the freezing density towards zero (see Figure 5.1). The particle dispersions were arrested prior to imaging, allowing the acquisition of large volumes with high signal-to-noise ratios. The radial distribution functions $g(r)$ calculated from the particles coordinates obtained by particles fitting algorithms are plotted in Figure 5.1. As for Equation 5.6 a volume fraction close to zero is assumed, the three dispersions with $\phi < 0.02$ were used for the measurement of $\sigma_{eff}^{BH\ exp.}$. To do so, the radial distribution functions up to $\phi = 0.017$ were integrated using Equation 5.7, as listed in Table 5.1. Averaging the three values, results in an effective diameter $\sigma_{eff}^{BH\ exp.} = 2.17 \pm 0.12\ \mu$m.

The Barker-Henderson effective hard sphere diameter can also be determined from an estimate of the particle interactions. PMMA spheres in halogenated hydrocarbons are very well described by the hard-core screened Coulomb or Yukawa potential [31]:

$$\begin{aligned} \beta U(r) &= \infty && (r < \sigma_{hc}) \\ \beta U(r) &= \beta \epsilon_{r=\sigma_{hc}} \frac{exp(-\kappa(r-\sigma))}{r/\sigma_{hc}} && (r \geq \sigma_{hc}), \end{aligned}$$

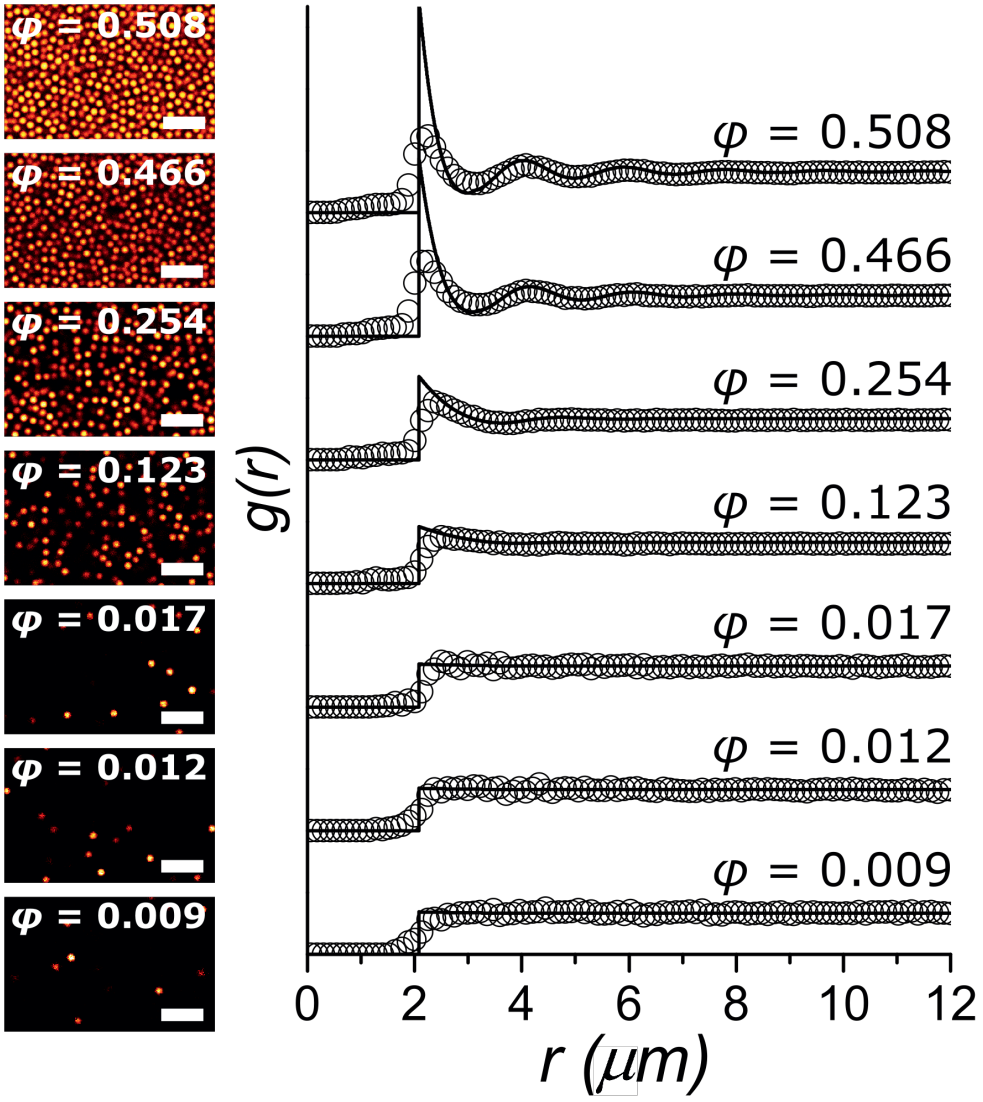


**Figure 5.1: Radial distribution functions of nearly hard sphere PMMA dispersions up to the freezing density.** Snapshots from confocal z-stacks of arrested dispersions of nearly hard sphere PMMA particles ($\sigma_{SLS} = 1.88$ $\mu$m) with different volume fractions $\phi$ (based on $\sigma_{eff}^{PY} = 2.08$ $\mu$m) and their corresponding radial distribution functions (open circles). The solid lines denote the Percus-Yevick curves for the corresponding densities with $\sigma_{eff}^{PY} = 2.08$ $\mu$m. Scale bars are 10 $\mu$m.

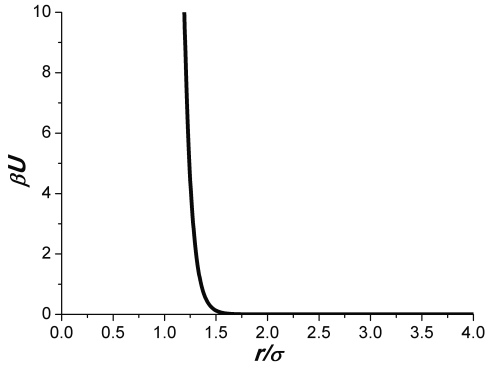


**Figure 5.2: Hard-core screened Coulomb or Yukawa potential.** Potential of PMMA particles in the ETPTA/CHB/cis-decalin mixture as estimated from the hard-core particle diameter $\sigma_{hc} = 1.88$ $\mu$m, the surface potential (-50 mV) and the Debye length (140 nm).

where $\beta$ is the inverse of $kT$, $\kappa$ the inverse Debye length and $\beta\epsilon_{r=\sigma_{hc}}$ the potential at contact, given by:

$$\beta\epsilon_{r=\sigma_{hc}} = \frac{(\beta e\psi_0)^2}{4}\frac{\sigma_{hc}}{\lambda_B}$$

where $\beta e\psi_0$ is the dimensionless surface potential and $\lambda_B$ the Bjerrum length [375]:

$$\lambda_B = \frac{\beta e^2}{4\pi\epsilon_0\epsilon_r},$$

where $e$ is the electron charge, $\epsilon_0$ the permittivity of free space and $\epsilon_r$ the dielectric constant of the continuous phase. The Debye length $\kappa^{-1}$ is a measure for the length scale over which the repulsion, due to the charge on the particles, is felt by other particles. This length scale is dependent on the concentration of ions, which screens the charges on the colloids, and is expressed by:

$$\kappa = \sqrt{4\pi\lambda_B\rho_i},$$

where $\rho_i$ is the number density of monovalent ions. The Debye length can be determined by measuring the conductivity of the solvent mixture [45, 356], in this case $\kappa^{-1} \approx$ 140 nm. In the case of the PHSA stabilized PMMA particles, the surface potential is similar to the zeta potential of the particles [45, 376] and can therefore be measured by electrophoresis [356, 363, 377]. Here, we estimated it to be -50 mV. Finally, the hard core diameter $\sigma_{hc}$ can be estimated from the diameter as measured by SLS: $\sigma_{hc} = 1.88$ $\mu$m. The resulting hard core Yukawa potential is shown in Figure 5.2. From this potential, using Equation 5.7, an effective hard sphere diameter $\sigma_{eff}^{BH\ est.} \approx 2.6$ $\mu$m is found.

Another way of estimating the effective diameter is by fitting measured radial distribution functions with Percus-Yevick theory [372]. Here, we used the analytical equation

as presented by Trokhymchuk *et al.* [373]. The 3D imaging of the particles dispersions with confocal microscopy in combination with the particle localization, allows for the measurement of the number density $\eta$. The radial distribution functions of these dispersions can then be fitted with Pervus-Yevick theory by a single fitting parameter: $\sigma_{eff}$. We fitted the equation to the $g(r)$ of $\phi = 0.254$ (Figure 5.1), where the equation is fitted using a nonlinear least-squares solver starting from $r = 2.5$ $\mu$m, to obtain the best results. This resulted in an effective diameter $\sigma_{eff}^{PY} = 2.08$ $\mu$m, where a small change in the lower $r$ value of the fitting range, resulted in a change of $\sim$0.02 $\mu$m. Using $\sigma_{eff}^{PY}$, the Percus-Yevick curves for the other densities are plotted along with the experimental $g(r)$ in Figure 5.1.

The found value of $\sigma_{eff}^{PY}$ falls within the range of the error in the value of $\sigma_{eff}^{BH\ exp.}$. The $\sigma_{eff}^{BH\ est.}$, however, is somewhat larger, but as it depends on an estimated surface potential, it is the least reliable of the three obtained values. Therefore, we have used the value of $\sigma_{eff}^{PY}$ for the calculation of $\phi$ in this chapter ($\sigma_{eff} = \sigma_{eff}^{PY} = 2.08$ $\mu$m).

### 5.3.2 Crystallization of nearly hard sphere dispersions

For the structural characterization of nuclei formed during homogeneous nucleation of the PMMA dispersion, an electric bottle cell was loaded with the dispersion. Before an electric field was applied, a confocal z-stack was recorded in the electrode-free slit to determine the initial volume fraction ($\phi = 0.529$). Next, a 1 MHz AC field of 0.17 $V_{pp}/\mu$m was applied. After nuclei started to form ($\sim$110 minutes), the dispersion was locally arrested by UV exposure in the center of the capillary. After an additional 40 minutes, a spot closer to the side of the capillary was arrested. Large confocal z-stacks were recorded of the areas with nuclei, which were characterized using bond order analysis and local density calculations. To ensure the absence of wall effects, particles within $\sim$30 $\mu$m from the upper or lower wall were left out in the analysis. Although the particles were density matched with the solvent mixture, sedimentation of the particles was visible from the distribution of the $Z$ coordinates of the particles (not shown here).

Figure 5.3 shows the computer rendering of the particles in a z-stack, where the light blue particles are identified as crystalline and the pink ones as fluid, where the particles were considered crystalline if for at least 8 nearest neighbors $c_l(ij) > 0.5$ [15, 177]. For improvement of the visibility, the fluid particles are shown ten times smaller. The volume fraction $\phi$ of the dispersion was 0.542, which corresponds to a compression rate $\frac{\Delta\phi}{t}$ of 0.0015 per hour, assuming a linear compression. The analyzed volume contained a total of $\sim$250,000 particles, of which $\sim$33,000 were found to be crystalline. In the fluid, single crystalline particles are present, next to $\sim$8 larger nuclei with sizes ranging from $\sim$1000 to

| $\phi$ | $\sigma_{eff}^{BH\ exp.}$ ($\mu$m) |
|---|---|
| 0.009 | 2.03 |
| 0.012 | 2.27 |
| 0.017 | 2.21 |

**Table 5.1:** The experimental Barker-Henderson effective diameter $\sigma_{eff}^{BH\ exp.}$ derived from the $g(r)$ at different volume fractions $\phi$ (based on $\sigma_{eff}^{PY} = 2.08$ $\mu$m).

∼3000 particles. The random orientation of the hexagonal planes of the crystallites with respect to the wall (or the $XY$ plane) confirms the crystallization was indeed homogeneous.

Figure 5.4 shows the computer reconstruction of a second confocal z-stack. The volume fraction $\phi$ of this dispersion was 0.531, corresponding to a compression rate $\frac{\Delta\phi}{t}$ of 0.0011 per hour. The analyzed volume contained a total of ∼450,000 particles of which, using bond order parameters, ∼57,000 particles were considered crystalline, which mainly reside in two large, ∼25,000 particle sized crystallites. Again, the hexagonal planes of the crystallites are misaligned with respect to the glass wall, indicating homogeneous crystallization. In comparison to the data set at $\phi = 0.542$, the number of crystallites was much lower, while crystallites were composed of ∼10 times more particles.

Surprisingly the volume fraction of the second z-stack was lower than the volume fraction of the first z-stack, despite a longer compression time, resulting in two different compression rates. We hypothesize this is due to the position of the z-stacks in the cell. The cell is composed of a rectangular capillary, which is known to be rounded towards the capillary edges [274]. This results in a shorter distance between the electrodes towards the capillary edge, causing an in-homogeneous electric field in the direction perpendicular to the long axis of the capillary. This in-homogeneous field leads to density differences inside the electrode-free slit. The measured lower volume fraction agreed with the amount of nuclei found: while at higher volume fraction or super-saturation ∼8 nuclei were found, in the lower volume fraction or super-saturation case only 3 nuclei were observed, in an even larger volume.

In addition, the local volume fractions in the two data sets were calculated. To do this, of each particle their Voronoi cell was calculated and averaged over the Voronoi volumes of its neighbors. The distribution of these local densities of the crystalline and liquid particles in the two data sets (Figure 5.3 and 5.4) are shown in Figure 5.5. For the first data set ($\phi = 0.542$) with on average smaller nuclei, the local density of the crystalline particles was 0.562, while the crystalline particles in the second data set ($\phi = 0.531$) with larger nuclei had a slightly higher local density of 0.565. Consequently, the density difference between the crystalline and liquid particles is larger in the data set with the lower supersaturation ($\phi = 0.531$).

Despite the compression of the colloidal dispersions by the electric bottle and therefore a non-constant volume fraction $\phi$ during the nucleation, an estimate of the nucleation rate $J$ can be made. Here we estimate the nucleation rate as the number of nuclei in the final data set, per total volume of the data set and per unit time. The unit time is defined as the time between the start of the compression and the arrest. For the data set with $\phi = 0.542$, this results in $J = 5.6 \times 10^{-10}$ $\mu$m$^{-3}$ s$^{-1}$. For the other data set with $\phi = 0.531$, a nucleation rate $J = 8.4 \times 10^{-11}$ $\mu$m$^{-3}$ s$^{-1}$ can be estimated. For comparison to literature values, the nucleation rates $J$ are made dimensionless by the (free) diffusion constant $D_0$ and effective diameter $\sigma_{eff}$ of the particles: $J\sigma_{eff}^5/D_0 = 2.5 \times 10^{-7}$ ($\phi = 0.542$) and $J\sigma_{eff}^5/D_0 = 3.8 \times 10^{-8}$ ($\phi = 0.531$). These values collapse on the trend of nucleation rates for hard sphere crystallization as a function of volume fraction for weak sedimenting experimental systems as given recently by Wood *et al.* [319].

To get insight in the local crystal symmetry of the crystalline particles, the local bond order parameter $\bar{w}_4$ of the crystalline particles in both data sets was calculated [178]. The parameter $\bar{w}_4$ can be used to distinguish FCC symmetry from HCP symmetry, where for

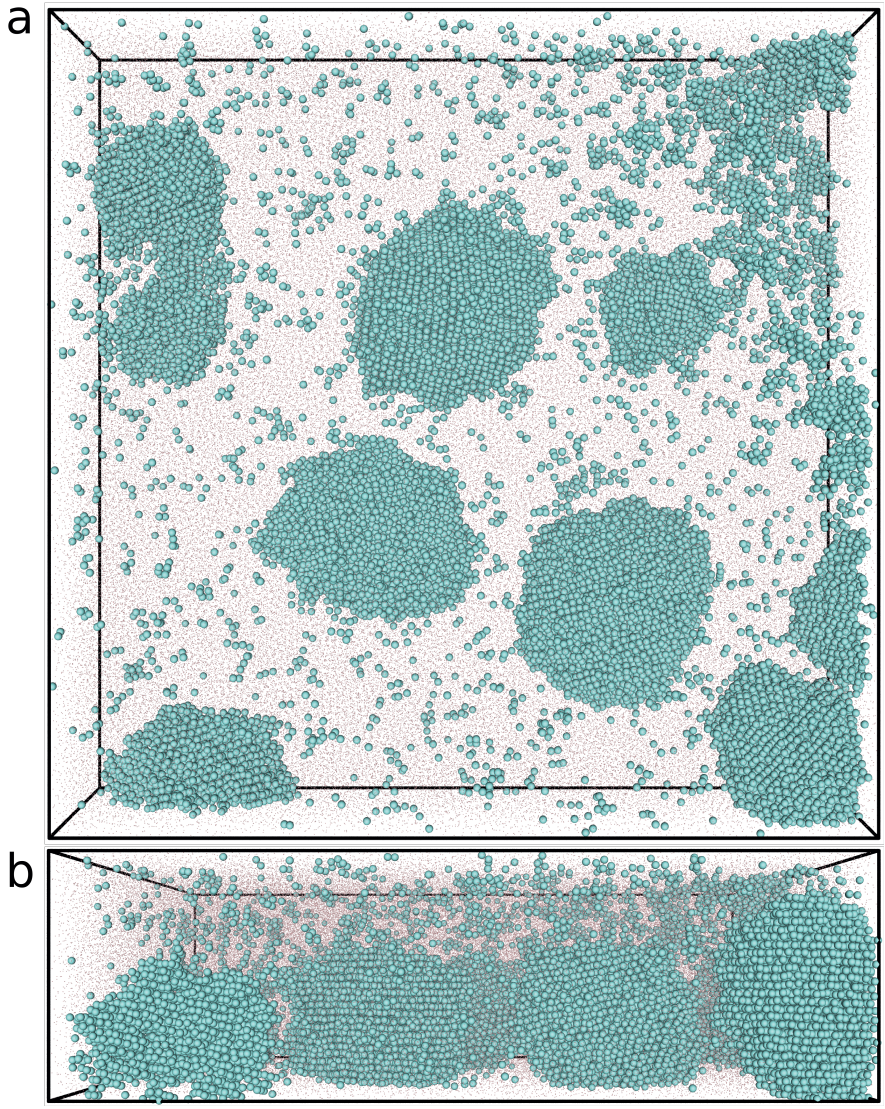


**Figure 5.3: Computer reconstruction of the nuclei formed in hard sphere-like nucleation at $\phi = 0.542$.** Computer rendering of the coordinates obtained from a confocal z-stack of a crystallizing PMMA dispersion after arrest, from the top (a) and side (b). Using bond order parameters the particles were considered crystalline (light blue) or fluid (pink). The size of the fluid particles are reduced to 1/10th of the original size, to increase the visibility of the structure.

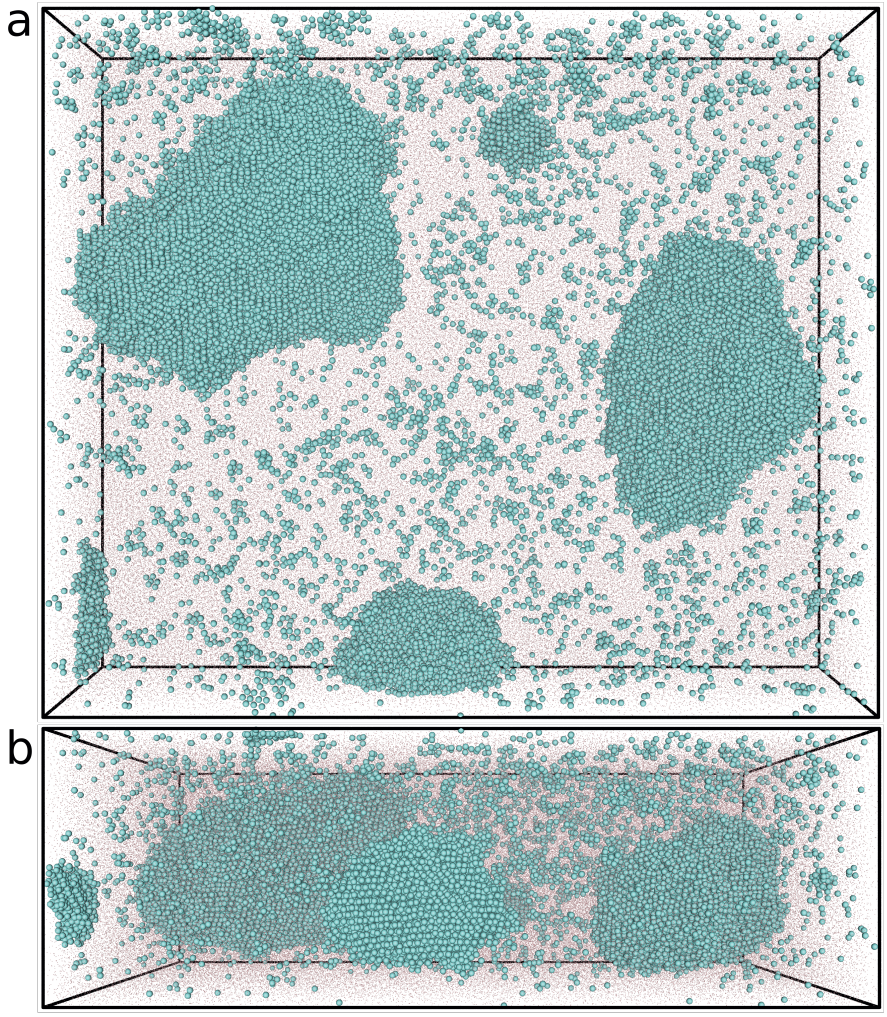


**Figure 5.4: Computer reconstruction of the nuclei formed in hard sphere-like nucleation at $\phi = 0.531$.** Computer rendering of the coordinates obtained from a confocal z-stack of a crystallizing PMMA dispersion after arrest, from the top (a) and side (b). Using bond order parameters the particles were considered crystalline (light blue) or fluid (pink). The size of the fluid particles are reduced to 1/10th of the original size, to increase the visibility of the structure.

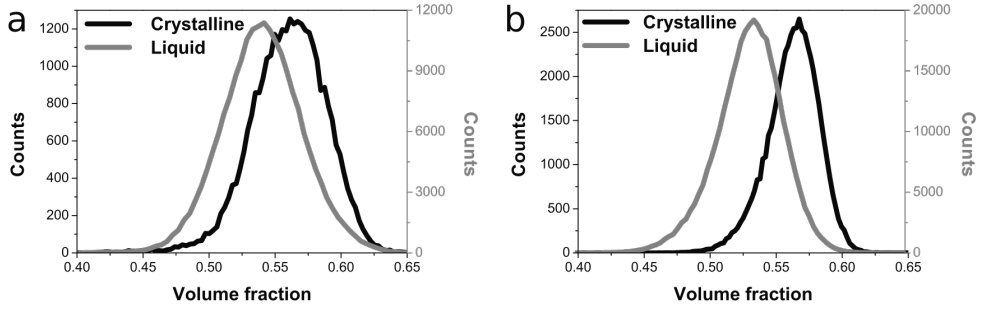


**Figure 5.5: Local density distributions of crystalline and liquid particles in the two data sets in Figure 5.3 and 5.4.** Distributions of the local volume fractions of the crystalline and liquid particles in the data sets with total volume fractions $\phi = 0.542$ (a) and $\phi = 0.531$ (b), calculated from the Voronoi volumes of the particles averaged over the local volume of their nearest neighbors. The fitted averaged densities of the crystalline and liquid particles from the density distributions are, respectively, 0.562 and 0.540 for (a) and 0.565 and 0.534 for (b).

FCC $\bar{w}_4 < 0$ and for HCP $\bar{w}_4 > 0$ [178]. Figures 5.6a and b show the $\bar{w}_4$ distribution of the crystalline particles in the data sets shown in Figures 5.3 and 5.4, respectively. The distribution of $\bar{w}_4$ values shows a very slight preference for values above zero, equivalent to a local HCP symmetry. It is worth noting that the $\bar{w}_4$ parameter averages over the nearest neighbors of the particle of interest. In addition this averaging means that for particles close to the nuclei edge, the $\bar{w}_4$ was averaged with the liquid particles close to the nuclei. Still, when the particles are colored to their $\bar{w}_4$ value, layers which are locally part of either an HCP (red) or FCC (blue) stacking sequence can be identified (see Figure 5.6c,d).

## 5.4 Discussion

### 5.4.1 Estimation of the effective hard sphere diameter $\sigma_{eff}$

We have compared three different methods for the estimation of the effective hard sphere diameter $\sigma_{eff}$. The outcome of the experimental measurement of the Barker-Henderson effective diameter and the fitting of the experimental radial distribution functions with Percus-Yevick theory resulted in similar outcomes. The calculation of the Barker-Henderson effective diameter from the estimated inter-particle potential resulted in a larger value for the effective diameter. For the latter, three input parameters were used with their own weaknesses. The surface potential was estimated to be -50 mV, but should be measured by electrophoresis in future work [363, 377]. The particle hard-core diameter was determined by SLS, while the particles were suspended in hexane. It is known that halogenated solvents swell PMMA particles, which would result in an even higher diameter [29]. In addition, the effect of the monomer ETPTA on the swelling of PMMA particles has not been studied. Finally, the estimate of the Debye length, by measurement of the conductivity of the solvent mixture, assumes that no ions are introduced by the particles after dispersing.

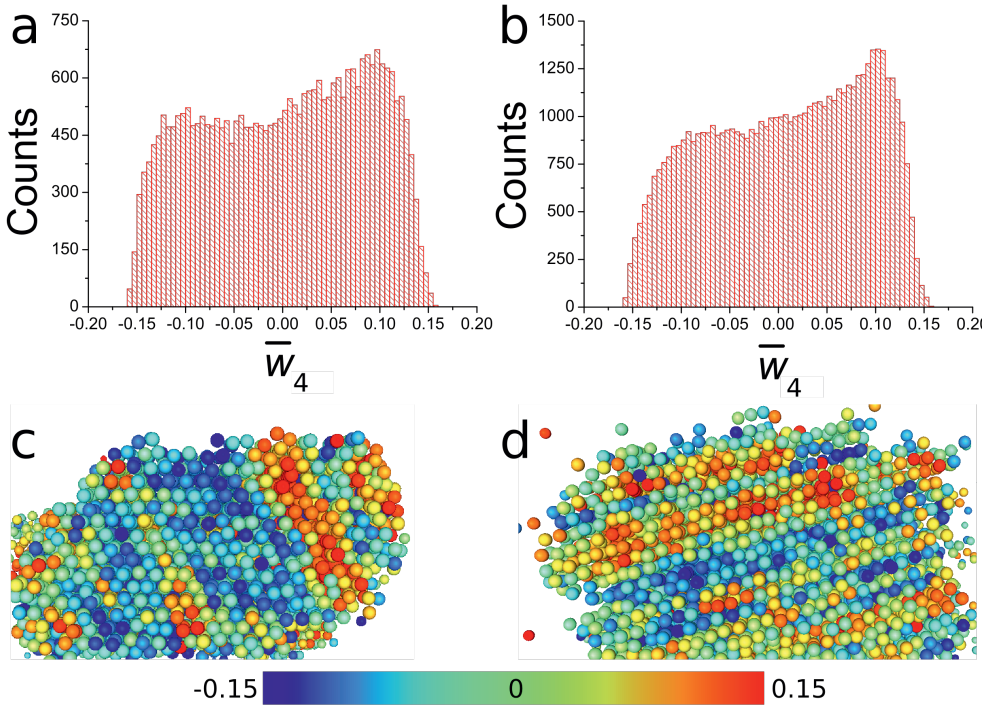


**Figure 5.6: Bond order analysis of the crystalline particles in the two data sets in Figure 5.3 and 5.4.** The distribution of bond order parameter $\bar{w}_4$ of the crystalline particles in the data sets in Figure 5.3 ($\phi = 0.542$) (a) and Figure 5.4 ($\phi = 0.531$) (b). Both distributions show a very slight preference to higher $\bar{w}_4$ values, corresponding to the HCP stacking sequence, as opposed to the FCC stacking sequence. Computer renderings of fragments of nuclei present in the data sets in Figure 5.3 (c) and 5.4 (d), where the particle colors correspond to the $\bar{w}_4$ values of the particles. Local HCP structure corresponds to $\bar{w}_4$ values above zero (red) and local FCC structure corresponds to $\bar{w}_4$ values below zero (blue).

Moreover, the conductivities measured were in the low range of the conductivity meter, likely to result in a relatively large error in the measured value.

For the experimental Barker-Henderson and Percus-Yevick methods the estimate depends highly on the measured $g(r)$, which is sensitive to particle miscounting [338]. In our case two deviations in the $g(r)$ were visible in comparison to those of hard spheres (or Percus-Yevick theory). The first is the absence of a sudden jump at $r/\sigma = 1$, which is caused by the softness of the particle interactions, as expected for nearly hard spheres [29]. Second, at $r < r_{firstpeak}$ a small non-zero bump is visible, most likely due to incorrect particle tracking when particles are close to each other in the axial direction. This bump increases with higher densities, where the probability of finding particles in proximity to each other increases.

The experimental Barker-Henderson estimation is insensitive to the intrinsic softness of the particles, as no prior assumptions to the potential are made. Still, miscounting of particles in the $g(r)$ will lead to a deviation in the estimate. The two deviations of the $g(r)$ (caused by softness and particle mistracking) made it harder to fit the Percus-Yevick equation to the experimental sets. By choosing the range for the fit starting just after the first peak, the effects of the two deviations were minimized and an acceptable fit in that range was found, of which the fit value corresponds to literature values.

### 5.4.2 Crystallization of nearly hard sphere dispersions

We have studied the homogeneous crystallization of nearly hard spheres over a volume containing up to 500,000 particles. In correspondence to earlier simulations and experiments we find no preference for the FCC structure in respect to the HCP structure in the nuclei [15, 328, 361, 362]. The amount of particles that can be studied using this method can be even higher when the full working distance of the objective (300 $\mu$m for the used glycerol objective) is used. In addition, as the particles are arrested, the stitching of confocal images can be employed to images areas larger than the lateral field of view of the objective. This enables the study of nucleation at low supersaturation where the nucleation rates are even lower, as well as the gathering of structural data of nuclei with high statistics.

While we studied the nucleation of a nearly hard sphere system, the method can also be applied to colloidal system with different interparticle potentials. For instance soft spheres, where intermediate structures during crystallization have been reported [136, 341]. The use of a electric bottle to tune the density of the particles, allows the study of different supersaturations from a single starting particle dispersion. This is for instance beneficial for the study of long range repulsive systems of PMMA particles in deionized CHB/cis-decalin, where the particle interaction is density dependent [378].

## 5.5 Conclusions and Outlook

In this chapter, we characterized nuclei formed during homogeneous crystallization of a nearly hard sphere colloidal dispersion. The nucleation was induced by dielectrophoretic compression using an electric bottle cell, after which the dispersion was arrested by poly-

merization of a part of the continuous phase. The arrest allowed for the real-space imaging of volumes containing up to ∼500,000 particles using confocal microscopy. The large volumes resulted in the characterization of crystallites formed at small supersaturation, with sizes up to ∼25,000 particles. Using Voronoi cell calculations, the local densities of the liquid and crystalline particles in the crystallizing dispersion were determined. In addition, we estimated the nucleation rates of two data sets with different degrees of supersaturation, which both agreed to literature values.

We found that crystalline particles were stacked in a random hexagonal close packed (RHCP) stacking, with a very slight preference for the hexagonally close-packed (HCP) stacking, in contrast to simulation studies, where a preference for face-centered cubic (FCC) stacking was reported for the critical nucleus. In addition, we compared three methods for the estimation of the effective hard sphere diameter: by calculating the Barker-Henderson effective diameter from measured radial distribution functions $g(r)$ in the limit of low densities, by the calculation of the Barker-Henderson effective diameter from the estimated hard-core Yukawa inter-particle potential and the fitting of the measured $g(r)$ with Percus-Yevick theory. The latter resulted in a value comparable to values for similar systems in literature, within the error of the measurement of the Barker-Henderson diameter. Currently, work is in progress to compare the found values to the measurement of the effective diameter by compression of the (almost) density matched particles by hard centrifugation and measurement of the interparticle distance of the resulting colloidal crystal. In addition, we are investigating the local five-fold symmetry of the liquid particles in our data sets and comparing them to simulations, using the topological cluster classification [319, 379].

The use of an electric bottle to study homogeneous nucleation allows for the tuning of the degree of supersaturation of a single dispersion. While here the highest supersaturation studied was at $\phi = 0.542$, higher densities can be reached by faster compression. This can be achieved by either higher electric fields or a smaller distance between the electrodes, for instance by placing the electrode on the inside of the dispersion container. Lower supersaturations can also be studied, but require larger data sets, as the likelihood of a nucleation event decreases. With the arrest of the particles, multiple z-stacks can be recorded and combined in the analysis. The methods used here can be used for the study of the crystallization of colloidal dispersions with other potentials as well. Finally, the arrest allows for the imaging of the particles with super-resolution techniques such as stimulated emission depletion (STED). This would enable the study of the nucleation of the closest to ideal hard spheres in real-space: $\leq 200$ nm sterically stabilized PMMA particles in index matched hydrocarbons [29].

## 5.6 Acknowledgements

This work was done in collaboration with Anna Nikolaenkova. Johan Stiefelhagen performed particle synthesis and SLS measurement. Peter Helfferich is thanked for technical assistance.

# 6

# Real-space analysis of Laves phase supraparticles

Colloidal crystals made from two different particles, binary crystals, offer a far greater range to tune materials properties than those composed of single components, enabling for instance synergy between combinations of magnetic, plasmonic or (di)electric effects on the collective properties of (luminescent) semiconductor particles. By performing a crystallization self-assembly step inside a slowly drying droplet, the SA can be arrested naturally at a length scale defined by the dispersion droplet allowing for the creation of 'supraparticles'. In this chapter, we show the significantly increased possibilities to analyze binary crystal structures composed of nanocrystals in real-space with electron microscopy tomography, which allows for an analysis of the local symmetry of neighboring particles and thus crystal defects using bond orientational order by the SP geometry. We show that, surprisingly, a binary $MgZn_2$-Laves crystal structure is hardly influenced by spherical confinement when the experimental binary species have a slight off-stoichiometry and contains the expected stacking faults for a bulk crystal. Moreover, there are no significant numbers of particles missing in the experimental crystals, in contrast to earlier work on binary NaCl crystals composed of micron-sized particles. Upon tuning the stoichiometry to closely match that of a perfect Laves crystal, five-fold symmetry as observed in single component supraparticles is recovered in the self-assembled binary supraparticles. In addition, a significant fraction of the structure is turned into that of the $MgCu_2$ structure which is strongly interesting for photonic applications. Full analysis of the complicated 3D structure is currently under way, possibly linking the structures formed by the spherical confinement to a 3D quasicrystal.

## 6.1 Introduction

Structuring matter by self-assembly (SA) with either nanoparticles (NPs) or micron-sized colloids has progressed significantly over the last decades [55, 57, 62, 380–383]. Compared to single component assemblies, the fundamental advantage of assembling binary components into a complexer structure is the possibility of creating materials with novel enhanced collective properties that are distinct from the sum of the two components. The properties can be modulated through not only the size- and shape-dependent nature of the individual building block, but also through the interactions between the binary components and the binary configurations and symmetries [62, 384, 385]. Laves phases, crystal structures with a $LS_2$ stoichiometry where the small ($S$) species and the large ($L$) species have a size ratio $\gamma$ around 0.82, were first found in intermetallic compounds: $MgZn_2$, $MgCu_2$ and $MgNi_2$ [386]. The $MgZn_2$ Laves crystal structure was found in binary colloidal crystals [382, 387–394], single component superlattices [395, 396], as well as in polydisperse single component silica dispersions [355], either with hard sphere-like (HS) [382, 388–393, 393] or soft potentials [355, 387, 394–396, 396]. For binary HSs at size ratios in the $0.76 \leq \gamma \leq 0.84$ range, the $MgZn_2$ structure is the thermodynamically stable structure, although the free energy difference between the three Laves structures is small ($\approx 10^{-3}$ kT per particle) [70]. One therefore expects to find stacking faults in bulk experimental crystals, similarly as are found for a face-centered cubic (FCC) crystal of particles with a HS-like potential [360]. The Laves phases are appealing from a photonic materials science perspective because the $MgCu_2$ structure consists of a diamond crystal of $L$ spheres and a pyrochlore lattice of $S$ spheres, which both display a photonic band gap [70]. Recently, the $MgCu_2$ Laves phase was predicted as the thermodynamically stable phase for a system composed of HSs and hard tetramers [74]. Similar building blocks, pre-assembled (and overlapping) tetrahedral clusters and colloidal spheres, were used in a SA study to form $MgCu_2$ crystals, with a typical grain size of ten lattice spacings, through attractions induced by DNA coatings [73].

It is well known that the material properties of crystals strongly depend on the presence of defects [140] that, at finite temperatures, are always present. Depending on the growth conditions and interactions, defects are found at vastly different concentrations and kinds [397, 398]. Analyzing the local structure at for instance grain boundaries and defects in crystals is, unfortunately, hard to do with techniques such as (small-angle) X-ray diffraction and electron crystallography, as these strongly bias for regularity in the structure [101, 103]. Recently, 2D electron micrscopy (EM) imaging using projections has been applied to analyze defects in binary nanocrystal superlattices (BNSLs), however the thickness was limited to 3-5 unit cells [391]. Only within the last decade has it become possible to study quantitatively in 3D the real-space structure of colloidal crystals of NPs [101, 399, 400] and more recently, also the real-space atomic structure within a single NC using EM tomography allowing 3D defect analysis on the atomic scale [397, 398]. A quantitative 3D real-space analysis is not only instrumental to analyze defects, sometimes it is even essential to identify the correct crystal structure [101]. With respect to the result presented in this chapter, it is important to remark that EM tomography studies were mostly carried out on planar self-assembled binary component superstructures of limited sample thickness (<6 layers) [101, 383, 401], making the effects of the boundaries

possibly quite important, but also making it impossible to investigate stacking order in these crystals, for which one requires more layers. When investigating planar assemblies with EM tomography, tilting the sample to high angles will result in too long path lengths for the electron beam to pass through the crystals, making the reconstruction of the tomogram impossible. This can be overcome by imaging a structure with a spherical geometry, where the path length is independent of the tilt angle.

One promising route to assemble colloidal particles into spherical configuration is by drying emulsions droplets containing colloidal particles to form so-called supraparticles (SPs) [62, 102, 402, 403]: particles made from particles. This new length scale allows *e.g.* Mie resonances to influence the material properties [404], but also allows for further SA of hierarchical superstructures. The advantage of a concentration increase induced by a drying droplet instead of methods based on the introduction of attractions through *e.g.* solvophobic effects [220], is that it does not depend on the detailed surface chemistry of the particles and can thus be applied to a wider range of systems and particles with more complex shapes [405]. It has been discovered by our group that when less than about 100,000 spherical particles with a HS potential are confined in a drying emulsion droplet, the lowest free energy is achieved by a structure with an icosahedral symmetry if a volume fraction close to 50% is reached [102]. The crystallization of binary colloidal particles is generally harder to achieve than the crystallization of a single component, because the parameter space to achieve the optimum thermodynamic (driving force) and kinetic effects are much larger. In addition to the size and polydispersity there may also be more complex interactions present between the particles, which makes the parameter space significantly more complicated. We speculate that these combined effects are the reasons why there have been only a few reports on SPs in which binary colloidal crystals were successfully demonstrated [406–410]. Additionally, none of these binary SPs were analyzed quantitatively in real space.

In this chapter, we quantitatively analyze binary SPs in real-space through EM tomography which allows us to investigate the local symmetry of neighboring particles using a bond orientational order (BOO) analysis [178]. We first study the bulk phase behaviour of a mixture of small CdSe and large PbSe spherical nanocrystals (NCs) with a size ratio $\gamma \approx 0.76$, where we find they self-assemble into the $MgZn_2$ Laves crystal structure. We demonstrate experimentally that in slowly drying emulsion droplets [102] the CdSe and PbSe NCs can be made to crystallize into binary colloidal crystalline SPs. We show that by only analyzing 2D EM projections of the binary SPs one would conclude to have found a $MgZn_2$ crystal structure similarly as presented in literature [382, 388–390]. However, because we are able to obtain real-space coordinates of both species of our binary SPs using EM tomography and advanced reconstruction techniques [103, 411], we are able to also detect stacking errors. An interesting finding is that if the stoichiometry is not exactly right (in this case 1:2), the spherical confinement hardly influences the crystallization, while if the stoichiometry is right the structure strongly deviates and five-fold symmetry can often be observed from 2D EM projections. We think it is likely that if the stoichiometry is off, the excess species will stay liquid-like until late in the SA, effectively alleviating the stress of the spherical confinement. This conclusion still needs confirmation through computer simulations.

## 6.2 Methods

### 6.2.1 Chemicals

Chemicals used were dextran from Leuconostoc mesenteroides (Sigma Aldrich, mol. wt. 1.500.000-2.800.000), cyclohexane (Sigma Aldrich, ≥99.8%), n-hexane (Sigma Aldrich, ≥99.5%), 1-octadecene (1-ODE, Sigma Aldrich, 90%) Sodium dodecyl sulfate (SDS, Sigma Aldrich, ≥99.0%), oleic acid (OA, Sigma Aldrich, ≥99.0%), isopropanol (Sigma Aldrich, ≥99.5%), diphenylphosphine (Sigma Aldrich, >90%), trioctylphosphine (TOP, Sigma Aldrich, 97%), selenium shot (Se, Alfa Aesar, 99.999%), lead (II) oxide (PbO, Sigma Aldrich, 99.999%), cadmium oxide (CdO, Sigma Aldrich, ≥99.99%), toluene (Sigma Aldrich, anhydrous, 99.8%), diethylene glycol (DEG, Sigma Aldrich, 99%). For de-ionized water (DI $H_2O$) a Millipore Direct-Q UV3 reverse osmosis filter apparatus was used (18 MΩ at 25 °C).

### 6.2.2 Nanocrystal synthesis

All NC syntheses were carried out under nitrogen atmosphere using standard Schlenk line techniques.

5.1 nm CdSe NCs (7.6 nm total diameter due to interdigitating ligands, and a total polydispersity of 2% by counting 130 CdSe NCs) were synthesized by cation exchange from 5.1 nm PbSe template based on reported recipes [412]. 750 mg of CdO, 5.0 mL of OA and 25 mL 1-ODE were mixed and degassed at 105 °C for 30 minutes. Then the mixture was heated to 250 °C in a nitrogen atmosphere to get a clear solution. The solution was kept at 250 °C for 20 minutes, then allowed to cool down to 105 °C. It was degassed again for 1 hour and then heated to 210 °C. 150 mg of PbSe NCs were dispersed to 3.0 mL of toluene and swiftly injected into the reaction flask. The solution turns red in a few seconds, indicating the formation of CdSe NCs. The reaction was kept at 210 °C for 45 minutes and then cooled down to RT. The as-synthesized CdSe NCs were purified with isoproponal three times, dispersed in n-hexane and stored in a glove box.

The 7.6 nm PbSe NCs (9.9 nm total diameter due to interdigitating ligands, and a total polydispersity of 1% by counting 170 PbSe NCs) were synthesized following reported recipes [413]. Specifically, 0.895 g of PbO, 3.0 mL of OA, and 20 mL of 1-ODE were mixed and degassed at 105 °C for 1.5 hours. Then the solution was heated to 105 °C in a nitrogen atmosphere. 71 µL of diphenyl phosphine was mixed with 8.0 mL of TOP-Se solution (1 M). The mixture was swiftly injected into the reaction flask. The NCs were allowed to grow at 105 °C for 10 minutes and then quenched by an ice bath. The as-synthesized PbSe NCs were purified with isoproponal three times, dispersed in n-hexane and stored in a glove box.

### 6.2.3 Self-assembly of binary NCs in bulk

Binary NC superlattices (BNSLs) were formed at the liquid-air interface [414] in a glovebox that maintains oxygen and moisture free conditions. To prepare a typical $MgZn_2$-type BNSL, 5.1 nm CdSe and 7.6 nm PbSe NCs were separately dispersed in n-hexane at a

concentration of 10 mg/mL. The two samples were mixed 1:1 by volume to give the right number ratio of NCs and form a high-quality $MgZn_2$-type BNSL film. Then 10 µL of the mixture was dropcasted onto the surface of DEG in a square Teflon well. A glass slide was placed to cover the well and reduce the evaporation rate of hexane. After 30 minutes, a solid film was obtained on the liquid-air interface.

### 6.2.4 Experimental SA of binary NCs in spherical confinement

For a typical binary NCs SA in spherical confinement experiment, 6.5 mg of PbSe NCs and 6.5 mg of CdSe NCs were dispersed in 1.0 mL of cyclohexane and added to a mixture of 400 mg of dextran and 70 mg of SDS in 10 mL of DI $H_2O$. The resulting emulsion was agitated by shear with a shear rate of $1.56 \times 10^5\ s^{-1}$, using a Couette rotor-stator device (gap spacing 0.100 mm) following the procedure and home-built equipment described by Mason and Bibette [415]. The emulsion droplets were then evaporated at RT while mixing the emulsion with a VWR VV3 vortex mixer for 48 hours. The resulting SPs suspension was purified by centrifugation with a speed of 2,500 rpm for 15 minutes using an Eppendorf 5415C centrifuge, followed by redispersing in DI $H_2O$. The above-mentioned procedure was repeated twice.

### 6.2.5 EM sample preparation and measurements

Conventional transmission electron microscopy (TEM) and 2D High angle annular dark field-scanning transmission electron microscopy (HAADF-STEM) measurements were performed on a FEI Talos F200X transmission electron microscope (TEM), equipped with a high-brightness field emission gun (X-FEG) and operated at 200 kV.

3D HAADF-STEM measurements were performed using a cubed FEI Titan transmission electron microscope, operated at 300 kV. To prepare a sample for EM tomography analysis, 3 µL of the supraparticles (SPs) suspension in DI $H_2O$ were deposited on a Quantifoil (2/2, 200 mesh) copper grid and plunge frozen in liquid ethane, using a Vitrobot Mark2 plunge freezer at temperatures around 90 K. The sample was then freeze-dried over a period of 8 hours under vacuum at 177 K and subsequently allowed to warm to room temperature (RT) prior to electron microscopy analysis. A Fischione model 2020 single tilt holder was used for the acquisition of the tilt series within a tilt range from $-72\,^\circ$ to $+66\,^\circ$ for the 115 nm SP and $-76\,^\circ$ to $+62\,^\circ$ for the 150 nm SP, with an increment of $2\,^\circ$. The tilt series were aligned using cross-correlation routines [416] implemented Matlab, and the reconstruction was performed using the Simultaneous Iterative Reconstruction Technique (SIRT) [411] algorithm from the ASTRA toolbox [417, 418], and the Sparse Sphere Reconstruction (SSR) technique, also implemented in Matlab as described by Zanaga *et al.* [103].

2D energy dispersive X-Ray spectroscopy (EDX) chemical mapping measurements were performed using FEI Talos F200X TEM, equipped with a high-brightness field emission gun (X-FEG) and a Super-X G2 EDX detector operated at 200 kV. Images and elemental EDX maps were acquired using Bruker Esprit analytical and imaging software in scanning transmission mode. Elemental EDX maps of 418×416 pixels, and 408×349 pixels were acquired with a 15 min acquisition time to get a good signal-to-noise ratio.

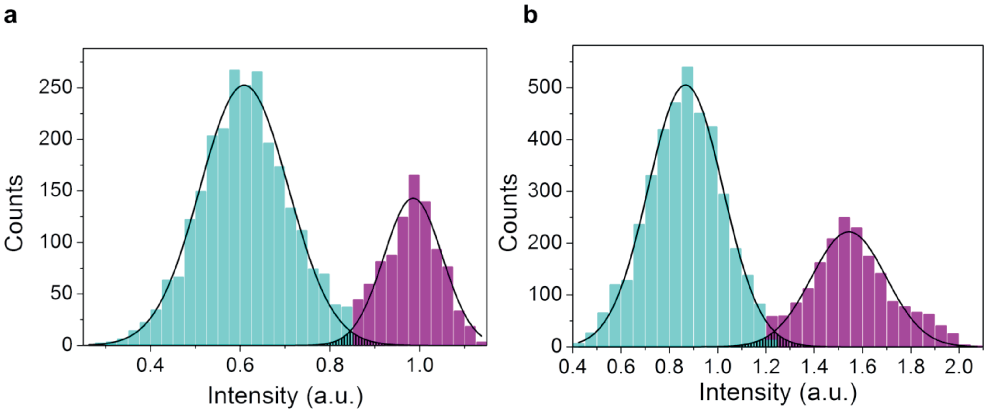


**Figure 6.1: Pixel intensity distributions of reconstructed particles.** Distribution of the summed pixel intensities of the particles in the a) 115 nm and b) 150 nm sized SPs. The black curves are two Gaussian curves fitted to the distributions, from which threshold values were determined to differentiate between the CdSe NCs (cyan) and PbSe NCs (magenta). The overlap between the two Gaussian curves gives an estimate for the percentage of particles that might be misidentified (∼1% for both SPs).

### 6.2.6 EM tomography reconstruction and species determination

In order to get coordinates of the binary species in self-assembled SPs, we applied the SSR algorithm to two tilt series of experimental SPs. The SSR algorithm has been developed for the quantitative reconstruction of assemblies of spherical particles [103]. By using prior knowledge about the size (radius) of the building blocks, the technique yields a tomographic reconstruction including number and coordinates of the particles. The SSR technique [103] was first applied to the tilt series of a 115 nm SP by setting the basis shape radius to a single size, the radius in pixels of the smaller NC species. In this case the tilt series was binned to a size of 228 × 228 pixels, and the two particles radius were estimated to be 9 and 7 pixels, for the PbSe (brighter due to the higher Z number of Pb) and CdSe NCs respectively. Since the two types of NCs only differ for few pixels, in practice for the reconstruction algorithm they are equivalent. First, we got a sparse solution, where the centers of the NCs are blurred due to the experimental limitations and undersampling. In the case of NCs of different size and different contrast, the result is analogous, with slightly more diffused intensity for bigger NCs. Extracting the local maxima positions therefore produces a list of coordinates for both NCs indistinctively.

After the coordinates of all NCs were determined by the SSR technique, the particles were assigned being a $S$ (CdSe NC) or $L$ (PbSe NC) species. For that, the total pixel intensity in a sphere with a radius of 7 pixels (the size of the smallest species) around each coordinate in the SIRT reconstruction [411] was determined. The intensity distributions were fitted with two Gaussian distributions, where the intersection of the two was taken as the threshold value to distinguish the two species. The overlap of the two curves gives an estimate of the percentage of particles that might be misidentified (∼1%, see Figure 6.1a).

The same analysis was performed on a bigger SP with a diameter of approximately 150 nm (see Figure 6.1b).

### 6.2.7 Radial distribution function (RDF)

The RDF $g(r)$ of the NCs in spherical confinement were calculated as follows: first, the distances between all pairs of particles were calculated, next the volume of the droplet was estimated by wrapping the particles with a convex hull. This hull was then randomly filled with $N_{ig}$ ideal gas particles, whose pair distances were used to divide the distribution of distances of the $N_{np}$ NCs. In case $N_{ig} \neq N_{np}$, the distribution was normalized by a factor of $(N_{ig}/N_{np})^2$. For the $g(r)$ of the Laves phases from computer simulations, the ideal gas particles were generated in a box (instead of a convex hull) defined by the minimum and maximum values of the coordinates in the three dimensions of the data sets.

### 6.2.8 Bond orientational order (BOO) analysis

Averaged local BOO parameters $\bar{q}_4$ and $\bar{q}_6$ were used to determine the symmetry of the individual NCs, for the $L$ (PbSe NCs) and $S$ (CdSe NCs) species seperately [178]. First, a set of numbers was calculated for every particle, based on spherical harmonics $Y_{lm}$:

$$q_{lm}(i) = \frac{1}{n_c(i)} \sum_{j=1}^{n_c(i)} Y_{lm}(\hat{\mathbf{r}}_{ij}), \tag{6.1}$$

where $n_c(i)$ is the number of nearest neighbours of particle $i$, $l$ an integer (in our case 4 or 6), $m$ an integer running from $-l$ to $l$ and $\hat{\mathbf{r}}_{ij}$ the unit vector pointing from particle $i$ to particle $j$. The nearest neighbours are defined as the particles within cut-off distance $r_c$ from particle $i$. This cut-off was determined from the first minimum of the radial distribution function $g(r)$, corresponding to $r_c \approx 1.4d$. Next, the $q_{lm}$ set of numbers of particle $i$ is averaged with the values of its neighbours:

$$\bar{q}_{lm}(i) = \frac{1}{N_c(i)} \sum_{k=0}^{N_c(i)} q_{lm}(k), \tag{6.2}$$

where $N_c(i)$ is the number neighbours $n_c(i)$ of particle $i$ plus itself. This set of numbers then yields the averaged local bond orientational order parameter:

$$\bar{q}_l(i) = \sqrt{\frac{4\pi}{2l+1} \sum_{m=-l}^{l} |\bar{q}_{lm}(i)|^2}. \tag{6.3}$$

In the BOO calculations, particles too close to the surface of the SP were excluded from the calculation of $\bar{q}_l$, since their lower amount of nearest neighbours influences the parameter values. In practice, this corresponds to two layers of particles excluded from the surface. In order to identify the crystal structure of the SPs we compared the $\bar{q}_6 - \bar{q}_4$ scatter plot of the simulated Laves phases at coexistence density of both the $L$ *and* $S$ species with the experimental data sets. By coloring the particles in the computer reconstructions according to their position in the $\bar{q}_6 - \bar{q}_4$ scatter plot and therefore their

local symmetry, the local crystal structure could be identified. For the $L$ particles two regions were specified: $0.4 < \bar{q}_6 < 0.6$ & $0.285 < \bar{q}_4 < 0.45$ (red, hexagonal diamond symmetry) and $0.445 < \bar{q}_6 < 0.645$ & $0.45 < \bar{q}_4 < 0.57$ (blue, cubic diamond symmetry). For the $S$ particles three regions were defined: $0.4 < \bar{q}_6 < 0.555$ & $0.165 < \bar{q}_4 < 0.21$ (blue), $0.325 < \bar{q}_6 < 0.525$ & $0.116 < \bar{q}_4 < 0.165$ (magenta) and $0.325 < \bar{q}_6 < 0.465$ & $0.0425 < \bar{q}_4 < 0.116$ (red).

### 6.2.9 Monte Carlo (MC) computer simulations

We performed MC computer simulations in the isothermal-isobaric (NPT) ensembles on the three perfect Laves crystal structures for a binary hard-sphere mixture with size ratio $\gamma = 0.76$. The simulations were performed at a pressure close to the melting pressure, $\beta P \sigma_L^3 = 30.0$, of the Laves phase as read from the phase diagram of binary hard spheres for size ratio $\gamma = 0.76$ [419]. This was done in order to obtain a distribution in the values of the BOO parameters $\bar{q}_4$ and $\bar{q}_6$ which should be broad enough to distinguish the Laves-ordered NCs from a high density disordered fluid as far as possible. The NPT simulations were equilibrated for 50,000 cycles and anisotropic volume change moves were used for the non-cubic Laves crystal structures, *i.e.* the $MgZn_2$ and $MgNi_2$ structures.

## 6.3 Results

### 6.3.1 The structure of the Laves phases

The Laves structures ($LS_2$) are three closely related structures, composed of $S$ and $L$ spheres: the hexagonal C14 structure, the cubic C15 structure and the hexagonal C36 structure, as found for the intermetallic compounds $MgZn_2$, $MgCu_2$ and $MgNi_2$, respectively [420, 421]. For the C14 and C15 structures the packing of the $L$ spheres corresponds to the hexagonal diamond and (cubic) diamond structures, respectively, while for the C36 structure the $L$ spheres occupy the sites of the 4H SiC structure [422, 423]. In the C14 and C15 structures the $S$ spheres pack like tetrahedra around the $L$ spheres. In the C15 structure the tetrahedra are jointed point-to-point throughout the structure (forming a pyrochlore structure [424]), while in the C14 structure they alternate between base-to-base and point-to-point [425]. In the C36 structure the $S$ spheres pack in tetrahedra where some points are shared, resulting in a structure which resembles both C14 and C15 [425]. The three structures can also be identified when viewing along the $[11\bar{2}0]$ or [110] projections of the hexagonal or cubic structures, respectively (Figs. 6.2a-c). In these projections, sets of four lines of particles can be identified, consisting of a single line $s$ of $S$ spheres and a triple-line stack ($t$ or $t$') which contains two lines of $L$ spheres separated by a line of $S$ spheres (*e.g.* Fig. 6.2b). The two forms of the triple-line stacks $t$ and $t$', are mirror reflections in the single line $s$ of $S$ spheres to each other. The C14, C15 and C36 structures differ in the stacking order of the $s$, $t$ and $t$' lines, namely, the C14, C15 and C36 structures exhibit repeated *...s t s t'...*, *...s t...* and *...s t s t s t' s t'...* stacking sequences, respectively (Figs. 6.2a-c) [426]. The three Laves phases can also be identified from the stacking sequence of their $L$ spheres in the projections in Figs. 6.2a-c. Specifically, the stacking of $L$ sphere-pairs in the C14, C15 and C36 structures is *...aabb...*, *...aabbcc...* and

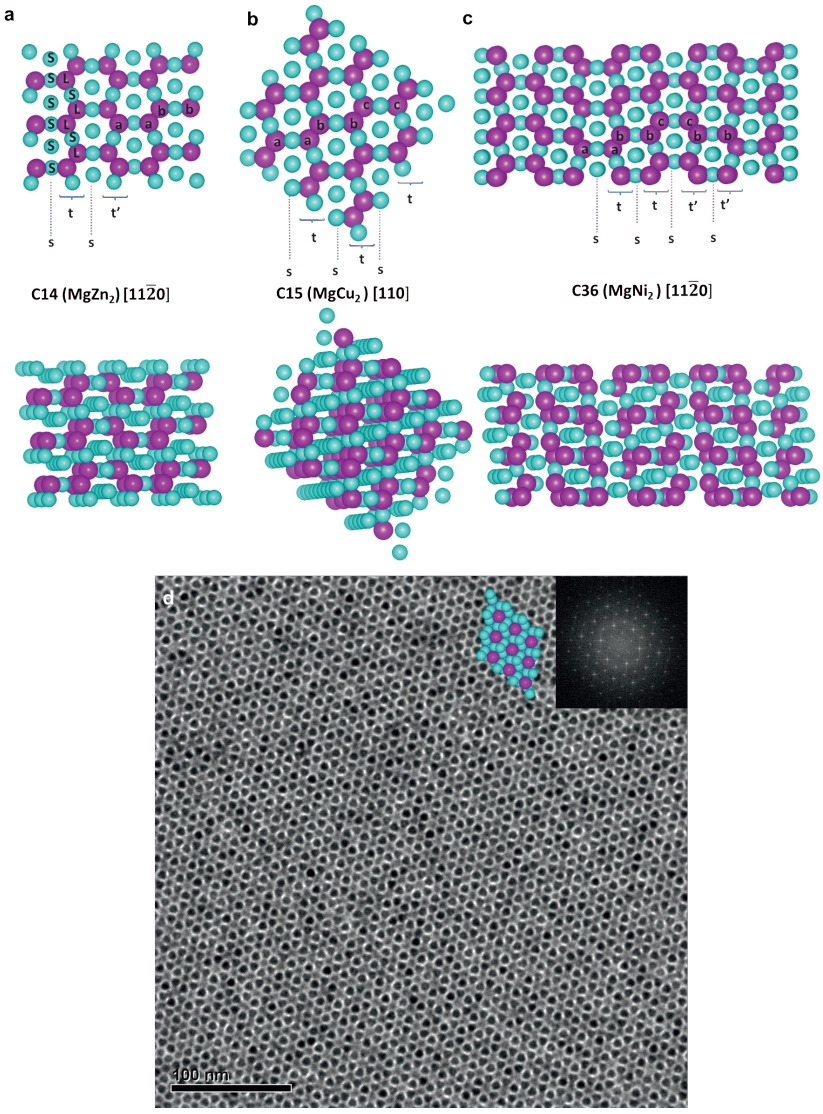


**Figure 6.2: Binary Laves crystal structures.** $L$ spheres are magenta and $S$ spheres are cyan. First row: a) C14 ($MgZn_2$) structure viewed along the [11$\bar{2}$0] projection, b) C15 ($MgCu_2$) structure viewed along the [110] projection, c) C36 ($MgNi_2$) structure viewed along the [11$\bar{2}$0] projection. Second row: 3D views of the C14, C15 and C36 structures. d) TEM image of a self-assembled BNSL showing $MgZn_2$-like structure viewed along the [0001] projection. FFT of the entire image with a structure model viewed along the [0001] projection as insets in top right corner, showing a hexagonal symmetry.

*...aabbccbb...* (or *...aabbaacc...*), respectively (Figs. 6.2a-c) [70]. These different stackings can be compared to the *...abc...* and *...ab...* stackings of hexagonal planes in FCC and hexagonal close-packed (HCP) crystals, respectively [70]. Hereafter, we will refer to the different structures by the name of their most common intermetallic compounds: $MgZn_2$ (C14), $MgCu_2$ (C15) and $MgNi_2$ (C36).

### 6.3.2 Self-assembly in bulk

We synthesized small CdSe NCs ($S$) with a total diameter of 5.1 nm (7.6 nm total diameter including the ligands; 2% total polydispersity) and large PbSe NCs ($L$) with a total diameter of 7.6 nm (9.9 nm total diameter including the ligands; 2% total polydispersity), resulting in a size ratio $\gamma \approx 0.76$. Our buildings blocks (cores and ligands) are similar to the work of Evers *et al.* [388], and we therefore decided to describe our experimental system with a HS-like potential as well, although we are aware that (small) deviations of a HS potential are likely. To investigate the bulk assembly behaviour of the experimental binary components, a mixture of both NCs was allowed to self-assemble on a diethylene glycol surface, according to a well developed liquid-air interface method [427]. The self-assembled binary NC superlattice projection shown in Fig. 6.2d is in good agreement with the [0001] projection of a $MgZn_2$ lattice. The FFT pattern (inset) shows hexagonal order, which corresponds to the [0001] projection of the $MgZn_2$ structure. Although the hexagonal pattern is compatible with a $MgZn_2$ structure, we cannot exclude stacking faults, or even the $MgNi_2$ structure. At least four stackings of $L$ particle pairs are needed to distinguish the two hexagonal Laves structures (*...aabb...* and *...aabbaacc...*), which corresponds to $> 40$ nm for our combination of particles. The assembly method used here results typically not in a thickness over 100 nm as for thicker structures the electron beam is not able to penetrate the film [389, 401, 427]. This thickness is not enough to confidently exclude the $MgNi_2$ structure. However, we can definitely rule out the cubic $MgCu_2$ Laves phase.

### 6.3.3 Self-assembly in spherical confinement

We also let the binary mixture of CdSe/PbSe NCs self-assemble in slowly drying emulsion droplets [102]. To investigate the self-assembled superstructures composed of CdSe/PbSe binary NCs, we first discuss high angle annular dark field scanning transmission electron microscopy (HAADF-STEM) images of the self-assembled binary SPs (Fig. 6.3a). Each SP consists of a highly ordered core composed of both NCs and a few curved outer layers of close-packed CdSe NCs (Fig. 6.3a). The binary structure of the SPs is consistent with energy-dispersive X-ray spectroscopy (EDX) chemical mapping (Figs. 6.3d-f). The elemental distributions of lead and cadmium show a slight core-shell morphology of the SP with respect to the CdSe and PbSe NCs, where the PbSe NCs are only detected in the core of the SP. We ascribe the shell formation to the binary NCs species having a slightly different stoichiometric amount, compared to that of the ordered cores during the SA in the drying emulsion droplets, such that the $S$ spheres were left as an excess (crystal) phase after the binary crystallization was finished, probably remaining as a colloidal liquid during the binary SA. For SA with such a small excess of $S$ spheres, we investigated two self-assembled SPs with a diameter of 115 and 150 nm, respectively (Figs. 6.3b,c). From

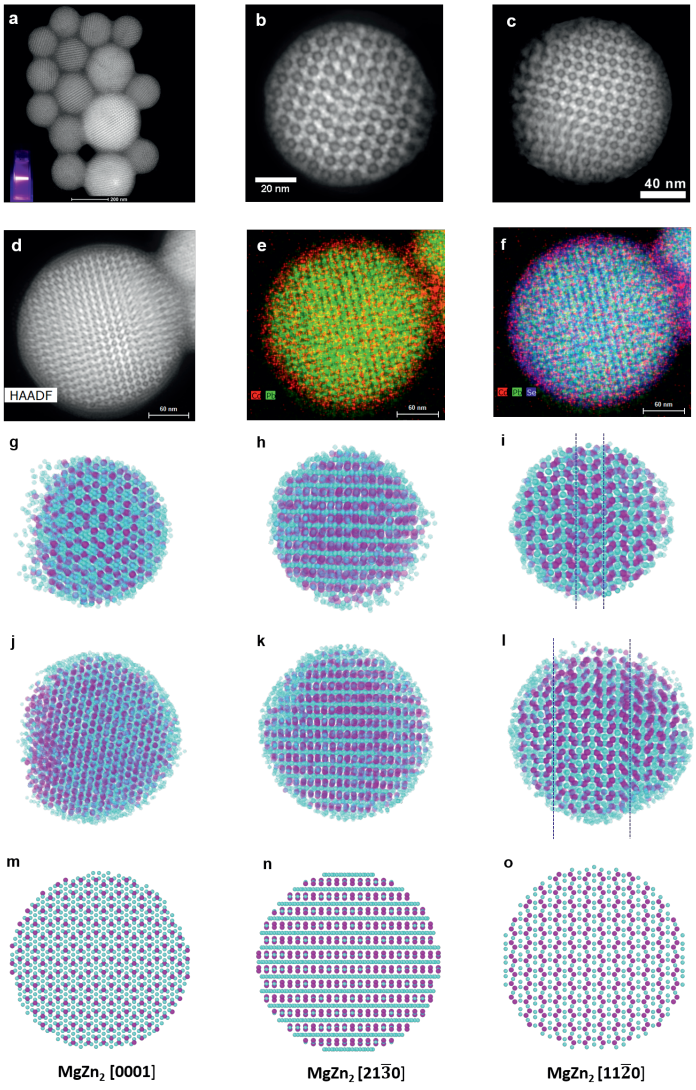


**Figure 6.3: Self-assembled binary Laves SPs.** 2D HAADF-STEM projections of a) SP overview, b) 115 nm sized SP, c) 150 nm sized SP and d) a SP for EDX chemical mapping study viewed along the [11$\bar{2}$0] projection. Superimposition of e) lead and cadmium and f) lead, cadmium and selenium. SSR reconstruction renderings of g-i) 115 nm sized SP and j-l) 150 nm sized SP viewed along the g,j) [0001], h,k) [21$\bar{3}$0] and i,l) [11$\bar{2}$0] projection, respectively. m-o) Structure model of a perfect $MgZn_2$ SP viewed along the m) [0001], n) [21$\bar{3}$0] and o) [11$\bar{2}$0] projection, respectively. Stacking faults are marked with blue dashed lines. A digital photograph of a SP dispersion under a laser pen illumination with a wavelength of $\lambda = 405$ nm can be found in the inset in (a), showing photoluminescence of the SP dispersion at room temperature.

2D HAADF-STEM images, the stacking is compatible with that of a $MgZn_2$ crystal viewed along the $[11\bar{2}0]$ projection (Fig. 6.3o).

To explore the structure of the self-assembled binary NCs in spherical confinement on the single NP level, HAADF-STEM tomograms of the two self-assembled binary SPs were recorded. The coordinates of the NCs in the SP were obtained from a Sparse Sphere Reconstruction (SSR) [103], after which the two species were distinguished by calculating the local intensities of all the coordinates in the reconstruction obtained through a Simultaneous Iterative Reconstruction Technique (SIRT) [411], resulting in two populations based on the $Z$ contrast of the CdSe and PbSe NCs. The crystal structure was determined to be the $MgZn_2$ structure from main zone axis projections of coordinates of both SPs (Figs. 6.3g-l), and this was further confirmed by comparison to the projections of a spherical model of a perfect $MgZn_2$ crystal (Figs. 6.3m-o). In addition, two defect lines were identified in the $[11\bar{2}0]$ projections of the 115 nm sized SP (Fig. 6.3i), as well as the 150 nm sized SP (Fig. 6.3l). Finally, we note that five-fold symmetry, which was found in previous work on SA of single species NCs in spherical confinement [102], is absent in both SPs, most likely due to the slight mismatch from the perfect stoichiometric ratio of 1:2.

### 6.3.4 Radial distribution function analysis

Based on the coordinates of the binary NCs, the radial distribution function (RDF) of the found structures were calculated and compared to reference crystal structures. We used Monte Carlo (MC) simulations to equilibrate the three (HS) perfect Laves structures at coexistence pressure, that we read from the phase diagram for $\gamma = 0.76$ by Hynninen *et al.* [419]. In Figure 6.4a,b the RDFs (of both the $L$ and $S$ species) of the reference structures are plotted. In the RDF of the $L$ species the height ratio of the 4th and 5th peak $\frac{g(r/\sigma=2.4)}{g(r/\sigma=2.6)}$ can be used to distinguish the three different Laves structures: for $MgZn_2$ $\frac{g(r/\sigma=2.4)}{g(r/\sigma=2.6)} > 1$, for $MgNi_2$ $\frac{g(r/\sigma=2.4)}{g(r/\sigma=2.6)} \approx 1$ and for $MgCu_2$ $\frac{g(r/\sigma=2.4)}{g(r/\sigma=2.6)} < 1$. In the RDF of the $S$ species, however, the difference between the distributions is minimal. Therefore the RDF of the $S$ species cannot be used to distinguish the different Laves crystal structures. Figure 6.4c shows the RDF of the $L$ species (PbSe NCs) in the 115 and 150 nm sized SPs. Since we find that the ratio of the 4th and 5th peak in the distribution is larger than 1, the RDF is compatible with the $MgZn_2$ structure. Although the RDF comparison confirms our previous finding, it is limited: the RDF calculations are based on the real-space coordinates of the particles, but still is an ensemble measurement and therefore defects remain hidden.

### 6.3.5 BOO analysis

In order to gain more insight into the local structure of the binary SPs, we carried out a BOO analysis to determine the local symmetry of both the PbSe and CdSe NCs. In the BOO analysis the local symmetry of every particle with respect to its neighbours is determined through the calculation of spherical harmonics [176]. In this work we used the averaged local BOO parameters $\bar{q}_4$ and $\bar{q}_6$, for which we also take into account the second shell of neighbours around each particle [178]. In order to get an estimate of the upper limit of the effect of randomness on the BOO analysis, which is most likely

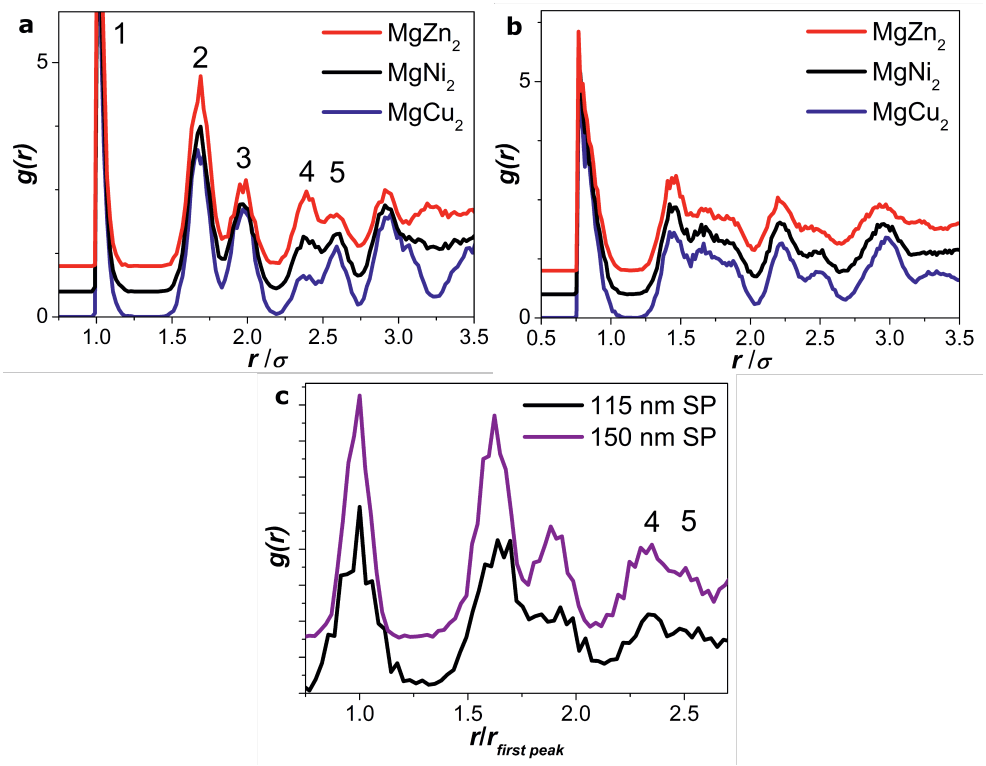


**Figure 6.4: Radial distribution functions (RDF) of the Laves crystal structures and the SPs.** RDF of a) the $L$ and b) $S$ species in the reference equilibrated Laves crystal structures as obtained from Monte Carlo simulations: $MgZn_2$ (red), $MgNi_2$ (black) and $MgCu_2$ (blue), where $\sigma$ is the diameter of the $L$ species. c) RDF of the $L$ species in the 115 (black) and 150 (purple) nm sized SPs.

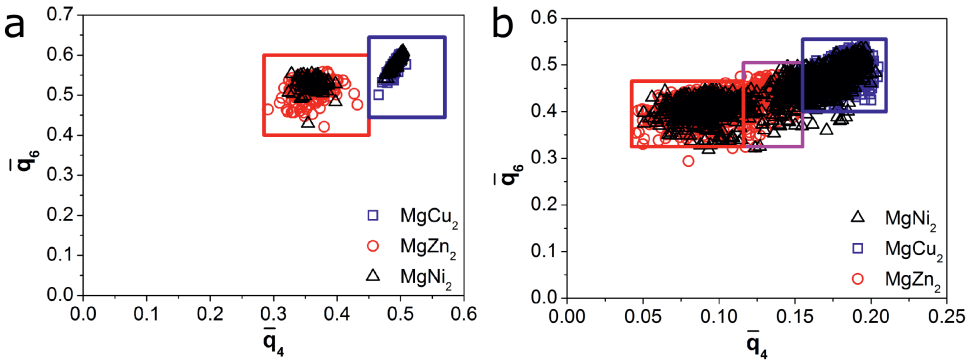


**Figure 6.5: BOO of the *L* and *S* species in simulated Laves phases.** Scatter plots of the BOO values of the $L$ species (a) and $S$ species (b) in the simulated Laves phases $MgCu_2$ (blue), $MgZn_2$ (red) and $MgNi_2$ (black). For the $L$ species, the particles with $\bar{q}_6$ and $\bar{q}_4$ values within the colored rectangles were considered to have local $MgZn_2$ (red) and $MgCu_2$ (blue) symmetry.

less than the effects of polydispersity in our system since our crystals were compressed to the highest density, we use the equilibrated Laves crystal structures as described in the previous paragraph. Next, we distinguished the three Laves phases by assigning the local symmetry of each particle according to specific areas in the $\bar{q}_6 - \bar{q}_4$ scatter plot of the $L$ species. The different symmetries of the $L$ species in the $MgZn_2$ phase (hexagonal diamond) and $MgCu_2$ phase ((cubic) diamond) lead to a distinct grouping of these two Laves phases in the scatter plot (see Figure 6.5a). The BOO parameter values of the $L$ species in $MgNi_2$ are split between the above-mentioned two symmetries as this Laves phase can be seen as a mixture of the other two phases. Figs. 6.6a-c show the $L$ species in the three Laves phases with assigned symmetries: the $L$ species in $MgCu_2$ and $MgZn_2$ have the same symmetries throughout the whole structure, while in the $MgNi_2$ structure the (cubic) diamond and hexagonal diamond symmetries of the $L$ species alternate. Figs. 6.6d,f show the scatter plots calculated from the coordinates of the $L$ species obtained through the EM tomographic reconstruction of both the 115 nm and 150 nm sized SPs. When assigning the symmetry of each $L$ particle according to their BOO parameter values, we find that most $L$ species exhibit a hexagonal diamond symmetry, with stacking faults with (cubic) diamond symmetry present in both SPs (Figs. 6.6e,g).

When the BOO analysis is extended to the $S$ species, a more complex scatter plot is obtained (see Figure 6.5b). Assigning the local symmetry to each $S$ particle reveals a clear difference between the three Laves structures: all the $S$ species have the same symmetry in the $MgCu_2$ phase, while the $S$ species have two and three different symmetries in the $MgZn_2$ and $MgNi_2$ phases, respectively (see Figs. 6.7a-c). The BOO parameter values in the $\bar{q}_6 - \bar{q}_4$ scatter plots of the $S$ particles in the two experimental SPs are less grouped in distinct distributions compared to those of the $L$ ones (Figs. 6.7d,f). However, assigning the local symmetries to the $S$ species, reveals the stacking faults (Figs. 6.7e,g) similar to the ones found from the $L$ species BOO analysis in both experimental SPs (Figs. 6.6e,g). Interestingly, the stacking of both the $S$ and $L$ species remains identical throughout the

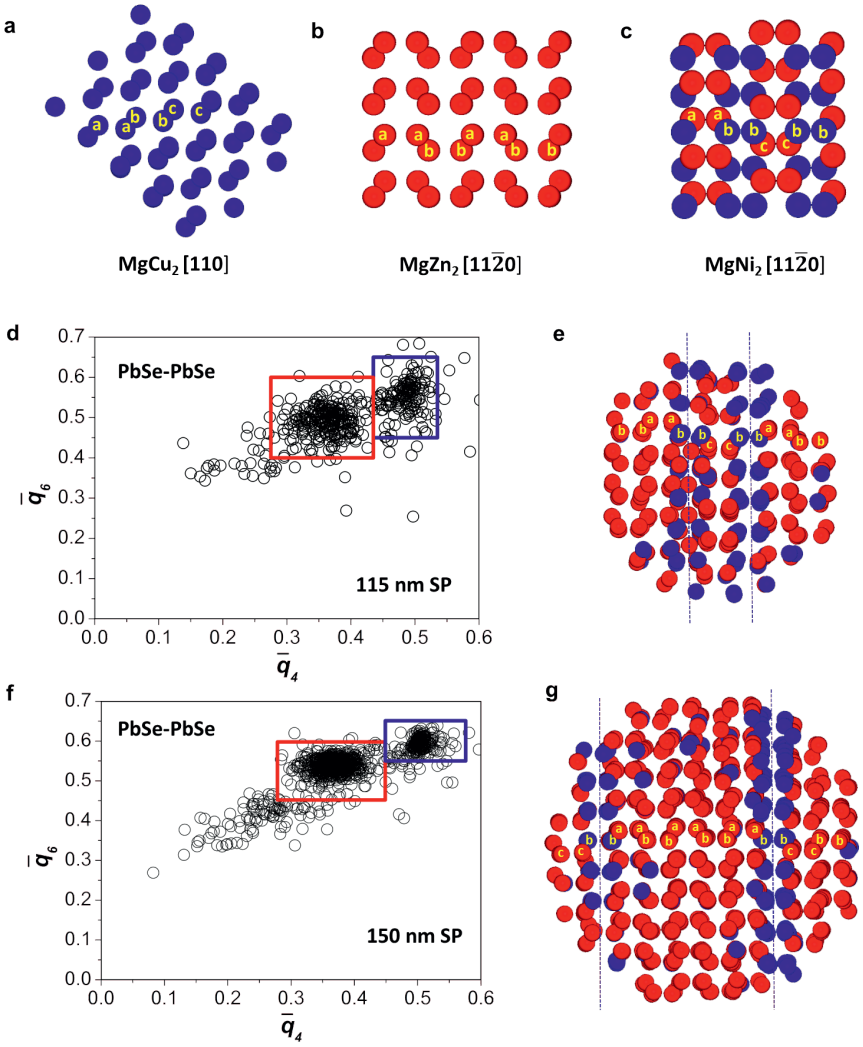


**Figure 6.6: BOO analysis of *L* species (PbSe NCs).** Computer renderings of the $L$ species (PbSe NCs) in perfect Laves phases a) $MgCu_2$, b) $MgZn_2$ and c) $MgNi_2$, where the particles are colored according to their BOO parameter value. Scatter plots of the BOO parameters of the d) 115 nm and f) 150 nm sized SPs, showing two distinct distributions corresponding to the diamond (blue) and hexagonal diamond (red) symmetries. Computer renderings of the $L$ species with BOO parameter values within the blue or red rectangles in the e) 115 nm and g) 150 nm sized SPs, revealing the stacking faults in the crystal.

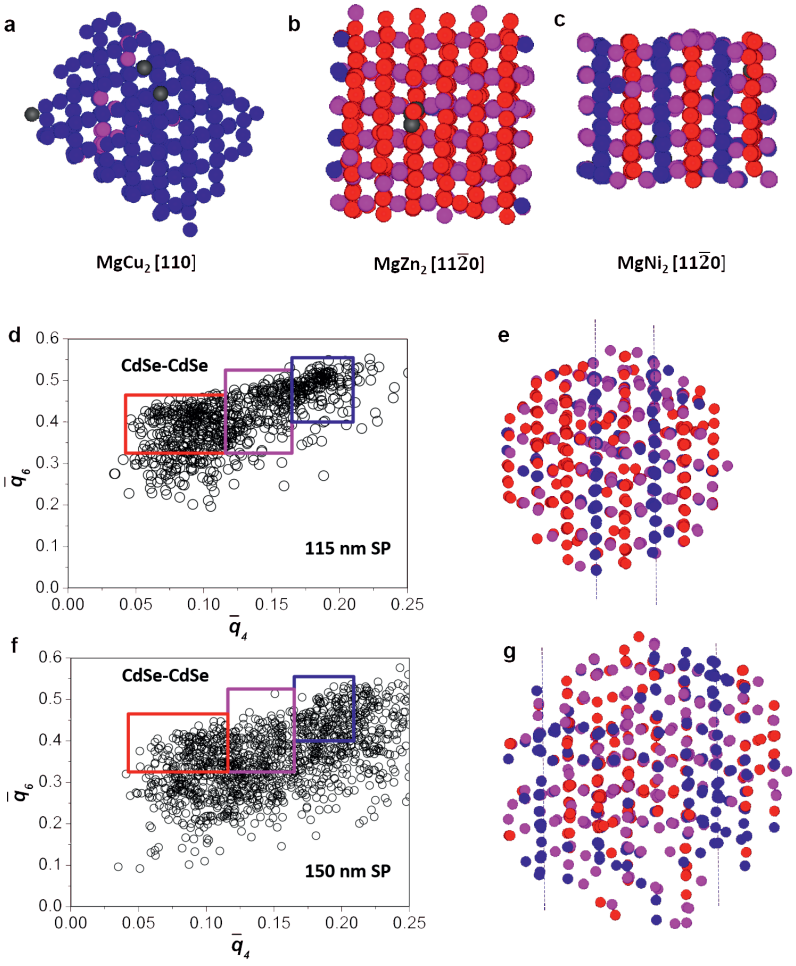


**Figure 6.7: BOO analysis of *S* species (CdSe NCs).** Computer renderings of the *S* species (CdSe NCs) in simulated Laves phases a) $MgCu_2$, b) $MgZn_2$ and c) $MgNi_2$, where the particles are colored according to their BOO parameter values. Scatter plots of the BOO parameters of the d) 115 nm and f) 150 nm sized SPs, showing less well defined distributions compared to the *S* species (CdSe). Computer renderings of the small species with BOO parameter values within the blue, magenta or red rectangles in the e) 115 nm and g) 150 nm sized SPs, revealing the stacking faults in the crystal.

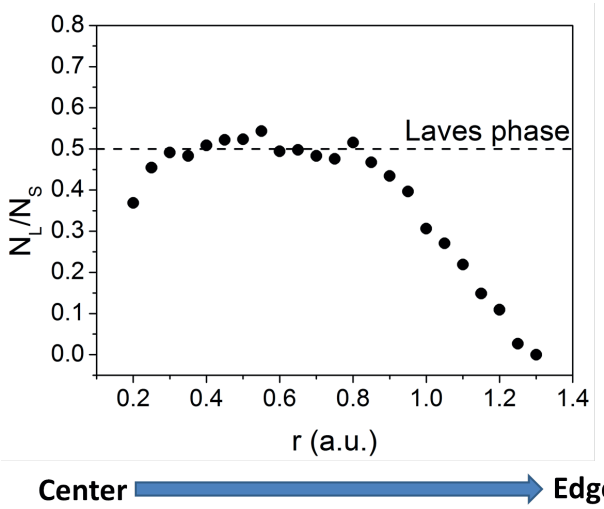


**Figure 6.8: Number ratio of $L$ to $S$ species in 115 nm SP.** The number ratio $\frac{N_L}{N_S}$ of $L$ (PbSe NCs) to $S$ (CdSe NCs) species was calculated by drawing a shell with radius $r$ and thickness $d = 0.2$ around the center of mass of the SP. At $r < 0.3$ too few particles were taken into account to get proper statistics, while at $r > 0.8$ the shell reaches outside the Laves crystal, where there is an excess of $S$ species. In the region $0.3 \leq r \leq 0.8$, $\langle \frac{N_L}{N_S} \rangle = 0.50$ ($\sigma = 0.02$), in accordance with the Laves phase stoichiometry.

structure, making the stacking faults continuous transitions from one structure to the other for both species.

As mentioned above, the BOO parameter values in the $\bar{q}_6 - \bar{q}_4$ scatter plots of the $S$ species in the two SPs are significantly less grouped in distinct clouds compared to those of the $L$ species, resulting in less clearly defined planes of similar colored particles (Figs. 6.7d-g). We speculate this is due to the more complex structure of the $S$ species compared to the $L$ species. Also, the size ratio $\gamma = 0.76$ of our system is on the lower end of the size ratio range where the Laves phases form. This means that the $S$ particles have more room to move relative to the $L$ particles, leading to less well-defined coordinates of the $S$ particles with respect to the $L$ particles and therefore a less well defined distribution of the BOO parameter values as compared to an ideal lattice. In addition, the distribution of the BOO parameter values of the $S$ particles in the 150 nm sized SP is less concentrated than the values of the 115 nm sized SP (Figs. 6.7d,f). We speculate this is due to the large size and structure complexity of the 150 nm sized SP. When the SP becomes too thick, the reconstruction algorithm is not able to retrieve all particles with lower $Z$ contrast (*i.e.* $S$ particles (CdSe NCs) in this case), resulting in missing particles, which leads to lower BOO parameter values of the identified $S$ spheres. This is supported by calculating the number ratio $\frac{N_L}{N_S}$ of $L$ to $S$ species (0.5 for Laves phases) for the 115 nm and 150 nm sized SPs: 0.50 and 0.57, respectively, indicating missing $S$ species in the 150 nm sized SP (see Figure 6.8). The number ratio of the $L$ and $S$ spheres inside the binary crystal

region of the 115 nm sized SP matches the ratio of the perfect Laves crystal ($\frac{N_L}{N_S} = 0.5$): this observation is in contrast with earlier work on HS binary NaCl crystals. In previous studies we demonstrated that for binary HS crystals with a size ratio $\gamma \approx 0.3$, forming NaCl-type binary crystals, the $S$ species do not fill their stoichiometric number of lattice positions, unless their osmotic pressure is quite high, and the crystals can therefore be better described as an interstitial solid solution with tunable lattice doping [428, 429]. This discrepancy of the stoichiometry in the binary structure was due to the increased entropy associated with this 'imperfect' lattice filling.

The BOO analysis identified the stacking faults to have local $MgCu_2$ symmetry, for both the $L$ and $S$ species (see Figs. 6.6e,g and Figs. 6.7e,g). The stacking faults consist of a pair of $L$ species from two adjacent triple-line ($t$ or $t$') stacks (*e.g.* *bb* in Figs. 6.6e,g) and a single line of $S$ species (particles align along the blue dashed lines in Figs. 6.7e,g), all with $MgCu_2$ symmetry. This is equivalent to an insertion of a $s\ t$ unit in a $MgZn_2$ structure (*e.g.* $s\ t\ s\ t'\ s\ t\ \mathbf{s}\ \mathbf{t}\ s\ t'\ s\ t\ s\ t'$ instead of $s\ t\ s\ t'\ s\ t\ s\ t'\ s\ t\ s\ t'$). In the 150 nm sized SP the stacking faults are several $L$ pairs apart, leading to two $MgZn_2$ zones which are slightly shifted with respect to each other (*i.e.* *...aabbaa...* and *...bbccbb...*, see Fig. 6.6g). In the 115 nm sized SP, however, the two defect lines are one pair of $L$ spheres apart, and can therefore be seen as a single mis-stacking of the *cc* layer in an otherwise perfect $MgZn_2$ *...aabb...* stacking (see Fig. 6.6e). Since the stacking faults are only one pair of $L$ spheres away from each other, one can also interpret the majority of the 115 nm sized SP to be the $MgNi_2$ structure. This emphasizes the importance of thick enough samples for proper distinction of the $MgZn_2$ and $MgNi_2$ Laves crystals. In addition it let us conclude that it is conceivable that also some other examples from the literature where the phase identified as that of a pure Laves phase, it may in fact have been more closely described as that of a mixture of the three Laves phases in the sense of more random stacking of the binary $L$ species. Even in our analysis of the binary SPs, we do not have enough statistics to reliably determine a stacking probability (as has been done before for HS crystals see *e.g.* [360]).

It has been shown that in $MgZn_2$ crystals, the formation of dislocations with the $MgCu_2$ symmetry can be described as the simultaneous shear of two sub-layers along different directions, a mechanism known as synchroshear [430, 431]. The synchroshear can result in dislocations with $MgCu_2$ symmetry with varying thickness: ... $s\ t'\ s\ t\ s\ t\ s\ t\ s\ t'$ ... (also refered to an $I_2$ stacking fault [432]) and ... $s\ t'\ s\ t\ s\ t\ s\ t\ s\ t\ s\ t\ s\ t'$ ... , so with either three or five repeating $s\ t$ units [430]. Further synchroshear applied to the $I_2$ stacking fault can form the twin-like stacking fault $T_2$ with the $MgNi_2$ symmetry [432], corresponding to the structure found in our experimental 115 nm sized SP. In the 150 nm sized SP, we have only found dislocations with a thickness of two repeating $s\ t$ units, which is the simplest stacking fault possible in the Laves phases and cannot be formed from a perfect $MgZn_2$ crystal using the synchroshear mechanism. We therefore speculate that the stacking faults in the $MgZn_2$ crystal structure form in the SPs as a result of mis-stacking during crystal growth, which have not been able to anneal out within the time-scale of the emulsion droplet drying, a process which was found to be very slow for HS particles [433]. Further studies are needed to analyze the stacking probability in more detail and determine its origins.

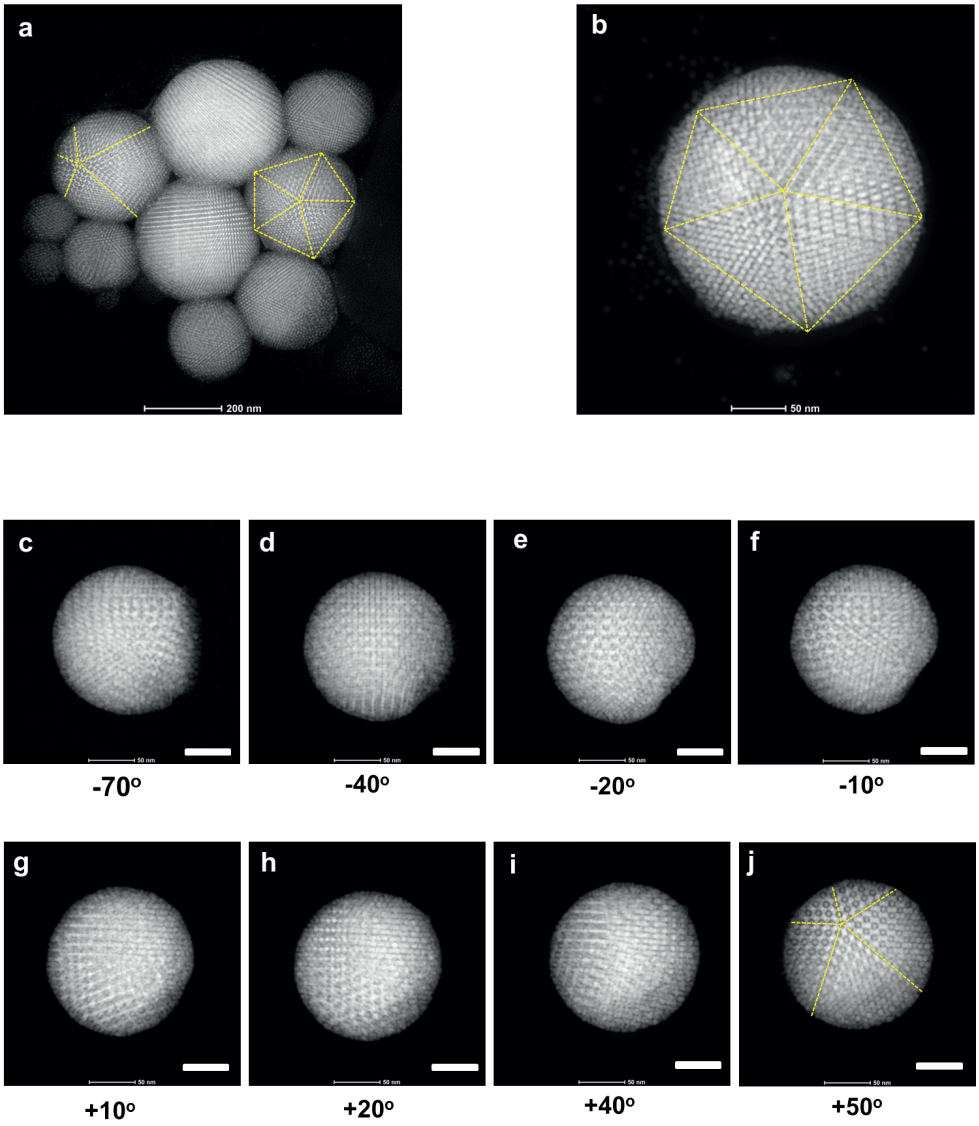


**Figure 6.9: Self-assembled Laves SPs with icosahedral geometry.** a) Overview of self-assembled Laves SPs with icosahedral geometry, where multiply-twinned crystalline domains can be seen in all SPs and the five-fold symmetry is visibly marked with yellow dashed lines. b) A self-assembled SP with a diameter of 235 nm showing five-fold symmetry. c-j) 2D HAADF-STEM images of a self-assembled SP with a diameter of 160 nm at different tilting angles. The five-fold symmetry can be viewed at a tilting angle of +50°. Scale bars in c-j): 50 nm.

### 6.3.6 The influence of the ratio between the species on their assembly

As aforementioned, no five-fold symmetry was found in the SPs when the stoichiometry of the overall NP ratio was slightly off 1:2. By finely tuning the stoichiometry of the experimental binary species (minimizing the amount of CdSe NCs) to more closely match that of the Laves crystals, we recently found the five-fold symmetry in a high percentage ($\sim$ 78%) self-assembled binary SPs (Fig. 6.9). Crystalline domains with different orientations were observed in the SPs with five-fold symmetry (Figs. 6.9a and b). It is not trivial to confirm if a self-assembled SP has the five-fold symmetry without tilting the sample to different angles (Figs. 6.9c-j). The formed Laves SPs, appear to be icosahedral quasicrystals with five-fold symmetry (Figs. 6.9 a and j), with the majority of the particles having a local $MgCu_2$ symmetry and are most likely related to the icosahedral structure as found in single species SPs [102]. A full analysis is in progress, either for the experimental systems or the computer simulations of slightly repulsive binary particles for which similar structures were recently found [434]. In contrast to the SPs containing the $MgZn_2$ structure discussed in this work earlier, almost no extra layers of small CdSe NCs were found around the SPs with five-fold symmetry.

## 6.4 Conclusions and Outlook

To conclude, we studied the structure and defects of two SPs formed by the self-assembly of a binary mixture of CdSe/PbSe NCs in spherical confinement. The spherical geometry of the SPs enabled us to obtain real-space coordinates of a binary crystal composed of over 50 layers through EM tomography. With the coordinates of both sized species obtained, it was possible to analyze the stacking order in the SPs using BOO analysis, making it more likely that the structure should be characterized as a mixture of the three Laves phases, similarly as single HSs are prone to form randomly stacked close packed layers. We also have shown that several other ways of looking at the real space structure, such as through the radial distribution function and a projection from directions not sensitive to randomness in the [0001] stacking direction, might lead one to conclude that the crystal phase is $MgZn_2$. We found that the stoichiometry in the binary Laves phase was close to 0.5, in contrast to earlier work on binary HS NaCl crystals [428, 429]. The stacking faults we found in our two SPs, locally induced a $MgCu_2$ symmetry, which can be ascribed to the fact that the free energy difference between the three Laves structures is quite small. Furthermore, we found that an excess amount of the $S$ species (CdSe NCs) did not lead to the spherical confinement changing the structure, while if an excess of the $S$ spheres was absent, the spherical confinement did lead to significant occurrence of SPs with five-fold symmetries and increased local $MgCu_2$ environments. Currently, the resulting SPs of systems with more exact stoichiometry are being analyzed in both experiments and simulations. Insights in the formation of $MgCu_2$ structure will provide a promising route for the experimental realization of photonic crystals with a bandgap in the visible region by using sub-micron-sized colloids [73]. Moreover, the absence of a strong influence on binary SA in the case where the stoichiometry is (even slightly) off means that SA of

larger colloids can be used to analyze binary colloidal crystallization with (STED) confocal microscopy.

## 6.5 Acknowledgements

The work in this chapter was done in collaboration with Da Wang, Tonnishtha Dasgupta, Thomas Altantzis, Daniele Zanaga, Yaoting Wu, Marjolein Dijkstra, Sara Bals and Chris Murray. Da Wang and Yaoting Wu synthesized the particles, Da Wang assembled the supraparticles and performed the electron microscopy measurements and reconstruction with Thomas Atlantzis and Daniele Zanaga. Tonnishtha Dasgupta performed computer simulations. We thank Tonnishtha Dasgupta, Giulia Fiorucci, Berend van der Meer, Gabriele Coli, Simone Dussi, Laura Filion and Marjolein Dijkstra for many useful discussions.

# A

# Supplementary files

Please scan QR codes for links to the supporting files or (in case of a digital version of this thesis) click the titles.

### 4.1 Arrest of a long range repulsive crystal

A 2D confocal micrograph time sequence of the arrest of a long range repulsive colloidal crystal of PMMA colloids in a de-ionized mixture of cyclohexyl bromide, cis-decalin and ETPTA by exposure to UV light.

### 4.2 Arrested long range repulsive crystal

Computer rendering of the arrested long range repulsive crystal of PMMA colloids in a de-ionized mixture of cyclohexyl bromide, cis-decalin and ETPTA.

### 4.3 Arrested AC electric field induced strings

Computer rendering of arrested AC electric field induced strings of PMMA colloids in a mixture of cyclohexyl bromide, cis-decalin and ETPTA saturated with TBAB salt.

# References


[1] P.-G. de Gennes, *Soft matter (nobel lecture).* Ang. Chem., 31(7):842–845, 1992.

[2] H. Löwen, *Colloidal soft matter under external control.* J. Phys. Condens. Matter, 13(24):R415, 2001.

[3] Y. L. Wu, D. Derks, A. van Blaaderen, and A. Imhof, *Melting and crystallization of colloidal hard-sphere suspensions under shear.* Proc. Natl. Acad. Sci. U.S.A., 106(26):10564–10569, 2009.

[4] A. van Blaaderen, M. Dijkstra, R. van Roij, A. Imhof, M. Kamp, B. W. Kwaadgras, T. Vissers, and B. Liu, *Manipulating the self assembly of colloids in electric fields.* Eur. Phys. J. Spec. Top., 222(11):2895–2909, 2013.

[5] C. N. Likos, *Soft matter with soft particles.* Soft Matter, 2:478–498, 2006.

[6] E. Nelson. *Dynamical theories of Brownian motion*, volume 3. Princeton university press, 1967.

[7] R. Brown, *Xxvii. a brief account of microscopical observations made in the months of june, july and august 1827, on the particles contained in the pollen of plants; and on the general existence of active molecules in organic and inorganic bodies.* Philos. Mag., 4(21):161–173, 1828.

[8] R. Brown, *Xxiv. additional remarks on active molecules.* Philos. Mag., 6(33):161–166, 1829.

[9] W. Sutherland, *Lxxv. a dynamical theory of diffusion for non-electrolytes and the molecular mass of albumin.* Philos. Mag., 9(54):781–785, 1905.

[10] A. Einstein, *Über die von der molekularkinetischen theorie der wärme geforderte bewegung von in ruhenden flüssigkeiten suspendierten teilchen.* Ann. Phys., 322(8):549–560, 1905.

[11] M. Von Smoluchowski, *Zur kinetischen theorie der brownschen molekularbewegung und der suspensionen.* Ann. Phys., 326(14):756–780, 1906.

[12] S. Lundqvist and N. Foundation. *Nobel Lectures in Physics 1922-1941.* World Scientific, 1998.

[13] J. Perrin. *Les atomes.* Librairie Félix Alcan, 1913.

[14] R. Newburgh, J. Peidle, and W. Rueckner, *Einstein, perrin, and the reality of atoms: 1905 revisited.* Am. J. Phys., 74(6):478–481, 2006.

[15] U. Gasser, E. R. Weeks, A. Schofield, P. N. Pusey, and D. A. Weitz, *Real-space imaging of nucleation and growth in colloidal crystallization.* Science, 292(5515):258–262, 2001.

[16] D. Grier and C. Murray, *The microscopic dynamics of freezing in supercooled colloidal fluids.* J. Chem. Phys., 100(12):9088–9095, 1994.

[17] K. Sandomirski, S. Walta, J. Dubbert, E. Allahyarov, A. B. Schofield, H. Löwen, W. Richtering, and S. U. Egelhaaf, *Heterogeneous crystallization of hard and soft spheres near flat and curved walls.* Eur. Phys. J. Spec. Top., 223(3):439–454, 2014.

[18] A. van Blaaderen and P. Wiltzius, *Real-space structure of colloidal hard-sphere glasses.* Science, 270(5239):1177–1179, 1995.

[19] W. K. Kegel and A. van Blaaderen, *Direct observation of dynamical heterogeneities in colloidal hard-sphere suspensions.* Science, 287(5451):290–293, 2000.

[20] E. R. Weeks, J. C. Crocker, A. C. Levitt, A. Schofield, and D. A. Weitz, *Three-dimensional direct imaging of structural relaxation near the colloidal glass transition.* Science, 287(5453):627–631, 2000.

[21] D. Frenkel, *Order through entropy.* Nat. Mater., 14:9–12, 2014.

[22] B. J. Alder and T. E. Wainwright, *Phase transition for a hard sphere system.* J. Chem. Phys., 27(5):1208–1209, 1957.

[23] W. W. Wood and J. D. Jacobson, *Preliminary results from a recalculation of the monte carlo equation of state of hard spheres.* J. Chem. Phys., 27(5):1207–1208, 1957.

[24] J. D. Bernal, *Geometry of the structure of monatomic liquids.* Nature, 185(4706):68, 1960.

[25] J. L. Finney, *Bernal's road to random packing and the structure of liquids.* Philos. Mag., 93(31–33):3940–3969, 2013.

[26] J. Kepler. *The Six-Cornered Snowflake.* Paul Dry Books, 2010.

[27] T. Hales, M. Adams, G. Bauer, T. D. Dang, J. Harrison, L. T. Hoang, C. Kaliszyk, V. Magron, S. Mclaughlin, T. T. Nguyen, Q. T. Nguyen, T. Nipkow, S. Obua, J. Pleso, J. Rute, A. Solovyev, T. H. A. Ta, N. T. Tran, T. D. Trieu, J. Urban, K. Vu, and R. Zumkeller, *A formal proof of the kepler conjecture.* Forum Math. Pi, 5:e2, 2017.

[28] P. N. Pusey and W. van Megen, *Phase behaviour of concentrated suspensions of nearly hard colloidal spheres.* Nature, 320(6060):340–342, 1986.

[29] C. P. Royall, W. C. K. Poon, and E. R. Weeks, *In search of colloidal hard spheres.* Soft Matter, 9:17–27, 2013.

[30] H. M. Lindsay and P. M. Chaikin, *Elastic properties of colloidal crystals and glasses.* J. Chem. Phys., 76(7):3774–3781, 1982.

[31] C. P. Royall, M. E. Leunissen, and A. van Blaaderen, *A new colloidal model system to study long-range interactions quantitatively in real space.* J. Phys. Condens. Matter, 15(48):S3581, 2003.

[32] A. van Blaaderen, *From the de broglie to visible wavelengths: Manipulating electrons and photons with colloids.* MRS Bulletin, 23(10):39–43, 1998.

[33] A. Yethiraj and A. van Blaaderen, *A colloidal model system with an interaction tunable from hard sphere to soft and dipolar.* Nature, 421(6922):513–517, 2003.

[34] A.-P. Hynninen and M. Dijkstra, *Phase diagrams of hard-core repulsive yukawa particles.* Phys. Rev. E, 68:021407, 2003.

[35] C. Fenzl, T. Hirsch, and O. S. Wolfbeis, *Photonic crystals for chemical sensing and biosensing.* Angew. Chem. Int. Ed., 53(13):3318–3335, 2014.

[36] S. A. Asher, J. Holtz, L. Liu, and Z. Wu, *Self-assembly motif for creating submicron periodic materials. polymerized crystalline colloidal arrays.* J. Am. Chem. Soc., 116(11):4997–4998, 1994.

[37] J. M. Weissman, H. B. Sunkara, A. S. Tse, and S. A. Asher, *Thermally switchable periodicities and diffraction from mesoscopically ordered materials.* Science, 274(5289):959–963, 1996.

[38] J. H. Holtz and S. A. Asher, *Polymerized colloidal crystal hydrogel films as intelligent chemical sensing materials.* Nature, 389:829–832, 1997.

[39] K. Lee and S. A. Asher, *Photonic crystal chemical sensors: ph and ionic strength.* J. Am. Chem. Soc., 122(39):9534–9537, 2000.

[40] G. Haacke, H. P. Panzer, L. G. Magliocco, and S. A. Asher. *Narrow band radiation filter films*, 1993. US Patent 5266238.

[41] R. H. Baughman, S. O. Dantas, S. Stafström, A. A. Zakhidov, T. B. Mitchell, and D. H. E. Dubin, *Negative poisson's ratios for extreme states of matter.* Science, 288(5473):2018–2022, 2000.

[42] J. Israelachvili. *Intermolecular and Surface Forces.* Academic Press, 1992.

[43] H. N. W. Lekkerkerker and R. Tuinier. *Colloids and the Depletion Interaction.* Springer, 2011.

[44] N. Urakami, M. Imai, Y. Sano, and M. Takasu, *The isotropic-nematic transition and the phase separation of the tobacco mosaic virus particles with polysaccharide.* J. Chem. Phys., 111(5):2322–2328, 1999.

[45] M. Leunissen. *Manipulating colloids with charges & electric fields.* PhD thesis, Utrecht University, 2007.

[46] S. Sacanna and D. J. Pine, *Shape-anisotropic colloids: Building blocks for complex assemblies.* Curr. Opin. Colloid Interface Sci., 16(2):96–105, 2011.

[47] S.-M. Yang, S.-H. Kim, J.-M. Lim, and G.-R. Yi, *Synthesis and assembly of structured colloidal particles.* J. Mater. Chem., 18:2177–2190, 2008.

[48] A. van Blaaderen, *Materials science: colloids get complex.* Nature, 439(7076):545, 2006.

[49] S. C. Glotzer and M. J. Solomon, *Anisotropy of building blocks and their assembly into complex structures.* Nat. Mater., 6(8):557–562, 2007.

[50] A. Walther and A. H. E. Müller, *Janus particles.* Soft Matter, 4:663–668, 2008.

[51] Q. Chen, S. C. Bae, and S. Granick, *Directed self-assembly of a colloidal kagome lattice.* Nature, 469(7330):381, 2011.

[52] G. Gompper, C. Bechinger, S. Herminghaus, R. Isele-Holder, U. B. Kaupp, H. Löwen, H. Stark, and R. G. Winkler, *Microswimmers – from single particle motion to collective behavior.* Eur. Phys. J. Spec. Top., 225(11):2061–2064, 2016.

[53] M. Driscoll and B. Delmotte, *Leveraging collective effects in externally driven colloidal suspensions: Experiments and simulations.* Curr. Opin. Colloid Interface Sci., 40:42–57, 2019.

[54] A. Aubret, S. Ramananarivo, and J. Palacci, *Eppur si muove, and yet it moves: Patchy (phoretic) swimmers.* Curr. Opin. Colloid Interface Sci., 30:81–89, 2017.

[55] V. N. Manoharan, *Colloidal matter: Packing, geometry, and entropy.* Science, 349(6251):1253751, 2015.

[56] N. Vogel, M. Retsch, C.-A. Fustin, A. del Campo, and U. Jonas, *Advances in colloidal assembly: the design of structure and hierarchy in two and three dimensions.* Chem. Rev., 115(13):6265–6311, 2015.

[57] M. Grzelczak, J. Vermant, E. M. Furst, and L. M. Liz-Marzán, *Directed self-assembly of nanoparticles.* ACS Nano, 4(7):3591–3605, 2010.

[58] E. M. Furst, *Directed self-assembly.* Soft Matter, 9(38):9039–9045, 2013.

[59] G.-R. Yi, D. J. Pine, and S. Sacanna, *Recent progress on patchy colloids and their self-assembly.* J. Phys. Condens. Matter, 25(19):193101, 2013.

[60] S. A. Mallory, C. Valeriani, and A. Cacciuto, *An active approach to colloidal self-assembly.* Ann. Rev. Phys. Chem., 69:59–79, 2018.

[61] Z. Nie, A. Petukhova, and E. Kumacheva, *Properties and emerging applications of self-assembled structures made from inorganic nanoparticles.* Nat. Nanotech., 5:15–25, 2010.

[62] M. A. Boles, M. Engel, and D. V. Talapin, *Self-assembly of colloidal nanocrystals: From intricate structures to functional materials.* Chem. Rev., 116(18):11220–11289, 2016.

[63] N. Vogel, S. Utech, G. T. England, T. Shirman, K. R. Phillips, N. Koay, I. B. Burgess, M. Kolle, D. A. Weitz, and J. Aizenberg, *Color from hierarchy: Diverse optical properties of micron-sized spherical colloidal assemblies.* Proc. Natl. Acad. Sci. USA, 112(35):10845–10850, 2015.

[64] G. von Freymann, V. Kitaev, B. V. Lotsch, and G. A. Ozin, *Bottom-up assembly of photonic crystals.* Chem. Soc. Rev., 42(7):2528–2554, 2013.

[65] J. Teyssier, S. V. Saenko, D. Van Der Marel, and M. C. Milinkovitch, *Photonic crystals cause active colour change in chameleons.* Nat. Commun., 6:6368, 2015.

[66] R. W. Corkery and E. C. Tyrode, *On the colour of wing scales in butterflies: iridescence and preferred orientation of single gyroid photonic crystals.* Interface focus, 7(4):20160154, 2017.

[67] D. M. Carr, A. A. Ellsworth, G. L. Fisher, W. W. Valeriano, J. P. Vasco, P. S. S. Guimarães, R. R. de Andrade, E. R. da Silva, and W. N. Rodrigues, *Characterization of natural photonic crystals in iridescent wings of damselfly chalcopteryx rutilans by fib/sem, tem, and tof-sims.* Biointerphases, 13(3):03B406, 2018.

[68] G. Z. Mashanovich, *Electronics and photonics united.* Nature, 556:316–318, 2018.

[69] A. Blanco, E. Chomski, S. Grabtchak, M. Ibisate, S. John, S. W. Leonard, C. Lopez, F. Meseguer, H. Miguez, J. P. Mondia, et al., *Large-scale synthesis of a silicon photonic crystal with a complete three-dimensional bandgap near 1.5 micrometres.* Nature, 405(6785):437, 2000.

[70] A.-P. Hynninen, J. H. J. Thijssen, E. C. M. Vermolen, M. Dijkstra, and A. van Blaaderen, *Self-assembly route for photonic crystals with a bandgap in the visible region.* Nat. Mater., 6:202–205, 2007.

[71] W. Liu, M. Tagawa, H. L. Xin, T. Wang, H. Emamy, H. Li, K. G. Yager, F. W. Starr, A. V. Tkachenko, and O. Gang, *Diamond family of nanoparticle superlattices.* Science, 351(6273):582–586, 2016.

[72] Y. Wang, I. C. Jenkins, J. T. McGinley, T. Sinno, and J. C. Crocker, *Colloidal crystals with diamond symmetry at optical lengthscales.* Nat. Commun., 8:14173, 2017.

[73] É. Ducrot, M. He, G.-R. Yi, and D. J. Pine, *Colloidal alloys with preassembled clusters and spheres.* Nat. Mater., 16:652–657, 2017.

[74] G. Avvisati, T. Dasgupta, and M. Dijkstra, *Fabrication of colloidal laves phases via hard tetramers and hard spheres: bulk phase diagram and sedimentation behavior.* ACS Nano, 11(8):7702–7709, 2017.

[75] J. Pawley. *Handbook of Biological Confocal Microscopy.* Springer, New York, 2010.

[76] V. Prasad, D. Semwogerere, and E. R. Weeks, *Confocal microscopy of colloids.* J. Phys.: Condens. Matter, 19(11):113102, 2007.

[77] M. Petráň, M. Hadravský, M. D. Egger, and R. Galambos, *Tandem-scanning reflected-light microscope.* J. Opt. Soc. Am., 58(5):661–664, 1968.

[78] P. Saggau, *New methods and uses for fast optical scanning.* Curr. Opin. Neurobiol., 16(5):543–550, 2006.

[79] P. Shaw and D. Rawlins, *The point-spread function of a confocal microscope: its measurement and use in deconvolution of 3-d data.* J. Microsc., 163:151–165, 1991.

[80] R. Cole, T. Jinadasa, and C. Brown, *Measuring and interpreting point spread functions to determine confocal microscope resolution and ensure quality control.* Nat. Protoc., 6:1929–1941, 2011.

[81] T. H. Besseling, J. Jose, and A. van Blaaderen, *Methods to calibrate and scale axial distances in confocal microscopy as a function of refractive index.* J. Microsc., 257:142–150, 2014.

[82] C. J. de Grauw, J. M. Vroom, H. T. M. van der Voort, and H. C. Gerritsen, *Imaging properties in two-photon excitation microscopy and effects of refractive-index mismatch in thick specimens.* Appl. Opt., 38(28):5995–6003, 1999.

[83] A. Diaspro, F. Federici, and M. Robello, *Influence of refractive-index mismatch in high-resolution three-dimensional confocal microscopy.* Appl. Opt., 41(4):685–690, 2002.

[84] T. H. Besseling. *Self-assembly of colloidal spheres and rods in external fields.* PhD thesis, Utrecht University, 2014.

[85] W. Wallace, L. Schaefer, and J. Swedlow, *A workingperson's guide to deconvolution in light microscopy.* BioTechniques, 31:1076–1097, 2001.

[86] J. B. de Monvel, S. Le Calvez, and M. Ulfendahl, *Image restoration for confocal microscopy: Improving the limits of deconvolution, with application to the visualization of the mammalian hearing organ.* Biophys. J., 80(5):2455–2470, 2001.

[87] Y. Chen, M. Chen, L. Zhu, J. Y. Wu, S. Du, and Y. Li, *Measure and model a 3-d space-variant psf for fluorescence microscopy image deblurring.* Opt. Express, 26:14375–14391, 2018.

[88] S. W. Hell, *Far-field optical nanoscopy.* Science, 316(5828):1153–1158, 2007.

[89] G. Vicidomini, P. Bianchini, and A. Diaspro, *STED super-resolved microscopy.* Nat. Methods, 15(3):173–182, 2018.

[90] T. A. Klar, S. Jakobs, M. Dyba, A. Egner, and S. W. Hell, *Fluorescence microscopy with diffraction resolution barrier broken by stimulated emission.* Proc. Natl. Acad. Sci. U.S.A., 97(15):8206–8210, 2000.

[91] D. Wildanger, R. Medda, L. Kastrup, and S. W. Hell, *A compact sted microscope providing 3d nanoscale resolution.* J. Microsc., 236:35–43, 2009.

[92] B. Harke, C. K. Ullal, J. Keller, and S. W. Hell, *Three-dimensional nanoscopy of colloidal crystals.* Nano Lett., 8(5):1309–1313, 2008.

[93] S. Deng, L. Liu, Y. Cheng, R. Li, and Z. Xu, *Effects of primary abberations on the fluorescence depletion patterns of sted microscopy.* Opt. Express, 18:1657–1666, 2010.

[94] B. R. Patton, D. Burke, D. Owald, T. J. Gould, J. Bewersdorf, and M. J. Booth, *Three-dimensional sted microscopy of aberrating tissue using dual adaptive optics.* Opt. Express, 24(8):8862–8876, 2016.

[95] J. Antonello, D. Burke, and M. J. Booth, *Aberrations in stimulated emission depletion (sted) microscopy*. Opt. Commun., 404:203–209, 2017.

[96] N. T. Urban, K. I. Willig, S. W. Hell, and U. V. Nägerl, *Sted nanoscopy of actin dynamics in synapses deep inside living brain slices*. Biophys. J., 101:1277–1284, 2011.

[97] L. Holzer and M. Cantoni. *Nanofabrication Using Focused Ion and Electron Beams - Principles and Applications*, pages 410–435. Oxford University Press, New York, 2012.

[98] M. Cantoni and L. Holzer, *Advances in 3d focused ion beam tomography*. MRS Bulletin, 39(4):354–360, 2014.

[99] C. Hamon, M. N. Sanz-Ortiz, E. Modin, E. H. Hill, L. Scarabelli, A. Chuvilin, and L. M. Liz-Marzán, *Hierarchical organization and molecular diffusion in gold nanorod/silica supercrystal nanocomposites*. Nanoscale, 8:7914–7922, 2016.

[100] T. Altantzis, D. Zanaga, and S. Bals, *Advanced electron tomography of nanoparticle assemblies*. EPL, 119(3):38001, 2017.

[101] H. Friedrich, C. J. Gommes, K. Overgaag, J. D. Meeldijk, W. H. Evers, B. de Nijs, M. P. Boneschanscher, P. E. de Jongh, A. J. Verkleij, K. P. de Jong, A. van Blaaderen, and D. Vanmaekelbergh, *Quantitative structural analysis of binary nanocrystal superlattices by electron tomography*. Nano Lett., 9(7):2719–2724, 2009.

[102] B. de Nijs, S. Dussi, F. Smallenburg, J. D. Meeldijk, D. J. Groenendijk, L. Filion, A. Imhof, A. van Blaaderen, and M. Dijkstra, *Entropy-driven formation of large icosahedral colloidal clusters by spherical confinement*. Nat. Mater., 14(1):56–60, 2015.

[103] D. Zanaga, F. Bleichrodt, T. Altantzis, N. Winckelmans, W. J. Palenstijn, J. Sijbers, B. de Nijs, M. A. van Huis, A. Sánchez-Iglesias, L. M. Liz-Marzán, et al., *Quantitative 3d analysis of huge nanoparticle assemblies*. Nanoscale, 8(1):292–299, 2016.

[104] D. Wang. *Quantitative real-space analysis of colloidal supraparticles self-assembled from monodisperse nanoparticles*. PhD thesis, Utrecht University, 2018.

[105] J. C. Crocker and D. G. Grier, *Methods of digital video microscopy for colloidal studies*. J. Colloid Interface Sci., 179(1):298–310, 1996.

[106] E. Weeks and J. Crocker. *Particle tracking using IDL*, 2018. http://www.physics.emory.edu/faculty/weeks/idl/.

[107] D. B. Allan, T. Caswell, N. C. Keim, and C. M. van der Wel. *trackpy: Trackpy v0.4.1*, 2018. https://doi.org/10.5281/zenodo.1226458.

[108] D. Blair and E. Dufresne. *The matlab particle tracking code repository*, 2018. http://site.physics.georgetown.edu/matlab/.

[109] T. Caswell. *Particle identification and tracking*, 2018. http://tacaswell.github.io/tracking/html/.

[110] U. Dassanayake, S. Fraden, and A. van Blaaderen, *Structure of electrorheological fluids*. J. Chem. Phys., 112(8):3851–3858, 2000.

[111] A. D. Dinsmore, E. R. Weeks, V. Prasad, A. C. Levitt, and D. A. Weitz, *Three-dimensional confocal microscopy of colloids*. Appl. Opt., 40(24):4152–4159, 2001.

[112] B. D. Leahy, N. Y. Lin, and I. Cohen, *Quantitative light microscopy of dense suspensions: Colloid science at the next decimal place*. Curr. Opin. Colloid Interface Sci., 34:32–46, 2018.

[113] M. Jenkins and S. Egelhaaf, *Confocal microscopy of colloidal particles: Towards reliable, optimum coordinates*. Adv. Colloid Interface Sci., 136(1):65–92, 2008.

[114] Y. Gao and M. L. Kilfoi, *Accurate detection and complete tracking of large populations of features in three dimensions*. Opt. Express, 17(6):4685–4704, 2009.

[115] M. Leocmach and H. Tanaka, *A novel particle tracking method with individual particle size measurement and its application to ordering in glassy hard sphere colloids*. Soft Matter, 9:1447–1457, 2013.

[116] P. J. Lu, M. Shutman, E. Sloutskin, and A. V. Butenko, *Locating particles accurately in microscope images requires image-processing kernels to be rotationally symmetric*. Opt. Express, 21(25):30755–30763, 2013.

[117] K. E. Jensen and N. Nakamura, *Note: An iterative algorithm to improve colloidal particle locating*. Rev. Sci. Instrum., 87(6):066103, 2016.

[118] M. Bierbaum, B. D. Leahy, A. A. Alemi, I. Cohen, and J. P. Sethna, *Light microscopy at maximal precision*. Phys. Rev. X, 7:041007, 2017.

[119] B. D. Leahy, M. Bierbaum, J. Sethna, and I. Cohen, *Biases in particle localization algorithms*. ArXiv e-prints, 2018. arXiv:1801.03581v2.

[120] A. Mohraz and M. J. Solomon, *Direct visualization of colloidal rod assembly by confocal microscopy*. Langmuir, 21(12):5298–5306, 2005.

[121] Y. Han, A. M. Alsayed, M. Nobili, J. Zhang, T. C. Lubensky, and A. G. Yodh, *Brownian motion of an ellipsoid*. Science, 314(5799):626–630, 2006.

[122] G. L. Hunter, K. V. Edmond, M. T. Elsesser, and E. R. Weeks, *Tracking rotational diffusion of colloidal clusters*. Opt. Express, 19(18):17189–17202, 2011.

[123] T. H. Besseling, M. Hermes, A. Kuijk, B. de Nijs, T. S. Deng, M. Dijkstra, A. Imhof, and A. van Blaaderen, *Determination of the positions and orientations of concentrated rod-like colloids from 3D microscopy data*. J. Phys. Condens. Matter, 27(19):194109, 2015.

[124] J. Roller, P. Pfleiderer, J.-M. Meijer, and A. Zumbusch, *Detection and tracking of anisotropic core-shell colloids*. J. Phys.: Condens. Matter, 30(39):395903, 2018.

[125] D. Wang, M. Hermes, R. Kotni, Y. Wu, N. Tasios, Y. Liu, B. de Nijs, E. B. van der Wee, C. B. Murray, and A. van Blaaderen, *Interplay between spherical confinement and particle shape on the self-assembly of rounded cubes*. Nat. Commun., 9(2228):2041–1723, 2018.

[126] F. Montanarella, T. Altantzis, D. Zanaga, F. T. Rabouw, S. Bals, P. Baesjou, D. Vanmaekelbergh, and A. van Blaaderen, *Composite supraparticles with tunable light emission*. ACS Nano, 11(9):9136–9142, 2017.

[127] L. M. Liz-Marzán and P. V. Kamat. *Nanoscale Materials*. Kluwer Academic Publishers, 2003.

[128] Y. Kang, X. Ye, J. Chen, L. Qi, R. E. Diaz, V. Doan-Nguyen, G. Xing, C. R. Kagan, J. Li, R. J. Gorte, E. A. Stach, and C. B. Murray, *Engineering catalytic contacts and thermal stability: Gold/iron oxide binary nanocrystal superlattices for co oxidation*. J. Am. Chem. Soc., 135(4):1499–1505, 2013.

[129] A. Ivlev, H. Löwen, G. Morfill, and C. P. Royall. *Complex Plasmas and Colloidal Dispersions: Particle-Resolved Studies of Classical Liquids and Solids*. Series in Soft Condensed Matter. World Scientific, 2012.

[130] V. J. Anderson and H. N. W. Lekkerkerker, *Insights into phase transition kinetics from colloid science*. Nature, 416(6883):811–815, 2002.

[131] A. van Blaaderen, R. Ruel, and P. Wiltzius, *Template-directed colloidal crystallization.* Nature, 385(6614):321–323, 1997.

[132] A. D. Dinsmore and D. A. Weitz, *Direct imaging of three-dimensional structure and topology of colloidal gels.* J. Phys. Condens. Matter, 14(33):7581, 2002.

[133] E. R. Weeks and D. A. Weitz, *Properties of Cage Rearrangements Observed near the Colloidal Glass Transition.* Phys. Rev. Lett., 89(9):095704, 2002.

[134] A. M. Alsayed, M. F. Islam, J. Zhang, P. J. Collings, and A. G. Yodh, *Chemistry: Premelting at defects within bulk colloidal crystals.* Science, 309(5738):1207–1210, 2005.

[135] A. Kuijk, D. V. Byelov, A. V. Petukhov, A. van Blaaderen, and A. Imhof, *Phase behavior of colloidal silica rods.* Faraday Discuss., 159:181, 2012.

[136] P. Tan, N. Xu, and L. Xu, *Visualizing kinetic pathways of homogeneous nucleation in colloidal crystallization.* Nat. Phys., 10:73–79, 2014.

[137] Z. Wang, F. Wang, Y. Peng, Z. Zheng, and Y. Han, *Imaging the homogeneous nucleation during the melting of superheated colloidal crystals.* Science, 338(6103):87–90, 2012.

[138] F. Montanarella, J. J. Geuchies, T. Dasgupta, P. T. Prins, C. van Overbeek, R. Dattani, P. Baesjou, M. Dijkstra, A. V. Petukhov, A. van Blaaderen, and D. Vanmaekelbergh, *Crystallization of nanocrystals in spherical confinement probed by in situ x-ray scattering.* Nano Lett., 18(6):3675–3681, 2018.

[139] A. V. Petukhov, J.-M. Meijer, and G. J. Vroege, *Particle shape effects in colloidal crystals and colloidal liquid crystals: Small-angle x-ray scattering studies with microradian resolution.* Curr. Opin. Colloid Interface Sci., 20(4):272 – 281, 2015.

[140] R. J. D. Tilley. *Defects in solids.* John Wiley & Sons, Inc., 2008.

[141] T. A. Waigh and C. Rau, *X-ray and neutron imaging with colloids.* Curr. Opin. Colloid Interface Sci., 17(1):13 – 22, 2012.

[142] J. Thieme, J. Niemeyer, P. Guttmann, T. Wilhein, D. Rudolph, and G. Schmahl. *X-ray microscopy studies of aqueous colloid systems.* In M. J. Schwuger and F. H. Haegel, editors, *Surfactants and Colloids in the Environment*, pages 135–138. Steinkopff, 1994.

[143] D. V. Byelov, J.-M. Meijer, I. Snigireva, A. Snigirev, L. Rossi, E. van den Pol, A. Kuijk, A. Philipse, A. Imhof, A. van Blaaderen, G. J. Vroege, and A. V. Petukhov, *In situ hard X-ray microscopy of self-assembly in colloidal suspensions.* RSC Adv., 3(36):15670, 2013.

[144] J. Hilhorst, M. M. van Schooneveld, J. Wang, E. de Smit, T. Tyliszczak, J. Raabe, A. P. Hitchcock, M. Obst, F. M. F. de Groot, and A. V. Petukhov, *Three-dimensional structure and defects in colloidal photonic crystals revealed by tomographic scanning transmission x-ray microscopy.* Langmuir, 28(7):3614–3620, 2012.

[145] A. G. Shabalin, J.-M. Meijer, R. Dronyak, O. M. Yefanov, A. Singer, R. P. Kurta, U. Lorenz, O. Y. Gorobtsov, D. Dzhigaev, S. Kalbfleisch, J. Gulden, A. V. Zozulya, M. Sprung, A. V. Petukhov, and I. A. Vartanyants, *Revealing three-dimensional structure of an individual colloidal crystal grain by coherent x-ray diffractive imaging.* Phys. Rev. Lett., 117:138002, 2016.

[146] F. M. F. de Groot, E. de Smit, M. M. van Schooneveld, L. R. Aramburo, and B. M. Weckhuysen, *In-situ scanning transmission x-ray microscopy of catalytic solids and related nanomaterials.* ChemPhysChem, 11(5):951–962, 2010.

[147] J. Wang, C. Morin, L. Li, A. P. Hitchcock, A. Scholl, and A. Doran, *Radiation damage in soft x-ray microscopy.* J. Electron. Spectrosc. Relat. Phenom., 170(1):25–36, 2009.

[148] S. Disch, E. Wetterskog, R. P. Hermann, G. Salazar-Alvarez, P. Busch, T. Brückel, L. Bergström, and S. Kamali, *Shape induced symmetry in self-assembled mesocrystals of iron oxide nanocubes.* Nano Lett., 11(4):1651–1656, 2011.

[149] S. van Aert, K. J. Batenburg, M. D. Rossell, R. Erni, and G. Van Tendeloo, *Three-dimensional atomic imaging of crystalline nanoparticles.* Nature, 470(7334):374–377, 2011.

[150] M. S. Elliot and W. C. K. Poon, *Conventional optical microscopy of colloidal suspensions.* Adv. Colloid Interface Sci., 92(1-3):133–194, 2001.

[151] A. van Blaaderen, A. Imhof, W. Hage, and A. Vrij, *Three-dimensional imaging of submicrometer colloidal particles in concentrated suspensions using confocal scanning laser microscopy.* Langmuir, 8(6):1514–1517, 1992.

[152] A. van Blaaderen, *Quantitative real-space analysis of colloidal structures and dynamics with confocal scanning light microscopy.* Prog. Colloid Polym. Sci., 104:59–65, 1997.

[153] N. Martini, J. Bewersdorf, and S. W. Hell, *A new high-aperture glycerol immersion objective lens and its application to 3d-fluorescence microscopy.* J. Microsc., 206(2):146–151, 2002.

[154] M. Hermes and A. van Blaaderen. *Determining the positions and orientations of non-spherical particles.* To be submitted.

[155] C. R. Perrey, C. B. Carter, J. R. Michael, P. G. Kotula, E. A. Stach, and V. R. Radmilovic, *Using the fib to characterize nanoparticle materials.* J. Microsc., 214(3):222–236, 2004.

[156] D. A. M. de Winter, F. Meirer, and B. M. Weckhuysen, *Fib-sem tomography probes the mesoscale pore space of an individual catalytic cracking particle.* ACS Catal., 6(5):3158–3167, 2016.

[157] J. W. Galusha, M. R. Jorgensen, and M. H. Bartl, *Diamond-structured titania photonic-bandgap crystals from biological templates.* Adv. Mater., 22(1):107–110, 2009.

[158] K. Narayan and S. Subramaniam, *Focused ion beams in biology.* Nat. Methods, 12(11):1021–1031, 2015.

[159] D. A. M. de Winter, C. T. W. M. Schneijdenberg, M. N. Lebbink, B. Lich, A. J. Verkleij, M. R. Drury, and B. M. Humbel, *Tomography of insulating biological and geological materials using focused ion beam (fib) sectioning and low-kv bse imaging.* J. Microsc., 233(3):372–383, 2009.

[160] Y. Liu, H. E. King, M. A. van Huis, M. R. Drury, and O. Plümper, *Nano-tomography of porous geological materials using focused ion beam-scanning electron microscopy.* Minerals, 6(4):1–19, 2016.

[161] X. Ye, C. Zheng, J. Chen, Y. Gao, and C. B. Murray, *Using binary surfactant mixtures to simultaneously improve the dimensional tunability and monodispersity in the seeded growth of gold nanorods.* Nano Lett., 13(2):765–771, 2013.

[162] J. Turkevich, P. C. Stevenson, and J. Hillier, *A study of the nucleation and growth processes in the synthesis of colloidal gold.* Discuss. Faraday Soc., 11:55–75, 1951.

[163] I. Ojea-Jiménez, N. G. Bastús, and V. Puntes, *Influence of the sequence of the reagents addition in the citrate-mediated synthesis of gold nanoparticles.* J. Phys. Chem. C, 115(32):15752–15757, 2011.

[164] N. G. Bastús, J. Comenge, and V. Puntes, *Kinetically controlled seeded growth synthesis of citrate-stabilized gold nanoparticles of up to 200 nm: Size focusing versus ostwald ripening.* Langmuir, 27(17):11098–11105, 2011.

[165] C. Graf, D. L. J. Vossen, A. Imhof, and A. van Blaaderen, *A general method to coat colloidal particles with silica.* Langmuir, 19:6693–6700, 2003.

[166] K. Osseo-Asare and F. J. Arriagada, *Preparation of $SiO_2$ nanoparticles in a non-ionic reverse micellar system.* Colloids and Surf., 50:321–339, 1990.

[167] A. van Blaaderen and A. P. M. Kentgens, *Particle morphology and chemical microstructure of colloidal silica spheres made from alkoxysilanes.* J. Non-Cryst. Solids, 149(3):161–178, 1992.

[168] W. Stöber, A. Fink, and E. Bohn, *Controlled growth of monodisperse silica spheres in the micron size range.* J. Colloid Interface Sci., 69:62–69, 1968.

[169] H. Giesche, *Synthesis of monodispersed silica powders i. particle properties and reaction kinetics.* J. Eur. Ceram. Soc., 14(3):189–204, 1994.

[170] H. Giesche, *Synthesis of monodispersed silica powders ii. controlled growth reaction and continuous production process.* J. Eur. Ceram. Soc., 14(3):205–214, 1994.

[171] A. Van Blaaderen and A. Vrij, *Synthesis and characterization of colloidal dispersions of fluorescent, monodisperse silica spheres.* Langmuir, 8(12):2921–2931, 1992.

[172] P. Jiang, J. F. Bertone, K. S. Hwang, and V. L. Colvin, *Single-crystal colloidal multilayers of controlled thickness.* Chem. Mat., 11(8):2132–2140, 1999.

[173] J.-M. Meijer, F. Hagemans, L. Rossi, D. V. Byelov, S. I. Castillo, A. Snigirev, I. Snigireva, A. P. Philipse, and A. V. Petukhov, *Self-assembly of colloidal cubes via vertical deposition.* Langmuir, 28(20):7631–7638, 2012.

[174] C. Messaoudi, T. Boudier, C. Sanchez Sorzano, and S. Marco, *Tomoj: tomography software for three-dimensional reconstruction in transmission electron microscopy.* BMC Bioinform., 8:288, 2007.

[175] J. Illingworth and J. Kittler, *A survey of the hough transform.* Computer Vision, Graphics, and Image Processing, 44(1):87–116, 1988.

[176] P. J. Steinhardt, D. R. Nelson, and M. Ronchetti, *Bond-orientational order in liquids and glasses.* Phys. Rev. B, 28:784–805, 1983.

[177] P. R. ten Wolde, M. J. Ruiz-Montero, and D. Frenkel, *Numerical calculation of the rate of crystal nucleation in a Lennard-Jones system at moderate undercooling.* J. Chem. Phys., 104(24):9932–9947, 1996.

[178] W. Lechner and C. Dellago, *Accurate determination of crystal structures based on averaged local bond order parameters.* J. Chem. Phys., 129(11):114707, 2008.

[179] L. Landau and E. Lifschitz. *Quantum Mechanics.* Pergamon, London, 1965.

[180] C. Hamon, S. M. Novikov, L. Scarabelli, D. M. Solís, T. Altantzis, S. Bals, J. M. Taboada, F. Obelleiro, and L. M. Liz-Marzán, *Collective plasmonic properties in few-layer gold nanorod supercrystals.* ACS Photonics, 2(10):1482–1488, 2015.

[181] B. Liu, T. H. Besseling, M. Hermes, A. F. Demirörs, A. Imhof, and A. van Blaaderen, *Switching plastic crystals of colloidal rods with electric fields.* Nat. Commun., 5:3092, 2014.

[182] B. Liu, T. H. Besseling, A. van Blaaderen, and A. Imhof, *Confinement induced plastic crystal-to-crystal transitions in rodlike particles with long-ranged repulsion.* Phys. Rev. Lett., 115:078301, 2015.

[183] J. P. Hoogenboom, P. Vergeer, and A. van Blaaderen, *A real-space analysis of colloidal crystallization in a gravitational field at a flat bottom wall.* J. Chem. Phys., 119(6):3371–3383, 2003.

[184] J. H. J. Thijssen. *Characterization of photonic colloidal crystals in real and reciprocal space.* PhD thesis, Utrecht University, 2007. available at www.colloid.nl.

[185] C. P. Royall, E. C. M. Vermolen, A. van Blaaderen, and H. Tanaka, *Controlling competition between crystallization and glass formation in binary colloids with an external field.* J. Phys. Condens. Matter, 20(40):404225, 2008.

[186] T. H. Loeber, B. Laegel, S. Wolff, S. Schuff, F. Balle, T. Beck, D. Eifler, J. H. Fitschen, and G. Steidl, *Reducing curtaining effects in fib/sem applications by a goniometer stage and an image processing method.* J. Vac. Sci. Technol. B, 35(6):06GK01, 2017.

[187] D. Wang, M. Hermes, S. Najmr, N. Tasios, Y. Liu, M. Dijkstra, C. B. Murray, and A. van Blaaderen. *Quantitative real-space analysis of supraparticles composed of nanoplatelets.* To be submitted.

[188] D. Wang, Y. Wu, M. Hermes, Y. Liu, C. B. Murray, and A. van Blaaderen. *Cation exchange reaction on self-assembled supraparticles.* To be submitted.

[189] W. V. den Broek, A. Rosenauer, B. Goris, G. Martinez, S. Bals, S. V. Aert, and D. V. Dyck, *Correction of non-linear thickness effects in haadf stem electron tomography.* Ultramicroscopy, 116:8–12, 2012.

[190] N. A. Elbers, J. E. S. van der Hoeven, D. A. M. de Winter, C. T. W. M. Schneijdenberg, M. N. van der Linden, L. Filion, and A. van Blaaderen, *Repulsive van der waals forces enable pickering emulsions with non-touching colloids.* Soft Matter, 12:7265–7272, 2016.

[191] M. Booth, D. Andrade, D. Burke, B. Patton, and M. Zurauskas, *Abberations and adaptive optics in super-resolution microscopy.* Microscopy, 64:251–261, 2015.

[192] Y. Li, M. Mund, P. Hoess, J. Deschamps, U. Matti, B. Nijmeijer, V. J. Sabinina, J. Ellenberg, I. Schoen, and J. Ries, *Real-time 3d single-molecule localization using experimental point spread functions.* Nat. Methods, 15:367–369, 2018.

[193] F. R. Boddeke, L. J. van Vliet, and I. T. Young, *Calibration of the automated z-axis of a microscope using focus functions.* J. Microsc., 186:270–274, 1997.

[194] H. Bornfleth, K. Sätzler, E. R., and C. Cremer, *High-precision distance measurements and volume-conserving segmentation of objects near and below the resolution limit in three-dimensional confocal fluorescence microscopy.* J. Microsc., 189:118–136, 1998.

[195] K. E. Jensen, D. A. Weitz, and F. Spaepen, *A three-dimensional calibration device for the confocal microscope.* Rev. Sci. Instrum., 84:016018, 2013.

[196] P. F. G. Rodríguez, Y. Wu, H. Singh, H. Zhao, L. Toro, and E. Stefani. *Current Microscopy Contributions to Advances in Science and Technology*, pages 791–800. Formatex Research Center, Badajoz, Spain, 2012.

[197] J. J. Schmied, M. Raab, C. Forthmann, E. Pibiri, B. Wünsch, T. Dammeyer, and P. Tinnefeld, *Dna origami–based standards for quantitative fluorescence microscopy.* Nat. Protoc., 9:1367–1391, 2014.

[198] F. Göttfert, T. Pleiner, J. Heine, V. Westphal, D. Görlich, S. J. Sahl, and S. W. Hell, *Strong signal increase in sted fluorescence microscopy by imaging regions of subdiffraction extent.* Proc. Natl. Acad. Sci. U.S.A., 114:2125–2130, 2017.

[199] J. Hanne, H. J. Falk, F. Görlitz, P. Hoyer, J. Engelhardt, S. J. Sahl, and S. W. Hell, *Sted nanoscopy with fluorescent quantum dots.* Nat. Commun., 6:7127, 2015.

[200] X. Yang, K. Zhanghao, H. Wang, Y. Liu, F. Wang, X. Zhang, K. Shi, J. Gao, D. Jin, and P. Xi, *Versatile application of fluorescent quantum dot labels in super-resolution fluorescence microscopy.* ACS Photonics, 3:1611–1618, 2016.

[201] C. Fouquet, J.-F. Gilles, N. Heck, M. Dos Santos, R. Schwartzmann, V. Cannaya, M.-P. Morel, R. S. Davidson, A. Trembleau, and S. Bolte, *Improving axial resolution in confocal microscopy with new high refractive index mounting media.* PLoS One, 10:1–17, 2015.

[202] F. J. Arriagada and K. Osseo-Asare, *Synthesis of nanosize silica in a nonionic water-in-oil microemulsion: Effects of the water/surfactant molar ratio and ammonia concentration.* J. Colloid Interface Sci., 211:210–220, 1999.

[203] A. Imhof, M. Megens, J. J. Engelberts, D. T. N. de Lang, R. Sprik, and W. L. Vos, *Spectroscopy of fluorescein (fitc) dyed colloidal silica spheres.* J. Phys. Chem. B, 103, 1999.

[204] N. A. M. Verhaegh and A. van Blaaderen, *Dispersions of rhodamine-labeled silica spheres: synthesis, characterization, and fluorescence confocal scanning laser microscopy.* Langmuir, 96:1427–1438, 1994.

[205] R. Koole, M. M. van Schooneveld, J. Hilhorst, C. de Mello Donegá, D. C. 't Hart, A. van Blaaderen, D. Vanmaekelbergh, and A. Meijerink, *On the incorporation mechanism of hydrophobic quantum dots in silica spheres by a reverse microemulsion method.* Chem. Mater., 20:2503–2512, 2008.

[206] F. A. Jenkins and H. E. White. *Fundamentals of Optics.* McGraw Hill Education, 1976.

[207] S. Wiederseiner, N. Andreini, G. Epely-Chauvin, and C. Ancey, *Refractive-index and density matching in concentrated particle suspensions: A review.* Exp. Fluids, 50(5):1183–1206, 2011.

[208] F. García-Santamaria, H. Míguez, M. Ibisate, F. Meseguer, and C. López, *Refractive index properties of calcined silica submicrometer spheres.* Langmuir, 18:1942–1944, 2002.

[209] R. G. Lebel and D. A. I. Goring, *Density, Viscosity, Refractive Index, and Hygroscopicity of Mixtures of Water and Dimethyl Sulfoxide.* J. Chem. Eng. Data, 7(1):100–101, 1962.

[210] V. Alonso, J. A. González, I. G. de la Fuente, and J. C. Cobos, *Dielectric and refractive index measurements for the systems 1-pentanol+2,5,8,11,14-pentaoxapentadecane, or for 2,5,8,11,14-pentaoxapentadecane+octane at (293.15–303.15)k.* Thermochim. Acta, 551:70–77, 2013.

[211] J. Zhang, H. Liu, Z. Wang, and N. Ming, *Assembly of high-quality colloidal crystals under negative pressure.* J. Appl. Phys., 103:8–12, 2008.

[212] S. Wong, V. Kitaev, and G. A. Ozin, *Colloidal crystal films: advances in universality and perfection.* J. Am. Chem. Soc., 125:15589–15598, 2003.

[213] J. Schindelin, I. Arganda-Carreras, E. Frise, V. Kaynig, M. Longair, T. Pietzsch, S. Preibisch, C. Rueden, S. Saalfeld, B. Schmid, J. Y. Tinevez, D. J. White, V. Hartenstein, K. Eliceiri, P. Tomancak, and A. Cardona, *Fiji: an open-source platform for biological-image analysis.* Nat. Methods, 9:676–682, 2012.

[214] M. D. Uchic, L. Holzer, B. J. Inkson, E. L. Principe, and P. Munroe, *Three-dimensional microstructural characterization using focused ion beam tomography.* MRS Bull., 32:408–416, 2007.

[215] C. A. Volkert and A. M. Minor, *Focused ion beam microscopy and micromachining.* MRS Bull., 32:389–399, 2007.

[216] M. Mačković, F. Niekiel, L. Wondraczek, and E. Spiecker, *Direct observation of electron-beam-induced densification and hardening of silica nanoballs by in situ transmission electron microscopy and finite element method simulations.* Acta Mater., 79:363–373, 2014.

[217] S. Hell, G. Reiner, C. Cremer, and E. H. K. Stelzer, *Aberrations in confocal fluorescence microscopy induced by mismatches in refractive index.* J. of Microsc., 169:391–405, 1993.

[218] S. W. Bea, W. Tan, and J. I. Hong, *Fluorescent dye-doped silica nanoparticles: new tools for bioapplications.* Chem. Commun., 48:2270–2282, 2012.

[219] R. P. Bagwe, C. Yang, H. L. R., and W. Tan, *Optimization of dye-doped silica nanoparticles prepared using a reverse microemulsion method.* Langmuir, 20:8336–8342, 2004.

[220] T. Wang, X. Wang, D. LaMontagne, Z. Wang, Z. Wang, and Y. C. Cao, *Shape-controlled synthesis of colloidal superparticles from nanocubes.* J. Am. Chem. Soc., 134(44):18225–18228, 2012.

[221] X. Zhao, R. Bagwe, and W. Tan, *Development of organic-dye-doped silica nanoparticles in a reverse microemulsion.* Adv. Mater., 16:173–176, 2004.

[222] R. Boonsin, G. Chadeyron, J. Roblin, D. Boyer, and R. Mahiou, *Silica encapsulated fluorescein as a hybrid dye for blue-led based lighting devices.* J. Mater. Chem. C, 4:6562, 2016.

[223] O. Tovmachenko, C. Graf, D. van den Heuvel, A. van Blaaderen, and H. C. Gerritsen, *Fluorescence enhancement by metal-core/silica-shell nanoparticles.* Adv. Mater., 18:91–95, 2006.

[224] N. T. Urban, M. R. Foreman, S. W. Hell, and Y. Sivan, *Nanoparticle-assisted sted nanoscopy with gold nanospheres.* ACS Photonics, 5:2574–2583, 2018.

[225] C. de Mello Donegá, *Synthesis and properties of colloidal heteronanocrystals.* Chem. Soc. Rev, 40:1512–1546, 2011.

[226] M. Darbandi, R. Rhoman, and T. Nann, *Single quantum dots in silica spheres by microemulsion synthesis.* Chem. Mater., 17:5720–5725, 2005.

[227] B. G. Jeong, Y.-S. Park, J. H. Chang, I. Cho, J. K. Kim, H. Kim, K. Char, J. Cho, V. I. Klimov, P. Park, D. C. Lee, and W. K. Bae, *Colloidal spherical quantum wells with near-unity photoluminescence quantum yield and suppressed blinking.* ACS Nano, 10:9297–9305, 2016.

[228] N. Wang, S. Koh, B. G. Jeong, D. Lee, K. W. D., K. Park, M. K. Nam, K. Lee, Y. Kim, B. H. Lee, K. Lee, W. K. Bae, and D. C. Lee, *Highly luminescent silica-coated cds/cdse/cds nanoparticles with strong chemical robustness and excellent thermal stability.* Nanotechnology, 28:185603, 2017.

[229] D. Jin, P. Xi, B. Wang, L. Zhang, J. Enderlein, and A. M. van Oijen, *Nanoparticles for super-resolution microscopy and single-molecule tracking.* Nat. Methods, 15:415–423, 2018.

[230] Y.-K. Tzeng, O. Faklaris, B.-M. Chang, Y. Kuo, J. H. Hsu, and H.-C. Chang, *Superresolution imaging of albumin-conjugated fluorescent nanodiamonds in cells by stimulated emission depletion.* Angew. Chem. Int. Ed., 50:2262–2265, 2011.

[231] Y. Liu, Y. Lu, X. Yang, X. Zheng, S. Wen, F. Wang, X. Vidal, J. Zhao, D. Liu, Z. Zhou, C. Ma, J. Zhou, J. A. Piper, P. Xi, and D. Jin, *Amplified stimulated emission in upconversion nanoparticles for super-resolution nanoscopy.* Nature, 543:229–233, 2017.

[232] G. Leménager, E. De Luca, Y.-P. Sun, and P. P. Pompa, *Super-resolution fluorescence imaging of biocompatible carbon dots.* Nanoscale, 6:8617–8623, 2014.

[233] A. Bumb, S. K. Sarkar, N. Billington, M. W. Brechbiel, and K. C. Neuman, *Silica encapsulation of fluorescent nanodiamonds for colloidal stability and facile surface functionalization.* J. Am. Chem. Soc., 135:7815–7818, 2013.

[234] H. S. Qian, H. C. Guo, P. C.-L. Ho, R. Mahendran, and Y. Zhang, *Mesoporous-silica-coated up-conversion fluorescent nanoparticles for photodynamic therapy.* Small, 5:2285–2290, 2009.

[235] Y. Lin, C. Wang, L. Li, H. Wang, K. Liu, K. Wang, and B. Li, *Tunable fluorescent silica-coated carbon dots: A synergistic effect for enhancing the fluorescence sensing of extracellular cu$^{2+}$ in rat brain.* ACS Appl. Mater. Interfaces, 7:27262–27270, 2015.

[236] A. F. Demirörs, A. Jannasch, P. D. J. van Oostrum, E. Schäffer, A. Imhof, and A. van Blaaderen, *Seeded growth of titania colloids with refractive index tunability and fluorophore-free luminescence.* Langmuir, 27:1626–1634, 2011.

[237] A. Jannasch, A. F. Demirörs, P. D. J. van Oostrum, A. van Blaaderen, and E. Schäffer, *Nanonewton optical force trap employing anti-reflection coated, high-refractive-index titania microspheres.* Nat. Photon., 6:469–473, 2012.

[238] A. F. Demirörs, A. van Blaaderen, and A. Imhof, *Synthesis of eccentric titania-silica core-shell and composite particles.* Chem. Mater., 21:979–984, 2009.

[239] J. P. Hoogenboom, C. Rétif, E. de Bres, M. van de Boer, A. K. van Langen-Suurling, J. Romijn, and A. van Blaaderen, *Template-induced growth of close-packed and non-close-packed colloidal crystals during solvent evaporation.* Nano Lett., 4:205–208, 2004.

[240] M. Minsky, *Memoir on inventing the confocal scanning microscope.* Scanning, 10(4):128–138, 1988.

[241] W. Amos and J. White, *How the confocal laser scanning microscope entered biological research.* Biol. Cell, 95(6):335–342, 2003.

[242] T. Lee, B. Senyuk, R. P. Trivedi, and I. I. Smalyukh. *Optical Microscopy of Soft Matter Systems*, pages 165–185. John Wiley & Sons, Inc., 2016.

[243] A. van Blaaderen, A. Imhof, W. Hage, and A. Vrij, *Three-dimensional imaging of submicrometer colloidal particles in concentrated suspensions using confocal scanning laser microscopy.* Langmuir, 8(6):1514–1517, 1992.

[244] M. E. Leunissen, C. G. Christova, A.-P. Hynninen, C. P. Royall, A. I. Campbell, A. Imhof, M. Dijkstra, R. van Roij, and A. van Blaaderen, *Ionic colloidal crystals of oppositely charged particles.* Nature, 437(6251):235–240, 2005.

[245] R. P. A. Dullens, D. G. A. L. Aarts, and W. K. Kegel, *Direct measurement of the free energy by optical microscopy.* Proc. Natl. Acad. Sci. U.S.A., 103(3):529–531, 2006.

[246] P. Schall, D. A. Weitz, and F. Spaepen, *Structural rearrangements that govern flow in colloidal glasses.* Science, 318(5858):1895–1899, 2007.

[247] J. Brujić, C. Song, P. Wang, C. Briscoe, G. Marty, and H. A. Makse, *Measuring the coordination number and entropy of a 3d jammed emulsion packing by confocal microscopy.* Phys. Rev. Lett., 98:248001, 2007.

[248] E. M. Herzig, K. A. White, A. B. Schofield, W. C. K. Poon, and P. S. Clegg, *Bicontinuous emulsions stabilized solely by colloidal particles.* Nat. Mater., 6(12):966–971, 2007.

[249] L. Li, S. Sosnowski, C. E. Chaffey, S. T. Balke, and M. A. Winnik, *Surface morphology of a polymer blend examined by laser confocal fluorescence microscopy.* Langmuir, 10(8):2495–2497, 1994.

[250] S. Fransson, O. Peleg, N. Lorén, A.-M. Hermansson, and M. Kröger, *Modelling and confocal microscopy of biopolymer mixtures in confined geometries.* Soft Matter, 6:2713–2722, 2010.

[251] E. Manders, J. Stap, G. Brakenhoff, R. van Driel, and J. Aten, *Dynamics of three-dimensional replication patterns during the s-phase, analysed by double labelling of dna and confocal microscopy.* J. Cell Sci., 103(3):857–862, 1992.

[252] I. Viola, I. E. Palama, A. M. L. Coluccia, M. Biasiucci, B. Dozza, E. Lucarelli, F. Di Maria, G. Barbarella, and G. Gigli, *Physiological formation of fluorescent and conductive protein microfibers in live fibroblasts upon spontaneous uptake of biocompatible fluorophores.* Integr. Biol., 5:1057–1066, 2013.

[253] S. Mohan, J. Jose, A. Kuijk, S. J. Veen, A. van Blaaderen, and K. P. Velikov, *Revealing and quantifying the three-dimensional nano- and microscale structures in self-assembled cellulose microfibrils in dispersions.* ACS Omega, 2(8):5019–5024, 2017.

[254] I. Lelidis, C. Blanc, and M. Kléman, *Optical and confocal microscopy observations of screw dislocations in smectic-a liquid crystals.* Phys. Rev. E, 74:051710, 2006.

[255] K. Higashiguchi, K. Yasui, and H. Kikuchi, *Direct observation of polymer-stabilized blue phase i structure with confocal laser scanning microscope.* J. Am. Chem. Soc., 130(20):6326–6327, 2008.

[256] T. Wilson, *Techniques of optical scanning microscopy.* J. Phys. E: Sci. Instrum., 22(8):532, 1989.

[257] M. Yamanaka, N. I. Smith, and K. Fujita, *Introduction to super-resolution microscopy.* Microscopy, 63(3):177–192, 2014.

[258] O. Nevskyi, D. Sysoiev, A. Oppermann, T. Huhn, and D. Wöll, *Nanoscopic visualization of soft matter using fluorescent diarylethene photoswitches.* Angew. Chem. Int. Ed., 55(41):12698–12702, 2016.

[259] T. H. Besseling, M. Hermes, A. Fortini, M. Dijkstra, A. Imhof, and A. van Blaaderen, *Oscillatory shear-induced 3d crystalline order in colloidal hard-sphere fluids.* Soft Matter, 8:6931–6939, 2012.

[260] C. P. Royall, R. van Roij, and A. van Blaaderen, *Extended sedimentation profiles in charged colloids: The gravitational length, entropy, and electrostatics.* J. Phys. Condens. Matter, 17(15):2315–2326, 2005.

[261] J. Goodwin. *Colloids and Interfaces with Surfactants and Polymers.* Wiley, 2009.

[262] M. Kogan, C. J. Dibble, R. E. Rogers, and M. J. Solomon, *Viscous solvent colloidal system for direct visualization of suspension structure, dynamics and rheology.* J. Colloid Interface Sci., 318(2):252–263, 2008.

[263] L. T. Shereda, R. G. Larson, and M. J. Solomon, *Local stress control of spatiotemporal ordering of colloidal crystals in complex flows.* Phys. Rev. Lett., 101:038301, 2008.

[264] L. T. Shereda, R. G. Larson, and M. J. Solomon, *Boundary-driven colloidal crystallization in simple shear flow.* Phys. Rev. Lett., 105:228302, 2010.

[265] S. L. Gawali, M. Zhang, S. Kumar, V. K. Aswal, D. Danino, and P. A. Hassan, *Dynamically arrested micelles in a supercooled sugar urea melt.* Commun. Chem., 1:1, 2018.

[266] P. Jiang and M. J. McFarland, *Large-scale fabrication of wafer-size colloidal crystals, macroporous polymers and nanocomposites by spin-coating.* J. Am. Chem. Soc., 126(42):13778–13786, 2004.

[267] Y.-L. Wu. *Control over colloidal crystallization by shear and electric fields.* PhD thesis, Utrecht University, 2007.

[268] S. H. Kim, J. G. Park, T. M. Choi, V. N. Manoharan, and D. A. Weitz, *Osmotic-pressure-controlled concentration of colloidal particles in thin-shelled capsules.* Nat. Commun., 5:3068, 2014.

[269] J.-G. Park, S.-H. Kim, S. Magkiriadou, T. M. Choi, Y.-S. Kim, and V. N. Manoharan, *Full-spectrum photonic pigments with non-iridescent structural colors through colloidal assembly.* Angew. Chem. Int. Ed., 53(11):2899–2903, 2014.

[270] J. Ge, L. He, J. Goebl, and Y. Yin, *Assembly of magnetically tunable photonic crystals in nonpolar solvents.* J. Am. Chem. Soc., 131(10):3484–3486, 2009.

[271] W. M. Heston, E. J. Hennelly, and C. P. Smyth, *Dielectric constants, viscosities, densities, refractive indices and dipole moment calculations for some organic halides.* J. Am. Chem. Soc., 72(5):2071–2075, 1950.

[272] R. W. Crowe and C. P. Smyth, *The dielectric and polymorphic behavior of cyclohexanol, cyclohexanone, chlorocyclohexane and cyclohexane.* J. Am. Chem. Soc., 73(11):5406–5411, 1951.

[273] D. El Masri, T. Vissers, S. Badaire, J. C. P. Stiefelhagen, H. R. Vutukuri, P. Helfferich, T. H. Zhang, W. K. Kegel, A. Imhof, and A. van Blaaderen, *A qualitative confocal microscopy study on a range of colloidal processes by simulating microgravity conditions through slow rotations.* Soft Matter, 8:6979–6990, 2012.

[274] S. R. Liber, G. Indech, E. B. van der Wee, A. V. Butenko, T. E. Kodger, P. J. Lu, A. B. Schofield, D. A. Weitz, A. van Blaaderen, and E. Sloutskin, *Axial confocal tomography of capillary-contained colloidal structures.* Langmuir, 33(46):13343–13349, 2017.

[275] P. Bartlett, P. N. Pusey, and R. H. Ottewill, *Colloidal crystallization under time-averaged zero gravity.* Langmuir, 7(2):213–215, 1991.

[276] G. Bosma, C. Pathmamanoharan, E. H. de Hoog, W. K. Kegel, A. van Blaaderen, and H. N. Lekkerkerker, *Preparation of monodisperse, fluorescent pmma-latex colloids by dispersion polymerization.* J. Colloid Interface Sci., 245(2):292–300, 2002.

[277] M. T. Elsesser and A. D. Hollingsworth, *Revisiting the synthesis of a well-known comb-graft copolymer stabilizer and its application to the dispersion polymerization of poly(methyl methacrylate) in organic media.* Langmuir, 26(23):17989–17996, 2010.

[278] A. Kuijk, A. van Blaaderen, and A. Imhof, *Synthesis of monodisperse, rodlike silica colloids with tunable aspect ratio.* J. Am. Chem. Soc., 133(8):2346–2349, 2011.

[279] A. Kuijk, A. Imhof, M. H. W. Verkuijlen, T. H. Besseling, E. R. H. van Eck, and A. van Blaaderen, *Colloidal silica rods: Material properties and fluorescent labeling.* Part. Part. Syst. Charact., 31(6):706–713, 2014.

[280] S. C. Ligon, B. Husár, H. Wutzel, R. Holman, and R. Liska, *Strategies to reduce oxygen inhibition in photoinduced polymerization.* Chem. Rev., 114(1):557–589, 2014.

[281] Y.-L. Wu, J. H. J. Brand, J. L. A. van Gemert, J. Verkerk, H. Wisman, A. van Blaaderen, and A. Imhof, *A new parallel plate shear cell for in situ real-space measurements of complex fluids under shear flow*. Rev. Sci. Instrum., 78(10):103902, 2007.

[282] P. R. ten Wolde, M. J. Ruiz-Montero, and D. Frenkel, *Numerical evidence for bcc ordering at the surface of a critical fcc nucleus*. Phys. Rev. Lett., 75:2714–2717, 1995.

[283] T. Savin and P. S. Doyle, *Static and dynamic errors in particle tracking microrheology*. Biophys. J., 88(1):623–638, 2005.

[284] J. W. Park, G. S. Shim, J. G. Lee, S. W. Jang, H. J. Kim, and J. N. Choi, *Evaluation of UV curing properties of mixture systems with differently sized monomers*. Materials, 11(4):509, 2018.

[285] H. R. Vutukuri, J. Stiefelhagen, T. Vissers, A. Imhof, and A. van Blaaderen, *Bonding assembled colloids without loss of colloidal stability*. Adv. Mater., 24(3):412–416, 2011.

[286] R. P. A. Dullens, D. Derks, A. van Blaaderen, and W. K. Kegel, *Monodisperse core-shell poly(methyl methacrylate) latex colloids*. Langmuir, 19(15):5963–5966, 2003.

[287] R. Piazza, *Settled and unsettled issues in particle settling*. Rep. Prog. Phys., 77(5):056602, 2014.

[288] C. Allain and M. Cloitre, *The effects of gravity on the aggregation and the gelation of colloids*. Adv. Colloid Interface Sci., 46:129–138, 1993.

[289] P. Bartlett and R. Ottewill, *Gravitational effects on the phase behaviour of dispersions*. Adv. Colloid Interface Sci., 50:39–50, 1994.

[290] J. Zhu, M. Li, R. Rogers, W. Meyer, R. H. Ottewill, W. B. Russel, and P. M. Chaikin, *Crystallization of hard-sphere colloids in microgravity*. Nature, 387(6636):883–885, 1997.

[291] S. Ketzetzi, J. Russo, and D. Bonn, *Crystal nucleation in sedimenting colloidal suspensions*. J. Chem. Phys., 148(6):064901, 2018.

[292] H. E. Bakker. *Directed assembly of colloidal rods, spheres and their mixtures*. PhD thesis, Utrecht University, 2017.

[293] H. Ding, C. Liu, H. Gu, Y. Zhao, B. Wang, and Z. Gu, *Responsive colloidal crystal for spectrometer grating*. ACS Photonics, 1(2):121–126, 2014.

[294] H. Yang and P. Jiang, *Large-scale colloidal self-assembly by doctor blade coating*. Langmuir, 26(16):13173–13182, 2010.

[295] P. J. Lu, J. C. Conrad, H. M. Wyss, A. B. Schofield, and D. A. Weitz, *Fluids of clusters in attractive colloids*. Phys. Rev. Lett., 96:028306, 2006.

[296] G. Wu, H. Cho, D. A. Wood, A. D. Dinsmore, and S. Yang, *Confined assemblies of colloidal particles with soft repulsive interactions*. J. Am. Chem. Soc., 139(14):5095–5101, 2017.

[297] B. Ackerson, *Shear induced order of hard sphere suspensions*. J. Phys. Condens. Mat., 2(S):SA389, 1990.

[298] D. Erdemir, A. Y. Lee, and A. S. Myerson, *Nucleation of crystals from solution: Classical and two-step models*. Acc. Chem. Res., 42(5):621–629, 2009.

[299] S. Karthika, T. K. Radhakrishnan, and P. Kalaichelvi, *A review of classical and nonclassical nucleation theories*. Cryst. Growth Des., 16(11):6663–6681, 2016.

[300] T. Palberg, *Crystallization kinetics of repulsive colloidal spheres*. J. Phys. Condens. Mat., 11(28):R323, 1999.

[301] R. P. Sear, *Nucleation: theory and applications to protein solutions and colloidal suspensions*. J. Phys. Condens. Mat., 19(3):033101, 2007.

[302] U. Gasser, *Crystallization in three- and two-dimensional colloidal suspensions*. J. Phys. Condens. Mat., 21(20):203101, 2009.

[303] P. J. Lu and D. A. Weitz, *Colloidal particles: Crystals, glasses, and gels*. Ann. Rev. Condens. Mat. Phys., 4(1):217–233, 2013.

[304] T. Palberg, *Crystallization kinetics of colloidal model suspensions: recent achievements and new perspectives*. J. Phys. Condens. Mat., 26(33):333101, 2014.

[305] D. M. Herlach, T. Palberg, I. Klassen, S. Klein, and R. Kobold, *Overview: Experimental studies of crystal nucleation: Metals and colloids*. J. Chem. Phys., 145(21):211703, 2016.

[306] Z. Cheng. *Colloidal Crystallization*, chapter 12, pages 203–248. Wiley-Blackwell, 2016.

[307] G. C. Sosso, J. Chen, S. J. Cox, M. Fitzner, P. Pedevilla, A. Zen, and A. Michaelides, *Crystal nucleation in liquids: Open questions and future challenges in molecular dynamics simulations*. Chem. Rev., 116:7078–116, 2016.

[308] R. P. Sear, *The non-classical nucleation of crystals: microscopic mechanisms and applications to molecular crystals, ice and calcium carbonate*. Int. Mater. Rev., 57(6):328–356, 2012.

[309] S. Auer and D. Frenkel. *Numerical Simulation of Crystal Nucleation in Colloids*, pages 149–208. Springer Berlin Heidelberg, Berlin, Heidelberg, 2005.

[310] P. N. Pusey, E. Zaccarelli, C. Valeriani, E. Sanz, W. C. K. Poon, and M. E. Cates, *Hard spheres: crystallization and glass formation*. Phil. Trans. R. Soc. A, 367(1909):4993–5011, 2009.

[311] M. Volmer and A. Weber, *Keimbildung in übersättigten gebilden*. Z. Phys. Chem., 119U(1):277–301, 1926.

[312] R. Becker and W. Döring, *Kinetische behandlung der keimbildung in übersättigten dämpfen*. Ann. Phys. (Berl.), 416(8):719–752, 1935.

[313] J. Frenkel, *A general theory of heterophase fluctuations and pretransition phenomena*. J. Chem. Phys., 7(7):538–547, 1939.

[314] P. G. Vekilov, *The two-step mechanism of nucleation of crystals in solution*. Nanoscale, 2:2346–2357, 2010.

[315] J. Russo and H. Tanaka, *Nonclassical pathways of crystallization in colloidal systems*. MRS Bull., 41(5):369–374, 2016.

[316] J. H. Hollomon and D. Turnbull, *Nucleation*. Prog. Metal Phys., 4:333–388, 1953.

[317] K. Iland, J. Wölk, R. Strey, and D. Kashchiev, *Argon nucleation in a cryogenic nucleation pulse chamber*. J. Chem. Phys., 127(15):154506, 2007.

[318] J. Taffs, S. R. Williams, H. Tanaka, and C. P. Royall, *Structure and kinetics in the freezing of nearly hard spheres*. Soft Matter, 9:297–305, 2013.

[319] N. Wood, J. Russo, F. Turci, and C. P. Royall, *Coupling of sedimentation and liquid structure: Influence on hard sphere nucleation*. J. Chem. Phys., 149(20):204506, 2018.

[320] J. Taffs and C. P. Royall, *The role of fivefold symmetry in suppressing crystallization*. Nat. Commun., 78:13225, 2016.

[321] J. K. G. Dhont, C. Smits, and H. N. W. Lekkerkerker, *A time resolved static light scattering study on nucleation and crystallization in a colloidal system.* J. Colloid Interface Sci., 152(2):386–401, 1992.

[322] R. Beyer, M. Franke, H. J. Schöpe, E. Bartsch, and T. Palberg, *From nuclei to microstructure in colloidal crystallization: Investigating intermediate length scales by small angle laser light scattering.* J. Chem. Phys., 143(6):064903, 2015.

[323] J. G. Kirkwood, E. K. Maun, and B. J. Alder, *Radial distribution functions and the equation of state of a fluid composed of rigid spherical molecules.* J. Chem. Phys., 18(8):1040–1047, 1950.

[324] A. Vrij, J. W. Jansen, J. K. G. Dhont, C. Pathmamanoharan, M. M. Kops-Werkhoven, and H. M. Fijnaut, *Light scattering of colloidal dispersions in non-polar solvents at finite concentrations. silica spheres as model particles for hard-sphere interactions.* Faraday Discuss. Chem. Soc., 76:19–35, 1983.

[325] M. D. Rintoul and S. Torquato, *Metastability and crystallization in hard-sphere systems.* Phys. Rev. Lett., 77:4198–4201, 1996.

[326] S. Auer and D. Frenkel, *Prediction of absolute crystal-nucleation rate in hard-sphere colloids.* Nature, 409(6823):1020, 2001.

[327] S. Auer and D. Frenkel, *Quantitative prediction of crystal-nucleation rates for spherical colloids: A computational approach.* Ann. Rev. Phys. Chem., 55(1):333–361, 2004.

[328] L. Filion, M. Hermes, R. Ni, and M. Dijkstra, *Crystal nucleation of hard spheres using molecular dynamics, umbrella sampling, and forward flux sampling: A comparison of simulation techniques.* J. Chem. Phys., 133(24):244115, 2010.

[329] J. Russo and H. Tanaka, *The microscopic pathway to crystallization in supercooled liquids.* Sci. Rep., 2:505, 2012.

[330] L. Filion, R. Ni, D. Frenkel, and M. Dijkstra, *Simulation of nucleation in almost hard-sphere colloids: The discrepancy between experiment and simulation persists.* J. Chem. Phys., 134(13):134901, 2011.

[331] T. Schilling, S. Dorosz, H. J. Schöpe, and G. Opletal, *Crystallization in suspensions of hard spheres: a monte carlo and molecular dynamics simulation study.* J. Phys. Condens. Mat., 23(19):194120, 2011.

[332] T. Schilling, H. J. Schöpe, M. Oettel, G. Opletal, and I. Snook, *Precursor-mediated crystallization process in suspensions of hard spheres.* Phys. Rev. Lett., 105:025701, 2010.

[333] J. T. Berryman, M. Anwar, S. Dorosz, and T. Schilling, *The early crystal nucleation process in hard spheres shows synchronised ordering and densification.* J. Chem. Phys., 145(21):211901, 2016.

[334] M. Radu and T. Schilling, *Solvent hydrodynamics speed up crystal nucleation in suspensions of hard spheres.* EPL, 105(2):26001, 2014.

[335] C. Valeriani, E. Sanz, P. N. Pusey, W. C. K. Poon, M. E. Cates, and E. Zaccarelli, *From compact to fractal crystalline clusters in concentrated systems of monodisperse hard spheres.* Soft Matter, 8:4960–4970, 2012.

[336] W. G. Hoover and F. H. Ree, *Melting transition and communal entropy for hard spheres.* J. Chem. Phys., 49(8):3609–3617, 1968.

[337] V. I. Kalikmanov. *Nucleation Theory*. Lecture Notes in Physics. Springer Netherlands, 2012.

[338] W. C. K. Poon, E. R. Weeks, and C. P. Royall, *On measuring colloidal volume fractions*. Soft Matter, 8:21–30, 2012.

[339] J. Russo, A. C. Maggs, D. Bonn, and H. Tanaka, *The interplay of sedimentation and crystallization in hard-sphere suspensions*. Soft Matter, 9:7369–7383, 2013.

[340] J. R. Savage and A. D. Dinsmore, *Experimental evidence for two-step nucleation in colloidal crystallization*. Phys. Rev. Lett., 102:198302, 2009.

[341] K. Kratzer and A. Arnold, *Two-stage crystallization of charged colloids under low supersaturation conditions*. Soft Matter, 11:2174–2182, 2015.

[342] M. Dijkstra, *Capillary freezing or complete wetting of hard spheres in a planar hard slit?* Phys. Rev. Lett., 93:108303, 2004.

[343] K. Sandomirski, E. Allahyarov, H. Löwen, and S. U. Egelhaaf, *Heterogeneous crystallization of hard-sphere colloids near a wall*. Soft Matter, 7:8050–8055, 2011.

[344] P. Wette, A. Engelbrecht, R. Salh, I. Klassen, D. Menke, D. M. Herlach, S. V. Roth, and H. J. Schöpe, *Competition between heterogeneous and homogeneous nucleation near a flat wall*. J. Phys. Condens. Mat., 21(46):464115, 2009.

[345] M. Franke, A. Lederer, and H. J. Schöpe, *Heterogeneous and homogeneous crystal nucleation in colloidal hard-sphere like microgels at low metastabilities*. Soft Matter, 7:11267–11274, 2011.

[346] V. W. A. de Villeneuve, R. P. A. Dullens, D. G. A. L. Aarts, E. Groeneveld, J. H. Scherff, W. K. Kegel, and H. N. W. Lekkerkerker, *Colloidal hard-sphere crystal growth frustrated by large spherical impurities*. Science, 309(5738):1231–1233, 2005.

[347] A. Cacciuto, S. Auer, and D. Frenkel, *Onset of heterogeneous crystal nucleation in colloidal suspensions*. Nature, 428:404–406, 2004.

[348] V. W. A. de Villeneuve, D. Verboekend, R. P. A. Dullens, D. G. A. L. Aarts, W. K. Kegel, and H. N. W. Lekkerkerker, *Hard sphere crystal nucleation and growth near large spherical impurities*. J. Phys. Condens. Mat., 17(45):S3371, 2005.

[349] E. Allahyarov, K. Sandomirski, S. U. Egelhaaf, and H. Löwen, *Crystallization seeds favour crystallization only during initial growth*. Nat. Commun., 6:7110, 2015.

[350] J. R. Espinosa, C. Vega, C. Valeriani, and E. Sanz, *Seeding approach to crystal nucleation*. J. Chem. Phys., 144(3):034501, 2016.

[351] A. Cacciuto and D. Frenkel, *Simulation of colloidal crystallization on finite structured templates*. Phys. Rev. E, 72:041604, 2005.

[352] M. Hermes, E. C. M. Vermolen, M. E. Leunissen, D. L. J. Vossen, P. D. J. van Oostrum, M. Dijkstra, and A. van Blaaderen, *Nucleation of colloidal crystals on configurable seed structures*. Soft Matter, 7:4623–4628, 2011.

[353] S. Auer and D. Frenkel, *Suppression of crystal nucleation in polydisperse colloids due to increase of the surface free energy*. Nature, 413:711–713, 2001.

[354] B. A. Lindquist, R. B. Jadrich, and T. M. Truskett, *Communication: From close-packed to topologically close-packed: Formation of laves phases in moderately polydisperse hard-sphere mixtures*. J. Chem. Phys., 148(19):191101, 2018.

[355] B. Cabane, J. Li, F. Artzner, R. Botet, C. Labbez, G. Bareigts, M. Sztucki, and L. Goehring, *Hiding in plain view: colloidal self-assembly from polydisperse populations.* Phys. Rev. Lett., 116:208001, 2016.

[356] T. Vissers. *Oppositely charged colloids out of equilibrium.* PhD thesis, Utrecht University, 2010.

[357] S. Auer and D. Frenkel, *Crystallization of weakly charged colloidal spheres: a numerical study.* J. Phys. Condens. Matter, 14(33):7667, 2002.

[358] S. Auer, W. C. K. Poon, and D. Frenkel, *Phase behavior and crystallization kinetics of poly-12-hydroxystearic-coated polymethylmethacrylate colloids.* Phys. Rev. E, 67:020401, 2003.

[359] P. N. Pusey, W. van Megen, P. Bartlett, B. J. Ackerson, J. G. Rarity, and S. M. Underwood, *Structure of crystals of hard colloidal spheres.* Phys. Rev. Lett., 63:2753–2756, 1989.

[360] J. P. Hoogenboom, D. Derks, P. Vergeer, and A. van Blaaderen, *Stacking faults in colloidal crystals grown by sedimentation.* J. Chem. Phys., 117(24):11320–11328, 2002.

[361] S. Auer and D. Frenkel, *Numerical prediction of absolute crystallization rates in hard-sphere colloids.* J. Chem. Phys., 120(6):3015–3029, 2004.

[362] B. O'Malley and I. Snook, *Structure of hard-sphere fluid and precursor structures to crystallization.* J. Chem. Phys., 123(5):054511, 2005.

[363] M. N. van der Linden, J. C. P. Stiefelhagen, G. Heessels-Gürboğa, J. E. S. van der Hoeven, N. A. Elbers, M. Dijkstra, and A. van Blaaderen, *Charging of poly(methyl methacrylate) (pmma) colloids in cyclohexyl bromide: Locking, size dependence, and particle mixtures.* Langmuir, 31(1):65–75, 2015.

[364] M. E. Leunissen, M. T. Sullivan, P. M. Chaikin, and A. van Blaaderen, *Concentrating colloids with electric field gradients. i. particle transport and growth mechanism of hard-sphere-like crystals in an electric bottle.* J. Chem. Phys., 128(16):164508, 2008.

[365] A. Jouyban, S. Soltanpour, and H.-K. Chan, *A simple relationship between dielectric constant of mixed solvents with solvent composition and temperature.* Int. J. Pharm., 269(2):353–360, 2004.

[366] P. Jiang, T. Prasad, M. J. McFarland, and V. L. Colvin, *Two-dimensional nonclose-packed colloidal crystals formed by spincoating.* Appl. Phys. Lett., 89(1):011908, 2006.

[367] P. Staudhammer and W. F. Seyer, *The dielectric constant of cis- and trans-decahydronaphthalene and cyclohexane as a function of temperature and frequency.* J. Am. Chem. Soc., 80(24):6491–6494, 1958.

[368] C. Rycroft. *Voro++*, 2018. http://math.lbl.gov/voro++/.

[369] A. Stukowski. *Ovito - open visualization tool*, 2018. http://www.ovito.org.

[370] A. Stukowski, *Visualization and analysis of atomistic simulation data with ovito–the open visualization tool.* Model. Simul. Mater. Sci. Eng., 18(1):015012, 2010.

[371] J. A. Barker and D. Henderson, *What is "liquid"? understanding the states of matter.* Rev. Mod. Phys., 48:587–671, 1976.

[372] J. K. Percus and G. J. Yevick, *Analysis of classical statistical mechanics by means of collective coordinates.* Phys. Rev., 110:1–13, 1958.

[373] A. Trokhymchuk, I. Nezbeda, J. Jirsák, and D. Henderson, *Hard-sphere radial distribution function again.* J. Chem. Phys., 123(2):024501, 2005.

[374] A. A. Louis, *Effective potentials for polymers and colloids: beyond the van der waals picture of fluids?* Philos. Trans. R. Soc. London, Ser. A, 359(1782):939–960, 2001.

[375] M. van der Linden. *Long-range repsulsive charged colloids in and out of equilibrium.* PhD thesis, Utrecht University, 2013.

[376] R. J. Hunter. *Zeta potential in colloid science. Principles and applications.* Academic Press, London, 1981.

[377] T. Vissers, A. Imhof, F. Carrique, Ángel V. Delgado, and A. van Blaaderen, *Electrophoresis of concentrated colloidal dispersions in low-polar solvents.* J. Colloid Interface Sci., 361(2):443–455, 2011.

[378] C. P. Royall, M. E. Leunissen, A.-P. Hynninen, M. Dijkstra, and A. van Blaaderen, *Re-entrant melting and freezing in a model system of charged colloids.* J. Chem. Phys., 124(24):244706, 2006.

[379] A. Malins, S. R. Williams, J. Eggers, and C. P. Royall, *Identification of structure in condensed matter with the topological cluster classification.* J. Chem. Phys., 139(23):234506, 2013.

[380] F. Li, D. P. Josephson, and A. Stein, *Colloidal assembly: the road from particles to colloidal molecules and crystals.* Angew. Chem. Int. Ed., 50(2):360–388, 2011.

[381] F. X. Redl, K.-S. Cho, C. B. Murray, and S. O'Brien, *Three-dimensional binary superlattices of magnetic nanocrystals and semiconductor quantum dots.* Nature, 423:968–971, 2003.

[382] E. V. Shevchenko, D. V. Talapin, N. A. Kotov, S. O'Brien, and C. B. Murray, *Structural diversity in binary nanoparticle superlattices.* Nature, 439(6251):55–59, 2006.

[383] M. Cargnello, A. C. Johnston-Peck, B. T. Diroll, E. Wong, B. Datta, D. Damodhar, V. V. T. Doan-Nguyen, A. A. Herzing, C. R. Kagan, and C. B. Murray, *Substitutional doping in nanocrystal superlattices.* Nature, 524(6251):450–453, 2015.

[384] R. Tan, H. Zhu, C. Cao, and O. Chen, *Multi-component superstructures self-assembled from nanocrystal building blocks.* Nanoscale, 8:9944–9961, 2016.

[385] C. Yan and T. Wang, *A new view for nanoparticle assemblies: from crystalline to binary cooperative complementarity.* Chem. Soc. Rev., 46:1483–1509, 2017.

[386] F. Laves and H. Witte, *Der einfluß von valenzelektronen auf die kristallstruktur ternärer magnesiumlegierungen.* Metallw., 15:840–842, 1936.

[387] X. Ye, C. Zhu, P. Ercius, S. N. Raja, B. He, M. R. Jones, M. R. Hauwiller, Y. Liu, T. Xu, and A. P. Alivisatos, *Structural diversity in binary superlattices self-assembled from polymer-grafted nanocrystals.* Nat. Commun., 6:10052, 2015.

[388] W. H. Evers, B. D. Nijs, L. Filion, S. Castillo, M. Dijkstra, and D. Vanmaekelbergh, *Entropy-driven formation of binary semiconductor-nanocrystal superlattices.* Nano Lett., 10(10):4235–4241, 2010.

[389] Y. Wu, S. Li, N. Gogotsi, T. Zhao, B. Fleury, C. R. Kagan, C. B. Murray, and J. B. Baxter, *Directional carrier transfer in strongly coupled binary nanocrystal sperlattice films formed by assembly and in situ ligand exchange at a liquid-air interface.* J. Phys. Chem. C, 121(8):4146–4157, 2017.

[390] E. A. Gaulding, B. T. Diroll, E. D. Goodwin, Z. J. Vrtis, C. R. Kagan, and C. B. Murray, *Deposition of wafer-scale single-component and binary nanocrystal superlattice thin films via dip-coating.* Adv. Mater., 27(18):2846–2851, 2015.

[391] M. I. Bodnarchuk, E. V. Shevchenko, and D. V. Talapin, *Structural defects in periodic and quasicrystalline binary nanocrystal superlattices.* J. Am. Chem. Soc., 133(51):20837–20849, 2011.

[392] Z. Chen and S. O'Brien, *Structure direction of ii-vi semiconductor quantum dot binary nanoparticle superlattices by tuning radius ratio.* ACS Nano, 2(6):1219–1229, 2008.

[393] N. Schaertl, D. Botin, T. Palberg, and E. Bartsch, *Formation of laves phases in buoyancy matched hard sphere suspensions.* Soft Matter, 14:5130–5139, 2018.

[394] Z. Yang, J. Wei, P. Bonville, and M.-P. Pileni, *Engineering the magnetic dipolar interactions in 3d binary supracrystals via mesoscale alloying.* Adv. Funct. Mater., 25:4908–4915, 2015.

[395] S. Hajiw, B. Pansu, and J.-F. Sadoc, *Evidence for a c14 frank-kasper phase in one-size gold nanoparticle superlattices.* ACS Nano, 9(8):8116–8121, 2015.

[396] B. Pansu and J.-F. Sadoc, *Metallurgy of soft spheres with hard core: from bcc to frank-kasper phases.* Eur. Phys. J. E, 40(11):102, 2017.

[397] J. Miao, P. Ercius, and S. J. L. Billinge, *Atomic electron tomography: 3d structures without crystals.* Science, 353(6306), 2016.

[398] T. Willhammar, K. Sentosun, S. Mourdikoudis, B. Goris, M. Kurttepeli, M. Bercx, D. Lamoen, B. Partoens, I. Pastoriza-Santos, J. Pérez-Juste, L. M. Liz-Marzán, S. Bals, and G. Van Tendeloo, *Structure and vacancy distribution in copper telluride nanoparticles influence plasmonic activity in the near-infrared.* Nat. Commun., 8:14925, 2017.

[399] T. Udayabhaskararao, T. Altantzis, L. Houben, M. Coronado-Puchau, J. Langer, R. Popovitz-Biro, L. M. Liz-Marzán, L. Vuković, P. Král, S. Bals, and R. Klajn, *Tunable porous nanoallotropes prepared by post-assembly etching of binary nanoparticle superlattices.* Science, 358(6362):514–518, 2017.

[400] S. Bals, B. Goris, L. M. Liz-Marzán, and G. Van Tendeloo, *Three-dimensional characterization of noble-metal nanoparticles and their assemblies by electron tomography.* Angew. Chem. Int. Ed., 53(40):10600–10610, 2014.

[401] X. Ye, J. Chen, M. Eric Irrgang, M. Engel, A. Dong, S. C. Glotzer, and C. B. Murray, *Quasicrystalline nanocrystal superlattice with partial matching rules.* Nat. Mater., 16(1):214–219, 2017.

[402] Y. Xia and Z. Tang, *Monodisperse inorganic supraparticles: formation mechanism, properties and applications.* Chem. Commun., 48(51):6320–6336, 2012.

[403] S. Wintzheimer, T. Granath, M. Oppmann, T. Kister, T. Thai, T. Kraus, N. Vogel, and K. Mandel, *Supraparticles: functionality from uniform structural motifs.* ACS Nano, 12:5093–5120, 2018.

[404] D. Vanmaekelbergh, L. K. van Vugt, H. E. Bakker, F. T. Rabouw, B. d. Nijs, R. J. van Dijk-Moes, M. A. van Huis, P. J. Baesjou, and A. van Blaaderen, *Shape-dependent multiexciton emission and whispering gallery modes in supraparticles of cdse/multishell quantum dots.* ACS Nano, 9(4):3942–3950, 2015.

[405] F. Bai, D. Wang, Z. Huo, W. Chen, L. Liu, X. Liang, C. Chen, X. Wang, Q. Peng, and Y. Li, *A versatile bottom-up assembly approach to colloidal spheres from nanocrystals.* Angew Chem. Int. Ed., 46(35):6650–6653, 2007.

[406] T. Kister, M. Mravlak, T. Schilling, and T. Kraus, *Pressure-controlled formation of crystalline, janus, and core-shell supraparticles.* Nanoscale, 8:13377–13384, 2016.

[407] Z. Yang, T. Altantzis, D. Zanaga, S. Bals, G. V. Tendeloo, and M.-P. Pileni, *Supracrystalline colloidal eggs: epitaxial growth and feestanding three-dimensional spracrystals in nanoscaled colloidosomes.* J. Am. Chem. Soc., 138(10):3493–3500, 2016.

[408] O. Chen, L. Riedemann, F. Etoc, H. Herrmann, M. Coppey, M. Barch, C. T. Farrar, J. Zhao, O. T. Bruns, H. Wei, P. Guo, J. Cui, R. Jensen, Y. Chen, D. K. Harris, J. M. Cordero, Z. Wang, A. Jasanoff, D. Fukumura, R. Reimer, M. Dahan, R. K. Jain, and M. G. Bawendi, *Magneto-fluorescent core-shell supernanoparticles.* Nat. Commun., 5:5093, 2014.

[409] S. Egly, C. Fröhlich, S. Vogel, A. Gruenewald, J. Wang, R. Detsch, A. R. Boccaccini, and N. Vogel, *Bottom-up assembly of silica and bioactive glass supraparticles with tunable hierarchical porosity.* Langmuir, 34(5):2063–2072, 2018.

[410] P.-p. Wang, Q. Qiao, Y. Zhu, and M. Ouyang, *Colloidal binary supracrystals with tunable structural lattices.* J. Am. Chem. Soc., 2018.

[411] P. Gilbert, *Iterative methods for the three-dimensional reconstruction of an object from projections.* J. Theor. Biol., 36(1):105–117, 1972.

[412] J. M. Pietryga, D. J. Werder, D. J. Williams, J. L. Casson, R. D. Schaller, V. I. Klimov, and J. A. Hollingsworth, *Utilizing the lability of lead selenide to produce heterostructured nanocrystals with bright, stable infrared emission.* J. Am. Chem. Soc., 130(14):4879–4885, 2008.

[413] J. S. Steckel, B. K. H. Yen, D. C. Oertel, and M. G. Bawendi, *On the mechanism of lead chalcogenide nanocrystal formation.* J. Am. Chem. Soc., 128(40):13032–13033, 2006.

[414] A. Dong, J. Chen, P. M. Vora, J. M. Kikkawa, and C. B. Murray, *Binary nanocrystal superlattice membranes self-assembled at the liquid-air interface.* Nature, 466:474–477, 2010.

[415] T. G. Mason and J. Bibette, *Shear rupturing of droplets in complex fluids.* Langmuir, 13(17):4600–4613, 1997.

[416] M. Guizar-Sicairos, S. T. Thurman, and J. R. Fienup, *Efficient subpixel image registration algorithms.* Opt. Lett., 33(2):156–158, 2008.

[417] W. Palenstijn, K. Batenburg, and J. Sijbers, *Performance improvements for iterative electron tomography reconstruction using graphics processing units (gpus).* J. Struct. Biol., 176(2):250–253, 2011.

[418] W. van Aarle, W. J. Palenstijn, J. D. Beenhouwer, T. Altantzis, S. Bals, K. J. Batenburg, and J. Sijbers, *The astra toolbox: A platform for advanced algorithm development in electron tomography.* Ultramicroscopy, 157:35–47, 2015.

[419] A.-P. Hynninen, L. Filion, and M. Dijkstra, *Stability of ls and ls2 crystal structures in binary mixtures of hard and charged spheres.* J. Chem. Phys., 131(6):064902, 2009.

[420] J. B. Friauf, *The crystal structures of two intermetallic compounds.* J. Am. Chem. Soc., 49(12):3107–3114, 1927.

[421] R. L. Berry and G. V. Raynor, *The crystal chemistry of the Laves phases.* Acta Cryst., 6(2):178–186, 1953.

[422] B. S. Murty, J. W. Yeh, and S. Ranganathan. *High-entropy alloys.* Butterworth-Heinemann, 2014.

[423] A. Bauer, J. Kräußlich, L. Dressler, P. Kuschnerus, J. Wolf, K. Goetz, P. Käckell, J. Furthmüller, and F. Bechstedt, *High-precision determination of atomic positions in crystals: The case of* 6*h- and* 4*h-sic.* Phys. Rev. B, 57:2647–2650, 1998.

[424] H. Nyman, S. Andersson, B. Hyde, and M. O'Keeffe, *The pyrochlore structure and its relatives.* J. of Solid State Chem., 26(2):123–131, 1978.

[425] R. E. Smallman and R. J. Bishop. *Metals and materials: science, processes, applications.* Butterworth-Heinemann, 1995.

[426] K. Kumar and P. Hazzledine, *Polytypic transformations in laves phases.* Intermetallics, 12(7):763–770, 2004.

[427] A. Dong, J. Chen, P. M. Vora, J. M. Kikkawa, and C. B. Murray, *Binary nanocrystal superlattice membranes self-assembled at the liquid-air interface.* Nature, 466:474–477, 2010.

[428] E. C. M. Vermolen, A. Kuijk, L. C. Filion, M. Hermes, J. H. J. Thijssen, M. Dijkstra, and A. van Blaaderen, *Fabrication of large binary colloidal crystals with a NaCl structure.* Proc. Natl. Acad. Sci. USA, 106(38):16063–16067, 2009.

[429] L. Filion, M. Hermes, R. Ni, E. C. M. Vermolen, A. Kuijk, C. G. Christova, J. C. P. Stiefelhagen, T. Vissers, A. van Blaaderen, and M. Dijkstra, *Self-assembly of a colloidal interstitial solid with tunable sublattice doping.* Phys. Rev. Lett., 107:168302, 2011.

[430] M. F. Chisholm, S. Kumar, and P. Hazzledine, *Dislocations in complex materials.* Science, 307(5710):701–703, 2005.

[431] P. Hazzledine and P. Pirouz, *Synchroshear transformations in laves phases.* Scripta. Met., 28(10):1277–1282, 1993.

[432] L. Ma, T.-W. Fan, B.-Y. Tang, L.-M. Peng, and W.-j. Ding, *Ab initio study of i2 and t2 stacking faults in c14 laves phase mgzn2.* Eur. Phys. J. B, 86(4):188, 2013.

[433] S. Pronk and D. Frenkel, *Can stacking faults in hard-sphere crystals anneal out spontaneously?* J. Chem. Phys., 110(9):4589–4592, 1999.

[434] D. Wang, T. Dasgupta, E. B. van der Wee, D. Zanaga, T. Altantzis, Y. Wu, S. Bals, C. B. Murray, M. Dijkstra, and A. van Blaaderen. *Binary icosahedral quasicrystals of hard spheres in spherical confinement.* In preparation.

# Summary

Colloidal dispersions are a much studied soft matter system, with properties that are sensitive to mild chemical or physical changes. Milk is the most well known example of a colloidal dispersion in nature. In addition, in our daily life a lot of engineered colloidal dispersions can be encountered: mayonaise, paints, creams, break fluids, electronic ink, etc. These colloids, typically with a size somewhere between 1 and 1000 nm, undergo Brownian motion when suspended in a liquid: a random walk induced by a constant collision of the surrounding molecules in the liquid. Next to their practical use, colloidal dispersions have proven to be a good model system for physical phenomena in condensed matter physics, such as homogeneous and heterogeneous nucleation and the glass transition. As the colloidal particles are much larger than single atoms or molecules, they are also much slower, making it possible to study the processes in details. Moreover, the larger size of the particles makes it possible to study them with microscopy. It was with light microscopy that the Brownian motion of colloidal particles was first observed. Where bright-field microscopy allows for the characterization of 2D systems of colloids close to a micrometer in diameter, confocal microscopy is the most often used technique to characterize 3D colloidal assemblies in real-space. In combination with image analysis, the particle coordinates can be determined in these assemblies, allowing direct comparison to simulations or theory. For colloidal particles with a smaller size electron microscopy allows for the characterization of their assemblies.

In this thesis we quantitatively study arrested colloidal assemblies and processes, by means of both light and electron microscopy. As the acquisition time of these techniques is often longer than the timescale of the dynamics of the particles, we arrest the particles, either by controlled assembly or by the polymerization of the surrounding continuous phase. From the acquired 3D real-space data we extract the coordinates of the particles in the arrested systems, and use them for a quantitative analysis of these systems.

We start this work in **Chapter 2** where we show how focused ion beam scanning electron microscopy (FIB-SEM) tomography can be used to characterize 3D colloidal assemblies. In FIB-SEM tomography the assembly is imaged in 3D by first milling with an ion beam to created a surface, which is then imaged using the electron microscope, after which the next slice is milled for imaging and the process is repeated. The positions (and orientations) of the particles in this 3D image stack can then be retrieved using a localization algorithm. We show that FIB-SEM tomography fills the gap left by transmission electron tomography and confocal microscopy. Where the former is able to retrieve the 3D structure of nanoparticle assemblies, the thickness of these assemblies is limited to $\sim$500 nm. The latter is able to image thicker assemblies, but requires a minimal particle size of $\sim$500 nm. We show that with FIB-SEM tomography assemblies of gold nanorods too thick for imaging with transmission electron tomography can be imaged. In addition, we show how ordered and disordered assemblies of particles with a size close to the resolving power of a confocal microscope can be imaged with FIB-SEM tomography. We find that for a colloidal crystal of particles assembled by controlled drying, there is a slight deformation

of the crystal lattice in the direction of growth, as found before in scattering studies of a similarly grown colloidal crystal.

In **Chapter 3** we present a sample for the alignment, calibration and measurement of the point spread function of confocal STED microscopes. The sample is composed of a colloidal crystal of a mixture of silica particles with either a fluorescently labeled or gold core. The periodicity of the crystal in both the lateral, as well as the axial direction, is used as a ruler for the calibration of distances measured by the microscope. The gold cores in the crystal are used for the alignment of the excitation and depletion laser of the STED microscope at variable depths. The fluorescently labeled cores can be used to measure the point spread function (PSF), the response function of the microscope, at variable depths. By measuring the PSF the resolving power of the microscope can be monitored, which highly depends on the alignment of the microscope. Moreover, the PSF can be used for an accurate restoration of the images recorded with the microscope.

In **Chapter 4** we present a method to arrest colloidal dispersions by the polymerization of a part of the continuous phase. By adding a trifunctional monomer, as well as a photo initiator, to the solvent mixture of the colloidal dispersion, the dispersion can effectively be arrested within a second by the exposure to a UV light pulse. As the monomer is added at a low concentration, the particle interactions are still governed by the solvent mixture. We demonstrate that this method can therefore be applied to particle interactions including nearly hard sphere, long range repulsive, induced dipolar and depletion induced attractive interactions. Moreover, we show that the method is applicable to the two most common particles systems used in confocal microscopy studies of colloidal dispersions: silica and poly(methyl methacrylate) (PMMA) particles, where the particles can be refractive index matched to the solvent mixture, resulting in optimal imaging conditions and the minimization of the attractive van der Waals forces. The method allows for the structural characterization of large 3D colloidal dispersions with dynamics faster than the acquisition speeds of current fast point scanning confocal microscopes. In addition, the arrest allows for the preservation of external field induced meta-stable colloidal assemblies that would otherwise disassemble when the external field is removed. We demonstrate this by the arrest of electric field induced dipolar strings, as well as shear induced colloidal crystals. Finally, we show that this method can be used on systems where the effects of gravity have been canceled out by slow rotations, to study for instance the depletion induced crystallization/agglomeration of density mismatched silica rods. While this chapter focuses on the use of this method for confocal microscopy studies, it can also be used for the arrest of colloidal dispersion for accurate imaging using super-resolution microscopy, as well as FIB-SEM tomography, as described in **Chapter 2**.

We also applied the arrest method to study the homogeneous nucleation of nearly hard spheres, as shown in **Chapter 5**. The method is combined with the dielectrophoretic compression of the spheres, to bring the volume fraction of the particle dispersion to higher supersaturation. The particle dispersion studied was composed of PMMA particles dispersed in a solvent mixture containing halogenated alkanes with added salt, monomer and photo initiator. As the particles in this solvent mixture are known to be slightly charged and swollen, we compare three methods to determine the effective hard sphere diameter of the spheres, for comparison of the phase behavior to literature. The local arrest of the dispersion allows for the probing of the dispersion at different volume fractions,

where a density dependent nucleation rate is found. Moreover, as the dispersion is arrested before imaging, large volumes containing up to 500,000 particles can be characterized. This is of importance for the study of nucleation at low supersaturation, where nucleation events are rare. Using bond order parameters, the crystal structure of the nuclei was found to be randomly hexagonal close-packed (RHCP), with a very slight preference for a hexagonal close-packed (HCP) stacking.

In the final chapter of this thesis, **Chapter 6**, we study a self-assembled binary mixture of nanoparticles in spherical confinement. The mixture was composed of monodisperse CdSe and PbSe nanocrystals with a size ratio of 0.76, which were found to assemble into the hexagonal Laves phase $MgZn_2$ in bulk. The mixture was allowed to crystallize in a slowly drying emulsion droplet and investigated using transmission electron tomography. By using advanced reconstruction algorithms the real-space coordinates of both particles species were retrieved. Bond orientational order parameters were used to distinguish the three Laves phases: $MgZn_2$, $MgCu_2$ and $MgNi_2$. In spherical confinement the same phase as in bulk assembly was found: $MgZn_2$, contrary to earlier studies of the spherically confined assembly of single species where an icosahedral assembly with wedges composed of a cubic crystal was found. We found stacking faults in the $MgZn_2$ structure with local $MgCu_2$ symmetry, which can be explained by the small free energy differences per particles between the two Laves phases. In addition, we found that in contrast to earlier studies of NaCl binary crystals, the small species of the binary mixture are hardly missing. Upon a slight variation of the number ratio (and therefore the stoichiometry) of the two species, we found a large percentage of assemblies to exhibit five-fold symmetry. We therefore hypothesize that the confinement effect of the drying droplet was softened by the presence of a liquid layer of excess small species on the surface of the droplet. The newly found structure with five-fold symmetry is currently under investigation and hints at the formation of a quasicrystalline structure.

# Samenvatting voor een breder publiek

In deze thesis bestuderen wij assemblages van colloïdale deeltjes: deeltjes met een grootte van een miljoenste tot een duizendste millimeter. Deze deeltjes zijn onder andere te vinden als vetdruppeltjes in melk, waterdruppeltjes in mayonaise en het pigment in de inkt van e-readers. Deze mengsels worden suspensies genoemd: een mengsel van kleine deeltjes in een vloeistof waarin deze deeltjes niet oplossen. In dit werk bestuderen wij deeltjes gemaakt van goud, glas, plexiglas en halfgeleidermaterialen. Doordat de deeltjes zo klein zijn, zijn ze onderhevig aan Brownse beweging: een willekeurige beweging van de colloïdale deeltjes door constante botsingen met de moleculen van de vloeistof waarin de deeltjes zich bevinden. Naast het praktische nut van deze deeltjes in dagelijkse toepassingen, worden ze ook gebruikt als modelsysteem voor het fasegedrag van materialen, bijvoorbeeld wanneer en hoe een kristal of glas vormt uit een vloeistof. Inzicht hierin is van belang voor de optimale en gecontroleerde productie van materialen, zoals metalen.

Wanneer de interacties tussen de deeltjes zo worden afgestemd dat ze niet onomkeerbaar elkaar aantrekken, kan een colloïdale suspensie een georganiseerde assemblage vormen. Dit proces heet zelfassemblage: het uit zichzelf ordenen van de deeltjes, zonder hulp van buitenaf. De colloïdale kristallen die door middel van dit proces gevormd kunnen worden zijn interessant voor optische toepassingen. Doordat de periodiciteit van de colloïdale kristallen vergelijkbaar is met de golflengte van zichtbaar licht, kunnen deze gebruikt worden om licht te manipuleren, zoals de reflectie van een specifieke golflengte. In de natuur zijn dergelijke kristallen te vinden op de vleugels van tropische vlinders en in opaal stenen.

Colloïdale deeltjes met een grootte, vergelijkbaar met de golflengte van zichtbaar licht, worden vaak bestudeerd door middel van lichtverstrooiing of lichtmicroscopie. In het geval van lichtverstrooiing worden de afstanden in de colloïdale mengsels gemeten in de zogenaamde reciproke ruimte, terwijl met lichtmicroscopie de afstanden direct in the reële ruimte worden gemeten. Colloïdale deeltjes te klein voor lichtmicroscopie kunnen worden bestudeerd door middel van elektronenmicroscopie, waar elektronen in plaats van fotonen (lichtdeeltjes) worden gebruikt om de deeltjes af te beelden. Een voordeel van microscopie is dat individuele deeltjes kunnen worden afgebeeld, terwijl bij lichtverstrooiing de gemeten afstanden gemiddeld zijn over alle deeltjes, wat het bestuderen van lokale structuren erg lastig maakt. Tegenwoordig is het zowel met licht- als elektronenmicroscopie mogelijk om colloïdale assemblages te bestuderen en de individuele posities van de deeltjes te bepalen. Door middel van deze posities kunnen er vervolgens berekeningen gedaan worden aan assemblages en maakt dit het mogelijk deze direct te vergelijken met simulaties en theoriën.

Hoewel het mogelijk is de posities van de deeltjes te bepalen, kan dit tot nu toe alleen nog voor systemen waar de colloïdale deeltjes stilstaan door de trage acquisitietijd van de microscopietechnieken. Dit kan worden gerealiseerd door te kijken naar mengsels met zeer hoge dichtheden waar de deeltjes op de tijdschaal van de acquisitie bijna niet bewegen. Om toch meer dynamische colloïdale suspensies te kunnen bestuderen, presenteren wij in deze thesis een methode om de deeltjes vast te zetten alvorens deze te kunnen afbeelden met (licht)microscopie.

Nadat in **Hoofdstuk 1** een inleiding wordt gegeven om het werk in deze thesis in context te plaatsen, laten we in **Hoofdstuk 2** zien hoe de posities van deeltjes in een colloïdale assemblage door middel van een combinatie van een gefocuseerde ionenbundel en rasterelektronenmicroscopie kunnen worden verkregen. In deze techniek wordt een driedimensionaal beeld van de assemblage verkregen door plakjes van het materiaal weg te halen met een ionenbundel. Elke keer nadat er een plakje is weggehaald wordt met de elektronenmicroscoop een plaatje gemaakt. Doordat deze plakjes zo dun als een paar nanometer (een miljoenste millimeter) kunnen worden gemaakt en de elektronenmicroscoop een zelfs iets betere oplossend vermogen (of resolutie) heeft, kan met grote precisie de assemblage afgebeeld worden. In een vervolgstap worden dan de posities van de deeltjes uit deze data gehaald.

Waar de huidige lichtmicroscopie niet in staat is assemblages met deeltjes met een diameter onder de 500 nm (1/2000ste millimeter) te karakteriseren, en het het karakteriseren door middel van de huidige elektronenmicroscopie gelimiteerd is in de dikte van de assemblages van kleine colloïdale deeltjes (tot ∼500 nm), is het met de in dit hoofdstuk gepresenteerde methode mogelijk dit gat op te vullen. Met de hier gepresenteerde methode zijn wij in staat een deformatie van de kristalstructuur van een assemblage gemaakt door het gecontroleerd drogen van een colloïdale suspensie waar te nemen. Iets wat tot op heden alleen door middel van verstrooiingstechnieken mogelijk was. Dit maakt het mogelijk de lokale effecten van deze deformatie te bestuderen, en te onderzoeken wat hier de oorsprong van is.

In **Hoofdstuk 3** presenteren wij een preparaat dat gebruikt kan worden voor de kwaliteitscontrole van zogenaamde confocale and STED-microscopen. Bij confocale microscopie wordt een specimen afgebeeld door deze puntsgewijs te scannen met een laser en op elk punt de intensiteit te meten. Wanneer het specimen gekleurd is met een fluorescerende kleurstof, kan met confocale microscopie een 3D-beeld gemaakt worden. Doordat er voor de detector van het licht een *pinhole* (een zeer kleine opening) wordt geplaatst, wordt al het licht dat niet in focus is geblokkeerd. Hierdoor is de confocale microscoop, in tegenstelling tot een normale lichtmicroscoop, in staat dikke samples in kaart te brengen.

STED-microscopie is een recentere techniek gebaseerd op confocale microscopie, waar door middel van het manipuleren van de fluorescente kleurstof moleculen in het sample, het oplossend vermogen van de microscoop kan worden verhoogd. Voor de uitvinding van de STED-microscoop ontving Stefan Hell in 2014 de Nobelprijs voor Scheikunde. Voor beide geavanceerde technieken is een optimale configuratie van het systeem noodzakelijk voor een maximaal oplossend vermogen.

Met ons sample kunnen de microscopen worden gekalibreerd (hoe groot is de afstand die wij meten in de drie dimensies) en uitgelijnd (valt de laserbundel op de juiste plaats en komt het licht optimaal terug de detector in?). Het preparaat bestaat uit een assemblage van twee soorten colloïdale deeltjes gemaakt van glas. In de eerste is er in de kern van het deeltje kleurstof ingebouwd. In het andere deeltje is een klein goudbolletje opgenomen. Doordat de assemblage een kristal is, kan de periodiciteit in de afstand tussen de deeltjes gebruikt worden als een soort liniaal om de microscoop te kalibreren. Het uitlijnen van de lasers kan door te kijken naar het reflectiesignaal van de goudkernen, waarna de resulterende prestatie van de microscoop kan worden gecontroleerd met de fluorescente kernen. Deze controle wordt gedaan door de zogenaamde responsfunctie van de microscoop

te meten: het beeld dat een microscoop zou maken van een ideale puntbron van licht. Deze responsfunctie kan ook gebruikt worden om opgenomen 3D-afbeeldingen te restaureren, door met de responsfunctie terug te rekenen hoe het sample onder de microscoop er precies uit ziet. Tot op heden worden voor al de bovengenoemde controles/metingen verscheidene preparaten gebruikt. Wij combineren deze controles/metingen in een enkel preparaat.

Wij vervolgen de thesis in **Hoofdstuk 4** waar wij laten zien hoe colloïdale mengsels vastgezet kunnen worden. Door een deel van de vloeistof waarin de colloïdale deeltjes zich bevinden te polymeriseren, ontstaat er een netwerk van polymeer dat de deeltjes op zijn plaats houdt, en voorkomt dat door Brownse beweging de deeltjes van positie veranderen. Doordat de polymerisatie kan worden geïnduceerd door de blootstelling van de dispersie aan ultraviolet licht, kan het vastzetten van het mengsel worden getimed. Dit komt van pas wanneer de structuur van een colloïdaal mengsel bepaald moet worden, en de technieken waarmee dat gedaan wordt langzamer zijn dan de tijdschaal waarop de deeltjes Brownse beweging ondergaan. Een voorbeeld hiervan is confocale microscopie: doordat voor een driedimensionale meting veel punten in het volume moeten worden gescand, is dit een relatief langzame techniek. Wanneer met een geavanceerde confocale microscoop een werkbaar volume moet worden afgebeeld, dan is de opnametijd van een enkele 3D-dataset ongeveer 10 seconden. Ter vergelijking: een colloïdaal deeltje met een diameter $\sim$1 $\mu$m in water diffundeert over een afstand gelijk aan zijn eigen diameter in $\sim$1 seconde. Dit maakt dat confocale microscopie een te langzame techniek is om dynamische colloïdale mengsels in 3D in beeld te brengen. Wij laten zien dat onze methode kan worden ingezet bij het bestuderen van suspensies van PMMA-deeltjes (plexiglas) en silicadeeltjes (glas) in oplosmiddelen die vaak worden gebruikt voor het bestuderen van colloïdale mengsels door middel van confocale microscopie.

Naast het bestuderen van dynamische mengsels, kan de methode ook gebruikt worden voor het preserveren van meta-stabiele structuren. Denk hierbij aan geordende structuren die zijn geïnduceerd door een extern veld, maar uiteen vallen wanneer dit extern veld wordt verwijderd. Een voorbeeld zijn draden van deeltjes die zich vormen wanneer een wisselspanning op het colloïdaal mengsel wordt gezet, of geordende mengsels die ontstaan wanneer een alternerende vloeistofstroom wordt geïnduceerd.

In **Hoofdstuk 5** passen we de methode beschreven in het vorige hoofdstuk toe in het bestuderen van het ontstaan van kristallen in een geconcentreerd mengsel van colloïdale deeltjes. Het mengsel dat we hier bestuderen is een veel bestudeerd mengsel van PMMA-deeltjes (plexiglas) deeltjes in een mengsel van apolaire (watervrezende) oplosmiddelen. In dit mengsel interacteren de deeltjes alsof ze biljartballen zijn: ze kunnen niet overlappen en worden op langere afstanden niet tot elkaar aangetrokken of afgestoten. Deze *harde bollen* interactie is een veel onderzochte (in theorie en simulaties) en goed begrepen interactie. Desondanks is het lastig om deze te realiseren voor confocale microscopiestudies: in experimenten zijn de deeltjes altijd een klein beetje geladen, waardoor de interacties iets afwijken. Om toch de resultaten te kunnen vergelijken met theorie en simulaties, schatten wij de *effectieve* harde-bollen-diameter in door middel van verschillende in de literatuur beschreven methodes, en vergelijken de uitkomsten hiervan.

Om het ontstaan van de kristallen te initiëren, verhogen wij lokaal de concentratie van de deeltjes door middel van een wisselstroom. Dit maakt het mogelijk de uiteindelijke concentratie van de deeltjes te variëren doordat deze afhankelijk is van het toegepaste

voltage. Daarnaast kunnen we door het op verschillende tijden lokaal vastzetten van het mengsel verschillende concentraties bestuderen. Doordat de deeltjes worden vastgezet, kunnen zeer grote volumes met tot wel een half miljoen deeltjes in beeld worden gebracht, hetgeen zonder het vastzetten niet mogelijk is. De grote volumes zijn van nut voor het bestuderen van het ontstaan van kristallen bij relatief lage concentraties, waar het ontstaan van kristallen een zeldzame gebeurtenis is en er dus veel statistiek nodig is om het waar te nemen. Uit de opgenomen data schatten wij de nucleatiesnelheid af en vinden dat deze afhangt van de concentratie van het mengsel en vinden hierin overeenstemming met de literatuur. Tenslotte bepalen wij de lokale structuur van de deeltjes door middel van het berekenen van zogenaamde orde-parameters op basis van de coördinaten van de deeltjes. Wij vinden dat de lokale symmetrie van de deeltjes in de kristalkernen overeenkomt met een combinatie van twee hexagonale kristalstructuren (hexagonaal dichtst gepakt en vlak-gecentreerd kubisch).

In het laatste hoofdstuk van deze thesis, **Hoofdstuk 6**, bestuderen we een colloïdale assemblage bestaande uit een combinatie van twee deeltjes met verschillende groottes. De deeltjes, bestaande uit halfgeleider materiaal, hadden een grootteverhouding van 0.76. Deze grootteverhouding komt overeen met die van de Laves-kristalstructuren: $MgZn_2$, $MgCu_2$ en $MgNi_2$. Door het deeltjesmengsel te laten kristalliseren in langzaam opdrogende emulsiedruppeltjes, wordt de uiteindelijke assemblage bolvormig. Dit maakt het ideaal voor transmissie elektronen tomografie, waarin het sample langzaam geroteerd wordt en er onder verschillende hoeken een afbeelding wordt gemaakt. Uit deze serie afbeeldingen kan vervolgens een 3D-beeld worden gereconstrueerd. Deze methode is vergelijkbaar met een CT-scan, waar röntgenstralen worden gebruikt in plaats van elektronen. Doordat de assemblage sferisch is, is de weglengte van de elektronen voor elk plaatje hetzelfde. Uit de verkregen 3D-data hebben we vervolgens de coördinaten van alle deeltjes bepaald. Met deze coördinaten hebben we door middel van orde-parameters de lokale symmetrieën van de deeltjes berekend en konden we de drie Laves-kristalstructuren onderscheiden.

In de bolvormige begrenzing van de opdrogende emulsiedruppel vormde het mengsel van colloïdale deeltjes de (niet-kubische) $MgZn_2$-structuur, overeenkomend met de kristalstructuur die wordt gevonden bij de kristallisatie zonder begrenzing (of in bulk). Dit in tegenstelling tot eerder werk waar deeltjes van één enkele soort in een bolvormige begrenzing kristalliseerden tot een icosaëdrische assemblage. Deze assemblage was opgebouwd uit 3D-taartpunten waar de deeltjes een vlak-gecentreerde kubische kristalstructuur hadden.

Wanneer echter de verhouding in het aantal kleine en grote deeltjes in ons mengsel werd aangepast, namen we wel de icosaëdrische symmetrieën waar. Wij vermoeden dat dit komt doordat eerder een overschot aan kleine deeltjes een vloeibaar laagje vormde op het oppervlak van het kristal, en daarmee het effect van de bolvormige begrenzing teniet deed. De icosaëdrische structuur die wij alsnog vonden wordt nu onderzocht en het heeft er alle schijn van dat dit een quasikristallijne structuur heeft. Dit betekent dat de structuur geen repetitie vertoont (zoals een normaal kristal), maar wel andere regelmatigheden in de structuur heeft. Deze quasikristallen zijn pas in de jaren tachtig van de vorige eeuw ontdekt en de ontdekker, Daniel Shechtman, werd daar in 2011 voor bekroond met de Nobelprijs voor de Scheikunde.

# Acknowledgements

This thesis could not have been completed with the support and help of the many people that were around during my PhD. Here I would like to acknowledge them all for their guidance, inspiration, distraction and being there for me.

First and foremost I would like to thank my supervisor and *promotor* Alfons van Blaaderen for guiding me through the process. Your knowledge of our research field (and beyond) and the literature never ceased to amaze me. In addition, your enthusiasm and flow of new ideas where to go next were inspiring to me. This combined with the freedom to try new techniques and directions allowed me to broaden my knowledge. Thanks for the comprehensive (scientific) discussions during meetings and the extensive coffee breaks.

I would also like to thank the staff of Soft Condensed Matter and Biophysics for their help and advice. Although this PhD thesis was completed without a *co-promotor*, your help has highly contributed to this work and I have much appreciated the willingness to answer my questions. I want to thank Hans for sharing his knowledge on microscopy. I really enjoyed our collaboration on the calibration/alignment sample project. In addition, I want to thank Marjolein for the collaboration on the binary quasicrystal project, which was, sadly enough, beyond the scope of this thesis. Next to the collaboration, I enjoyed all the discussions during work or at the many conferences or schools. I also want to thank Arnout for all the help and advice during my PhD, but also during the earlier projects I did in the group, I always found your door open for questions (unless it was of course a well deserved *papadag*). Gerhard, thanks for the *Mozartkugeln* and the 3D printing. Finally, I want to thank Laura, Marijn, René, Patrick, Krassimir and Freddy for the nice discussions and advice in the past years.

Without the technical staff I would have felt lost on frequent occasions. First of all, Peter, it was a pleasure working together. I really enjoyed your company and your sense of humor, which was always there, even when things did not work as they were supposed to be. I also would like to thank Dave. Your technical knowledge you were always willing to share, but also the support in more difficult times. For any issues associated with the lab, I could always turn to Relinde, thanks for keeping the lab running in order. I also want to thank Chris and Hans for the nice encounters at the electron microscopes. Finally, I would like to thank Judith for all the help in the lab, the collaboration and your expertise. We miss you.

I would also like to thank all the people in OL061 for all the administrative support and the nice chats upon visiting the office: thanks Marion, Thea, Linda and Mijke. I would like to specifically thank Hester for the effort to arrange everything during the completion of this thesis, even when I was in a different time zone. In addition, I would like to thank Dianne for the nice chats and the help beyond the science.

My office mates were the ones who had to put up with me for the most time during the past 5 years. First of all: thanks Da for the amazing time. I really enjoyed our collaborations on the binary systems and I do not know if I ever encountered someone working that hard. I often think back of the Christmas holiday in 2017: your stubbornness has been rewarded. Thanks also for the monthly update on where to eat 点心, and finally

taking us there for dinner. Thanks also Srivatssan for the fun years. Da and me both apologize for keeping you from the window for all these years. I hope you enjoyed the last couple of weeks there. Finally, I would like to thank Weikai for the help in my first steps of coding, in the brief time we shared the office.

It was my pleasure to supervise Peter in his bachelor research project. I appreciated your directness, and your deadpan humor during presentation was a pleasure to watch. Although I did not officially supervise Marc: thanks for the nice collaboration on your master research project.

Before starting my PhD, I was a student myself and I would like to thank a number of people for their guidance in my earlier research projects. First of all Teun, thanks for your infectious enthusiasm. Bo and Rao, thanks for introducing me to particles synthesis and electric fields. Finally, Peter, Ronald and Erik, thanks for the good time in Vienna, which motivated me to do this PhD.

My office was neighbored by two offices with the most pleasant people. To start with OL012, I should thank Pepijn for the first and most successful(?) buddyship of SCM. Rainbows and unicorns indeed. Thanks again for hosting me and Lotte in Brooklyn, with bonus midnight entertainment. Anna, it was my pleasure to collaborate intensively with you in the last couple of months. Your *leergierigheid* and your enthusiasm has no limits, even while 'everything takes longer than it takes'. Sorry for pulling your work schedule further into the Dutch night while collaborating from the other side of the Atlantic ocean. Thanks Jessi for the nice early hours at work and the nice bike rides. It was a pleasure to work together on the FIB-SEM project. Wessel, thanks for the nice and sometimes lengthy discussions, being an excellent teammate in beating the Italians with foosball, the bird care and your vintage shirt on Fridays. It was an honor to be your conference/school roomie and *paranimf*. Henriëtte, Nina and Johan, thanks for being nice colleagues and the pleasant coffee breaks and cakes.

On the other side of my office was the OL016 simulation cave, to help me out on any coding issues or complex equations. To start with Tonnishtha, thanks for the work together on the binary systems, your help (even when you were super busy yourself), and for being around in the late hours. Still, I think you should join for lunch more often. Giulia, thanks for your laugh and the good times spend in the heat of Varenna. Siddarth, thanks for being the kind oasis of calm in your office and being open to questions at any time. Thanks Simone for the good times at the foosball table, Varenna and all other conferences and trips. But I am still waiting for that gnocchi that never came. John, you are the kindest person I have ever met, always helpful and in a good mood. Anjan, thanks for your excellent German, your infectious laugh and the dinner at your place.

They are some other colleagues who I have closely worked with over the past years I have not mentioned yet. Jantina, it was a pleasure working together on the calibration project, and I am thankful for your patience even when things went slow. I really enjoyed the trip to Bordeaux. Thijs, it was a pleasure working together, being it all the way back during Special Relativity classes or later at the SP8. I really enjoyed the times at the conferences and of course the *Bermudadreieck*. But most of all thanks for the final push to do this PhD research. Thanks, Wiebke, for being an awesome colleague with lots of good spirit and advice. I really enjoyed all social activities you organized, from beers with peers to the pubquiz. Thanks for the hospitality in Berlin, as well as a place to crash during

the final week of my stay at SCM. Fabian, thanks for sharing your chemical knowledge and answering all my questions on the subject. Matthijs, I enjoyed the long hours at the FIB-SEM together. And if there was no FIB-SEM, there was coffee, even if you were on the opposite side of *Princetonplein*. Thanks also for your elaborate comments on the writing.

Still, there are a lot more colleagues to thank. Zdenek, thanks for all the nice discussions and the occasional late night chess game in *De Rat*. Thanks also for showing me and Lotte around in Prague. Guido, thanks for all the fun times at the foosball table, challenging me to perform at my best every time. Thanks also for the time in Varenna. Thanks Chris, for being an awesome, laid-back person. Thank you Vasilis for your frequent visits to the office putting a smile on my face. Harini, thanks for the delicious food at you (former) place in Den Haag. It was a nice to see how quickly you mastered the Dutch language. Nick, it was good to see I was not the only one suffering from the extreme temperatures in Varenna. Thanks for the good times with you and Charlotte. And the list gets even longer, thanks to everyone for the good times in the Ornstein lab: Stijn, Naveed, Rama, Carmine, Sina, Tom, Jissy, Marlous, Berend, Federico, Tian-Song, Michiel, Robin, Robin, Yang, Maarten, Albert, Ajoy, Massi, Douglas, Gabriele, Xiaodan, Dnyaneshwar, Emanuele, Murphy, Frankje, Ravi, Rik, Somil, Xiaobin, Neftali, Sergei, Jaco, Elleke, Sajjad, Bram en Mathijs.

During my PhD research I also interacted with people outside of the Ornstein building. I would like to thank Daniele Zanaga, Thomas Altantzis, Yaoting Wu, Sara Bals and Chris Murray for the collaboration on the binary systems, Job Fermie for the advice on embedding resins, Eli Sloutskin for the collaboration on confocal tomography and Burak Eral for the discussion on the arrest of colloidal dispersions. Finally, I would like to thank Job Thijssen for working together, and I hope our work will be finished one day.

In the past months I have started working in a new group. I want to thank Michelle, Srishti, Phalguni and Joey for the nice new environment and I am looking forward to the coming time working together. In addition, I would like to thank the neighbors for the relaxing chats and lunches down the hall, thanks Deniz, Zack en Chirandjit.

Mijn wekelijkse afleiding op de dinsdagavond was het wekelijkse volleybaluurtje. Ik wil graag alle teamgenoten gedurende de jaren bedanken voor de leuke tijd: Caspar, Arjan, Rosa, Anne, Pieter, Samia, Nienke, Margriet, Rogier, Eline, Bertine, Karin, Guus, Tessa, Judith, Evan, Kim en Niels. Ik heb genoten van de wekelijkse nazit na het sporten, en de activiteiten daar buiten. Ik wil ook graag de Maandag EetClub (MEC) bedanken voor de ontspannen maandagavonden. Bedankt Bob, Ninke, Rogier, Lizelot, Lucie, Jaap, Petra en Anne voor de wekelijkse discussies en evaluaties van ieders avonturen in het leven. Ik waardeer ook enorm de vriendschap binnen de Duizend Baasheid crew. Bedankt Hugo, Mak, Arjan, Eduard, Laurens en Roel voor de leuke tijden samen, met of zonder plaatjes, en de steun door dik en dun. *Nosnost Buňky.* Tot slot wil ik ook Fokke-Jan bedanken voor de vriendschap en steun door de jaren heen, met hier en daar de nodige kritische opmerkingen.

Ik sluit af met het bedanken van mijn familie. Ik begin in Dordrecht. Bedankt Agnes, Henny, Oskar, Charlie en Nino voor al het gelach en het warme welkom elke keer als ik naar Dordrecht, een tweede thuis, afreis. Daarnaast, Henny, dank voor het ontwerp van de mooie cover van deze thesis.

Stefanie, Hugo, Natasja, Timur, Arina, Laurens en Evelien: bedankt voor jullie steun gedurende de jaren. Hugo en Laurens: dank ook voor jullie steun in de rug als *paranymfen*. Lieve Paul en Melanie, bedankt voor jullie onbeperkte steun in alles wat ik doe, waar ik ook ben, en voor het mij laten doen wat op mijn weg komt. Mijn liefste Lotte, dank voor het er altijd voor me zijn, ook als het niet meezit. Ik geniet elke dag van het leven met jou. Laten we vieren wat er nog komt.

# List of Publications

This thesis is based on the following publications:

- J. E. S. van der Hoeven / **E. B. van der Wee**, D. A. M. de Winter, M. Hermes, Y. Liu, J. Fokkema, M. Bransen, M. A. van Huis, H. C. Gerritsen, P. E. de Jongh and A. van Blaaderen, *Bridging the Gap: 3D Real-Space Characterization of Colloidal Assemblies via FIB-SEM Tomography*, manuscript submitted (Chapter 2)
- **E. B. van der Wee** / J. Fokkema, M. del Pozo Puig, C. L. Kennedy, D. A. M. de Winter, P. N. A. S. Speets, H. C. Gerritsen and A. van Blaaderen, *One 3D test sample for the calibration, alignment and measurement of point spread functions of super-resolution and confocal microscopes*, manuscript in preparation (Chapter 3)
- **E. B. van der Wee**, A. G. Nikolaenkova, A. Grau Carbonell, J. C. P. Stiefelhagen, A. K. Kandar, M. H. van Huis, P. J. Baesjou, A. Imhof and A. van Blaaderen, *Arrest of colloidal dispersions with conservation of structure for quantitative 3D real-space analysis*, manuscript in preparation (Chapter 4)
- **E. B. van der Wee** / A. G. Nikolaenkova, P. J. Baesjou, A. Imhof and A. van Blaaderen, *Confocal microscopy study of homogeneous crystallization of nearly hard sphere colloids by the arrest of the dispersion*, manuscript in preparation (Chapter 5)
- D. Wang / T. Dasgupta / **E. B. van der Wee**, D. Zanaga, T. Altantzis, Y. Wu, G. M. Coli, S. Bals, C. B. Murray, M. Dijkstra and A. van Blaaderen, *Binary icosahedral quasicrystals of hard spheres in spherical confinement*, manuscript in preparation (Chapter 6)
- D. Wang / **E. B. van der Wee** / Y. Wu, D. Zanaga, T. Altantzis, T. Dasgupta, S. Bals, M. Dijkstra, C. B. Murray and A. van Blaaderen, *Real-space analysis of Laves phase supraparticles*, manuscript in preparation (Chapter 6)

Other publications by the author:

- W. Albrecht, **E. B. van der Wee**, D. Wang and A. van Blaaderen, *Femtosecond laser-induced directed movement of Au NPs*, manuscript in preparation
- D. Wang / M. Hermes, R. Kotni, Y. Wu, N. Tasios, Y. Liu, B. de Nijs, **E. B. van der Wee**, C. B. Murray, M. Dijkstra and A. van Blaaderen, *Interplay between spherical confinement and particle shape on the self-assembly of rounded cubes* Nat. Commun. **8**, 2228 (2018)
- S. R. Liber, G. Indech, **E. B. van der Wee**, A. V. Butenko, T. E. Kodger, P. J. Lu, A. B. Schofield, D. A. Weitz, A. van Blaaderen and E. Sloutskin, *Axial confocal tomography of capillary-contained colloidal structures* Langmuir **33**, 13343–13349 (2017)

- P. G. Moerman, H. W. Moyes, **E. B. van der Wee**, D. G. Grier, A. van Blaaderen, W. K. Kegel, J. Groenewold and J. Brujic, *Solute-mediated interactions between active droplets* Phys. Rev. E **96**, 032607 (2017)
- F. Hagemans, **E. B. van der Wee**, A. van Blaaderen and A. Imhof, *Synthesis of Cone-Shaped Colloids from Rod-Like Silica Colloids with a Gradient in the Etching Rate* Langmuir **32**, 3970–3976 (2016)
- B. Peng, **E. B. van der Wee**, A. Imhof and A. van Blaaderen, *Synthesis of Monodisperse, Highly Cross-Linked, Fluorescent PMMA Particles by Dispersion Polymerization* Langmuir **28**, 6776–6785 (2012)

# About the author

Ernest van der Wee was born on the 22nd of December 1985 in Almelo, the Netherlands. In Almelo, he attended De Vrije School Almelo primary school and O.S.G. Erasmus secondary school. After that he studied at Utrecht University and obtained his bachelor degree in Chemistry in 2010 with a thesis project at the Soft Condensed Matter group under supervision of Teun Vissers and Arnout Imhof, entitled *Crystal formation of binary oppositely charged colloids with a size ratio of 0.5*. In 2013 he completed the master program Nanomaterials: Chemistry and Physics. During this program he visited the Universität für Bodenkultur Wien in Austria for an internship project in the group of Erik Reimhult entitled *Study on superparamagnetic iron-oxide nanoparticle stabilized Pickering emulsions* under supervision of Peter van Oostrum and Ronald Zirbs. His master thesis project was carried out in the Soft Condensed Matter group under supervision of Bo Peng, Rao Vutukuri, Arnout Imhof and Alfons van Blaaderen and was entitled *Flexible fluorescently labelled colloidal bead chains: synthesis and their real-space studies*. He then started his PhD research under supervision of Alfons van Blaaderen of which the main results are described in this thesis. His research has been presented at national and international conferences and published in peer-reviewed journals.

Currently, Ernest is working in the group of Michelle Driscoll at Northwestern University, Evanston, Illinois, USA. His research is now focused on magnetic field induced active colloids.